Technische Universität München
TUM School of Natural Sciences

Elucidating Dynamic Responsiveness in Model Rigid and Flexible Metal-Organic Frameworks

Jan Berger

Die vorliegende Dissertation wurde am Lehrstuhl für Anorganische und Metall-organische Chemie der Technischen Universität München im Zeitraum von Januar 2019 mit Dezember 2022 angefertigt.

"Unless, said I, either philosophers become kings in our states or those whom we now call our kings and rulers take to the pursuit of philosophy seriously and adequately, and there is a conjunction of these two things, political power and philosophical intelligence, while the motley horde of the natures who at present pursue either apart from the other are compulsorily excluded, there can be no cessation of troubles, dear Glaucon, for our states, nor, I fancy, for the human race either."

Dialog Between Socrates and Glaucon

THE REPUBLIC, BOOK V
PLATO

PREAMBLE
VORWORT

The transformation to a sustainable society, economy, and industry – a change that requires monumental, universal effort – is mandatory and overdue. At the center of this transformation are resource and energy sustainability and efficiency: use less resources to the same effect and make sure what is used can be reused or recycled. In my humble opinion and at the risk of appearing hypocritical or superficial, in today's circumstances every scientist should be conscious of these necessities in relation to their work. This does not mean everyone should solely do research on sustainable chemistry and every publication should start with "To save humanity and our planet, we herein present...". But it should be in scientists minds when considering the big picture and path of progression of their research field. Chapter 1 partially aims to incentivise this perspective even though the work presented in this thesis is fundamental in nature, not related to immediate applications.

This dissertation is written in English and directs to English references, however, some chapters are partially provided in German. These paragraphs can be found in the appendix.

Der Wandel hin zu einer nachhaltigen Gesellschaft, Wirtschaft und Industrie – unter monumentaler und universeller Anstrengungen – ist alternativlos und überfällig. Im Mittelpunkt dieser Transformation stehen die nachhaltige und effiziente Nutzung von Ressourcen und Energie: mit weniger Ressourcen das Gleiche erreichen und sicherstellen, dass das, was verwendet wird, wiederverwendet oder recycelt werden kann. Meiner bescheidenen Meinung nach, auch auf die Gefahr hin heuchlerisch oder oberflächlich zu erscheinen, sollten sich unter den heutigen Umständen alle Forschenden dieser notwendigen Transformation und dem Bezug zu ihrer Arbeit bewusst sein. Das bedeutet nicht, dass alle über nachhaltige Chemie forschen sollten und jede Veröffentlichung mit "Um die Menschheit und unseren Planeten zu retten, zeigen wir hier ..." beginnen muss. Aber es sollte im Bewusstsein der Forschenden präsent sein, wenn sie den Gesamtkontext und die Richtung der Entwicktlung ihres Forschungsgebiets reflektieren. Kapitel 1 soll diese Perspektive teilweise geben,

auch wenn die in dieser Dissertation vorgestellten Arbeiten fundamentalerer Natur sind und keinen unmittelbaren Bezug zu Anwendungen haben.

Diese Dissertation ist in Englisch geschrieben und referenziert in Englisch verfasste Publikationen. Manche Kapitel wurden ausschnittsweise ins Deutsche übersetzt. Diese Kapitel sind im Anhang dieser Arbeit zu finden.

ACKNOWLEDGMENTS
DANKSAGUNG

I, first and foremost, would like to thank PROF. DR. DR. H. C. ROLAND A. FISCHER for welcoming me to his group, supervising my thesis with great idealism and creativity, giving me the opportunity to pursue knowledge for its own sake, and providing the foundation and spirit on which this great group is built. I am very thankful to have been granted the opportunity for a research stay in Hokkaido, build cooperations with universities across the world, and naturally partake in numerous conferences and summer schools.

I am very thankful for the tireless work of PROF. DR. STEFAN KASKEL spearheading and organizing the FOR2433 project group – from my perspective behind the curtain – making many meetings and fruitful cooperations possible.

I was very fortunate to be part of DR. GREGOR KIESLICH's research sub-group and am grateful for and impressed by his style of leadership, communication, and creativity without which this work would not have been possible. I very much enjoyed both scientific discussions and social events within this dynamic group. I am still low-key happy the name *HyFM subgroup* stuck and am still convinced it also would make a great radio channel title.

I thank PROF. DR. SHIN-ICHIRO NORO for his role as mentor especially during my time at Hokkaido University and his friendliness and openness I was welcomed with into his group. I am grateful for the luxurious access times to measurement equipment and his efforts to continue some of our work even after I had to return to Munich.

I am incredibly thankful to DR. PIA VERVOORTS for both integrating me into the group, showing me the ropes of MOF research, sharing so many tips and knowledge, and being someone to look up to especially in the early phase in which a dissertation seems more daunting than doable.

I thank DR. ANDREAS SCHNEEMANN for supporting me in continuing work on the honeycomb MOFs and pointing out research opportunities which ultimately lead to

ABSTRACT

Metal-organic frameworks (MOFs) can combine porosity and smart responsiveness and are a highly tunable material class. This feature pairing has evident potential to greatly increase resource and energy efficiency in separation processes and may unlock new applications currently unfeasible on practical scale. MOFs are build from discrete building blocks; metal nodes and organic molecules linking these. This on one side simplistic concept allows for huge variety in combinations and the opportunity to tailor virtually any responsiveness desired. However, on the other side this creates incredible design complexity. As such, much of MOF research is focused on unraveling generalizable, underlying design principles in order to be able to purposefully design responsiveness as needed for application. The work within this thesis elucidates on two aspects of dynamic responsiveness in MOFs: its working principles as optional feature in rigid, otherwise unresponsive MOFs and the impact additional factors like attached nanoparticles and solvation medium have on flexible, intrinsically responsive MOFs.

The first study explores the key factors of conformationally dynamic functionalizations directing adsorptive-responsiveness in a rigid MOF. Therein the honeycomb-like $Zn_2(fu-bdc)_2bpy$ (fu-bdc^{2-} = 2,5-difunctionalized-1,4-benzenedicarboxylate; bpy = 4,4'-bipyridine) serves as model material due to its lack of features strongly directing adsorptive-responsiveness, like open-metal sites or big structural changes during physisorption, and its feasibility for extensive and homogeneous pore modification which improves correlation of responsiveness to linker functionalization. Sorption and separation properties towards C_2H_2 and CO_2 were selected as the study case. Ideal adsorbed solution theory (IAST) selectivities, isosteric enthalpies of adsorption, Henry constants, breakthrough experiments, and simulations of dynamic properties were correlated to a series of linker functionalizations. Ultimately, two dominating factors that determine responsiveness are identified: polarizability and sorption site accessibility. These parameters are shown to be accessible through linker modification and the results suggest transfer to other MOFs toward extrinsic gating for sophisticated modulation of their sorption selectivity.

The following two studies investigate the impact of surface-attached nanoparticles (NPs) on responsiveness of the supporting MOF in two NP@flexibleMOF composite series. One study looks at changes in thermal expansion (TE) of $Pt@Zn_2(DP-bdc)_2dabco$ (DP = 2,5-dipropoxy; dabco = 1,4-diazabicyclo[2.2.2]octane) in dependence of platinum NP loading. TE is highly relevant for the NP@MOF composite class because perspective applications in temperature-swing processes or catalysis subject them to significant fluctuations which can compromise performance if TE is mismanaged. Findings support the chemical intuition that surface-mounted NPs restrict deformation of the MOF and suggest that composite materials exhibit superior TE properties thereby excluding thermal stress as limiting factor for their potential application.

The other study looks at switchability within the unexplored NP@flexibleMOF hybrid materials, concretely $NP@Zn_2(BME-bdc)_2dabco$ (BME = 2,5-bismethoxy-ethoxy) with both platinum and SiO_2 NPs. This MOF responds to both CO_2 and temperature allowing subsequent assessment of both stimuli. Physisorption triggered switching is found to be fully retained and reversible in all NP@MOF composites; NPs stabilize the large pore (lp) state slightly. This stabilizing effect is also observed in temperature-induced switching. However, composites with Pt NPs loose long-range order during reversion to the narrow pore (np) state while SiO_2 NPs allow a fully reversible transition. These findings suggest that the exerted material strain triggering the switching is heavily dependent on NP size and stimulus applied, but importantly that guest-induced switchability can be fully realized in NP@flexMOF hybrid materials.

The fourth study consists of the initial experimental and methodological milestones towards elaborating solvent-switchability of the $Zn_2(fu-bdc)_2dabco$ family. A series of five functionalized derivatives with CO_2-induced phase transitions is investigated by powder X-ray diffraction (PXRD) and qualitative resolvation experiments with various polar protic and aprotic solvents. It is shown that even sterically demanding solvents are able to trigger a response irrespective of MOF functionalization. Only the $Zn_2(DP-bdc)_2dabco$ derivative exhibits pronounced differences in its responses which at this point can not be attributed to a single factor of either MOF or guest. Nevertheless, the diverse set of responses pose interesting questions about the directing factors waiting to be unraveled. Furthermore, a reproducible testing protocol for qualitative analysis was established laying the foundation for further studies investigating quantitative behavior by vapor physisorption experiments or similar methods observing transient states.

ZUSAMMENFASSUNG

Metallorganische Gerüststrukturen (engl. metal-organic frameworks, MOFs) sind eine hochgradig modifizierbare Klasse von Materialien, die Porosität und smarte Responsivität in sich kombinieren können. Diese Kombination hat das Potenzial die Ressourcen- und Energieeffizienz in Trennprozessen erheblich zu steigern und neue Anwendungen, die derzeit noch nicht in praktischem Maßstab realisierbar sind, zu erschließen. MOFs sind aus diskreten Bausteinen aufgebaut: Metallknotenpunkte und organische Moleküle, die diese miteinander verbinden. Dieses einfache Konzept erlaubt einerseits eine enorme Kombinationsvielfalt und die Möglichkeit, praktisch jede gewünschte Responsivität zu designen. Andererseits führt dies jedoch zu unglaublicher Komplexität. Daher konzentriert sich ein Großteil der MOF-Forschung darauf verallgemeinerbare Designprinzipien zu entschlüsseln, die es ermöglichen Responsivität nach Bedarf einstellen zu können. Die Arbeiten im Rahmen dieser Dissertation untersuchen zwei solcher potentiellen Prinzipien: optional integrierte Responsivität in starren MOFs und die Auswirkungen von verankerte Nanopartikel und das Solvatationsmedium auf flexible, responsive MOFs.

Die erste der vier Studie untersucht welche Faktoren von dynamischen Funktionalisierungen das Adsorptionsverhalten in starren MOFs steuern können. $Zn_2(fu-bdc)_2bpy$ (fu-bdc^{2-} = 2,5-difunktionalisiertes 1,4-Benzoldicarboxylat; bpy = 4,4'-Bipyridin) dient dabei als Modellmaterial, da es keine inherenten Merkmale aufweist, die das Adsorptionsverhalten stark beeinflussen und es sich für eine umfassende und homogene Porenmodifikation eignet. Die Studie untersucht die Sorptions- und Trennfähigkeit gegenüber C_2H_2 und CO_2. IAST-Selektivitäten (ideal adsorbed solution theory, IAST), isostere Adsorptionsenthalpien, Henry Konstanten, Durchflussexperimente und Simulationen der dynamischen Eigenschaften wurden mit einer Reihe von Linkerfunktionalisierungen korreliert. Zwei dominierende Faktoren konnten identifiziert werden, die die Responsivität bestimmen: die Polarisierbarkeit der Funktionalisierungen und die Zugänglichkeit der Sorptionsstelle. Diese Parameter sind durch Linkermodifikation zugänglich und die Ergebnisse deuten auf einen möglichen Transfer auf andere MOFs hin.

Die nächsten beiden Studien untersuchen die Auswirkungen von an der Oberfläche befindlichen Nanopartikeln (NPs) auf die Responsivität des MOF in zwei verschiedenen Kompositen. Eine Studie untersucht die Thermischen Expansion (TE) von Pt@Zn_2(DP−bdc)$_2$dabco (DP = 2,5-Dipropoxy; dabco = 1,4-Diazabicyclo[2.2.2]-oktan) in Abhängigkeit der Beladung mit Platin-NPs. TE ist für NP@MOF Materialien von großer Bedeutung, da explizit sie bei Anwendungen erheblichen Temperaturschwankungen ausgesetzt sind, die die Leistung beeinträchtigen können, wenn ihre TE nicht richtig gesteuert wird. Die Resultate spiegeln die chemische Intuition insoweit wieder, dass NPs die Verformung des MOF einschränken, und legen nahe, dass NP@MOF Komposite verbesserte TE-Eigenschaften aufweisen können. Die andere Studie untersucht die Responsivität neuer NP@flexMOF-Materialien, konkret NP@Zn_2(BME−bdc)$_2$dabco (BME = 2,5-Bismethoxy-Ethoxy) mit sowohl Platin als auch SiO_2 NPs. Dieser MOF ist responsiv gegenüber CO_2 und Temperatur, was eine Evaluierung beider Stimuli ermöglicht. Die durch Physisorption ausgelöste Phasenumwandlung wird in allen NP@MOF-Materialien vollständig und reversibel erhalten. Bei termperatur-induzierter Transformation verlieren die Verbundwerkstoffe mit Pt NPs jedoch bei der Reversion während dem Kühlen teilweise ihre Kristallinität, während SiO_2 NPs eine vollständig reversible Transformation ermöglichen. Diese Ergebnisse deuten darauf hin, dass durch Adsorbate induzierbare Schaltbarkeit in NP@flexMOF-Hybridmaterialien vollständig realisiert werden kann, aber auch, dass die die Phasenumwandlung auslösende Spannung stark von Größe der NPs und dem angewandten Stimulus abhängt.

Die abschließende vierte Studie besteht aus dem ersten experimentellen und methodischen Meilensteinen zur Erforschung der Lösungsmittel-Responsivität der Zn_2(fu−bdc)$_2$dabco-Familie. Eine Serie aus fünf funktionalisierten Derivaten wird mit Röntgendiffrakometrie und qualitativen Solvataionsexperimenten mit verschiedenen polaren protischen und aprotischen Lösungsmitteln untersucht. Es zeigt sich, dass selbst sterisch anspruchsvolle Lösungsmittel in der Lage sind, eine Transformation auszulösen – unabhängig von der MOF-Funktionalisierung. Lediglich Zn_2(DP−bdc)$_2$dabco weist deutliche Unterschiede in seiner Responsivität auf, die gegenwärtig nicht auf einen einzelnen Faktor des MOFs oder Solvents zurückgeführt werden können. Darüber hinaus wurde ein reproduzierbares Testprotokoll für die qualitative Analyse erstellt, das die Grundlage für weitere Studien zur Untersuchung des quantitativen Verhaltens durch z.B. Dampf-Physisorptionsexperimente bildet.

TABLE OF CONTENTS

ABBREVIATIONS

0D	zero-dimensional
1D	one-dimensional
2D	two-dimensional
3D	three-dimensional
4D	four-dimensional
bbcdc^{4-}	9,9'-([1,1'-biphenyl]-4,4'-diyl)bis(9H-carbazole-3,6-dicarboxylate)
bbdc^{2-}	5-tert-butyl-1,3-benzendicarboxylate
bdc^{2-}	1,4-benzendicarboxylate
bdp^{2-}	1,4-benzendipyrazolate
bpdc^{2-}	4,4'-biphenyldicarboxylate
bpndc^{2-}	4,4'-benzophenondicarboxylate
bpy	4,4'-bipyridine
btc^{3-}	1,3,5-benzentricarboxylate
CAU	Christian-Albrechts-Universitaet
CAU-10-OMe	Al(OH)(OMe−ip)
cdc^{2-}	9H-carbazole-3,6-dicarboxylate
CN	coordination network
COF	covalent organic framework
CP	coordination polymer
cp	closed pore
CPO-27	M$_2$(dobdc)
CSD	Cambridge Structure Database
Cu(OPTz)	Cu(OPTz−ip)
DAAD	German Academic Exchange Service
dabco	1,4-diazabicyclooctane
DFG	German Research Foundation
DMF	dimethylformamide

DMOF-1	$Zn_2(bdc)_2dabco$
dobdc^{4-}	2,5-dioxo-1,4-benzendicarboxylate
DUT	Dresden University of Technology
DUT-4	$Al(OH)ndc$
DUT-49	$Cu_2(bbcdc)$
DUT-5	$Al(OH)bpdc$
DUT-8	$Zn_2(ndc)_2dabco$
DUT-8(M)	$M_2(ndc)_2dabco$
ELM	elastic layered material
ELM-11	$Cu(bpy)(BF_4)(H_2O)_2 \cdot (bpy)$
fu-bdc^{2-}	2,5-difunctionalized-1,4-benzendicarboxylate
fum^{2-}	fumarate
HKUST	Hongkong University of Science and Technology
HKUST-1	$Cu_3(btc)_2$
IAST	ideal adsorbed solution theory
im$^-$	imidazolate
IUPAC	International Union of Pure and Applied Chemistry
JNU	Jinan University
JNU-3a	$Co(mptbdc) \cdot_3H_2O$
lp	large pore
MAMS	mesh-adjustable molecular sieve
MAMS-1	$Ni_8(bbdc)_6(\mu_3-OH)_4$
MIL	Materiaux de l'Institut Lavoisier
MIL-47	$V(O)bdc$
MIL-53	$Cr(OH)bdc$
MIL-53(Al)-FA	$Al(OH)fum$
MIL-53(M)	$M(OH)bdc$
MIL-88 series	$(M_3O(dicarboxylate)_3(H_2O)_2X$
mIm$^-$	2-methylimidazolate
MM-MOF	mixed-metal MOF
MOF	metal-organic framework
MOF-5	$Zn_4O(bdc)_3$
MOF-508b	$Zn_2(bdc)_2bpy$
MOF-74	$M_2(dobdc)$
mptbdc^{2-}	5-(3-methyl-5-(pyridin-4-yl)-4H-1,2,4-triazol-4-yl)-1,3-benzendicarboxylate
mvMOF	multivariate MOF
ndc^{2-}	2,6-naphthalendicarboxylate

NGA	negative gas adsorption
NMR	nuclear magnetic resonance (spectroscopy)
NP	nanoparticle
np	narrow pore
NP@MOF	nanoparticle@MOF
NTE	negative thermal expansion
OMe-ip^{2-}	5-methoxyisophthalate
OMS	open-metal sites
op	open pore
OPTz-ip^{2-}	5-(5,5-dioxide-10H-phenothiazin-10-yl)isophthalate
PSM	post-synthetic modification
PTE	positive thermal expansion
PXRD	powder X-ray diffraction
py	pyridine
R-ip^{2-}	5-halomethylisophthalate
R-PCP	$Zn_2(R-ip)(NO_3)_2(bpy)_2$
SBU	secondary building unit
SEM	scanning electron microscopy
SNU	Seoul National University
SNU-9	$Zn_2(bpndc)_2bpy$
SPC	soft porous crystal
ssMOF	solid-solution MOF
TE	thermal expansion
TEM	transmission electron microscopy
tpt	2,4,6-tri(4-pyridyl)-1,3,5-triazine
UiO	Universitetet i Oslo
UiO-66	$M_6O_4(OH)_4bdc_6$
VTPXRD	variable-temperature powder X-ray diffraction
ZIF	zeolitic imidazolate framework
ZIF-4	$Zn(im)_2$
ZIF-8	$Zn(mIm)_2$
ZTE	zero thermal expansion

LIST OF FIGURES

xxi

1

THE TRANSFORMATIVE POTENTIAL OF SMART, POROUS MATERIALS AND THE QUESTION OF HOW TO DESIGN THEM

Material chemistry is a vast research area combining a plethora of material classes, fields of expertise and applications. It is almost ubiquitously involved in our lives, be it in producing polymers/products from fossil fuels or renewable (i.e. lignin based) analogues, in facilitating food processing and conservation, in gas valorization (i.e. biogas purification), in enabling wind and solar power production and storage, or in microelectronics. Because of this leverage, it has a substantial role and potential in the overdue transformation to a sustainable society, economy, and industry – a change that requires monumental, universal effort.* At the center of this transformation are resource and energy sustainability and efficiency: use less resources to the same effect and make sure what is used can be reused or recycled.

The focus of this thesis lies on the class of smart, porous materials and their design, specifically, metal-organic frameworks (MOFs; what these are is topic of chapter 2). Therefore, if we look from within this MOF-branch of material chemistry at the ongoing sustainability transformation, two key questions arise:

1. How can smart, porous MOFs contribute to the sustainability transformation?

The term "smart" is more or less synonymous to "responsive" and describes the ability of a material to respond and adapt to an external stimulus, such as thermal, mechanical, optical, magnetic, or chemical stimuli, in a way which is purposefully utilized.[1] To give some everyday examples: self-tinting glasses (response to UV/visible light),

---

* Many journals (Nature for example) and universities have regular open access editorials and perspectives on this broad topic for the interested reader; search phrase "sustainable material science".

shape-memory alloys in camera auto focus devices (response to heating), or data storage cells (response to magnetic fields). The combination of "smartness" or responsiveness and porosity unlocks responsiveness towards guest molecules which can adsorb on the internal surface of such materials.

The addition of porosity suggests two ways to contribute to the transformation and directs the answers to question one: energy efficiency and resource sustainability. Regarding energy efficiency, impressive potential can be found for improving chemical separations. Purifying mixtures on industrial scale is still predominantly done by distillation, drying, or evaporation, so processes using staggering amounts of energy to heat or cool liquids and gases to separate them based on boiling point differences. If instead, separation could be facilitated by tailored, responsive materials selectively sieving (i.e. as membranes) or adsorbing some components of a mixture (and then cycling this in i.e. as pressure-swing-adsorption) consumption of heat energy could be significantly reduced. 80% of separation processes use heat, amounting to 10–15% of the global energy consumption, and 90% of this could be saved if membranes could be applied instead of distillation.[2] In perspective: in the US this would correspond to about 33% of the industry energy consumption or 3000TW/h (the total energy consumption of Germany is 2500TW/h).[3]*

Regarding resource sustainability, the biggest impact of metal containing solids is related to crude metal extraction and processing. Therefore, reducing the absolute metal content in materials for application is very important. Porous MOFs are empty scaffolds build from metals and organic molecules with significantly lower metal fraction than for example a non-porous metal oxide. Higher porosity correlates proportionally to reduced metal content. If a MOF can replace a metal oxide in its application, the overall reduction in metal used contributes significantly to resource sustainability (including the factor that it contains organic molecules made from petroleum). One such potential application are memory storage devices. These utilize the stimulus-responsive transitions of porous, switchable MOFs between two meta-stable states (i.e. 0 and 1) to store data. Current lab-scale materials reach state-of-the-art surface storage densities with very promising cyclability. Striking, however, is the fact that whereas some storage technologies do consume 20–30% of the current annual production of raw ores to satisfy their metal demand, MOF alternatives would only use up between single percentages and a few parts-per-million (ppm!) instead, depending on the element.[4]

Furthermore, a range of applications currently impeded by lack of suitable adsorbents are effectively in wait to be developed. Seawater desalination or metal-extraction from seawater are possible, but commercially not yet feasible on extended scale.[2] Similar the case for water harvesting from air, although some prototypes using MOFs look promising.[5]

---

* If in Germany 33% of industrial energy consumption could be saved, it would equal the fraction of industrial energy consumed in form of natural gas (37% in 2020).[3]

In summary, the first questions is easily answered and there is no shortage of improvements new responsive MOFs could bring. But to address the elephant in the room: there is yet no industrially relevant application for MOFs. The ongoing quest is to answer the second question and create, understand, and design responsive MOFs which meet the requirements for above mentioned applications.[6]

2. How can we design MOFs with tailored responsiveness and bring them into application?

The approach to unravel this is – as the question itself – twofold. On one side are investigations of the applicability of MOFs. Promising (often by chance discovered) materials need to be revisited to determine application-relevant properties not of importance in its lab-scale use, i.e. thermal expansion properties, stability under prolonged exposure to moisture, or synthesis up-scaling. Additionally, methods to process powders, i.e. shaping to pellets, need to be adapted as to not remove or reduce desired performance factors; new ways to fabricate MOF membranes or the in recent years discovered (porous) MOF glasses need to be brought to fruition before they can unfold their potential.[7] These procedures carve out both material features in high demand for and detrimental to application.

This is then the hotbed of the other side: addressing the fundamental challenge to divide, categorize, and abstract the virtually unlimited amount of synthesizable MOFs. We must be able to identify underlying design principles of responsiveness and subsequently find and create the material best suited to the respective desired task. Only then can we leverage the design versatility of MOFs to its fullest. However, the correlation of which features determine a certain property, like structural flexibility or dynamic responsiveness triggered by an external stimulus, and how these can be made experimentally accessible by/to the chemist in the lab remains largely in the dark. Fortunately, the modular building block principle of MOFs is a big accelerator in unraveling this. It enables comparison to other classes of crystalline coordination polymers which consist of different building block types but share certain aspects of responsiveness, like cyanide-based coordination networks and hybrid organic-inorganic perovskites,[8] and it allows to avoid the extremely inefficient trial-and-error loop in favor of the more strategic approach of searching for trends in structure-property relations within series of incrementally altered materials. With well correlatable trends, especially if persisting through different MOF families, and in-depth understanding of responsiveness-directing features predictive models can be created to guide through the enormous parameter space this material platform provides.[9,10] The combination of this conceptual guidance, awareness of interdisciplinary opportunities, and a broad perspective on utilization of responsiveness can ultimately bring smart MOFs to application.

So overall, the second question can not be answered with an easy recipe to follow, but the path towards its answer is clear. A step on this journey is presented in this dissertation.

2

HOW, WHAT AND WHY ARE MOFS?

Metal-organic frameworks (MOFs) are a special class of porous materials. Their most exceptional properties are in general tied to their porosity. The following sections outline how the discovery of this material class came to be, what MOFs are, showcase their design versatility which allows to tailor stimulus-responsive, smart frameworks, and elucidate why this is the key to unlocking their potential as efficient next-generation materials.

2.1 A BRIEF HISTORY OF METAL-ORGANIC FRAMEWORKS

The probably simplest MOF concept consists of one type of node (called secondary building unit (SBU)) build from metal ions or metal-oxo clusters and one type of organic molecule as strut/linker. A strut linearly connects two different nodes by coordination bonds and, if a node can connect to i.e. four struts along a plane, this results in a two-dimensional (2D) grid-like layer as sketched in figure 1. A structure consisting of multiple of such layers stacked on top of each other (like graphene layers or a stack of coasters) could be called a MOF. If in this example a node instead connects to six struts (octahedral), the result is a three-dimensional (3D) cube which extends in all directions and would also constitute a MOF. The central aspect of each structure is the connection between metal and organic ligand by a coordination bond and its two- or three-dimensional propagation. As such, the development of MOFs is closely tied the history of coordination chemistry; some compounds we now categorize as MOFs were discovered well before this material class was even defined or its potential recognized.

Modern coordination chemistry began with the fundamental understanding of the spatial arrangement of metals and ligands in complexes. When ALFRED WERNER
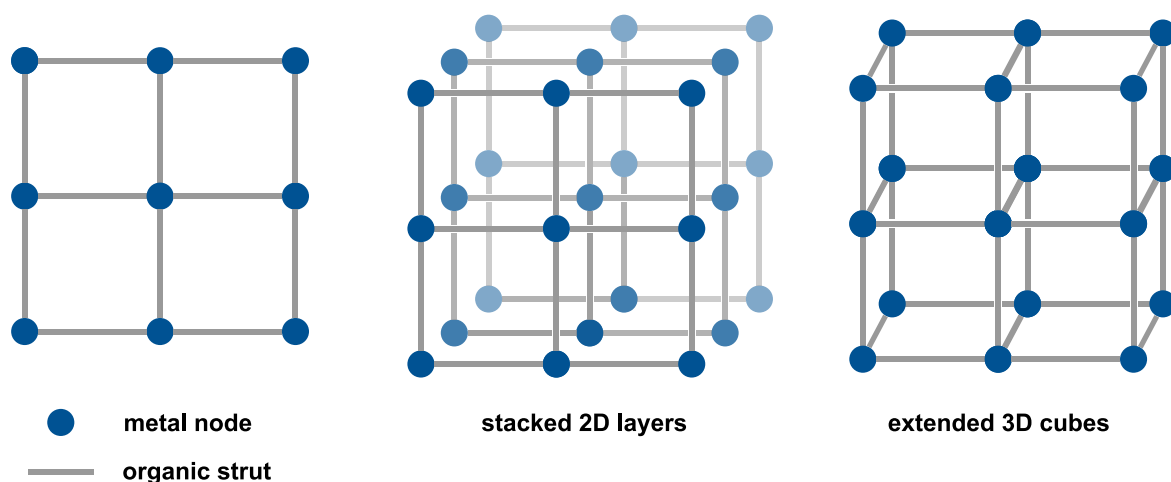
Figure 1. Simplified structural motif of a hypothetical MOF. Left, a plain 2D lattice consisting of metal containing nodes (blue) with four square-planar coordination sites each and organic molecules working as struts (grey) connecting two nodes. Center, multiple of the thereby spanned layers stacked. Right, a 3D option with nodes with six coordination sites resulting in layers connected by distinct struts instead of loose stacking.

proposed a structure for $[Co(NH_3)_6]Cl_3$ in 1893,[11] which turned out to be correct and lead to naming of the Werner-type complexes, this field of science underwent an uprooting transformation. It allowed both clear, more unambiguous definition of complexes which promoted scientific discourse and shifted research from arguments about structure to questions about structure-property correlations. * After this point, the feature to follow through history of coordination chemistry towards MOFs is dimensionality. WERNER's $[Co(NH_3)_6]Cl_3$ is a zero-dimensional (0D) complex, a single metal atom with six monodendate ammonia ligands surrounding it to form an octahedron without shared coordination bonds to the next $[Co(NH_3)_6]Cl_3$ octahedron. To extend this into a first, second or third dimension (which would be a line, layer, or cuboid, respectively), bridging bidendate ligands need to be present. Interestingly, one-dimensional (1D), 2D, and 3D coordination polymers (CPs) were all already created and used before or around the time of WERNER's breakthrough: the metal-cyanide Prussian Blue ($Fe_4[Fe(CN)_6]_3$) was used as dye since the 18th century and is a 3D CP, Palladium(II)-chloride ($PdCl_2$) is a 1D CP which first use for ethylene oxidation was developed by FRANCIS C. PHILLIPS in 1894,[12,13] and KARL A. HOFMANN reported $[Ni(CN)_2NH_3]C_6H_6$ (later called Hofmann clathrates) in 1897 which consists of 2D layered $Ni(CN)_2NH_3$ with benzene molecules in between.[14] However, limits in analysis techniques and equipment delayed structure solving of the Hofmann clathrates until the 1950s and even the long-known Prussian Blue until 1977.[15,16] Only with the increased analytical capabilities interest in specifically 3D coordination networks (CNs), crystal engineering,[17] and the concept of supramolecular synthons could bear fruit in the late 1980s and early 1990s. ROBSON and HOSKINS proposed in 1989 *"that a new and potentially extensive class of solid*

---

* MOFs quite visibly undergo the same transition, sometimes on a framework-by-framework basis.
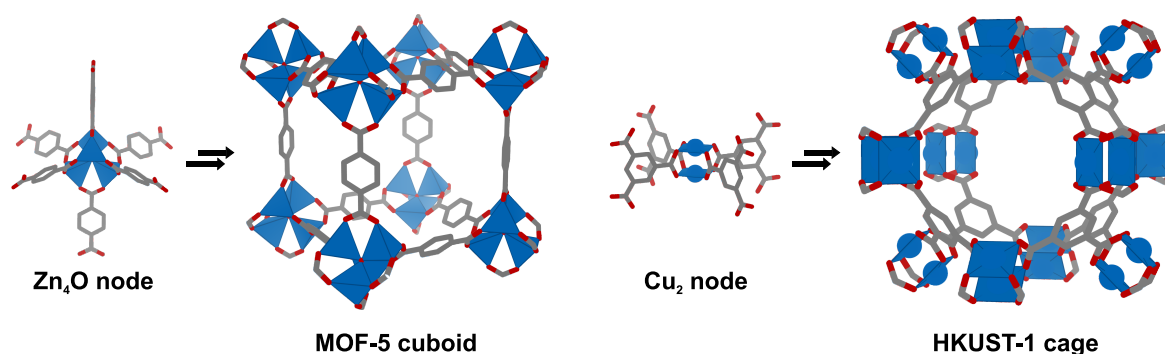
Figure 2. Structure of MOF-5 (left) and HKUST-1 (right). Shown in each case is a single metal SBU with coordinating organic linkers and the framework structure resulting from extending this motif to a complete pore. Blue, metals and coordination polyhedron; grey, carbon; red, oxygen; hydrogen omitted for clarity.

materials with unprecedented and possibly useful properties may be afforded by linking together centers with either a tetragonal or an octahedral array of valencies by rod-like connecting units. [...] These frameworks would generate a regular array of cavities, interconnected by windows."[18] They followed up one year later with a reappraisal of some metal-cyanide structures and the synthesis and structural analysis of crystalline polymers based on metal-nitrile complexes with voids occupied by counterions and solvent molecules.[19] In their study a key advantage of such materials is highlighted: their porosity and ordered/crystalline structure gives opportunity to include discrete (as opposed to random) chemical functionalization. They were able to combine a multidimensional network with an ordered structure and porosity, arguably creating the prototype of a MOF in all but name. Nevertheless, the at the time crucial last step of removing the solvent inside the pores without decomposing the material to create utilizable internal volume was an unsolved challenge.

In 1995 OMAR M. YAGHI and co-workers overcame this obstacle with their pioneering works on $Cu(bpy)_{1.5} \cdot NO_3(H_2O)_{1.25}$[20] and $CoC_6H_3(COOH_{1/3})_3(py)_2 \cdot \frac{2}{3} py$[21] in which they provide a glimpse of the incredible potential this type of material could have and coin the term "metal-organic framework". And while these two MOFs are maybe not intuitively exciting and structurally straight forward visualized, no later than 1999 two of the most iconic MOFs were prominently published: $Zn_4O(bdc)_3$ (MOF-5) by HAILIAN LI (associated to YAGHI) and co-workers and $Cu_3(btc)_2$ (HKUST-1) by STEPHEN S.-Y. CHUI (associated to IAN D. WILLIAMS) and co-workers, both structures are shown in figure 2.[22] With these examples and the immediate traction they generated because of their high accessible pore surface, low density, and good thermal stability,[23] very high interest in and a downright research trend around MOFs spread throughout the international chemistry community and ultimately a new, to this day high-profile field of materials science crystallized.

Its first 10–15 years were focused predominantly on creating new MOFs. Equally in order to try and exhaust the possibilities for MOF design (and inadvertently find even

more options) or to be the first to synthesize a framework, name it, and hope it has nice properties. In parallel, vital analytical and theoretical methods were developed and adjusted to meet the demands for characterization and explanation of these new materials. As methodology had progressed, by the mid to late 2010s investigations into the intricacies of MOFs, structure-property relations, exotic behavior normally not found in such solids, and the question of how to find and unravel more universal principles for MOF design and modulation of existing frameworks had become prominent.

Today, 2022, more than 100,000 MOF-like frameworks are registered in the Cambridge Structure Database (CSD)[24] and steady progress is made towards the purposeful design of MOFs. The research field itself has developed a rich canopy of different, intertwined branches: flexible MOFs,[25] switchable MOFs,[26] conductive MOFs,[27] amorphous MOFs,[28] MOF catalysts,[29,30] MOF glasses,[7,28] liquid MOFs,[28] nanoparticle (NP)-MOF composites,[31] core-shell MOFs,[32,33] and all their respective covalent organic framework (COF)[34] and sometimes zeolitic imidazolate framework (ZIF)[35] analogues – to name just a few and not even mention the corresponding sub-division into areas of application.[36] * Moreover, huge efforts are directed towards managing this enormous amount of collected and continuously added knowledge and data: curating high-quality databases (like the CSD MOF collection with currently just above 10,000 entries),[24] standardizing analytical procedures for better comparability of material characterization,[37,38] ensuring repeatability of syntheses, simulations and performances,[39] and achieving unambiguity in material and feature descriptors (see the following section 2.2.1). This aids the experimental chemist in evaluating suitable synthesis conditions and guiding intuition in the lab, but (as) importantly provides curated databases which can be used as input, references or training sets for simulations and machine-learning algorithms which were, are and will be a fundamental pillar of understanding and developing future MOFs.[10,40,41]

2.2 Versatility of Metal-Organic Framework Design

To understand why such a big trend developed around MOFs and why so many researchers see promise in this material class, one needs to look at the huge chemical freedom their structure design promises. The central aspect of each MOF is the connection between metal and organic ligand by a coordination bond. Every part, whether whole metal SBUs, some small fraction of metal atoms, complete linkers, or some linker substituents,[42–45] can be changed and will likely result in the same but slightly modified MOF as long as connectivity motifs are kept constant. Even if bigger

---

* The interested reader is directed to the here referenced (review) articles. Flexible and switchable MOFs are elaborated later in this work.

changes are implemented, if multidimensional, propagating coordination bonds are enabled to form a different MOF will likely crystallize.[46,47]*

Scaffolding components, structure topology and resulting void space within the material can be altered which enables discovery and creation of new MOFs, targeted feature design, and incremental structure-property correlation. It is one of the key advantages of MOFs and the reason they are adapted and considered future materials for so many applications.[9,51] Their tuneable internal pore volume is quantitatively utilized for gas storage (i.e. methane,[52] hydrogen[53]), gas separation and retention (i.e. CO_2 capture,[54] hydrocarbon mixtures,[55–57] isotopes[58]), liquid phase separation (i.e. liquid hydrocarbons,[59] dissolved (trace) impurities from water[60–62]), water harvesting from air,[5] or highly specific delivery systems both for inorganic NPs to create improved catalysts[63,64] or for organic substances like pharmaceuticals under physiological conditions.[65] Moreover, controllable porosity can be applied for sieving by MOF membranes,[66–68] building molecular sensors for detection of adsorbates or flow control,[69–71] or diffusion and dispersion control in nanoparticle@MOF (NP@MOF) composites.[72,73] If an application does not actively need internal porosity but a different MOF property, this pore space which makes up a significant fraction within the MOF can instead be used to provide or enhance the desired feature. This is exploited in MOFs as conductive materials[74] or dielectrics in microelectronics.[75] This list is by no means exhaustive, but highlights the bandwidth of options accessible through MOFs to help understand the enormous interest in this material class. MOFs are not yet at the point of cost-effective industrial application, but in light of the progress made from almost randomly discovering new frameworks a decade ago to purposefully unraveling and iterating features by now established concepts, this can well be expected to change in this decade.

2.2.1 Terminology and Naming Conventions

Terminology and naming conventions (or lack thereof) for MOFs are daily business for the experienced MOF-scientist and descriptors of MOFs mentioned in this thesis are elaborated in the respective chapters and the glossary. For the readership not (yet) intimately familiar with MOFs this topic can be confusing and warrants a short introduction.

The booming research activity in the field of MOFs ran ahead standardized terminology conventions for the better part of the last two decades. Often a MOF has multiple descriptors, for example based on its institution of discovery and/or experiment number, based on its molecular constituents, and maybe information on its topology. As striking example herein serves: (MM)-MOF-74, MOF number 74 with the initial

---

* This is strictly speaking not limited to coordination bonds as MOFs held together by different bond types exist, i.e. hydrogen bonding (HOFs),[48] supramolecular interactions (SOFs),[49] or colavent bonds (COFs).[50]
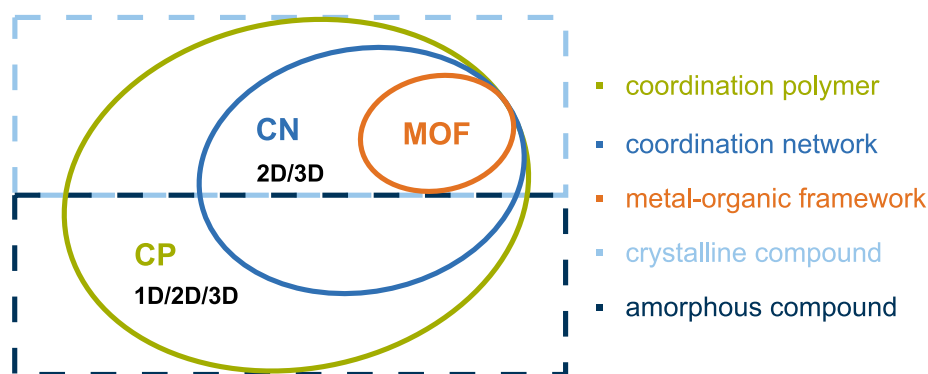
Figure 3. Venn diagram of the relation between coordination polymer (CP) coordination network (CN), and metal-organic framework (MOF).

(MM) sometimes indicating the one or two present metals and possibly written as suffix as in MOF-74-(MM), also known as CPO-27-(MM) (herein, CPO = coordination polymer) with similar (MM)-usage, also known as M$_2$(dobdc). Arguably, awareness was brought to chaotic naming schemes and this has been reduced to some degree – not least because databases need unambiguous and unique descriptors for each MOF to function though this is often achieved by adding *another* descriptor. * The differentiation between coordination material classes is more distinct (see figure 3). Based on the International Union of Pure and Applied Chemistry (IUPAC) report from 2013,[76] three nested sub-classes step-wise increasing in dimensionality of their expansion or inherent features are termed. CPs are defined as "A coordination compound with repeating coordination entities extending in 1, 2, or 3 dimensions.", their sub-set CNs are defined as "A coordination compound extending, through repeating coordination entities, in 1 dimension, but with cross-links between two or more individual chains, loops, or spiro-links, or a coordination compound extending through repeating coordination entities in 2 or 3 dimension.", and most specifically a MOF is defined as "a coordination network with organic ligands containing potential voids." This is the smallest common denominator. MOF sub-classes like ZIFs or MOF glasses are not yet IUPAC-defined and do not (yet) necessarily need to be. However, improving and updating the very broad IUPAC definition of a MOF is an ongoing process. The interested reader is directed to a publication by SAONA SETH and ADAM J. MATZGER[77] which reviews chemical composition, crystallinity, dimensionality, porosity, and robustness as concepts to propose an evolved definition of MOF.

---

* MOFid introduced by the Snurr group is the, from my point of view, most promising approach to this. More information for the interested reader can be found at snurr-group.github.io/web-mofid.

2.2.2 INTRODUCING SYSTEMATIC MODIFICATIONS

Modification and functionalization of MOFs can be achieved by a series of different methods which build on the core concept of (iso)reticular MOF chemistry – changing parts of the framework backbone or constituents without altering the overall topology and geometry of the MOF. Methods are grouped into modification before or during material synthesis and post-synthetic modification (PSM).[78]
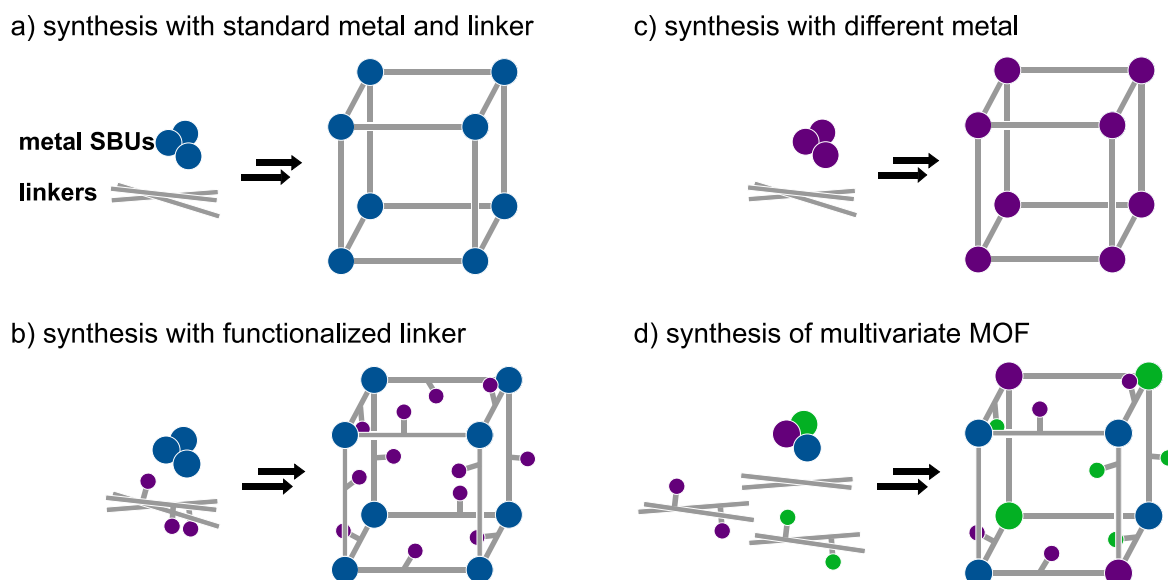
Figure 4. Concepts to create functionalized MOFs by providing respective derivatives for use in solvothermal MOF synthesis. Each pathway can be used for partial functionalization as well by using suited educt mixtures for synthesis. Big blue, purple and green spheres, different metal SBUs/nodes; grey rods, linkers; small purple and green spheres, linker functionalizations.

Figure 4 highlights options for implementing changes to the framework during its synthesis by providing functionalized linker versions or SBUs containing a different metal. This can also be applied to include multiple derivatives of a linker or different metals. The results are solid-solution MOFs (ssMOFs) in the former case and mixed-metal MOFs (MM-MOFs) in the latter.[79] MOFs with multiple variants of linkers and/or metals are overall surmised by the term multivariate MOFs (mvMOFs).[80]

Limiting factors for functionalization during synthesis are tolerance of the new building blocks or derivatives towards the (solvothermal) reaction conditions, solubility of the precursors, or interference with the coordination bonds between metal SBU and linkers. When moieties or constituents not suited to MOF synthesis conditions should be introduced and a different synthesis method is not feasible, PSM methods can provide a solution (some examples depicted in figure 5). Notably, the shown simplification of post-synthetic linker modification represents multiple synthetic approaches found in MOF chemistry, such as substitution, deprotection, or extension (i.e. by Diels-Alder or Click chemistry).[62,81–83] Furthermore, metalation of suited linker motifs

or pore space is also possible.[84,85] All modifications can be controlled to partially complete and create mvMOFs.
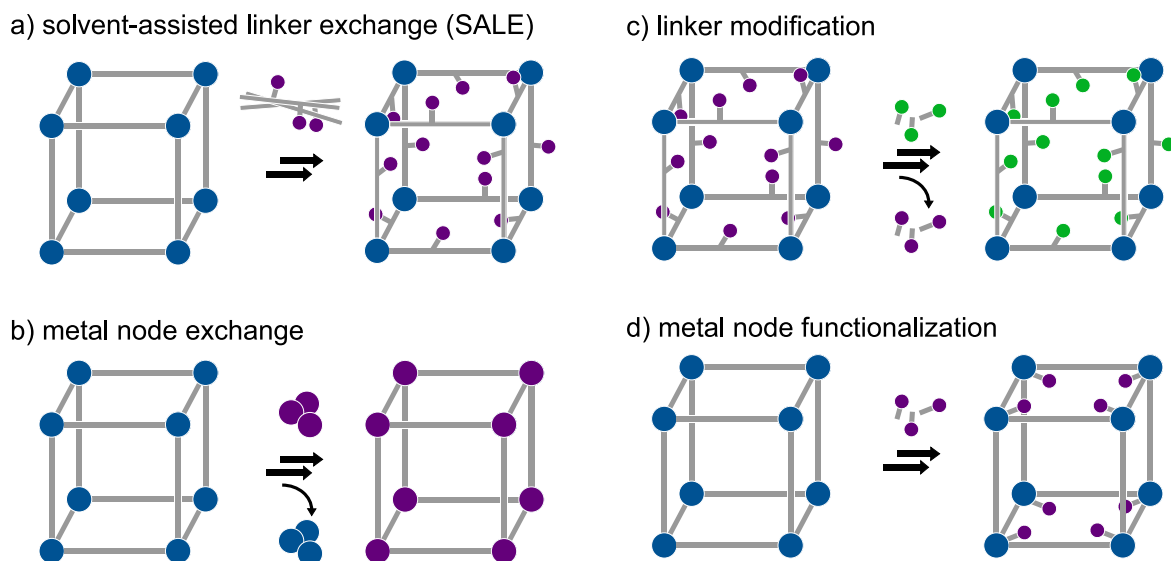
Figure 5. Concepts to create functionalized MOFs by post-synthetic modification (PSM). Each pathway can be used for partial functionalization as well to design multivariate MOFs (mvMOFs). Big blue and purple spheres, different metal SBUs/nodes; grey rods, linkers; small purple and green spheres, linker and metal functionalizations.

Two concluding prominent aspects of isoreticular MOF modification to be mentioned are first the isotropic (and if the topology allows it like in some pillared-layered materials also anisotropic) extension of a framework by elongation of its linkers, although this is less a functionalization and more creating a new topologically congruent but bigger MOF,[47,86] and second the purposeful design of scaffold defects (i.e. missing linkers or SBU vacancies).[87–89] Regarding the former aspect the interested reader is directed to the cited review articles, the latter aspect is revisited in section 2.3.1.3.

2.3 SMART, STIMULUS-RESPONSIVE METAL-ORGANIC FRAMEWORKS

With high amount of intricate and extensive modifyability MOFs are predestined for designing their responsiveness. While every MOF is responsive in some way, deliberate choice of linker, metal, topology, defects, crystal size, powder processing, and/or composite creation can enable precise control over a frameworks reaction to an external stimulus. This can be temperature, mechanical pressure, gas pressure/adsorbate presence, light, dispersion medium, etc. With this control comes the transition from a coincidental behavior to a usable, designed feature and potential application as part of a smart, stimulus-responsive material. The introductory examples mentioned in chapter 1, for example, need such design to be possible: data storage is enabled

by a MOF able to switch between two distinct states in response to external (i.e. magnetic) stimuli, while separation processes need highly selective materials which can differentiate between different adsorptives by their electronic properties – so respond to one adsorptive, but not the other.

To rationally approach this topic it is very helpful to distinguish between static responsiveness (responsive material) and dynamic responsiveness (*stimulus*-responsive or *smart* material). Static responsiveness describes a constant, stimulus-independent property of a MOF which results from primarily intra-framework interactions and does not involve structural changes of the material. Dynamic responsiveness describes a property changing as function of an external stimulus and the resulting structural changes. For example, a MOF selectively adsorbing guest molecules due to its pore aperture dimensions (size-exclusion sieving) is statically responsive. If such property changes depending on an external-stimulus, i.e. applied temperature changing the pore aperture resulting in different size-exclusion properties at different temperatures, the phenomenon constitutes dynamic responsiveness. These changes can occur on different length scales from thermal motion at sub-angstrom scale to crystal-to-crystal phase transitions spanning more than 1nm.[8] The dynamic aspect is most pronounced in flexible MOFs, however, in some cases rigid MOFs can exhibit dynamic responsiveness as well. The materials studied in this thesis cover both dynamic responsiveness in a structurally flexible and rigid MOF.

2.3.1 RESPONSIVENESS IN FLEXIBLE METAL-ORGANIC FRAMEWORKS

In the early stages of MOF research it was observed that some MOFs respond to removal of the solvent molecules in their pores – residual guests from the synthesis medium – by structural change. Some frameworks irreversibly collapsed, others retained their (rigid) structure and thereby gained accessible pore volume,* and a minor fraction of MOFs exhibited pronounced deformation (read: flexibility) of their scaffold but remained intact. MOFs with such behaviors were respectively classified into 1st, 2nd, and 3rd generation MOFs by SUSUMU KITAGAWA and MITSURU KONDO in 1998.[90] While therein the presence and importance of the flexible 3rd generation MOFs was more predicted than recounted, this inverted a decade and plethora of new MOF structures later when KITAGAWA et al. coined the term soft porous crystals (SPCs) to explicitly describe the class of flexible MOFs in their seminal review.[91]

They give a definition which is still applicable today: "*Soft porous crystals are defined as porous solids that possess both a highly ordered network and structural transformability. They are bistable or multistable crystalline materials with long-range structural ordering, a reversible transformability between states, and permanent*

---

* Strictly speaking a "non-response" in the sense of structural deformation, but precisely therein at the time a very important, not self-evident achievement and framework property.

porosity. The term permanent porosity means that at least one crystal phase possesses space that can be occupied by guest molecules, so that the framework exhibits reproducible guest adsorption. In soft porous crystals, two types of transformation are possible. In most cases transformations occur while retaining the crystalline state (crystal-to-crystal), but sometimes perfect crystallinity is lost during the transformation (from crystal to another form with imperfect crystallinity). Imperfect crystallinity does not mean that the form is amorphous, but that the long-range order of the framework is lost, without the polymer network collapsing."

MOFs exhibit higher softness (in terms of elasticity) or compressibility compared to traditional nanoporous materials. This is linked to the weaker nature of their coordination bonds, compared to i.e. the strong $Si-O$ or $Al-O$ bonds in zeolites, and their void fraction or porosity. The network transformability of a given material is further governed by deformability of its constituents and possibility of mutual displacement of secondary structures like sub-nets or layers. As such, the topology of a MOF is always a first indicator whether transformation modes can mechanically happen or not.[92] Figure 6 (a–d) highlight the four key modes of flexibility that can arise in flexible MOFs, together with two types of response (e, f) linked to rotational/conformational freedom of framework functionalizations that can be designed into flexible and rigid MOFs. Conceptually, the states flexible MOFs switch between are termed in pairs of closed pore (cp) to open pore (op) state and narrow pore (np) to large pore (lp) state. Few MOFs use different/more descriptors if additional meta-stable states exist as i.e. is the case for $Cr(OH)bdc$ (MIL-53).[93]

To give some details and direct to model materials for each mode: the breathing motion is an anisotropic transformation often linked to the wine-rack-type topology motif as found in MIL-53,[93,94] $Zn_2(ndc)_2dabco$ (DUT-8)[95,96] and $Zn_2(fu-bdc)_2dabco$ (further discussed in sections 2.4 and 2.4.1). Swelling in contrast, is an isotropic change along all structural directions. Prominent frameworks with this motion are the $(M_3O(dicarboxylate)_3(H_2O)_2X$ (MIL-88 series) with materials of various combinations of M^{3+} metals, bidendate dicarboxylate linkers and mono-anionic counterions.[97–99] Flexibility arising from stimulus-responsive layer spacing are for example found in the prototypical MOF $Cu(bpy)(BF_4)(H_2O)_2 \cdot (bpy)$ (ELM-11)[100,101] and derived systems.[102] Curiously, the above mentioned Hofmann clathrates have just recently been found to shown similar responsiveness.[103] As final mode, structural change as a result of sub-net displacement of catenated/interpenetrated nets was prominently discovered in $Zn_2(bpndc)_2bpy$ (SNU-9),[104] $Cu(dhbc)_2(bpy)$,[105,106] and $Zn_2(bdc)_2bpy$ (MOF-508b).[107,108] Interpenetration is relatively common in MOFs with cubic motifs (like most pillared-layered MOFs)[109] if pore openings and linker dimensions allow for it.[110] Two additional modes of responsive transformation related to linker functionalization are sometimes mentioned in context of flexible MOFs, although

a) breathing motion

b) swelling motion

c) layer spacing

d) sub-net displacement

e) linker rotation

f) functionalization moveability
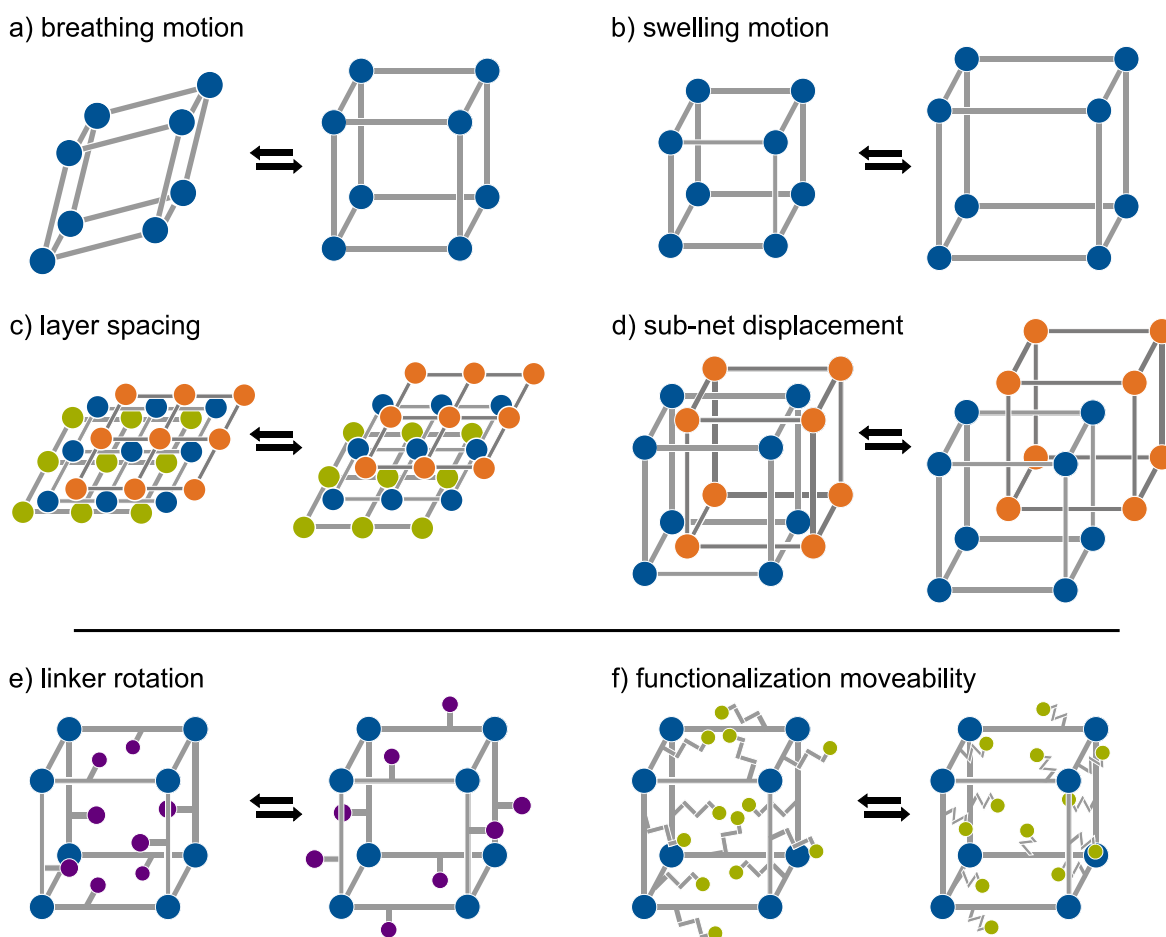
Figure 6. Visualization of modes of structural backbone transformation within flexible MOFs (a-d) and modes of linker functionalization moveability (e, f) which can arise in flexible and rigid MOFs. Big blue, green, and orange spheres, metal SBUs of different sub-nets; grey rods, linkers; small purple and green spheres on grey sticks, linker functionalizations.

they can also be found/implemented in rigid materials.* First, rotation/orientation of the linker can alter bulk framework properties. This is prominently found in (flexible) $Zn(mIm)_2$ (ZIF-8) which adsorbs molecules larger than its calculated pore window because linkers can rotate to (step-wise)[111] increase the aperture.[112] It is also the responsiveness directing mode in (rigid) MOFs with azo-benzene functionalizations which can be isomerized by light, i.e. to trap molecules inside the pores for eventual release,[113] or MOFs containing anisotropic linkers which can be directed by external stimuli, i.e. linkers with directional dipole moment in a magnetic field.[114] Second, linker functionalization can render frameworks flexible (i.e, $Zn_2(bdc)_2$dabco (DMOF-1), details in section 2.4.1) or exhibit inherent moveability to a high enough extend to direct stimulus-responsiveness in rigid MOFs (see sections 2.4.2 and 4.1).

---

* There exist some very unfortunate and confusing uses of "flexible" and "responsive" in context of linker functionalization when at the core static and dynamic responsiveness are tried to be distinguished. I sincerely hope the latter terms will be used more widely at some point.

The above definition of SPCs focuses on guest-adsorption as trigger for structural transformations because it was first observed and is relatively easy to test for by standard characterization techniques. However, other stimuli are put into new perspective as understanding of controlled flexibility (generally referred to as switchability) grows and awareness for this once exotic feature spread within the community. Next to adsorbates (gases or liquids), temperature,[115] mechanical pressure,[116] light,[113] magnetic fields,[114] or redox reactions[117] can also be applied to induce distinct structural changes.*

New classifications for MOFs have surfaced, as design and utilization of the different flexibility motifs, triggering stimuli, and versatility of material modification advance. Foremost, 4th generation porous materials were termed by KITAGAWA following his previous categorization, although it refers to a more comprehensive design of microstructures linking hierarchy, hybrid composition, anisotropy, asymmetry, disorder, and defects to complex functionality.[118] This rather broad definition will have to stand the test of time, but moreover it omits a possible spatiotemporal evolution: going beyond the scope of this thesis but undoubtedly pointing towards the future of MOF design are four-dimensional (4D) MOFs. EVANS et al. define these as frameworks with a controlled intrinsic timescale of engineered dynamic transformation and consider this time-axis as fourth dimension.[119] They point out a series of questions still in need of answering and stress the necessity to continuously improve state-of-the-art methods to proof feasibility of 4D design. However, if the history of unraveling switchability tells anything, I think if this less an insurmountable task and more a source of motivation for curious and persistent researchers.

2.3.1.1 Controlling Adsorbate-Induced Switchability

From the very discovery of stimulus-responsive, (meta-)stable flexible MOFs they have been studied to gain understanding of their inner workings, control magnitudes of responsiveness, and apply it to overcome present challenges in industry. Flexible MOFs can enable more efficient and sustainable gas separation, but adsorption preference and strength need to be tuned to a sweet spot of selectivity and cycleability; the working capacity generated by the material's phase transition needs to be tailored to be available in a relatively narrow temperature-pressure window. To achieve this the driving forces behind the guest-induced switching have to be understood which necessitates different conceptual approaches, experimental diligence, and state-of-the-art methodology and its progression.

---

* As awareness spread(s) more elaborate techniques and conditions are applied to probe for flexibility. Inadvertently, more MOFs with such features are found. Flexibility is by no means common, however, certain modes of structural response seem to be more material-inherent then was initially expected, see i.e. section 4.2.

This cooperation of analytic methods, theoretical models and experimental knowledge can exemplary be highlighted with the prototypical flexible ELM-11. Its adsorbate-responsiveness was initially observed for N_2 and Ar at cryogenic temperatures and CO_2 at 273K. The material changes its layer spacing and depicts a distinct increase in adsorption capacity at a certain (adsorptive) pressure (the gate-opening pressure).[100] This phenomenon occurs in thermal equilibrium and is initiated by small structural strain induced by adsorbate on the external surface. Once this strain pushes the layers apart far enough for the adsorbate to enter, a phase transition occurs almost instantaneously because of the positive feedback of more adsorbate leading to propagation of bigger layer-spacing which opens up more volume for more adsorbate.[120] For this MOF both adsorptive kinetic diameter and polarity (as correlated factor of host-guest-interaction strength) have an impact at which temperature and pressure the switching takes place. Complementary developed theoretical models allow to specify changes of internal free energy and entropy of the host in response to adsorbed guest molecules responsible for the switching. They provided a basis for simulating gas adsorption behavior to rationalize some of the isotherm features observed in experiment.[121] Meanwhile in more application focused perspective, the gating process was shown to be resilient enough to not be compromised by stress of repeated sorption cycles and pellet shaping.[122,123] This is important in light of recent pilot application studies: because of well understood phase transition thermodynamics and the material's fast gating properties, efficient separation of methane and carbon dioxide in a high-throughput pressure-vacuum-swing-adsorption process could be realized.[101]

This development emphasizes the necessary understanding of a material in order to bring it to application. The second crucial aspect is the search for underlying design principles which govern adsorbate-responsive flexibility in order to better control it and apply them in broader fashion – ideally to multiple flexible MOFs systems. Very detailed studies were and are conducted on phenomena observed in flexible, stimulus-responsive materials like the seminal works on the breathing motion in MIL-53 and V(O)bdc (MIL-47),[116,124–126] investigation of the reversible disorder-order transitions in DUT-8,[127] the in-depth analyzed negative gas adsorption (NGA) of $Cu_2(bbcdc)$ (DUT-49),[128–130] the multi-step breathing in M(bdp),[131,132] and functionalization-dependent responsiveness of $Zn_2(fu-bdc)_2dabco$.[44,115,133–136] Transferring insights to different MOFs is tricky, especially within the flexible MOF family. However, it is by now (in result to these studies) an accepted principle that the balance of dispersion and entropy stabilization of a meta-stable framework directs its switchability. This balance is both influenced by adsorbed species and linked to material features like intra-linker deformation or topology. Linker rotation, bending of the carboxylate group, and deformation of the metal coordination geometry can facilitate a breathing motion as it was observed in wine-rack type MOFs MIL-53 or MIL-47.[137] This is linked to the anisotropic MOF topology and in similar fashion found in pillared-layered MOFs sharing the wine-rack motif: DUT-8 revealed big pore volume changes when transitioning from its cp to its op state which is effectively enabled by the same

deformations as in MIL-53. However, DUT-8 does not form metal-oxo rods as SBUs like MIL-53 but metal-paddlewheels. Deformation of their coordination sphere is more sensitive to the metal type present which becomes a key parameter in its flexibility design. For example, DUT-8(Ni) and DUT-8(Co) both transform from their lp to a cp phase during activation after synthesis, but only the former re-opens by physisorption of nitrogen.[96] This example brings MM-MOF design to flexible materials, and tuning flexibility and adsorbate-responsiveness by linker functionalization or isoreticular expansion is as important a design principle as it is for rigid MOFs: functionalization with halogen or amino moieties, in rigid MOFs often observed to change CO_2 sorption selectivity,[138–141] can in similar fashion be applied to MIL-53(Al).[142] Moreover, the easily modifiable bdc-linker motif is leveraged successfully across different flexible MOFs. MOF-508b consists of two interpenetrated nets which relative moveability creates a switchable system.[107] GU et al. functionalized its linker with an amino group and thereby change the balance between deformation energy of the system and adsorbate interactions in $CHCl_3$ and CH_2Cl_2 physisorption.[143] The additional hydrogen bonding facilitated by the amino group leads to stabilization of a meta-stable state specifically during CH_2Cl_2 sorption, otherwise not observed for the unfunctionalized system or $CHCl_3$. A follow-up study by BONNEAU et al. utilizes a pair of NO_2- and NH_2-functionalized linkers in a ssMOF-approach to optimize the pressure range for acetylene storage and deliverability (see figure 7) – the crucial parameter which must be controlled in flexible MOFs to apply them in gas storage.[108] NO_2 groups lead to repulsive interactions with the carboxylate ligands in the cp form which reduces gate opening pressure, while NH_2 groups increase hydrogen bonding interaction with the 4,4'-bipyridine (bpy) and carboxylate ligands to increase the gate opening pressure.

But, minor linker changes can show very drastic (and/or surprising) impacts on switchability because of the intricate interplay of entropy and enthalpy that govern flexibility.[144] (To revisit a previously mentioned example: the amino functionalization of MIL-53(Al) also renders the material a reversible non-linear optical switch.[145]) The transformative effect additional linker substituents can have is very prominently researched for functionalized derivatives of DMOF-1, the $Zn_2(fu{-}bdc)_2dabco$ series. $Zn_2(bdc)_2dabco$ is not a flexible material with big accessible pore volume change,[146] however, by adding long side chains to the linker like in the derivatives $BME\text{-}bdc^{2-}$ (2,5-bismethoxyethoxy-1,4-benzenedicarboxylate) or 2-alkylamido-1,4-benzenedicarboxylate^{2-} the framework develops a meta-stable np phase when desolvated unlocking a wine-rack-type opening and closing motion accessible by CO_2 physisorption.[133,147] Initially only observed with very few functionalizations, it was later found that many shorter side chains also enable this transformation with up to 28% volume difference if they are in 2,5-position.[134]

Fully predicting adsorbate-induced switching is still beyond our knowledge because each adsorbate or framework functionalization essentially draws a different map of the overall free energy landscape which charts when a material undergoes a transition. Nevertheless, tailoring responsiveness of a not completely unknown material can
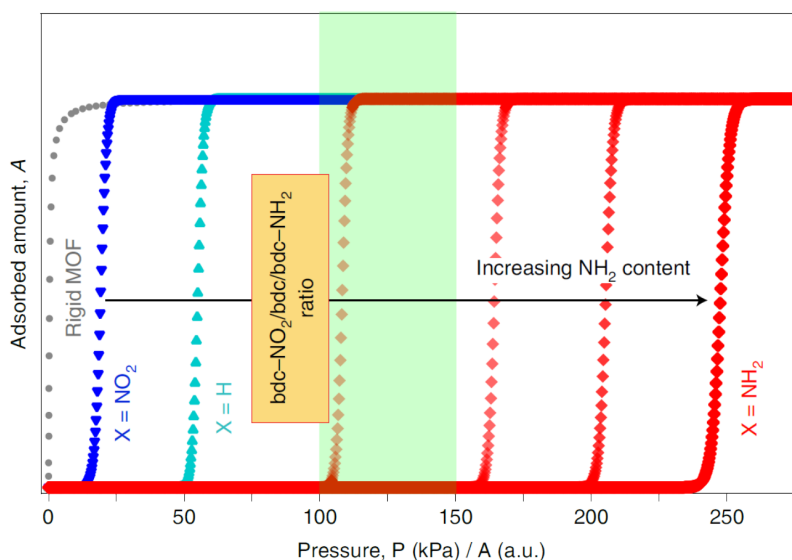
Figure 7. Schematic representation of the S-shape adsorption isotherms of $Zn_2(X-bdc)_2(bpy)$ depending on guest pressure and the ratio of $NO_2-bdc/bdc/NH_2-bdc$ linkers in the MOF. An exemplary type I adsorption isotherm of a rigid MOF is shown in grey for comparison. The functionalization of $Zn_2(bdc)_2(bpy)$ (light blue triangles) leads to a shift in the gate pressure to lower pressure with increasing NO_2 functionalization (dark blue inverse triangles) or higher pressure range with increasing NH_2 functionalization (various shades of red diamonds). The green area represents the targeted practical range (100–150 kPa) for safe acetylene use. Figure reproduced from here[108] under a Springer Nature License.

be guided by the principles uncovered so far, if its properties fall within a by now categorized set of features like a certain topology, modifyability, or transition mode.

2.3.1.2 Entropy-Dispersion-Balance in Temperature-Induced Switchability

Utilizing temperature to switch a flexible framework can be a practical advantage for application because it allows control over its state independently of its surrounding medium (as long as it conducts heat). Importantly, its influence on the thermodynamic energy landscape of flexible MOFs is conceptually more assessable because it is a single, universal stimulus, in contrast to adsorbate-induced switching wherein each different adsorbate is a separate stimulus.

WIEME et al. utilize this to shine a light on the delicate interplay of dispersion and entropy stabilization in the thermally induced phase transitions of MIL-53 which is the same transition observed in physisorption.[148] They calculated Helmholtz free energies and electronic energy profiles as a function of temperature and identify a bistable behavior of the MOF with a transition barrier between np and lp state. This is rationalized by experimental findings on intrinsic material imperfections – indicated by the fact that phase transitions are incomplete even at very low temperatures and that defect concentration impacts flexibility[137,149,150] – to identify a mechanism of

temperature-dependent breathing. WIEME et al. infer that thermal transition of a framework may nucleate through a combination of defects, temperature fluctuations and strains, after which the locally increased stress causes the transformation to propagate further through the lattice in a layer-by-layer fashion. (Not dissimilar to the adsorbate-triggered equivalent in ELM-11.) Moreover, it is strongly emphasized that long-range dispersion stabilization of the meta-stable phase at low temperature shifts to entropic stabilization at higher temperatures. These findings are visualized in the adapted figure 8. They elaborate this in a series of MOFs, each isoreticular to MIL-53 but with different π-π stacking interactions: first they remove such stacking and limit dispersion stabilization in Al(OH)fum (MIL-53(Al)-FA), which as a result assumes an lp structure over the entire temperature range, then increasing stacking and dispersion interactions in Al(OH)ndc (DUT-4) and Al(OH)bpdc (DUT-5), both of which can as a result not be stabilized in their lp form by entropy effects at high temperatures.

Parallels to framework design and thermal switchability can – with care – be drawn for prototypical pillared-layered MOFs like DMOF-1, $Zn_2(fu-bdc)_2dabco$, or DUT-8 which share the wine-rack topology of the studied MIL-53 or DUT-4. On one hand, DUT-8 consists of linkers with very high π-π stacking interactions and dispersion stabilization. Consequently, thermally induced opening from its cp to op phase is not observed. (Although it was recently discovered that a transition resulting from thermal bond breaking and rearrangement can take place.[152]) On the other hand, the in DMOF-1 observed effect of entropic contribution on temperature-dependent changes is limited because geometric restrictions prevent significant stacking of linker π-systems.[146] Conceptually in between are the functionalized $Zn_2(fu-bdc)_2dabco$ MOFs. Their linker substituents can provide both dispersion interactions at lower temperatures by conformally bridging linkers and entropic susceptibility at higher temperatures by their inherently large mobility. As such, derivatives with longer side chains (BME-bdc^{2-}, reversible transitions, and DB-bdc^{2-}, irreversible transition; BME = 2,5-bismethoxyethoxy, DB = 2,5-dibutoxy) exhibit both a distinct np phase and thermal switching to a lp state.[115] This reifies the principle of entropy-dispersion-balance manipulations by functionalizations — higher mobility in moieties stabilizes open states, higher dispersion interactions (i.e. by heteroatoms, hydrogen bonding, π-interactions) stabilize contracted states. Recent investigations on switching with mechanical pressure link to this fundamental aspect (therein further categorizing different entropic contributions of framework and functionalization).[144] The thermal contribution to this balance also plays a role when switching with other stimuli: in physisorption temperature influences phase transition (partial) pressures in flexible MOFs,[153] some via light switchable azo-benzene ligands may undergo isomerization under sufficient heat,[154,155] or, in an inverted case, infiltrated solvents in DMOF-1 can change (with dimethylformamide (DMF)) or inhibit (with benzene) symmetry transformations occurring during cooling when compared to the guest-free state.[146] This temperature-co-directed switchability adds complexity to a system, but might
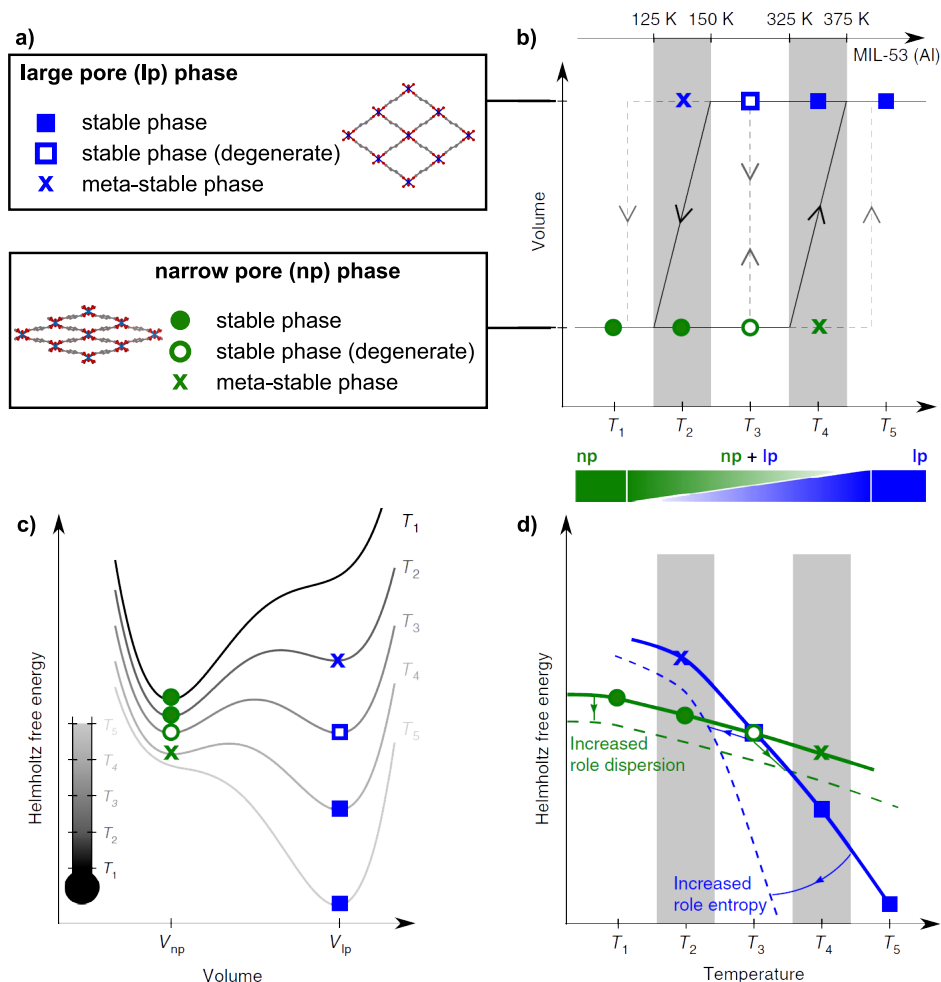
Figure 8. Temperature-induced breathing of a flexible wine-rack type MOF. a) Two (meta)stable phases of MIL-53(Al). b) Thermo-responsive behavior of MIL-53(Al) as measured by experiment. The system switches as a function of temperature between the np and lp phase with a hysteresis loop. Different transition regimes are indicated with arrows. c) Hypothetical Helmholtz free energy curves as a function of volume at different temperatures (T1-5) as an explanation for the observed experimental behavior. d) Hypothetical evolution of the Helmholtz free energy for the np and lp phase as a function of temperature. The gray shaded areas correspond to the experimentally measured transition regions. Definitions of the blue and green symbols are indicated in the top left panel. Figure reproduced and modified from here[148] and reused under the CC-BY-4.0 license.[151]

prove valuable in future MOF designs because it is potentially less dependent on the materials' thermal stability.

As final remark to temperature responsiveness thermal expansion (TE) should be mentioned. TE is a core property evaluated for every material or composite exposed to temperature fluctuations (from concrete of highway bridges to composite isolators of superconductors). Every MOF, whether rigid or flexible, which is envisioned to be applied under conditions with higher temperatures or temperature fluctuations should be evaluated in context of its TE performance: even single-percent changes can lead to distinct property deviations or mechanical failure.[156] It remains an open questions (which **STUDY II** works towards answering) if flexible MOFs tend to be negatively affected by their TE behavior because they exhibit less rigidity to withstand this stress, or are potentially even better suited to distribute this thermal strain across their scaffold because they allow for more flexibility and conformational and vibrational adjustment.

2.3.1.3 Impact of Defects on Switchability

Defects have an immediate effect on MOF properties. MOF structures can be solved almost on a per-atom level by powder X-ray diffraction (PXRD) and form periodic lattices which can be nicely visualized. While these figures then depict perfect structures, MOFs are all but. Imperfections – defects – can range from vacancies or exchanged atoms, linkers, or SBUs, to coexisting phases, amorphous regions, surface modifications, differing particle size and shapes, or extra-framework factors like leftover solvent molecules from synthesis. Defect engineering, research on how to design MOF properties by defects, is a multifaceted field within MOF science.[87,89,157,158] A defect in general is a source of disorder and the defect type determines its spatial impact scale; short-range (i.e. point defect), mid-range (i.e. mesopores) or long-range (i.e. amorphous region or phase coexistence). A generalization of this is visualized in figure 9.[159] (In the following section disorder is not explicitly named, but implied by the term defect.) *

The last two sections highlighted that flexibility is related to entropy; and equally so are defects. Both arise from the high dimensionality of the intra-molecular degrees of freedom of the materials, as well as the relatively weak nature of the interactions involved in the framework assembly.[162] In the given liberal definition of defects the two above mentioned examples of flexible MM-MOFs and ssMOFs (DUT-8(Ni) vs. DUT-8(Co) and $Zn_2(NO_2-bdc)_{1-x}(NH_2-bdc)_{1+x}bipy$) could be rationalized and interpreted as defects (inclusion of a second/ additional different liker or metal) impacting adsorbate triggered switchability. Similar findings have been made for

---

* A perfect, defect-free MOF does not exist. However, defect engineering also includes research on how to reduce defect amounts in MOFs. A nicely visualized example is the correlation of defects and color in HKUST-1.[160]
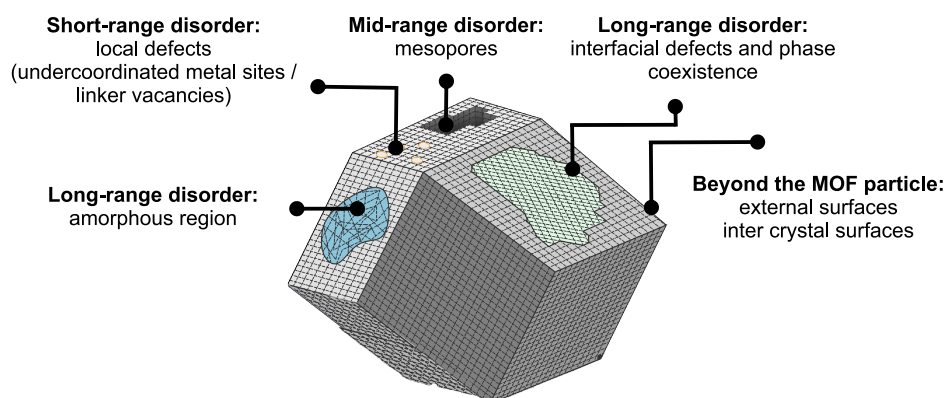
Figure 9. Various types of spatial heterogeneities at different length scales in a metal–organic framework particle. The different experimental and theoretical length scales relevant to interrogate these spatial heterogeneities are indicated. Reproduced and adapted from here[159] and reused under the CC BY-NC-ND 4.0 license.[161]

switching by mechanical pressure by dissecting the role of (configurational) entropy in flexibility.[144] However, the most immediate image of a defect is in the form of vacancies, so removed building blocks. Their impact can be illustrated by the mechanical responsiveness of $M_6O_4(OH)_4bdc_6$ (UiO-66) and its extended isoreticular framework family famous for its accessible defect engineering. These MOFs consists of twelve-connected metal SBUs and both present a pronounced inherent fraction of missing linkers (up to 10%) and allow for systematic defect concentration variation through use of modulators in their synthesis.[163,164] The inclusion of linker vacancies decreases its bulk, shear and elastic moduli and increases anisotropy at higher defect concentrations.[165]

One of the goals towards establishing design principles for responsiveness is to transfer defect engineering concepts to switchable materials, although to the best of my knowledge studies on vacancy-defect tailored switchable MOFs are exceedingly rare and do not cover all flexibility modes. The elucidation of the NGA phenomenon in DUT-49(Cu) is an example for the impact on a swelling-motion.[128] KRAUSE et al. synthesized a series of DUT-49 derivatives with increasing defect content by utilizing the solid-solution approach to gradually substitute the tetradentate 9,9'-([1,1'-biphenyl]-4,4'-diyl)bis(9H-carbazole-3,6-dicarboxylate) ($bbcdc^{4-}$) linker with the bidentate 9H-carbazole-3,6-dicarboxylate (cdc^{2-}).[129] This leads to open coordination sites at SBUs, missing linker defects, and at higher cdc^{2-} concentrations missing SBU defects. It was found that particle sizes decrease with increased defect amount and these in tandem affect sorption properties. However, relative to non-defect engineered samples (without any cdc^{2-}) with purposefully matched particle sizes, no effect on adsorption behavior was identified that solely correlated to defects (at any defect concentrations probable to occur in standard DUT-49 synthesis). So particle size effects outweigh the impact vacancy-defects have on flexibility,[166] or at least

likely have on swelling motions. *

This raises the question: what is the effect of particle size and particle surface? Understanding crystal size dependency of MOF properties and accompanying surface changes is essential. Especially if flexible MOFs are to be processed and used in applications – both of which might alter their crystallinity or particle shapes – it needs to be controllable which impact this has on switchability. A prominent example is DUT-8(Ni). Its micro-particles are rigid, while macro-particles are flexible exhibiting the adsorbate-induced breathing.[167,168] It is similarly found in DUT-8(Co) and although therein SBU deformability arises as additional factor, particle size is confirmed to have an overarching influence.[96,169] However, a recent study by THOMPSON et al shines a new light on size-dependent flexibility: they conclude that not directly particle size but concentration and amount of surface defects and related nucleation barriers of the phase transition govern material flexibility.[170] As consequence, surface modifications by modulators, capping agents, or anchored/attached species should offer the opportunity to manipulate the underlying MOF's flexibility. This idea is investigated in **STUDY II** and **III** which elaborate the impact mesoscopic, surface-mounted NPs – effectively mesoscopic surface-defects – have on the responsiveness of $Zn_2(DP-bdc)_2$dabco and $Zn_2(BME-bdc)_2$dabco.

2.3.2 RESPONSIVENESS IN RIGID METAL-ORGANIC FRAMEWORKS

If the backbone of a material is rigid and does not allow for network flexibility, dynamic responsiveness can still arise from either smaller backbone deformations or added moieties and extra-backbone components, i.e. linker functionalizations or counter ions, which can respond instead of the rigid scaffold. Such rigid stimulus-responsive MOFs could bring advantages in material cyclability and longevity, or enable the use of functionalization to create different responsiveness without risk of disrupting a balance of network flexibility thermodynamics (and thereby accidentally compromising the material). The scope of available stimuli is of comparable diversity to flexible materials (adsorbate, temperature, redox chemistry, light).[113,117,171–174]

However, much fewer of such rigid MOFs exist, i.e with adsorbate-responsiveness. $Cu_2(tpt)(CH_3CN)_2 \cdot 2\,BF_4$ utilizes moveability of its counter ions within its pore channel to create responsiveness.[175] These anions partition the pore channels and act as host-guest interaction-responsive gates opening as a function of the electronic property of the adsorptive, not it's size; conceptual parallels to trapdoor zeolites can be drawn.[176,177] $Co(mptbdc) \cdot 3H_2O$ (JNU-3a) shifts this channel partition by anion to orthogonally arranged pockets partitioned by linker moieties. The linkers forming

---

* It stands to reason that different motions show different defect sensitivities. From a mechanical point of view vacancy defects should have lower gravitas if within an as entity moving part (i.e. in a subnet that is displaced) than at a hinge at the center of the motion (i.e. in the rod-like connections in a wine-rack motion).

the apertures respond differently to different electronic properties of the adsorptives (therein moving slightly to open for propane at a different pressure than for propylene).[178] The concept shown in $Cu_2(tpt)(CH_3CN)_2 \cdot 2\,BF_4$ might yield some inspiration to design responsiveness in other MOFs and warrant further studies, i.e. with different counter ions, but JNU-3a is probably too specific in how its responsiveness is directed to yield information on design principles for MOFs not showing these exact same orthogonal pockets (though JNU-3a itself might be tuned to exhibit different responsiveness). A more simplistic design approach is reported by KANOO et al.[179] $Zn_2(R-ip)(NO_3)_2(bpy)_2$ (R-PCP) (with R = Cl, Br, I) enhances its adsorptive gating by virtue of introduced halomethyl functionalizations. The resulting physisorption isotherms look strikingly similar to typical stepped gate-opening/closing isotherms observed in flexible MOFs which arise from changes to adsorptive accessible pore volume. However, no such volume changes are observed in R-PCP and its performance is attributed to an amplified inclusion occurring due to host-guest interactions ordering/rearranging adsorbate within the pores. Which concrete design principles can be unraveled from this remains to be seen, the inner workings are still under investigation, but this MOF highlights the potential to fulfill a promise of stimulus-responsive, rigid materials: use of minimal functionalization to create drastically different performance without altering secondary properties.

2.4 FUNCTIONALIZED PILLARED-LAYERED AND HONEYCOMB-LIKE FRAMEWORKS

The studies in this thesis investigate two MOF systems with similar constitution, but very different topology, coordination motifs, modifyability, stimulus-responsiveness, and flexibility. $Zn_2(fu-bdc)_2dabco$ is part of the relatively populated sub-class of pillared-layered MOFs. It is studied especially for its pronounced anisotropic responsiveness, including flexibility, and extensive functionalization options altering its properties drastically. $Zn_2(fu-bdc)_2bpy$ forms a rigid, honeycomb-like motif with big hexagonal channels well suited for homogeneous pore functionalization with more gradual effects. The following sections outline their topologies and briefly (re-)iterate their key features.

2.4.1 THE PILLARED-LAYERED $Zn_2(fu-bdc)_2dabco$

Pillared-layered MOFs consist of two different types of linkers which enables their eponymous topology. The carboxylate linkers connect the metal SBUs in two dimensions, forming a square-lattice net, and the nitrogen-coordinating linkers stack ("pillar") these nets along the third dimension by connecting two metal SBUs from different

nets. This allows for targeted expansion along only certain directions or separate functionalization of linker and pillar. These options are elaborated in comprehensive reviews on this material subclass.[109,180] Specifically $Zn_2(bdc)_2dabco$ (DMOF-1) is accessible to extensive functionalization and big responsiveness changes. It and the $Zn_2(fu-bdc)_2dabco$ derivatives form a wine-rack topology which is visualized in figure 10 and topologically comparable to i.e. MIL-53 (see figure 8). The flexibility this motif exhibits in response to external stimuli can be tuned by its bdc^{2-}-substituents, both as distinct transition switching between crystalline phases or more gradual deformation. For example, while DMOF-1 shows negative thermal expansion (NTE) $Zn_2(TM-bdc)_2dabco$ (TM = tetramethyl) exhibits very notable positive thermal expansion (PTE). The overall observed TE can be tailored by the bdc^{2-}:$TMbdc^{2-}$ ratio in the respective ssMOFs.[136,181]
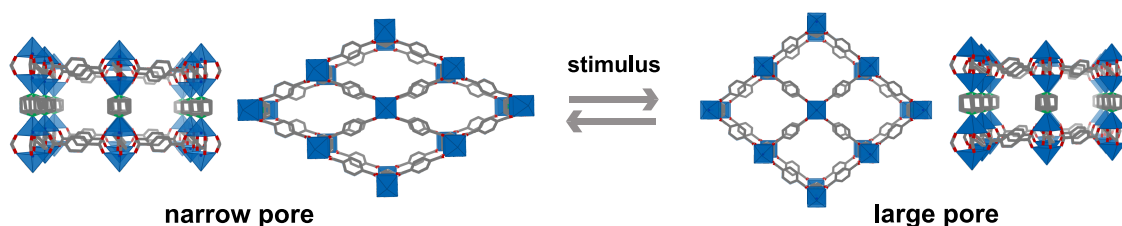
Figure 10. Topology visualization of $Zn_2(fu-bdc)_2dabco$ and its stimulus-inducable phase transitions from a np state (left) to a lp state (right). Shown is the view along the SBU-pillar axis onto the square- or lozenge-lattice nets (inner images) and the view along this net onto the pillars (outer images). Blue, metals and coordination polyhedron; grey, carbon; red, oxygen; hydrogen and functionalizations omitted for clarity, dabco pillars depicted with statistical disorder.

Switchability with distinct meta-stable np and lp states can be designed by introducing longer functionalizations. This was discovered for alkylamido or alkoxy chains as elaborated above.[133,147] Especially longer side chains enable additional stimuli to trigger switching: substituents with a length of five atoms (methoxyethoxy or butoxy) exhibit guest and temperature induced phase transitions,[115] plus the latter as third option – although only known for the copper MOF derivative – switching by mechanical pressure.[144] These effects can be rationalized by correlating linker functionalizations to dispersion and entropic stabilization (see work by WIEME et al. on MIL-53 and analogues elaborated above in section 2.3.1.2) and vibrational entropy as found in investigations on lattice dynamics of i.e. $Zn(im)_2$ (ZIF-4) and MIL-53.[182–184] The study on mechanical responsiveness of $Cu_2(DB-bdc)_2dabco$ by VERVOORTS et al. combines experiment and computation to correlate concrete thermodynamics of this material's phase transition. The key finding is that there exists an equal share of vibrational and configurational entropy stabilizing the lp state under mechanical pressure.[144]. The former is almost unaffected by the linker functionalizations, the latter only present because of the functionalizations. Longer side chains in $Zn_2(fu-bdc)_2dabco$ stabilize its np phase by providing dispersion stabilization, whereas they stabilize its lp phase by providing configurational entropy stabilization.

2.4.2 The Honeycomb-like $Zn_2(fu-bdc)_2bpy$

The MOF $Zn_2(fu-bdc)_2bpy$ constitutes a pillared-layered framework per its sum formula – effectively a $Zn_2(fu-bdc)_2dabco$ with elongated pillar. However, solvothermal reaction conditions determine whether it is formed as such or crystallizes as honeycomb-like MOF with hexagonal, 1D pore channels.[185] The pillared-layered version consists of interpenetrated scaffolds which exhibit some flexibility in the form of sub-net displacement;[108,186] the honeycomb-like version is structurally rigid.[187] Only the latter MOF is studied in this thesis (see section 4.1).
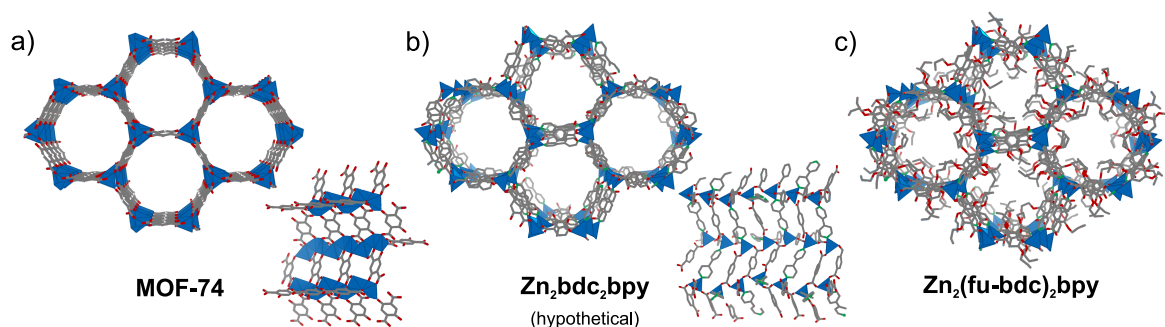
Figure 11. Topology comparison of MOF-74 (a) and $Zn_2(fu-bdc)_2bpy$. b) shows the hypothetical MOF without linker functionalizations, c) shows $Zn_2(DP-bdc)_2bpy$ (DP = 2,5-dipropoxy). Next to a) and b) are segments of pore walls highlighting the different rod-style of the SBUs: edge-sharing in MOF-74 vs. separated in $Zn_2(fu-bdc)_2bpy$. Blue, metals and coordination polyhedron; grey, carbon; red, oxygen; hydrogen omitted for clarity.

$Zn_2(fu-bdc)_2bpy$ is structurally similar to the prototypical $M_2(dobdc)$ (MOF-74).[188] Both form rod-like metal SBUs and 1D hexagonal pore channels with continuous walls consisting of the linker(s) connecting different SBUs (no distinct apertures connect adjacent channels, but the channel walls are permeable). Figure 11 visualizes the topology similarities of MOF-74 and $Zn_2(fu-bdc)_2bpy$, but important differences exist as indicated by small insets of pore channel sections. First, because $Zn_2(fu-bdc)_2bpy$ integrates two linkers (bdc^{2-} and bpy) so do the pore walls. They build two different walls: one with 1:1 ratio and one with 1:3 ratio of both linkers. Each hexagonal channel alternates both variants. Second, the rod-like SBU of MOF-74 consists of an infinite chain of edge-sharing coordination tetrahedra which creates open-metal sites, while $Zn_2(fu-bdc)_2bpy$'s metal SBU consists of separate coordination tetrahedra linked by bridging carboxylates. Each zinc atom is coordinatively saturated which is a crucial prerequisite for **Study I** because these would strongly direct sorption properties (as can be utilized in MOF-74)[189,190] and superimpose on more intricate changes induced by linker functionalizations.

3

OBJECTIVE

MOFs are a highly modifiable material platform predestined for design of dynamic, responsive, smart materials. The achievable property range – design for gas storage, sieving as membranes, sensing as thin films, or information storage as part of microelectronics – is in demand for next-generation applications aimed towards resource and energy sustainability and efficiency.

They enable, on one hand, step-by-step alteration of singular parameters coupled with relative ease of structural characterization. This allows methodical investigations on tailoring properties. On the other hand however, the enormous amount of modifications are impossible to analyze by manual trial-and-error. It is first necessary to understand how and which microscopic chemical changes can be utilized to manipulate macroscopic material properties and second to abstract the underlying principles of responsiveness design. Both aspects are under prominent attention of the research community as targeted synthesis of stimulus-responsive MOFs remains largely inaccessible and rapid progress is made to overcome this challenge.

The research unit "FOR2433 – Switchable MOFs", in which context this thesis is embedded, contributes to this endeavor.* Its main objective is improving the fundamental understanding of dynamic responsiveness and its ties to underlying structural design principles. This overarching goal is addressed in four objectives that are: 1) development of a predictive theoretical framework, 2) development of tailored in situ characterization techniques, 3) impact of cooperative phenomena, heterostructures (composites), disorder, and defects on switchability and 4) differentiation of specific vs. non-specific responsiveness. Herein presented studies explore how extensive functionalization of linkers impact adsorbate-triggered dynamic responsiveness in rigid

---

* Further information on this research unit funded by the German Research Foundation (DFG) (involved groups, all projects and publications, more detailed scope) can be found at gepris.dfg.de/gepris/projekt/279409724 and tu-dresden.de/mn/chemie/ac/ac1/forschung/forschergruppe-2433

and flexible MOFs and how switchability in flexible MOF composites with mesoscopic, surface-mounted nanoparticles is altered compared to the pristine materials.

STUDY I deals with unraveling specific functionalization-introduced, adsorbate-induced responsiveness in the rigid $Zn_2(fu-bdc)_2bipy$ (related to FOR2433 - objective 4). This MOF system, up to now to the best of my knowledge only reported on its discovery by HENKE et al. and later by COHEN et al. as topological template for a polymer-metal-organic framework,[186,187] boasts 1D pore channels which are homogeneously lined with linker functionalizations. The MOF is therefore well suited to investigate their impact on adsorbate responsiveness. The study asks and elaborates:

"Which factors of introduced linker functionalizations are responsible for the observed dynamic responsiveness in rigid MOFs?"

Relatively clear correlations between moieties and overall material performance can be drawn because only functionalizations are step-wise altered and no other aspect of the material is dynamic. Moreover, these findings are conceptually as straight forward to apply to other MOFs with similar topology as possible, because said linker moieties are the dominant directing factors (next to the presence of a metal SBU, which is ubiquitous for MOFs).

STUDY II and **III** investigate the impact of surface-mounted nanoparticles – effectively mesoscopic surface defects – on the responsiveness of $NP@Zn_2(fu-bdc)_2dabco$ composites (related to FOR2433 - objective 3). This flexible, pillared-layered MOF system is based on the rigid DMOF-1 but rendered flexible/switchable by added linker side chains. It was initially reported by COHEN et al.[147] and investigated in more detail by HENKE et al.[133,134] The MOF shows functionalization dependent switchability in response to physisorption and, for a specific linker side chain, additionally in response to temperature.[115] We took this 2-in-1 switchability as opportunity to investigate the hitherto unreported composite type NP@flexibleMOF and address the question:

"How do mesoscopic nanoparticles/defects influence the responsiveness of flexible MOFs?"

STUDY III directly looks at both stimuli-responses; nanoparticles are attached to the adsorbate- and temperature-switchable framework derivative. Property changes of the NP@MOF composites relative to the nanoparticle-free parent material are discussed, and the exerted influence of NPs with different sizes is probed. **STUDY II** in contrast tests $NP@Zn_2(fu-bdc)_2dabco$ composites based on a parent MOF not exhibiting a thermally induced phase transition. Instead its TE properties are observed which, however, correspond the same mechanical (topology determined) motion.

STUDY IV is dissimilar to the above mentioned in that it is not a finished/published study but consists of the first experimental and methodological milestone towards elaborating the solvent-switchability of a $Zn_2(fu-bdc)_2dabco$ series with various linker functionalizations. The perspective question(s) to be elaborated is (are):

"What is the scope of dynamic solvent-responsiveness in the $Zn_2(fu-bdc)_2dabco$ MOF series and which structural factors direct it?"

Presently, solvent-induced switching or sorption selectivity towards solvents (liquids at ambient conditions; instead of gases) is mostly studied if explicit applications are in mind, i.e. xylene isomer separation or trace impurity removal,[102,124,191,192] or if gas physisorption is not sufficient, i.e. for some MOF thin-film characterization if techniques like krypton sorption are unavailable. Fundamental investigation on solvent switchability have been conducted on few MOFs.[193,194] Findings on DUT-8(Ni)[195–197] motivated this conceptually closely related study on $Zn_2(fu-bdc)_2dabco$. Both an initial matrix correlating qualitative responsiveness, solvent, and linker functionalizations, as well as an experimental procedure for reproducible analysis are created for future work to build upon.

4

RESULTS AND DISCUSSION

4.1 STUDY I. Designing Adsorptive Gating via Linker Side-Chain Functionalization in a Honeycomb-MOF

This study investigates a series of isoreticular, functionalized MOF derivatives. It aims to draw a clear correlation between the chemistry of the system's functionalizations and resulting bulk material properties in order to unravel more general design principles which might be transferable to other frameworks. Methodically, kinetic and equilibrium gas physisorption of CO_2 and C_2H_2 coupled with Henry's law coefficients, and supporting ideal adsorbed solution theory (IAST), diffusivity, and pore size calculations are applied. The as backbone used honeycomb-like parent MOF was chosen because it has minimal impact on gas adsorption selectivity not stemming from the linker side-chain functionalizations. It has 1D, hexagonal pore channels with side-chains homogeneously presented on each face of the channel to maximize their effect, as well as no open-metal sites which would strongly interfere with physisorption selectivity. The MOF is rigid to avoid big structural changes during ad- and desorption. The only dynamic flexibility is introduced by the moveability of the side-chains. These are alkoxy groups (ethoxy, propoxy, butoxy, allyloxy, and propynyloxy motifs) substituted onto the terephthalic acid linker. By variation of both length and terminal saturation, we alter steric crowding and polarizability of the pore environment. Observed trends in above-mentioned methods ultimately show that both have distinct effects. Positive polarizability changes are reflected in higher interaction strength to polarizable adsorbates, while side chain sterics govern accessibility of the inherent preferred adsorption sites of the MOF. Overall, pronounced differences within 1 order of magnitude for sorption enthalpy and a selectivity range from 4.1 to 10.9 can be designed.

J.B. performed material synthesis and characterization, equilibrium physisorption measurements, data fitting and processing, and manuscript writing. A.S. provided the study design, and contributed to analysis and manuscript writing. I.H. and S.-I.N. enabled and performed initial physisorption experiments and contributed to manuscript writing. Y.J., T.T., and K.-I.S. performed and enabled breakthrough experiments and contributed to manuscript writing. J.P. and Y.H. provided structure modeling and contributed to manuscript writing. J.D.E. provided molecular simulations on PSD, sorption enthalpy, diffusion, and structure optimization. G.K. and R.A.F. provided the motivation of this work and contributed to manuscript writing.

Article

Designing Adsorptive Gating via Linker Side-Chain Functionalization in a Honeycomb-MOF

Jan Berger, Andreas Schneemann, Inke Hante, Yuan Jing, Jack D. Evans, Yuh Hijikata, Jenny Pirillo, Takashi Toyao, Ken-ichi Shimizu, Shin-ichiro Noro, Gregor Kieslich, and Roland A. Fischer*

Cite This: *J. Phys. Chem. C* 2022, 126, 12755−12764

Read Online

ACCESS | Metrics & More | Article Recommendations | Supporting Information

ABSTRACT: Metal−organic frameworks (MOFs) combine high guest-accessible porosity with high chemical versatility, which predestines tailor-making porous materials to overcome challenges in efficient next-generation gas separation processes. Adsorptive gating is an interesting material feature that enhances sorption selectivity, while its rational design is still beyond our knowledge. Herein, we report on a model system to explore the key factors of induced gating controlled by the implementation of conformationally flexible side chains at the linkers of a honeycomb-like, structurally rigid MOF, namely, Zn$_2$(2,5-difunctionalized-1,4-benzendicarboxylate)$_2$(4,4′-bipyridine). The sorption and separation properties of C$_2$H$_2$ and CO$_2$ were selected as the study case, and ideal adsorbed solution theory (IAST) selectivities, isosteric enthalpies of adsorption, Henry constants, breakthrough experiments, and simulations of dynamic properties were correlated with the linker functionalization. Two dominating factors that determine gating properties are identified: polarizability and sorption site accessibility. These factors are accessible through linker functionalization, and we show that adsorption strength differences can be influenced linearly within 1 order of magnitude, while breakthrough experiments show a selectivity increase toward C$_2$H$_2$, ranging from 4.1 to 10.9. The results suggest transfer to other MOFs toward extrinsic gating for sophisticated modulation of their sorption selectivity.
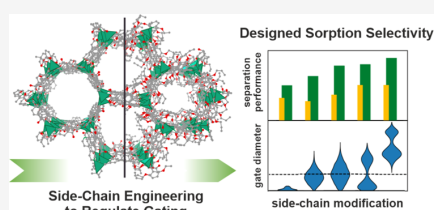
INTRODUCTION

The key feature of metal−organic frameworks (MOFs) is their guest-accessible porosity. The modular building-principle of MOFs and the virtually unlimited chemical parameter space for varying linker chemistry enable the design of MOFs with targeted linker and pore functionalities; both are routinely leveraged to create or enhance sorption capacity and selectivity to improve MOFs as adsorbents for gas storage and separation to name just a few applications.[1−4] The large chemical freedom to synthesize new materials has made trial-and-error experiments an inefficient approach. Consequently, research efforts in the field of MOF adsorbent design have moved more toward concept-based thinking, aiming to deepen our understanding of how structure and chemical functionality together impact a certain property and how to use this insight to design a property or combinations thereof in new materials.[5−7]

Separation of gas mixtures in MOFs can be achieved by various means,[8,9] with the most prominent being separation as a result of size exclusion/sieving at fixed pore apertures,[10,11] selective sorption via preferred coordination to open metal sites,[12−14] or selectivity direction by adsorptive-specific host−guest interactions, i.e., in tailored adsorption pockets or polarity gating processes in MOFs.[15−20] For a typical gating process, an adsorptive is hindered to adsorb into the bulk of a MOF due to insufficient enthalpic and entropic energies until a certain partial pressure is reached, after which the pore volume

becomes gradually more accessible or is stepwise created by virtue of a phase transition.[21,22] Importantly, the gating phenomenon is typically defined by the presence of a potential pressure-dependent or, more generally, a responsive dynamic factor, while conventional sieving relies on the presence of dedicated rigid moieties or scaffolds. In flexible MOFs, a subclass of MOFs with structurally flexible networks such as ELM-11,[23−26] MIL-53,[27−29] DUT-8,[30,31] and others,[32−35] gating is commonly present and enabled due to specific adsorptive−host interactions, which trigger a narrow-pore to large-pore phase transition. In contrast, only a few network-rigid materials are known that show such explicit gating behaviors. (See Table 1 for some important material examples, and see Figure 1 for a visualization of selected gating modes in response to guest sorption.) However, the absence of a phase transition during the separation process makes both key host−guest interactions more straightforward to investigate and promising gating features better transferable to other rigid systems. This transferability is of great importance to research
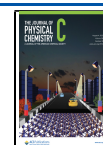
Table 1. Selected Examples of MOFs that Show Adsorptive Gating

MOF	network type	gating via[a]	refs
ELM-11	flexible	pore volume	23
MIL-53	flexible	pore volume	27
DUT-8(Ni)	flexible	pore volume	31
Cu(OPTz)	rigid	aperture size	46
JNU-3a	rigid	aperture size	47
Zn_2(ip-Cl) $(NO_3)_2$(bipy)$_2$	rigid	"amplified inclusion"	48
Zn_2(fu-bdc)$_2$bipy	rigid	pore volume	49, 50

[a]Property changing in response to adsorptive or directing factor.
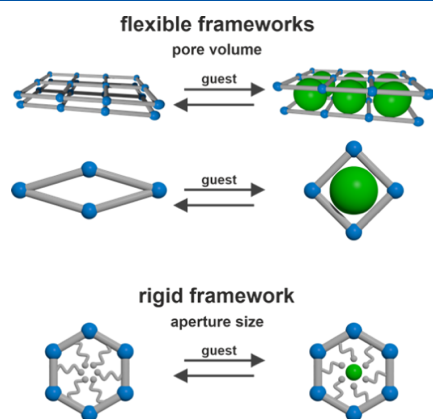
Figure 1. Selection of possible gating modes in flexible and rigid MOFs resulting in changes to pore volume or pore aperture (blue, metal node; gray, linker; green, accessible pore volume).

on next-generation MOF adsorbents, many of which rely on electronic (often coupled with kinetic) differentiation of gases and thereby could be improved or potentially modified to exhibit explicit gating. Their perspective applications range from enabling highly specialized lower-scale separations, i.e., toxic gas removal or acetylene separation,[36−38] improved gas capture and storage, i.e., CCS or carbon dioxide conversion,[39−41] to more energy-efficient industrial processes, i.e., natural gas upgrading and ethane/ethylene separation.[42−45] However, the targeted (a priori) design of functionalization-directed adsorptive gating is presently beyond our knowledge because underlying key principles still need to be unraveled.

Gating in rigid MOFs is often controlled by temperature. An early showcase for this is the mesh-adjustable molecular sieve (MAMS-1, Ni_8(bbdc)$_6$(μ_3-OH)$_4$, bbdc^{2-} = 5-*tert*-butyl-1,3-benzenedicarboxylate), which shows precise adsorptive gating arising from the thermal vibration of gating-directing linker moieties to separate adsorptives in a size range from nitrogen to isobutane.[51] Similar and more recently studied are materials such as CAU-10-OMe (Christian-Albrechts-Universität, Al-(OH)(OMe-ip), OMe-ip^{2-} = 5-methoxyisophthalate)[52] or Cu(OPTz) (Cu(OPTz-ip), OPTz-ip^{2-} = 5-(5,5-dioxide-10*H*-phenothiazin-10-yl)isophthalate), both of which change pore apertures to create sorption selectivity.[46] This thermally controlled size-exclusion sieving, however, does not differentiate based on electronic adsorptive properties.

Examples of rigid MOFs that demonstrate gating control via electronic adsorptive interactions are few but growing in numbers. For instance, the gating process in Cu_2(tpt)$_2$(CH$_3$CN)$_2$·2BF$_4$ (tpt = 2,4,6-tri($_4^-$pyridyl)-1,3,5-triazine) is based on channel partition by BF$_4^-$ anions that act as host−guest interaction-responsive gates and parallels exist to trapdoor zeolites.[53−55] Additionally, the recently investigated JNU-3a (Jinan University, Co(mptbdc)·3H$_2$O, mptbdc^{2-} = 5-(3-methyl-5-(pyridin-4-yl)-4*H*-1,2,4-triazol-4-yl)-1,3-benzenedicarboxylate) is comparable to the above-mentioned pore apertures controlled by temperature but controlled as a function of adsorptive interaction. The compound forms adsorption pockets with distinctly different gate-opening-pressures for propane or propylene.[47] These examples demonstrate that gating, even if caused by selfsame structural features, can be achieved by different means. In the search for transferable designs for gating in network-rigid MOFs, the study by Kanoo et al. reporting Cl/Br/I-PCP (Zn_2(ip-R)(NO$_3$)$_2$(bipy)$_2$, ip-R = 5-halomethyl-isophthalate, bipy = 4,4′-bipyridine) should be highlighted.[48] By virtue of the simple halomethyl functionalization of the linker, adsorptive gating is enhanced. Within its pore channels, amplified adsorptive interactions are identified as directing factors. It shows that opportunities to tune adsorptive gating by rather universal means can be created and there is huge potential for utilizing them, but their underlying design principles need to be understood.
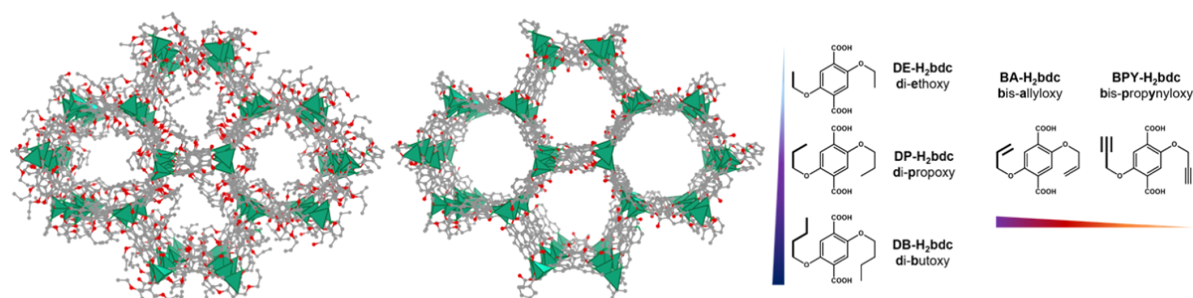
Figure 2. Depiction of the Zn_2(DP-bdc)$_2$bipy honeycomb-like structure with a view along the one-dimensional (1D) channels with propoxy functionalizations (left) and the hypothetical structure without side chains (center). Carbon, nitrogen, and oxygen atoms and the zinc coordination tetrahedron are shown in gray, light green, red, and dark green, respectively, and hydrogen atoms have been omitted for clarity. Right: Terephthalic acid derivatives used in creating isoreticular materials **DE**, **DP**, **BA**, **BPY**, and **DB**. Blue colors indicate an increase in the functionalization length and red colors indicate an increase in saturation.

In the pursuit to identify such principles, we here apply the previously discovered honeycomb-like MOF $Zn_2(fu\text{-}bdc)_2bipy$ ($fu\text{-}bdc^{2-}$ = 2,5-difunctionalized-1,4-benzendicarboxylate) as a model system (see Figure 2).[49,50,56] This system is rigid, shown to exhibit adsorptive polarity-dependent gating, and features an easily, even with extensive functionalizations, modifiable backbone. This study highlights two expanded series of isoreticular materials for exemplary C_2H_2/CO_2 separation: how to tune their adsorptive gating, how they intertwine with sorption strength, selectivity, and preference, and which key principles can be deduced.

■ METHODS

Material Synthesis. All chemicals were purchased from commercial suppliers (Sigma-Aldrich, Fluka, Alfa Aesar, ABCR and others) and used without further purification. Ethanol for solvent exchange was purchased as technical grade and redistilled prior to use. All linkers were synthesized via the Williamson etherification of dimethyl-2,5-dihydroxy-1,4-benzendicarboxylate with 1-bromoalkyl, -alkenyl, and -alkynyl reagents according to literature-known procedures,[57] albeit slightly altered/optimized based on functionalization (for individual and detailed procedures, see the Supporting Information S1.2). MOFs **DE** ($Zn_2(fu\text{-}bdc)_2bipy$; fu = 2,5-diethoxy), **DP** (fu = 2,5-di-propoxy), **BA** (fu = 2,5-bis-allyloxy), **BPY** (fu = 2,5-bis-propynyloxy), and **DB** (fu = 2,5-di-butoxy) were synthesized according to procedures of the original parent system.[49] Synthesis was scaled up to ca. 1 g scale, and the washing and activation procedure was adapted (for details, see Supporting Information S1.3). Microcrystalline powders were obtained with the coloration ranging from white to brown depending on the linkers used. All materials were stored under dry Ar to exclude any contamination or undesired gradual hydrolysis.

Analytical Methods. Liquid-state NMR spectra were measured on a Bruker Ultrashield DRX400 spectrometer at ambient temperature (for details, see Supporting Information S1.1). MOF samples were digested and subsequently measured in DMSO-d_6 with DCl; all other substances were dissolved and measured in DMSO-d_6. CHNS contents were determined via combustion analysis. Thermogravimetric analysis (TGA) was conducted on a Netzsch TG-DSC STA 449 F5 in the temperature range from 25 °C to 800 °C (for details, see Supporting Information S2). Powder X-ray diffraction (PXRD) patterns were measured in Debye−Scherrer geometry on a PANalytical Empyrean diffractometer (for details, see Supporting Information S3). Activated samples were filled in glass capillaries in a glovebox under an argon atmosphere. Adsorption measurements with N_2, CO_2, and C_2H_2 were carried out on a 3Flex Physisorption Instrument from Micromeritics Instrument Corp. Samples were activated at 80 °C for 5 h under dynamic vacuum using a SmartVacPrep by Micromeritics Instrument Corp. to ensure the absence of unwanted adsorbates as well as to ensure identical premeasurement states of all samples. The mass of the adsorbent was then recorded in the range of 70−100 mg (for more details, see Supporting Information S4). Breakthrough experiments were carried out with a self-assembly setup. MOF materials (1.0 g) were placed into a ∅ 3 × 350 mm glass cell and pretreated for 1 h at 120 °C under a helium flow of 10 mL/min to remove unwanted adsorbates. Experiments were performed for C_2H_2/CO_2 mixtures at a 1:1 ratio without a carrier gas at a combined flow rate of 5 mL/min at 303 K and ambient pressure. The input gas flow ratio was adjusted and controlled using mass flow controllers, and the output gas stream composition was monitored via a 990 Micro GC by Agilent Technologies Inc. equipped with a PoraPLOT Q column and a thermal conductivity detector (for more details, see Supporting Information S8). SEM images were obtained with a Jeol JSM-7500F field emission scanning electron microscope in the Gentle Beam mode with an accelerating voltage of 1 kV (see Supporting Information S10).

Adsorption Data Processing. All adsorption isotherms are accessible online free of charge as adsorption information files to counter issues with postpublishing adsorption data extraction and facilitate machine learning (see the Supporting Information).[58] Adsorption isotherms of C_2H_2 and CO_2 at 298, 288, and 278 K were fitted using a dual-site Langmuir−Freundlich equation, and the fitting parameters were used with the Clausius−Clapeyron expression to derive the isosteric enthalpy of adsorption values (for details on equations, plotted fits, and tabulated fitting parameters, see Supporting Information S5). Isotherms measured at 298 K were further used in the calculation of sorption selectivities based on the ideal adsorbed solution theory (for details, see Supporting Information S6).[59] All isotherms were in parallel, fitted using the virial equation of adsorption to derive Henry's law constants (for details on equations, plotted fits, and tabulated fitting parameters, see Supporting Information S7).

Theoretical Modeling. Geometry optimizations of the crystal structures of **DP**, **BA**, **BPY**, **DB**, and **DE** were initially performed using the self-consistent-charge density-functional tight-binding method[60] with the third-order expansion (DFTB3)[61] method as implemented in the DFTB+ program package version 1.3.1.[62] with periodic boundary conditions. Materials were subsequently optimized with lammps[63] using the UFF4MOF classical potentials,[64] as defined by the lammps-interface code[65] (for complete details on both optimizations, see Supporting Information S9.1). Molecular dynamics simulations were performed for each of the materials to capture the porosity changes relating to the dynamics of the side chains (for details, see Supporting Information S9.2). An inert spherical probe (1.3 Å) was used to determine the limiting pore diameter and the largest pore diameter along a free path in the structure. The resulting approach provides realistic distributions of the pore sizes present in the materials. The adsorption enthalpy and diffusivity for CO_2 and C_2H_2 were also investigated using the same classical approach (for details, see Supporting Information S9.3).

■ RESULTS AND DISCUSSION

Rigid Honeycomb-like MOFs. The employed MOF systems $Zn_2(fu\text{-}bdc)_2bipy$ were synthesized from $Zn(NO_3)_2$, bipy, and corresponding $fu\text{-}H_2bdc$ derivatives (see Figure 2) using an optimized procedure based on reported methods and were verified to be isoreticular to the reported parent system by PXRD.[49] Material composition and complete activation were confirmed via ^1H NMR spectroscopy, EA, TGA, and nitrogen physisorption (see the Supporting Information). The MOF has two similarly sized 1D hexagonal channels (Zn−Zn distances across channels: 20.1 and 20.9 Å) with two types of pore walls that alternate with $fu\text{-}bdc^{2-}$ and bipy stackings in a 1:1 and a 3:1 ratio; therefore, there is consistent and homogenous distribution of functionalization along all channel walls (see Figures S1.3-1 for pore wall visualization). These side chains fill the pore volume and decrease the effective pore
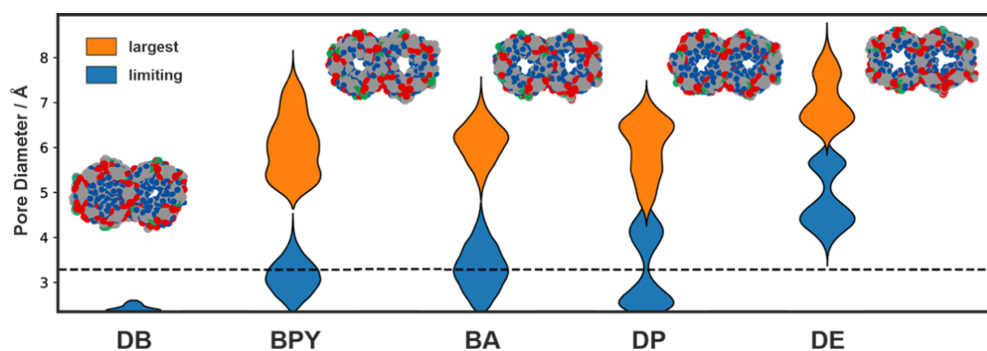
Figure 3. Dynamic pore size distributions for all materials with limiting (blue) and largest (orange) pore diameters accompanied by the visualized pore volume of both framework channels. The dotted line indicates the kinetic diameter of CO_2 and C_2H_2. Carbon, nitrogen, oxygen, zinc, and hydrogen atoms are shown with van der Waals radii in gray, light green, red, dark green, and blue, respectively.

Table 2. Performance Comparison of Materials of This Study

		selectivity C_2H_2/CO_2			CO_2 productivity (mmol/g)		working capacity (mmol/g)		diffusivity $\times 10^{-9}$ (m^2/s)	
	functionalization	IAST[a]	breakthrough	$d(-\Delta H_{ads})$ (kJ/mol)[b]	high purity[c]	total	C_2H_2	CO_2	C_2H_2	CO_2
DE	diethoxy	6.5	10.0	15.5	1.09	1.92	2.13	0.21	0.49	4.42
DP	dipropoxy	6.1	10.3	8.0	1.09	1.72	1.91	0.19	2.02	2.12
DB	dibutoxy	6.9	9.0	1.5	0.69	1.08	1.21	0.13	0.03	
BA	bis-allyloxy	5.1	10.9	7.2	0.79	1.68	1.85	0.17	0.65	1.34
BPY	bis-propynyloxy	3.6	4.1	3.2	0.59	1.36	1.80	0.44	0.27	0.98

[a]At 1 bar. [b]At 0.5 mmol/g loading. [c]>99.5% CO_2.

aperture. Dynamic pore size distributions (PSDs) were computed based on simulated structures including all functionalizations, which are not accessible from PXRD and single-crystal diffraction data due to their highly disordered nature. The distributions were determined by probing the accessible volume with an inert probe sphere (see Supporting Information S9.2) for snapshots from molecular dynamics simulation trajectories at 298 K. PSDs of the limited (smallest diameter along a free path) and largest (largest diameter along a free path) pore sizes show that all materials except for **DB** are guest-accessible; see Figure 3. Experimental results show that **DB** only is porous toward adsorptives with suitable host–guest interactions, enabling diffusion through formally blocked channels. Notably, the distribution of the pore aperture and the largest channel size behave in a nonlinear fashion. While all apertures and volumes (excluding **DB**) increase, this is significantly more pronounced for **BPY**. In **DP** and **DE**, two distinct pores in the framework produce a bimodal distribution of pore diameters, whereas for other structures, the distribution from the movement of side chains overlaps, leading to unimodal distributions.

C_2H_2 and CO_2 Physisorption and Ideal Adsorbed Solution Theory (IAST) Selectivity. This work focuses on investigating and identifying contributions to the overall observed adsorptive gating effect created by virtue of introduced functionalizations and changes thereof (Table 2). We chose C_2H_2 and CO_2 because both feature identical kinetic diameters and are equally affected by sterical changes to the side chains, which focuses the investigation on the other differentiating properties: differences in polarizability and quadrupole moments (see Table 3) create influenceability by electronic factors as are present in the selected linker derivatives. Furthermore, absolute CO_2 uptake is sufficiently

Table 3. Adsorptive Comparison of Properties Relevant for Separation via Gating[70]

	kinetic diameter (Å)	dipole polarizability ($\times 10^{-24}$ cm^3)	quadrupole moment ($\times 10^{-40}$ cm^2)[a]
C_2H_2	3.3	3.487	21.13
CO_2	3.3	2.507	−14.27

[a]The Θ_{zz} moment is tabulated in SI units.

high for all materials to avoid susceptibility to absolute measurement errors or fitting discrepancies, which in contrast we would anticipate for the otherwise viable C_2H_2/N_2 comparison. Most MOF systems designed for C_2H_2/CO_2 separation have sorption enthalpy differences of less than 20 kJ/mol with calculated selectivities toward C_2H_2 of 3–30 (see Table S8 for an overview).[66] Recent benchmark materials feature sorption enthalpy differences of 40–50 kJ/mol with selectivities of up to 54 and 185.[67,68] That gating is utilizable for this separation based solely on the differentiation of the quadrupole potential, and the orientation has been previously demonstrated with Mn(bdc)(dpe) (bdc^{2-} = 1,4-benzenedicarboxylate, dpe = 1,2-di(4-pyridyl)ethylene) whose twofold interpenetrated scaffolds adsorb CO_2 preferentially due to aligning quadrupole orientations.[69]

In single-gas adsorption experiments at 298 K, all materials show a higher C_2H_2 uptake compared to CO_2 and the total uptake correlates with the available free pore volume, as shown in Supporting Information S4.3. A notable exception is the lower CO_2 uptake of **DE** aligning with **BA** values. To quantify the separation efficiency, isotherms were fitted using a dual-site Langmuir–Freundlich equation, and selectivities were calculated using the ideal adsorbed solution theory (IAST) (see Supporting Information S6).[59] All MOFs show the highest IAST selectivities for adsorption of C_2H_2 over CO_2 at low

pressures, which slightly decrease as the pressure increases; see Figure 4.
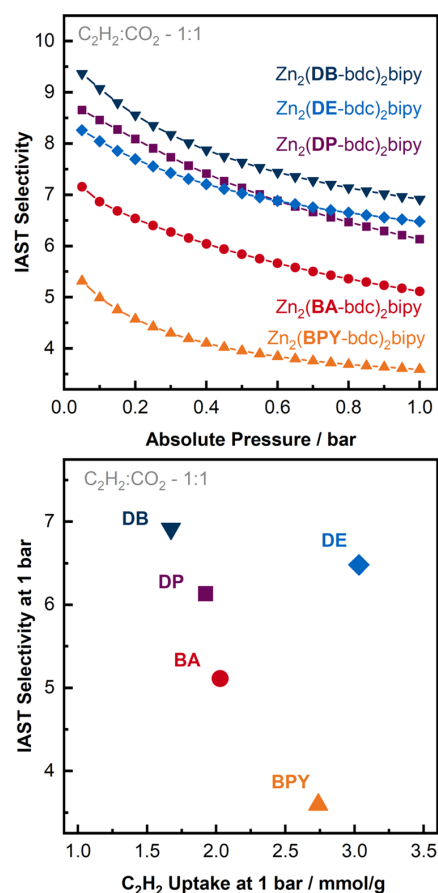
Figure 4. Top: Calculated IAST selectivities for a 1:1 ratio of C_2H_2/ CO_2 at 298 K. Bottom: Selectivities at a pressure of 1 bar correlated to their respective single-gas adsorption C_2H_2 uptake for **DE** (blue diamonds), **DP** (purple squares), **BA** (red circles), **BPY** (orange triangles), and **DB** (dark-blue upside-down triangles).

Tuning of the functionalization can overall result in doubling of the achievable IAST selectivity. Throughout the IAST pressure range, the selectivity trend of **DP > BA > BPY**, indicating a positive impact of low chain polarity and rigidity, is retained, while an initial trend with respect to chain length, i.e., **DB > DP > DE**, is lost in favor of **DE** over **DP**. Absolute differences in selectivities are the highest within the series with altering side-chain saturation. Correlating IAST selectivities to C_2H_2 uptake at a practically more relevant pressure of 1 bar shows a more detailed picture: throughout changes to functionalization polarity, the trends of both selectivity and uptake are maintained. Changes in chain length result in a higher uptake with a shorter length with no apparent selectivity trend present. However, a shortened side chain overall creates an equal or better IAST selectivity per C_2H_2 uptake ratio, with **DE** being the best performant.

Adsorption Strength. Isosteric enthalpy of adsorption (ΔH) calculations were conducted based on C_2H_2 and CO_2 isotherms collected at three different temperatures (298, 288, 278 K) and fitted with a dual-site Langmuir−Freundlich equation (see Supporting Information S5).

Adsorption enthalpies (see Figure 5) mirror the trend in side-chain saturation, as observed in IAST selectivities (**BPY < BA < DP**). Interestingly, the nonlinear ratio of changes in ΔH and IAST selectivities throughout both material series indicates the presence of another influential parameter or correlated effects. This is emphasized by the side-chain-length trend of ΔH: a decrease in chain length results in a pronounced absolute increase in the sorption enthalpy of C_2H_2 accompanied by higher ΔH differences between C_2H_2 and CO_2. This trend is also present for changes in side-chain saturation but to a lesser extent. Both trends can additionally be observed when comparing Henry's law constants. In the context of sorption on a solid interface, the calculated Henry's law constants are a qualitative measure of adsorbate volatility at low loading. They are as such strongly related to the adsorption enthalpy. In the given form (see Supporting Information S7), lower Henry's law constants correlate with higher ΔH. Values for C_2H_2 match ΔH observations of both material series in both trend and relative quantity. In contrast, IAST selectivities show a clear trend for changes in side-chain saturation only.
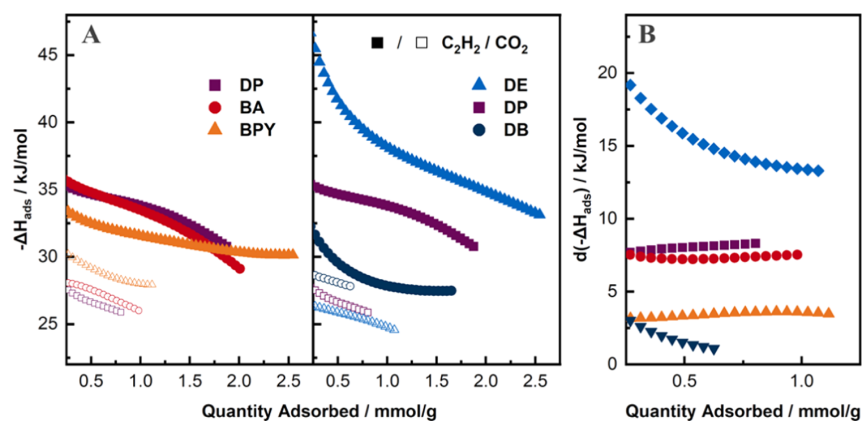
Figure 5. (A) Determined ΔH of C_2H_2 (full symbols) and CO_2 (open symbols) for all materials. Comparison of functionalization saturation (left; red color scale) and length (right; blue color scale). (B) Difference in ΔH of C_2H_2 to CO_2 at identical absolute loadings.

Overall, shortening the side-chain length leads to increased ΔH differences between C_2H_2 and CO_2, up to a tenfold increase from 1.5 to 15.5 kJ/mol. The same can be observed for changes in terminal side-chain saturation on a smaller scale from 3.2 kJ/mol up to a 2.5-fold increase to 8.0 kJ/mol. However, the determined IAST selectivities show discrepancies in this otherwise coherent behavior, and thus, the separation efficiency is more thoroughly analyzed and discussed by means of C_2H_2/CO_2 breakthrough experiments.

Breakthrough Experiments and Diffusivity Simulations. Dynamic two-component flow adsorption and adsorbent performance can reasonably be expected to differ from single-gas adsorption and findings from IAST-based calculations for the tested materials. While IAST generally tolerates higher adsorbate loadings and the observed ΔH differences of C_2H_2 and CO_2, even though both are deviations from ideal mixtures,[71−73] the introduced flexible moieties show adsorbate (partial) pressure-dependent shifting and a resulting change in the accessible pore volume as a significant nonideality factor.[74] This is most vividly observed with **DB** showing a pore aperture smaller than C_2H_2 or CO_2 when probed in simulations in its rigid, noninteractive idealized state, which contrasts the in-experiment-observed gas uptakes. This emphasizes the relevance of breakthrough experiments especially in the context of adsorbent systems with such a substantial degree of functionalization with nonrigid moieties within a rigid scaffold. Consequently, breakthrough experiments with all materials (1.0 g each) were performed with a 1:1 ratio of C_2H_2/CO_2 with a total flow rate of 5 mL/min at 303 K (see Supporting Information S8 for breakthrough curves and explanation of methodological factors). All materials preferentially adsorb and retain C_2H_2 and thereby show excess CO_2 productivity. Considering the total amount of excess CO_2 enriched in the effluent stream, effects of both side-chain saturation and length show clear trends; see Figure 6, bottom. On the one hand, CO_2 productivity is the lowest for **DB** and gradually increases with shorter chain lengths via **DP** to the highest value for **DE** with 1.92 mmol/g, indicating in total a 1.8-fold increase. On the other hand, CO_2 productivity is 1.3 times higher for **DP** than for **BPY** and correlates with the decrease in side-chain saturation (see Table 2). A comparison to the achievable high-purity (>99.5%) CO_2 output gives additional insights into changes in separation kinetics during competitive sorption. The ratio of the high-purity output to the total output is inversely related to the total CO_2 productivity for changes in the side-chain length: shortening the functionalization leads to lower productivity but an increased high-purity output fraction. This efficiency increase practically translates to equal absolute performance for **DP** and **DE** with both materials producing 1.09 mmol/g CO_2 as a >99.5% output fraction per breakthrough. In contrast, changes in the side-chain degree of saturation reduce the total productivity and the high-purity CO_2 fraction with decreasing saturation. This makes **DP** the most efficient material in this series, with a 1.8-times larger high-purity fraction compared to **BPY**.

Diffusivity simulations of C_2H_2 and CO_2 additionally carried out in all materials (see Table 2) overall match the breakthrough kinetics observable in experiments and the high-purity separation efficiencies (see Supporting Information S8 and S9.2). For all materials, CO_2 diffusivity is equal to or better than that for C_2H_2, and the limiting diffusivity of C_2H_2 correlates almost linearly either with a more gradual breakthrough or a slower output flow equilibration. **DP** shows a
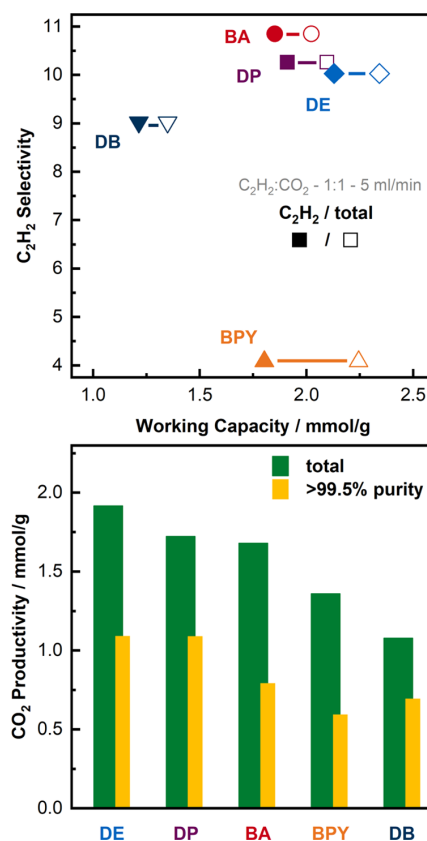
Figure 6. Top: C_2H_2 sorption selectivity and working capacities (total: open symbol; C_2H_2: filled symbol; CO_2: difference) of all materials based on gas adsorbed throughout the breakthrough experiments. Bottom: CO_2 productivity sorted by total amount (green) compared to the high-purity fraction (yellow) of total CO_2 productivity.

significantly higher minimum diffusivity, which matches its high-purity separation performance, while the noticeable difference in diffusivities in **DE** could be related to the similarly behaving ΔH; however, again the performance-limiting CO_2 diffusivity fits the experimental observations well. The mobility of CO_2 in **DB** was too low to be assessed by simulation, and it was therefore excluded.

Observations in total and high-purity fraction productivity do not correlate with the single-gas C_2H_2 sorption data of the materials (see Supporting Information S4), indicating that differentiating interactions of both simultaneously present adsorptives with the introduced side-chains are a strongly directing factor. Integrating and comparing the input and output flows of the breakthrough experiment until equilibrium is reached allow for deduction of C_2H_2 and CO_2 working capacities and adsorbate separation selectivities (α_{AC} = selectivity of C_2H_2 over CO_2) for comparison with IAST-derived values. This selectivity corresponds to the in-experiment physisorbed ratio of C_2H_2 over CO_2 (see Figure 6, top). **BPY** again features the lowest selectivity (4.1), while the best α_{AC} is almost three times higher and is achieved for **BA** (10.9). Overall, material breakthrough performances are very competitive to C_2H_2-selective adsorbents found in the literature (see Supporting Information S8 for an overview). All
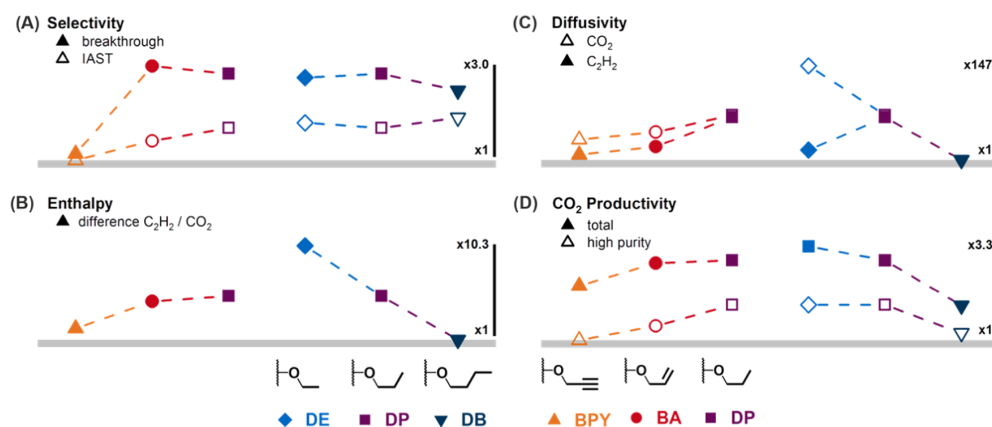
Figure 7. Summary of key material performance trends of both side-chain series (saturation, red color scale; length, blue color scale). Selectivities shown are derived from equilibrium-state adsorption capacities. Changes shown as multiplicative factors relative to the respective minimum value (×1) are indicated by the black bar.

materials feature notable differences from IAST-predicted selectivities. As elaborated above, limited precision of IAST-based calculations for these MOFs is expected, especially due to (partial) pressure-dependent shifting of the flexible functionalizations. It is notable that all values are underestimated and materials perform significantly better in experiment. We hypothesize this to be related to C_2H_2 partial pressure responsiveness, with a lower partial pressure increasing the performance.

C_2H_2 working capacities, CO_2 capacities, and the total amount adsorbed all strongly correlate with the shorter chain length, resulting in higher individual and total capacities. **DB** shows the lowest capacities for C_2H_2 and CO_2 of all materials, while **DE** shows the highest individual C_2H_2 capacity and total capacity. Increasing the degree of saturation slightly increases the C_2H_2 capacity from **BPY** to **BA** to **DP** but has a very pronounced nonlinear effect on CO_2 capacities: **BPY** adsorbs the maximum CO_2 of all materials, therefore resulting in the lowest α_{AC}, which is not observed in **BA** and **DP**, which have the overall best α_{AC} in this study.

Directing Factors. Following in-depth separation experiments, two factors can be deducted that strongly influence C_2H_2/CO_2 separation selectivities in the studied fu-MOF materials. First, the extrinsically flexible side chains exhibit a gating effect that differentiates C_2H_2 and CO_2 by means of polarizability and interaction with the CO_2 quadrupole moment. A more polarizable functionalization increases the CO_2 sorption strength and sorption preference and lowers the diffusivity. Second, steric demand and rigidity of the side chains altered by means of length and the terminal degree of saturation direct crowding or access of the preferred adsorption sites. In short, less-hindered access facilitates stronger C_2H_2 sorption.

The second factor contrasts the initially made deduction that both adsorptives should be equally affected by sterical changes in the pore environment and suggests that a hypothetically free adsorption site prefers C_2H_2 over CO_2. However, it can also be observed on **DE** that excessive free pore volume is unselective and the factors of free adsorption sites and free pore volume are inversely interrelated. Therefore, higher selectivity, better breakthrough performance, and better diffusivity all need to find a balance.

Both directing factors combined are coherent with all observed absolute adsorption enthalpy trends. Lowered side-chain saturation increases polarizability and subsequently interaction with CO_2 and ΔH. At the same time, shortening the saturated side chains drastically enhances C_2H_2 ΔH while simultaneously gradually decreasing CO_2 ΔH and partially improving the limiting diffusion. At high loading, **DB** features only small differences in isosteric enthalpies of adsorption of C_2H_2 and CO_2. This indicates that the gating effect of saturated and sterically very demanding functionalizations is almost indiscriminate toward both adsorptives when adsorption sites are blocked or occupied, and it is in agreement with both deducted directing factors. Selectivities and working capacities derived from breakthrough experiments show that in competitive sorption a sweet spot between directing C_2H_2 sorption strength and decreasing gating via functionalization shortening exists. All materials with saturated side chains feature good α_{AC}. **DP** having the highest α_{AC}, however, suggests that **DB** lacks accessible pore volume to quantitatively utilize C_2H_2-preferring adsorption sites, while **DE** exhibits less thorough gating and has more available pore volume for less-selective sorption. This is mirrored in the CO_2 working capacity slightly decreasing and high-purity CO_2 productivity increasing with a longer side-chain length. Ultimately, higher α_{AC} and better limiting diffusivity in **DP** lead to the best productivity efficiency.

Materials **BA** and **BPY** feature pronounced differences, with **BA** being high performing in α_{AC} and **BPY** exhibiting the lowest α_{AC}. On the one hand, the low α_{AC} can be attributed to the very favorable interaction of the **BPY** functionalization with CO_2, resulting in significantly lower ΔH differences of the adsorptives, along with a small increase in the available pore volume and low diffusion. These factors also lead to the highest observed CO_2 working capacity. On the other hand, **BA** shows sorption strengths for CO_2 and C_2H_2 as well as available pore volume comparable to that of **DP** and performs similarly—contrary to the initial prediction by IAST values. However, multibonds in **BA** and **BPY** and the accompanying increased rigidity and diffusion hinderance have a pronounced effect on high-purity CO_2 productivity on both materials. They have short and less-distinct CO_2 breakthrough plateaus, meaning diffusion-limited separation efficiencies, which also

compromise the high α_{AC} of **BA** in this regard. From a design principle point of view, it is notable that the CO_2 working capacity can be tripled by means of functionalization choice without sacrificing the gating behavior, which could have advantages in different fields apart from separation problems or the design of materials that preferentially adsorb CO_2.

■ CONCLUSIONS

Variation of linker side-chain functionalization in the rigid honeycomb-like MOF is shown to significantly impact adsorptive gating properties, which are summarized in Figure 7. With two interlinked isoreticular derivative series—one each for functionalization length and the degree of saturation—the exhibited gating was analyzed extensively to allow a conclusive deduction of gating-directing factors. Ultimately, two separate key contributions can be identified: adsorption site accessibility and functionalization polarizability. The former primarily affects C_2H_2 sorption preference linearly and is, within this study, manipulated to increase preference by factor ten, while the latter influences CO_2 affinity and capacity nonlinearly as well as limits CO_2 diffusivity. Both directing factors in tandem can be utilized to tune the gating behavior across a wide range of sorption strength differences (1.5–15.5 kJ/mol) and practically observed selectivities (4.1–10.9) for C_2H_2/CO_2 separation. It is notable that the pronounced nonideality of the MOF functionalizations highlights the importance of experimental breakthrough measurements for heavily functionalized frameworks to complement IAST selectivities in sorption studies.

Here, adsorptive gating and the resulting separation performance are exhibited by interchangeable side-chain functionalizations, and hence, we see significant potential to build upon the findings of this study to specifically design gating for other separation challenges and discriminate adsorptives based on their different multipole properties. It should be highlighted that the applied methodology and design principles are transferable to other rigid MOF systems. When homogeneous functionalization distribution within a material can be achieved, targeted gating and gating modulation could be easily introduced by elaborated means to become a material feature per choice.

■ ASSOCIATED CONTENT

Ⓢ Supporting Information

The Supporting Information is available free of charge at https://pubs.acs.org/doi/10.1021/acs.jpcc.2c01979.

> Synthesis procedures; ^1H NMR spectra information; elemental analysis; TGA; PXRD patterns; N_2, CO_2, and C_2H_2 sorption isotherms; fits for isosteric enthalpy of adsorption; fits for IAST selectivities and Henry's law constants; computational details; and SEM imaging and further information (PDF)

> Adsorption information files (ZIP)

■ AUTHOR INFORMATION

Corresponding Author

Roland A. Fischer − *Inorganic and Metal-Organic Chemistry, Technical University of Munich, 85748 Garching, Germany;* ⓞ orcid.org/0000-0002-7532-5286;
Email: Roland.Fischer@tum.de

Authors

Jan Berger − *Inorganic and Metal-Organic Chemistry, Technical University of Munich, 85748 Garching, Germany;* ⓞ orcid.org/0000-0002-9230-0398

Andreas Schneemann − *Inorganic Chemistry I, Technical University Dresden, 01069 Dresden, Germany;* ⓞ orcid.org/0000-0001-6801-2735

Inke Hante − *Inorganic Chemistry II, Ruhr University Bochum, 44780 Bochum, Germany*

Yuan Jing − *Institute for Catalysis, Hokkaido University, Sapporo 001-0021, Japan*

Jack D. Evans − *Centre for Advanced Nanomaterials and Department of Chemistry, The University of Adelaide, South Australia 5000, Australia;* ⓞ orcid.org/0000-0001-9521-2601

Yuh Hijikata − *Institute for Chemical Reaction Design and Discovery (WPI-ICReDD), Hokkaido University, Sapporo 001-0021, Japan;* ⓞ orcid.org/0000-0003-4883-5085

Jenny Pirillo − *Institute for Chemical Reaction Design and Discovery (WPI-ICReDD), Hokkaido University, Sapporo 001-0021, Japan;* ⓞ orcid.org/0000-0002-8866-4279

Takashi Toyao − *Institute for Catalysis, Hokkaido University, Sapporo 001-0021, Japan; Elements Strategy Initiative for Catalysis and Batteries, Kyoto University, Katsura, Kyoto 615-8520, Japan;* ⓞ orcid.org/0000-0002-6062-5622

Ken-ichi Shimizu − *Institute for Catalysis, Hokkaido University, Sapporo 001-0021, Japan; Elements Strategy Initiative for Catalysis and Batteries, Kyoto University, Katsura, Kyoto 615-8520, Japan;* ⓞ orcid.org/0000-0003-0501-0294

Shin-ichiro Noro − *Faculty of Environmental Earth Science, Hokkaido University, Sapporo 060-0810, Japan;* ⓞ orcid.org/0000-0003-4757-4741

Gregor Kieslich − *Inorganic and Metal-Organic Chemistry, Technical University of Munich, 85748 Garching, Germany;* ⓞ orcid.org/0000-0003-2038-186X

Complete contact information is available at:
https://pubs.acs.org/10.1021/acs.jpcc.2c01979

Author Contributions

The manuscript was written through contributions of all authors. All authors have given approval to the final version of the manuscript.

Notes

The authors declare no competing financial interest.

■ ACKNOWLEDGMENTS

■ REFERENCES

(1) Fan, W.; Zhang, X.; Kang, Z.; Liu, X.; Sun, D. Isoreticular chemistry within metal−organic frameworks for gas storage and separation. *Coord. Chem. Rev.* **2021**, *443*, No. 213968.

(2) Schneemann, A.; Henke, S.; Schwedler, I.; Fischer, R. A. Targeted manipulation of metal-organic frameworks to direct sorption properties. *ChemPhysChem* **2014**, *15*, 823−839.

(3) Li, B.; Wen, H.-M.; Zhou, W.; Xu, J. Q.; Chen, B. Porous Metal-Organic Frameworks: Promising Materials for Methane Storage. *Chem* **2016**, *1*, 557−580.

(4) Mukherjee, S.; Sensharma, D.; Chen, K.-J.; Zaworotko, M. J. Crystal engineering of porous coordination networks to enable separation of C2 hydrocarbons. *Chem. Commun.* **2020**, *56*, 10419−10441.

(5) Freund, R.; Zaremba, O.; Arnauts, G.; Ameloot, R.; Skorupskii, G.; Dincă, M.; Bavykina, A.; Gascon, J.; Ejsmont, A.; Goscianska, J.; et al. The Current Status of MOF and COF Applications. *Angew. Chem., Int. Ed.* **2021**, *60*, 23975−24001.

(6) Yang, H.; Wang, Y.; Krishna, R.; Jia, X.; Wang, Y.; Hong, A. N.; Dang, C.; Castillo, H. E.; Bu, X.; Feng, P. Pore-Space-Partition-Enabled Exceptional Ethane Uptake and Ethane-Selective Ethane-Ethylene Separation. *J. Am. Chem. Soc.* **2020**, *142*, 2222−2227.

(7) Pang, J.; Di, Z.; Qin, J.-S.; Yuan, S.; Lollar, C. T.; Li, J.; Zhang, P.; Wu, M.; Yuan, D.; Hong, M.; Zhou, H. C. Precisely Embedding Active Sites into a Mesoporous Zr-Framework through Linker Installation for High-Efficiency Photocatalysis. *J. Am. Chem. Soc.* **2020**, *142*, 15020−15026.

(8) Ji, Z.; Wang, H.; Canossa, S.; Wuttke, S.; Yaghi, O. M. Pore Chemistry of Metal−Organic Frameworks. *Adv. Funct. Mater.* **2020**, *30*, No. 2000238.

(9) Lin, R.-B.; Xiang, S.; Zhou, W.; Chen, B. Microporous Metal-Organic Framework Materials for Gas Separation. *Chem* **2020**, *6*, 337−363.

(10) Li, X.; Wang, J.; Bai, N.; Zhang, X.; Han, X.; da Silva, I.; Morris, C. G.; Xu, S.; Wilary, D. M.; Sun, Y.; et al. Refinement of pore size at sub-angstrom precision in robust metal-organic frameworks for separation of xylenes. *Nat. Commun.* **2020**, *11*, No. 4280.

(11) Chen, K.-J.; Madden, D. G.; Mukherjee, S.; Pham, T.; Forrest, K. A.; Kumar, A.; Space, B.; Kong, J.; Zhang, Q.-Y.; Zaworotko, M. J. Synergistic sorbent separation for one-step ethylene purification from a four-component mixture. *Science* **2019**, *366*, 241−246.

(12) Luna-Triguero, A.; Vicent-Luna, J. M.; Madero-Castro, R. M.; Gómez-Álvarez, P.; Calero, S. Acetylene Storage and Separation Using Metal-Organic Frameworks with Open Metal Sites. *ACS Appl. Mater. Interfaces* **2019**, *11*, 31499−31507.

(13) Bachman, J. E.; Reed, D. A.; Kapelewski, M. T.; Chachra, G.; Jonnavittula, D.; Radaelli, G.; Long, J. R. Enabling alternative ethylene production through its selective adsorption in the metal−organic framework Mn 2 (m -dobdc). *Energy Environ. Sci.* **2018**, *11*, 2423−2431.

(14) Dinakar, B.; Forse, A. C.; Jiang, H. Z. H.; Zhu, Z.; Lee, J.-H.; Kim, E. J.; Parker, S. T.; Pollak, C. J.; Siegelman, R. L.; Milner, P. J.; et al. Overcoming Metastable CO2 Adsorption in a Bulky Diamine-Appended Metal-Organic Framework. *J. Am. Chem. Soc.* **2021**, *143*, 15258−15270.

(15) Schneemann, A.; Jing, Y.; Evans, J. D.; Toyao, T.; Hijikata, Y.; Kamiya, Y.; Shimizu, K.-I.; Burtch, N. C.; Noro, S.-I. Alkyl decorated metal-organic frameworks for selective trapping of ethane from ethylene above ambient pressures. *Dalton Trans.* **2021**, *50*, 10423−10435.

(16) Fan, W.; Yuan, S.; Wang, W.; Feng, L.; Liu, X.; Zhang, X.; Wang, X.; Kang, Z.; Dai, F.; Yuan, D.; et al. Optimizing Multivariate Metal-Organic Frameworks for Efficient C2H2/CO2 Separation. *J. Am. Chem. Soc.* **2020**, *142*, 8728−8737.

(17) Ye, Y.; Ma, Z.; Lin, R.-B.; Krishna, R.; Zhou, W.; Lin, Q.; Zhang, Z.; Xiang, S.; Chen, B. Pore Space Partition within a Metal-Organic Framework for Highly Efficient C2H2/CO2 Separation. *J. Am. Chem. Soc.* **2019**, *141*, 4130−4136.

(18) Qazvini, O. T.; Scott, V.-J.; Bondorf, L.; Ducamp, M.; Hirscher, M.; Coudert, F.-X.; Telfer, S. G. Flexibility of a Metal−Organic Framework Enhances Gas Separation and Enables Quantum Sieving. *Chem. Mater.* **2021**, *33*, 8886−8894.

(19) Wang, P.; Kajiwara, T.; Otake, K.-I.; Yao, M.-S.; Ashitani, H.; Kubota, Y.; Kitagawa, S. Xylene Recognition in Flexible Porous Coordination Polymer by Guest-Dependent Structural Transition. *ACS Appl. Mater. Interfaces* **2021**, *13*, 52144−52151.

(20) Dong, Q.; Zhang, X.; Liu, S.; Lin, R.-B.; Guo, Y.; Ma, Y.; Yonezu, A.; Krishna, R.; Liu, G.; Duan, J.; et al. Tuning Gate-Opening of a Flexible Metal-Organic Framework for Ternary Gas Sieving Separation. *Angew. Chem., Int. Ed.* **2020**, *59*, 22756−22762.

(21) Schneemann, A.; Bon, V.; Schwedler, I.; Senkovska, I.; Kaskel, S.; Fischer, R. A. Flexible metal-organic frameworks. *Chem. Soc. Rev.* **2014**, *43*, 6062−6096.

(22) Elsaidi, S. K.; Mohamed, M. H.; Banerjee, D.; Thallapally, P. K. Flexibility in Metal−Organic Frameworks: A fundamental understanding. *Coord. Chem. Rev.* **2018**, *358*, 125−152.

(23) Li, D.; Kaneko, K. Hydrogen bond-regulated microporous nature of copper complex-assembled microcrystals. *Chem. Phys. Lett.* **2001**, *335*, 50−56.

(24) Hiraide, S.; Tanaka, H.; Miyahara, M. T. Understanding gate adsorption behaviour of CO2 on elastic layer-structured metal-organic framework-11. *Dalton Trans.* **2016**, *45*, 4193−4202.

(25) Hiraide, S.; Sakanaka, Y.; Kajiro, H.; Kawaguchi, S.; Miyahara, M. T.; Tanaka, H. High-throughput gas separation by flexible metal-organic frameworks with fast gating and thermal management capabilities. *Nat. Commun.* **2020**, *11*, No. 3867.

(26) Hiraide, S.; Arima, H.; Tanaka, H.; Miyahara, M. T. Slacking of Gate Adsorption Behavior on Metal-Organic Frameworks under an External Force. *ACS Appl. Mater. Interfaces* **2021**, *13*, 30213−30223.

(27) Serre, C.; Millange, F.; Thouvenot, C.; Noguès, M.; Marsolier, G.; Louër, D.; Férey, G. Very large breathing effect in the first nanoporous chromium(III)-based solids: MIL-53 or Cr(III)(OH) x O(2)C-C(6)H(4)-CO(2) x HO(2)C-C(6)H(4)-CO(2)H(x) x H(2)O(y). *J. Am. Chem. Soc.* **2002**, *124*, 13519−13526.

(28) Biswas, S.; Ahnfeldt, T.; Stock, N. New functionalized flexible Al-MIL-53-X (X = -Cl, -Br, -CH3, -NO2, -(OH)2) solids: syntheses, characterization, sorption, and breathing behavior. *Inorg. Chem.* **2011**, *50*, 9518−9526.

(29) Chanut, N.; Ghoufi, A.; Coulet, M.-V.; Bourrelly, S.; Kuchta, B.; Maurin, G.; Llewellyn, P. L. Tailoring the separation properties of flexible metal-organic frameworks using mechanical pressure. *Nat. Commun.* **2020**, *11*, No. 1216.

(30) Klein, N.; Herzog, C.; Sabo, M.; Senkovska, I.; Getzschmann, J.; Paasch, S.; Lohe, M. R.; Brunner, E.; Kaskel, S. Monitoring adsorption-induced switching by (129)Xe NMR spectroscopy in a new metal-organic framework Ni(2)(2,6-ndc)(2)(dabco). *Phys. Chem. Chem. Phys.* **2010**, *12*, 11778−11784.

(31) Ehrling, S.; Mendt, M.; Senkovska, I.; Evans, J. D.; Bon, V.; Petkov, P.; Ehrling, C.; Walenszus, F.; Pöppl, A.; Kaskel, S. Tailoring the Adsorption-Induced Flexibility of a Pillared Layer Metal−Organic Framework DUT-8(Ni) by Cobalt Substitution. *Chem. Mater.* **2020**, *32*, 5670−5681.

(32) Kitaura, R.; Seki, K.; Akiyama, G.; Kitagawa, S. Porous Coordination-Polymer Crystals with Gated Channels Specific for Supercritical Gases. *Angew. Chem., Int. Ed.* **2003**, *42*, 428−431.

(33) Uemura, K.; Yamasaki, Y.; Komagawa, Y.; Tanaka, K.; Kita, H. Two-step adsorption/desorption on a jungle-gym-type porous coordination polymer. *Angew. Chem., Int. Ed.* **2007**, *46*, 6662−6665.

(34) Park, H. J.; Suh, M. P. Stepwise and hysteretic sorption of N(2), O(2), CO(2), and H(2) gases in a porous metal-organic framework Zn(2)(BPnDC)(2)(bpy). *Chem. Commun.* **2010**, *46*, 610−612.

(35) Kavoosi, N.; Savchenko, T.; Senkovska, I.; Maliuta, M.; Bon, V.; Eychmüller, A.; Kaskel, S. Selective pore opening and gating of the pillared layer metal-organic framework DUT-8(Ni) upon liquid phase multi-component adsorption. *Microporous Mesoporous Mater.* **2018**, *271*, 169−174.

(36) Zhu, S.; Lin, Q.; Huang, X.; Chen, L.; Liu, L.; Yao, Z.; Xiang, S. Efficient Separation of Acetylene-Containing Mixtures Using ZIF-8 Membranes. *ACS Omega* **2021**, *6*, 33018−33023.

(37) Binaeian, E.; El-Sayed, E.-S. M.; Khanpour Matikolaei, M.; Yuan, D. Experimental strategies on enhancing toxic gases uptake of metal−organic frameworks. *Coord. Chem. Rev.* **2021**, *430*, No. 213738.

(38) Xing, S.; Liang, J.; Brandt, P.; Schäfer, F.; Nuhnen, A.; Heinen, T.; Boldog, I.; Möllmer, J.; Lange, M.; Weingart, O.; Janiak, C. Capture and Separation of SO2 Traces in Metal-Organic Frameworks via Pre-Synthetic Pore Environment Tailoring by Methyl Groups. *Angew. Chem., Int. Ed.* **2021**, *60*, 17998−18005.

(39) Banerjee, A.; Nandi, S.; Nasa, P.; Vaidhyanathan, R. Enhancing the carbon capture capacities of a rigid ultra-microporous MOF through gate-opening at low CO2 pressures assisted by swiveling oxalate pillars. *Chem. Commun.* **2016**, *52*, 1851−1854.

(40) Ding, M.; Flaig, R. W.; Jiang, H.-L.; Yaghi, O. M. Carbon capture and conversion using metal-organic frameworks and MOF-based materials. *Chem. Soc. Rev.* **2019**, *48*, 2783−2828.

(41) Lin, J.-B.; Nguyen, T. T. T.; Vaidhyanathan, R.; Burner, J.; Taylor, J. M.; Durekova, H.; Akhtar, F.; Mah, R. K.; Ghaffari-Nik, O.; Marx, S.; et al. A scalable metal-organic framework as a durable physisorbent for carbon dioxide capture. *Science* **2021**, *374*, 1464−1469.

(42) Ding, Q.; Zhang, Z.; Yu, C.; Zhang, P.; Wang, J.; Cui, X.; He, C.-H.; Deng, S.; Xing, H. Exploiting equilibrium-kinetic synergetic effect for separation of ethylene and ethane in a microporous metal-organic framework. *Sci. Adv.* **2020**, *6*, No. eaaz4322.

(43) Lyndon, R.; You, W.; Ma, Y.; Bacsa, J.; Gong, Y.; Stangland, E. E.; Walton, K. S.; Sholl, D. S.; Lively, R. P. Tuning the Structures of Metal−Organic Frameworks via a Mixed-Linker Strategy for Ethylene/Ethane Kinetic Separation. *Chem. Mater.* **2020**, *32*, 3715−3722.

(44) James, J. B.; Wang, J.; Meng, L.; Lin, Y. S. ZIF-8 Membrane Ethylene/Ethane Transport Characteristics in Single and Binary Gas Mixtures. *Ind. Eng. Chem. Res.* **2017**, *56*, 7567−7575.

(45) Belmabkhout, Y.; Bhatt, P. M.; Adil, K.; Pillai, R. S.; Cadiau, A.; Shkurenko, A.; Maurin, G.; Liu, G.; Koros, W. J.; Eddaoudi, M. Natural gas upgrading using a fluorinated MOF with tuned H2S and CO2 adsorption selectivity. *Nat Energy* **2018**, *3*, 1059−1066.

(46) Gu, C.; Hosono, N.; Zheng, J.-J.; Sato, Y.; Kusaka, S.; Sakaki, S.; Kitagawa, S. Design and control of gas diffusion process in a nanoporous soft crystal. *Science* **2019**, *363*, 387−391.

(47) Zeng, H.; Xie, M.; Wang, T.; Wei, R.-J.; Xie, X.-J.; Zhao, Y.; Lu, W.; Li, D. Orthogonal-array dynamic molecular sieving of propylene/propane mixtures. *Nature* **2021**, *595*, 542−548.

(48) Kanoo, P.; Matsuda, R.; Sato, H.; Li, L.; Hosono, N.; Kitagawa, S. Pseudo-Gated Adsorption with Negligible Volume Change Evoked by Halogen-Bond Interaction in the Nanospace of MOFs. *Chem. - Eur. J.* **2020**, *26*, 2148−2153.

(49) Henke, S.; Fischer, R. A. Gated channels in a honeycomb-like zinc-dicarboxylate-bipyridine framework with flexible alkyl ether side chains. *J. Am. Chem. Soc.* **2011**, *133*, 2064−2067.

(50) Henke, S.; Schneemann, A.; Kapoor, S.; Winter, R.; Fischer, R. A. Zinc-1,4-benzenedicarboxylate-bipyridine frameworks − linker functionalization impacts network topology during solvothermal synthesis. *J. Mater. Chem.* **2012**, *22*, 909−918.

(51) Ma, S.; Sun, D.; Wang, X.-S.; Zhou, H.-C. A mesh-adjustable molecular sieve for general use in gas separation. *Angew. Chem., Int. Ed.* **2007**, *46*, 2458−2462.

(52) Tan, Q.; Huang, H.; Peng, Y.; Chang, Y.; Zhang, Z.; Liu, D.; Zhong, C. A temperature-responsive smart molecular gate in a metal−organic framework for task-specific gas separation. *J. Mater. Chem. A* **2019**, *7*, 26574−26579.

(53) Kondo, A.; Yashiro, T.; Okada, N.; Hiraide, S.; Ohkubo, T.; Tanaka, H.; Maeda, K. Selective molecular-gating adsorption in a novel copper-based metal−organic framework. *J. Mater. Chem. A* **2018**, *6*, 5910−5918.

(54) Baerdemaeker, T.; Vos, D. Gas separation: Trapdoors in zeolites. *Nat. Chem.* **2013**, *5*, 89−90.

(55) Shang, J.; Li, G.; Singh, R.; Gu, Q.; Nairn, K. M.; Bastow, T. J.; Medhekar, N.; Doherty, C. M.; Hill, A. J.; Liu, J. Z.; Webley, P. A. Discriminative separation of gases by a "molecular trapdoor" mechanism in chabazite zeolites. *J. Am. Chem. Soc.* **2012**, *134*, 19246−19253.

(56) Zhang, Z.; Nguyen, H. T. H.; Miller, S. A.; Ploskonka, A. M.; DeCoste, J. B.; Cohen, S. M. Polymer-Metal-Organic Frameworks (polyMOFs) as Water Tolerant Materials for Selective Carbon Dioxide Separations. *J. Am. Chem. Soc.* **2016**, *138*, 920−925.

(57) Henke, S.; Schneemann, A.; Wütscher, A.; Fischer, R. A. Directing the breathing behavior of pillared-layered metal-organic frameworks via a systematic library of functionalized linkers bearing flexible substituents. *J. Am. Chem. Soc.* **2012**, *134*, 9464−9474.

(58) Evans, J. D.; Bon, V.; Senkovska, I.; Kaskel, S. A Universal Standard Archive File for Adsorption Data. *Langmuir* **2021**, *37*, 4222−4226.

(59) Myers, A. L.; Prausnitz, J. M. Thermodynamics of mixed-gas adsorption. *AIChE J.* **1965**, *11*, 121−127.

(60) Elstner, M.; Porezag, D.; Jungnickel, G.; Elsner, J.; Haugk, M.; Frauenheim, T.; et al. Self-consistent-charge density-functional tight-binding method for simulations of complex materials properties. *Phys. Rev. B* **1998**, *58*, 7260−7268.

(61) Yang, Y.; Yu, H.; York, D.; Cui, Q.; Elstner, M. Extension of the self-consistent-charge density-functional tight-binding method: third-order expansion of the density functional theory total energy and introduction of a modified effective coulomb interaction. *J. Phys. Chem. A* **2007**, *111*, 10861−10873.

(62) Aradi, B.; Hourahine, B.; Frauenheim, T. DFTB+, a sparse matrix-based implementation of the DFTB method. *J. Phys. Chem. A* **2007**, *111*, 5678−5684.

(63) Thompson, A. P.; Aktulga, H. M.; Berger, R.; Bolintineanu, D. S.; Brown, W. M.; Crozier, P. S.; Veld, P. J. in't.; Kohlmeyer, A.; Moore, S. G.; Nguyen, T. D.; et al. LAMMPS - a flexible simulation tool for particle-based materials modeling at the atomic, meso, and continuum scales. *Comput. Phys. Commun.* **2022**, *271*, No. 108171.

(64) Coupry, D. E.; Addicoat, M. A.; Heine, T. Extension of the Universal Force Field for Metal-Organic Frameworks. *J. Chem. Theory Comput.* **2016**, *12*, 5215−5225.

(65) Boyd, P. G.; Moosavi, S. M.; Witman, M.; Smit, B. Force-Field Prediction of Materials Properties in Metal-Organic Frameworks. *J. Phys. Chem. Lett.* **2017**, *8*, 357−363.

(66) Fu, X.-P.; Wang, Y.-L.; Liu, Q.-Y. Metal-organic frameworks for C2H2/CO2 separation. *Dalton Trans.* **2020**, *49*, 16598−16607.

(67) Niu, Z.; Cui, X.; Pham, T.; Verma, G.; Lan, P. C.; Shan, C.; Xing, H.; Forrest, K. A.; Suepaul, S.; Space, B.; et al. A MOF-based Ultra-Strong Acetylene Nano-trap for Highly Efficient C2 H2 /CO2 Separation. *Angew. Chem., Int. Ed.* **2021**, *60*, 5283−5288.

(68) Zhang, L.; Jiang, K.; Yang, L.; Li, L.; Hu, E.; Yang, L.; Shao, K.; Xing, H.; Cui, Y.; Yang, Y.; et al. Benchmark C2 H2 /CO2 Separation in an Ultra-Microporous Metal-Organic Framework via Copper(I)-Alkynyl Chemistry. *Angew. Chem., Int. Ed.* **2021**, *60*, 15995−16002.

(69) Foo, M. L.; Matsuda, R.; Hijikata, Y.; Krishna, R.; Sato, H.; Horike, S.; Hori, A.; Duan, J.; Sato, Y.; Kubota, Y.; et al. An Adsorbate Discriminatory Gate Effect in a Flexible Porous Coordination Polymer for Selective Adsorption of CO2 over C2H2. *J. Am. Chem. Soc.* **2016**, *138*, 3022−3030.

(70) Russell, D.; Johnson, Ill. *NIST Computational Chemistry Comparison and Benchmark Database*, NIST Standard Reference Database Number 101; National Institue of Standards and Technology: Gaithersburg, MD. http://cccbdb.nist.gov/ (retrieved May 12, 2022).

(71) Thommes, M.; Kaneko, K.; Neimark, A. V.; Olivier, J. P.; Rodriguez-Reinoso, F.; Rouquerol, J.; Sing, K. S. Physisorption of gases, with special reference to the evaluation of surface area and pore size distribution (IUPAC Technical Report). *Pure Appl. Chem.* **2015**, *87*, 1051−1069.

(72) Walton, K. S.; Sholl, D. S. Predicting multicomponent adsorption: 50 years of the ideal adsorbed solution theory. *AIChE J.* **2015**, *61*, 2757−2762.

(73) Billemont, P.; Heymans, N.; Normand, P.; Weireld, G. IAST predictions vs co-adsorption measurements for CO2 capture and separation on MIL-100 (Fe). *Adsorption* **2017**, *23*, 225−237.

(74) Coudert, F.-X. The osmotic framework adsorbed solution theory: predicting mixture coadsorption in flexible nanoporous materials. *Phys. Chem. Chem. Phys.* **2010**, *12*, 10904−10913.

4.1.1 MACROSCOPIC PARTICLE TOPOLOGY

The final chapter in the supplementary information of **STUDY I** in chapter 7 shows scanning electron microscopy (SEM) images of the different materials (for method details please refer to that section). In context of the publication this topic was only briefly discussed and we purposefully excluded the aspect of particle size and morphology from the study, because a) we were unable to separate the shown morphology mixture or synthesize crystallites with more uniform morphology and size, b) all powders consist of a similar ratio of different particles and aggregates which c) each are in a comparable size regime for each material. As such, size and morphology dependent changes were expected to average out across the studied MOF derivatives. However, at this point some more discussion should be added in light of future works. First it has to be reiterated that particle shape can have tremendous impact on the overall observable material properties. Differences in particle size or shape change the surface-defect concentration/amount and in anisotropic materials (like the honeycomb-like MOF) the ratio of outside-facing facets. The impact such changes can have on flexible MOFs are exemplary highlighted by DUT-8 which is only flexible if its crystallites are of a minimum size (a later study correlates this predominantly to surface-defects than particle size, though these are of course correlated).[169,170] Even if not looking to the complex interplay of framework flexibility and molecular diffusivity,[198] every material's adsorptive responsiveness is at least partially governed by mass transport and diffusion of adsorptive/adsorbate though its pore system.[199] And this in turn is affected by particle shape.*

All materials in **STUDY I** show formation of multiple micron-sized needles, crystallite aggregates, and bigger hexagonal structures with preferred growth direction seemingly consisting of needle-like substructures. The analyzed powders are not from a single batch, but a mixture of multiple (up to 5) batches. Each batch was of same molarity, absolute educt amount, and processed in parallel (details can found in the supplementary information of **STUDY I**). However, different glassware etc. was used and of course minuscule differences of the synthesis routine (fresher/older solvents, slightly less/more sonication time, different mechanical stress during handling) can always occur which might have had an impact on crystal growth. Figure 12 shows SEM images of the five $Zn_2(fu-bdc)_2bpy$ derivatives with different bdc^{2-}-linker functionalizations (fu) (DE = 2,5-diethoxy; DP = 2,5-dipropoxy; BA = 2,5-bisallyloxy; BPY = 2,5-bispropynyloxy; DB = 2,5-dibutoxy; BB = 2,5-bisbutenoxy).

---

* In consequence, both particle shape/size and gas diffusion should be measured as a step in the process of MOF characterization – at least if any sorption responsiveness is of interest or topic of the study. I admittedly come to this conclusion only now, after the fact of this thesis. However, I wholeheartedly recommend this publication by SON et al.[200] as easy-to-access starting point for practical implementation of this method.
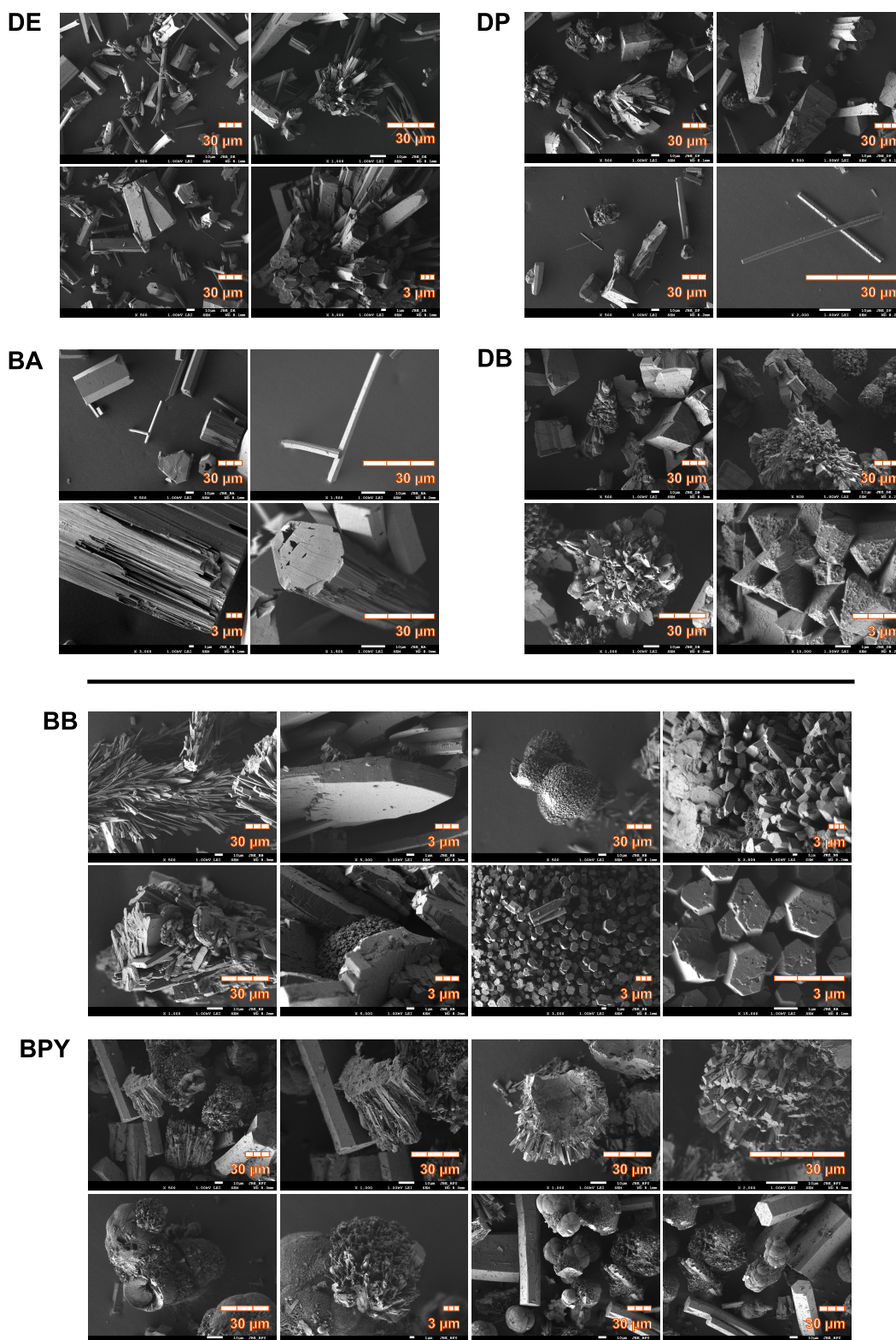
Figure 12. SEM images of honeycomb-like MOFs of **Study I**. While all materials form needle-like rods which themselves partially aggregate around or grow on shared nucleation sites, notably only BPY consists of at least four particle morphologies. Top set of four materials (**DE**, **DP**, **BA**, **DB**) show similar properties. Bottom set of two materials (**BB**, **BPY**) include different particle features. Scale bars 30μm or 3μm segmented into thirds.

Some of the honeycomb-like MOFs with short or unfunctionalized side chains (**DE**, **DP**, **BA**, **DB**) grow in relatively uniform needles/rods with bigger crystals consisting of a rod-like substructure. Needles reach up to 40μm diameter but a wide distribution of sizes is present. All materials show aggregates of multiple rods seemingly growing from a shared nucleation point or object resulting in some spiked, spherical macro-structures. Very notable is that both materials with longer side chains, **DB** and **BB**, show a higher degree of aggregation. This is particularly pronounced in **BB** which barely shows singular needles or rods with more than 10μm diameter. This might indicate that parallel-crystallization of the rods (as best observed in SEM images of BA) is partially inhibited by longer linker functionalizations. As these line the outside of each pore wall and thereby the crystal surface this correlation might be reasonable, however, in the series of **DE** to **DP** to **DB** no trend can be identified. To properly unravel side chain impact in particle size and morphology further studies need to be conducted.

As last point of interest **BPY** should be highlighted. Its powder consists of multiple very different particle types: rods, macro-structures build from finer needles (both as observed for the other derivatives), aggregates of very small rods forming almost spherical particles – at first glance reminding of metal-oxide particles, however their surface is distinctly textured like porous corals – and aggregates of needles using these spheres as nucleation point to grow spiked, spherical macro-structures. Why especially **BPY** shows this variance in particle shapes is yet unclear. Its functionalization is the thermally least stable of the five derivatives and side reactions during synthesis might play a role. MOF synthesis should be feasible at reduced temperatures to probe this effect. Moreover, if all or some morphologies could be reproduced in a single or different batches, it might also become clearer if the observed mixture is the result of mixing different batches before taking SEM images, and thereby synthesis condition deviations of potentially only a single batch, or if it is a statistical occurrence of each batch and therefore a more fundamental challenge to be addressed.

4.2 STUDY II. Reduced Thermal Expansion by Surface-Mounted Nanoparticles in a Pillared-Layered Metal-Organic Framework

This study looks into the TE properties of a series isoreticular pillared-layered MOFs with different amounts of surface-mounted platinum nanoparticles. The aim is to qualitatively and quantitatively investigate the differences in TE behavior arising from NP presence in the composite material when compared to the pure parent MOF. TE is an universally important property for every material used in application or devices with operating temperatures higher above or below ambient temperature. In these environments, materials are generally subjected to notable temperature fluctuations, i.e as designed in continuous process routines, isolation, or arising from repeated batch-wise operation. High NTE or PTE can then result in extensive material deformation leading to voids, tears, or brittleness. Curiously, despite NP@MOF materials being most promising for application with exactly such conditions, their TE properties are not really investigated. Therefore, we synthesized a series of four NP@MOF composites with very low but slightly increasing amounts of NPs attached to their surface, confirmed this with extensive transmission electron microscopy (TEM) analysis, investigated their TE by collecting variable-temperature powder X-ray diffraction (VTPXRD) patterns from 323–513K, and extracting information on principal axis strain. Overall, we found that at low temperatures TE of NP@MOF materials can be estimated by the parent framework's properties and some intricate effects of NPs on different expansion directions in this anisotropic MOF topology are present. However, at higher temperature and higher (herein 3%) NP loadings changes are significant which can result in zero thermal expansion (ZTE), a very desirable feature.

J.B. performed material synthesis, analysis, data processing and manuscript writing. A.-S.D. contributed to material prototyping, analysis, and manuscript writing. A.U. and H.B. performed electron microscopy, its visualization, and contributed to manuscript writing. R.A.F. provided the motivation of this work and contributed to manuscript writing. G.K. provided the motivation of this work and contributed to data processing and manuscript writing.

communications
chemistry

Check for updates

Reduced thermal expansion by surface-mounted nanoparticles in a pillared-layered metal-organic framework

Jan Berger [1], Alper-Sedat Dönmez[1], Aladin Ullrich [2], Hana Bunzen [2], Roland A. Fischer [1✉] & Gregor Kieslich [1✉]

Control of thermal expansion (TE) is important to improve material longevity in applications with repeated temperature changes or fluctuations. The TE behavior of metal-organic frameworks (MOFs) is increasingly well understood, while the impact of surface-mounted nanoparticles (NPs) on the TE properties of MOFs remains unexplored despite large promises of NP@MOF composites in catalysis and adsorbate diffusion control. Here we study the influence of surface-mounted platinum nanoparticles on the TE properties of Pt@MOF (Pt@Zn_2(DP-bdc)$_2$dabco; DP-bdc^{2-}=2,5-dipropoxy-1,4-benzenedicarboxylate, dabco=1,4-diazabicyclo[2.2.2]octane). We show that TE is largely retained at low platinum loadings, while high loading results in significantly reduced TE at higher temperatures compared to the pure MOF. These findings support the chemical intuition that surface-mounted particles restrict deformation of the MOF support and suggest that composite materials exhibit superior TE properties thereby excluding thermal stress as limiting factor for their potential application in temperature swing processes or catalysis.

[1] Chair of Inorganic and Metal-Organic Chemistry, TUM School of Natural Sciences, Technical University of Munich, Lichtenbergstr. 4, 85748 Garching, Germany. [2] Institute of Physics, University of Augsburg, Universitätsstr. 1, 86159 Augsburg, Germany. ✉email: roland.fischer@tum.de; gregor.kieslich@tum.de

ARTICLE

The magnitude and sign of thermal expansion (TE) coefficients of a solid material is a key property that needs to be considered for a wide range of applications. Some major research goals related to the materials' thermal expansion behavior are the inhibition of TE to minimize stress from application-related repeating temperature changes in order to increase material longevity, i.e. of adsorbents during temperature swing adsorption or of supports and catalysts during process temperature fluctuations[1–4], the combination of different materials with positive (PTE) and negative (NTE) TE to reach near-zero thermal expansion (ZTE) across a certain temperature range to prevent tears, voids, or deformation[5–7], or the design of large (anisotropic) thermal expansion as applied in temperature-controlled sieves or sensors[8]. Naturally, these goals are of great importance for metal-organic frameworks (MOFs) and their potential applications. MOFs are a chemically diverse material class with guest accessible void space based on a modular building principle, providing a fascinating material platform for studying of how structural changes impact the macroscopic properties important for designing sensors, adsorbents, supports or catalysts amongst many other examples[9,10].

Looking at the thermal expansion behavior of MOFs, most MOFs exhibit NTE, a property that is still considered counterintuitive for purely inorganic solids[11–13]. Molecular simulations on mesoporous MOFs draw clear correlations between porosity, transverse ligand vibration and NTE, underpinning the role of available pore space as a NTE directing factor[14,15]. Approaches for tuning the TE behavior of MOFs encompasses all controllable variables in MOF design such as expansivity control by defect-engineering[16], linker functionalization[17–19], or changing metals ions or organic linker length[14]. Important examples are $Zn_2(bdc)_{2-x}(TM-bdc)_x$dabco ($TM-bdc^{2-}$=tetramethyl-1,4-benzenedicarboxylate; dabco=1,4-diazabicyclo[2.2.2]octane) which exhibits a change from PTE to NTE as a function of bdc:TM-bdc ratio[20], and UiO-67 where linker functionalization leads to subtle changes in NTE behavior[21]. Additionally, certain network topologies can lead to pronounced anisotropic TE behavior and temperature-induced phase transitions, of which MOFs with a wine-rack type network such as MIL-53(Al), abovementioned $Zn_2(fu-bdc)_2$dabco, and [Ag(en)]NO_3 (en=ethylenediamine) are prototypical examples[17,22–24]. These insights are relevant for future MOF applications, because even single-percentage temperature-induced framework contraction can lead to considerable softening and greatly impact mechanical stability[25]. In addition to framework modification, external factors affecting porosity such as interstitial guest molecules can similarly impact TE[26]. Examples are DUT-49 that switches from NTE in the guest-free state to PTE when solvated[27], or Prussian blue derivative frameworks showing a continuous NTE-to-PTE transition in response to CO_2 sorption[28]. The impact of nanoparticles as external factor influencing TE of composites consisting of nanoparticles integrated into or surface-mounted onto MOFs (NP@MOF) is yet unexplored, to the best of our knowledge. This is despite the large interest in these composite systems for catalysis[29–32], and the known importance of these properties for nanoparticles, classical supported catalyst composites or thin film composites[3,5,8,33].

Here we provide the first step in elucidating the influence of nanoparticles on the thermal expansion behavior in NP@MOF composites. We synthesize Pt@MOF composites by using a capping agent-free, one-pot co-formation of MOF and nanoparticle and investigate the effects of low Pt nanoparticle loading (1–3 wt.%) on the TE of the model pillared-layered MOF system $Zn_2(DP-bdc)_2$dabco (DP-bdc^{2-}=2,5-dipropoxy-1,4-benzenedicarboxylate) (see Fig. 1 and Supplementary Section S1.4)[17]. The results suggest that TE properties of composite systems can be estimated based on the TE properties of the MOF support, and that thermal stress in composite systems is expected to be smaller when compared to the parent MOF.

Results and discussion

Pt@MOF composite synthesis. All Pt@$Zn_2(DP-bdc)_2$dabco composites were synthesized using a literature-inspired[34] co-crystallization approach which enables one-step one-pot crystallization of MOF and formation of Pt nanoparticles without the need for any capping agents. This method combines the MOF synthesis procedure, as known from literature[17], with a solvent mediated Pt^{2+} reduction and provides control over Pt nanoparticle loading on the surface of the MOF support. MOF precursors $Zn(NO_3)_2$, dabco, H_2DPbdc and the Pt nanoparticle precursor K_2PtCl_4 are suspended in dimethylformamide (DMF). During solvothermal MOF synthesis, DMF oxidizes in presence of water (originating from trace amounts of H_2O in DMF and the hydrated metal salt) and Pt^{2+} to form its carbamic acid derivative and reduced Pt^0, thereby facilitating nanoparticle formation[35]. Both MOF and nanoparticle form gradually and precipitate as composite. This circumvents the need for nanoparticle isolation and capping agents which is expected to improve reproducibility and correlation of nanoparticle impact and MOF behavior[36]. Modulation of reaction temperature, time and precursor concentration allows for some control over Pt nanoparticle formation kinetics and resulting deposition onto the MOF support. The here investigated series of isoreticular functionalized Pt@MOF composites comprises four materials based on $Zn_2(DP-bdc)_2$dabco (see Table 1).

After synthesis, all composites were washed, solvent exchanged, activated, and subsequently verified with respect to Pt content by atom absorption spectroscopy and photometry, and with respect to MOF composition and solvent removal by ^{1}H NMR spectroscopy and TGA (see Supplementary Sections S1.3 and S4). PXRD
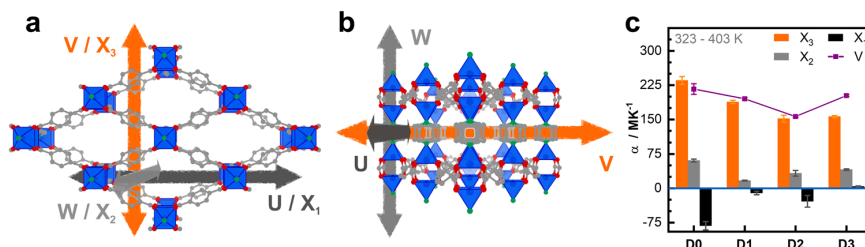
Fig. 1 Crystal structure and thermal expansivity of $Zn_2(DP-bdc)_2$dabco. View along (**a**) and perpendicular (**b**) to dabco pillars. Principal thermal expansion directions X_1, X_2, and X_3 approximately align to u, w, and v, respectively. **c** Thermal expansion coefficients (CTEs) for principal directions (columns) and net volume (connected points) of materials with and without Pt nanoparticle (**D#**: # wt.% Pt) are shown. See Supplementary Section S1.4 for structural formula of the linker, pillar, and paddlewheel unit. Grey, C; red, O; green, N; blue, Zn and coordination polyhedron; linker functionalizations and hydrogen atoms are not shown for clarity; error bars show standard deviation.

ARTICLE

Table 1 Pt content and thermal expansion coefficients $\alpha(X_{1-3})$ of Pt@MOF composites.

Pt@MOF	Pt [wt.%][a]	$\alpha(X_1)$[b] [MK^{-1}]	$\alpha(X_2)$[b] [MK^{-1}]	$\alpha(X_3)$[b] [MK^{-1}]
D0	-	−82	61	235
D1	1.4	−10	17	188
D2	1.9	−29	32	152
D3	3.1	4	41	156

[a]per atom absorption spectroscopy and photometry.
[b]more details in Supplementary Table 6.

confirms that all materials are isoreticular independent of the Pt content both in the as-synthesized state (**as**) directly after synthesis and washing, as well as in the activated state (**dry**) after solvent removal (see Supplementary Fig. 2). Materials crystallize in their large pore (lp) phase and are transitioned to their narrow pore (np) phase after solvent exchange and removal. This can be recognized by a shift of the 110 reflection and an intensity increase of the 001 reflection as reported in literature[37]. $Zn_2(DP-bdc)_2$dabco is further known to exhibit a reversible, CO_2 adsorption induced phase transition from the np to the lp phase[38]. Physisorption experiments reveal that this behavior is fully retained in all Pt@MOF composites as can be evidenced by their stepped CO_2 physisorption isotherms. NPs have a minor effect on accessible porosity and isotherm step shape (see Supplementary Fig. 3). The overall flexibility of this MOF system in response to solvents or adsorbates is briefly summarized in Supplementary Section S1.4. Thermogravimetric analysis (TGA) shows a Pt content correlated lowering of decomposition temperatures of up to 70 °C when comparing **D0** to **D3** under inert gas flow, while differential scanning calorimetry (DSC) confirms absence of any thermally induced first-order phase transitions irrespective of Pt loading (see Supplementary Fig. 4).

Nanoparticle allocation. The size, distribution and location of Pt nanoparticles were investigated by scanning transmission electron microscopy (STEM). The presence of Pt could be detected in all three samples (**D1-3**) by annular dark-field (ADF) STEM. The Pt nanoparticles could be localized based on the contrast difference which originates from a different electron density between Pt NPs and the MOF support (black background vs. grey to white Zn vs. bright white Pt). In all three samples we detected Pt NPs with approximately 1–3 nm in size with a relatively homogenous particle distribution across MOF crystals and limited aggregation. To further validate the presence of the Pt nanoparticles and to study their distribution, elemental mapping based on energy dispersive X-ray spectroscopy (EDS) was carried out. Both results are visualized in Fig. 2a and Supplementary Figs. 7–9. The recorded elemental distribution revealed a higher concentration of the Pt-element at the crystal edges which indicates presence of the Pt nanoparticles predominantly on the surface of the MOF crystals. To study the Pt nanoparticle distribution in more detail, electron tomography was conducted[39]. A series of STEM micrographs with incremental sample tilting steps were collected for composites **D1-3** (40–60 micrographs per sample; selection shown in Supplementary Fig. 10). This tilt-series was used to visualize the nanoparticles' position within the MOF crystals; see Supplementary Video 1 as example. Due to gradual sample decomposition under the electron beam during the series' acquisition and accompanied image quality consistency loss, only **D2** could be reconstructed by utilizing the TEMography™ software (Fig. 2b, see Supplementary Video 2); however, videos made from the recorded micrograph series of all three samples (**D1-3**)
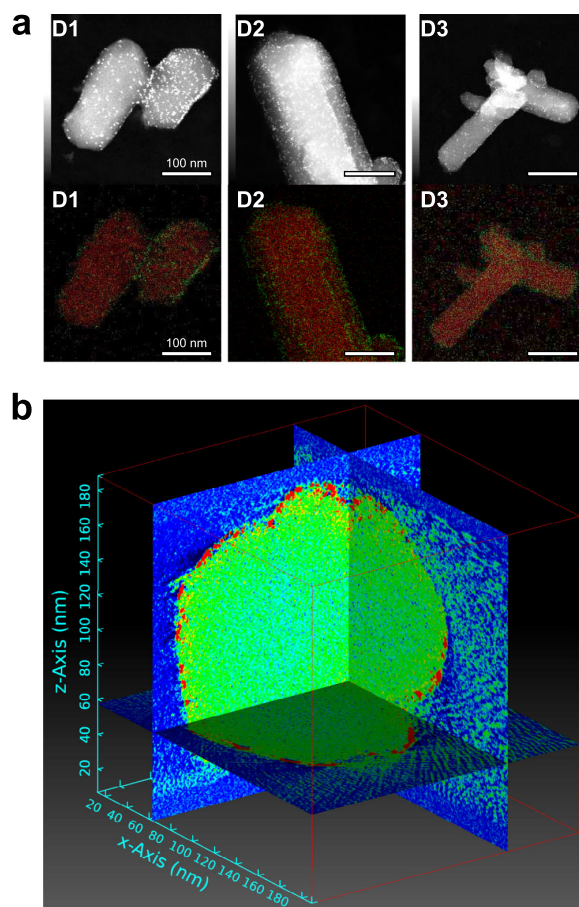
Fig. 2 Electron microscopy and tomography analysis. a ADF-STEM images (top row) showing Pt nanoparticles as bright dots distributed across the crystals and their corresponding EDS elemental mapping overlays (bottom row, contrast adjusted for visibility; red, Zn; green, Pt) revealing a higher concentration of the Pt-element along the edges of the MOF crystals. **b** A cut through a crystal of **D2** reconstructed from electron tomography, a video is available in the ESI. Red areas indicate high Z (Pt), while the MOF is represented by green color. Vacuum is colored blue.

clearly show a homogeneous distribution of uniform Pt nanoparticles deposited on the surface of the MOF crystals.

Thermal expansion. Thermal expansion behavior is investigated by variable temperature powder X-ray diffraction (VTPXRD). All composites were measured as **dry** samples in argon and therefore initially in their np state as shown in Fig. 1a, b and Supplementary Fig. 1. Each Pt@MOF composite was subjected to a heating and cooling cycle from 323 K to 513 K and back to 323 K. Diffraction patterns were collected every 20 K up to 443 K, every 10 K up to 513 K, and vice versa during cooling. The parent MOF $Zn_2(DP-bdc)_2$dabco (**D0**) reportedly exhibits significant thermal expansion and **D1**, **D2**, and **D3** show temperature-correlated shifts of reflection positions indicating similar responsiveness. An exemplary contour plot of VTPXRD data of **D1** is shown in Fig. 3 and plots of all other samples are given in the Supplementary Fig. 6. Most notable within the range of the composites' dominant reflections is a shift of the 110 peak from $2\theta = 4.55–4.40°$ during heating from 323 K to 443 K followed by a shift to $2\theta = 4.35°$ by 513 K. Raw data shows the intensity of both 110 and 001 (at $2\theta = 4.25°$) reflections slightly increase with temperature.

ARTICLE

Lattice parameters determined by Pawley profile fits and details of the outcomes are provided in tabulated form (Supplementary Table 2–5). In this work we focus to discuss volume changes and principal axis deformation instead of unit cell parameters for a better comparison with literature data. Accordingly, we transformed lattice parameters into principles axis by using PASCal[40], see Fig. 1 for a visualization of principal axis compared to unit cell directions and Supplementary Table 6 for a detailed overview. Fig. 4 shows the individual principal axis strains at each temperature step. All composites exhibit anisotropic thermal response and cell volume increases primarily due to elongation along the X_3 direction. The observed anisotropic TE is correlated to the anisotropic MOF topology: the pillared-layered $Zn_2(DP$-$bdc)_2$dabco is built from paddlewheel metal-nodes each connecting four linkers to span two-dimensional square-lattice nets which are stacked by dabco pillars to form a 3D network (see Supplementary Fig. 1). This results in the so-called wine-rack motif and motion, i.e. a transformation between a lozenge-type and square-type structure, which has been reported to occur upon

external stimuli changes such as temperature[17] and pressure;[41] in the context of flexible MOFs, this phenomenon is defined as breathing[42]. This is possible because bdc-linker molecules and metal nodes can adapt to stress via bending of the carboxylate moiety and distortion of the paddlewheel coordination sphere to change linker-node-linker angles and effective linker length[43–45]. Projected onto this motif and structural transition, axis X_3 corresponds to the short direction [010] of the lozenge-lattice and axis X_1 is approximately projected as [100]/[101] along the long lozenge-lattice direction. When expanding from a lozenge- to a square-lattice, X_3 exhibits PTE and X_1 NTE. X_2 lies along [001], the stacked metal nodes and dabco pillars, and is mechanically stationary in this motion.

Upon heating, **D0** shows a 4.5% linear unit cell volume increase up to 493 K. This is congruent to the behavior of the isoreticular, literature-reported $Zn_2(BME$-$bdc)_2$dabco (BME = 2,5-bismethoxyethoxy) which volume increases by 4.5% upon heating to 463 K[17]. Pt nanoparticles gradually decreases this to 3.9% (**D1** and **D2**) and 3.0% (**D3**). It is important to note, however, that for all materials two distinct temperature regions of thermal responsiveness can be observed; a low temperature region (up to approximately 403 K) where all materials display linear expansion behavior and a notable slope change in parameter evolution above this temperature for one or more unit cell parameters or principal directions, see Fig. 4. In the following, we will first elaborate on the linear TE region, then discuss the high-temperature behavior.

Within the lower temperature range, the most pronounced differences are observed from **D0** to **D1** indicating that changes in TE behavior are more related to Pt presence than amount. TE with the highest quality linear fits from 323 K to 403 K along each principal axis is summarized by the CTEs $\alpha(X_1)$, $\alpha(X_2)$, and $\alpha(X_3)$ in unit MK^{-1}, see Table 1 and Fig. 1c for an overview. **D0** exhibits anisotropic thermal expansion predominantly applying to X_3. Positive $\alpha(X_3)$ and negative $\alpha(X_1)$ correspond to the intuitively expected wine-rack opening motion which also aligns with the changes observed for the guest-induced phase transition of $Zn_2(DP$-$bdc)_2$dabco. This implies that this by guest adsorption in a single step triggered motion (see Supplementary Fig. 3) is also, but more gradually, accessible by temperature changes as second order phase transition. The addition of 1.4 wt.% Pt nanoparticles in **D1** leads to a partial inhibition of this wine-rack motion. In other words, for **D1** only PTE is present along the X_3 direction without concerted contraction of X_1. This effect persists for higher nanoparticle loadings in **D2** and **D3**. Furthermore, a relative reduction in $\alpha(X_3)$ of ca. 20% per step from **D0** > **D1** > **D2**/**D3** is observed. Interestingly, both absolute and relative changes in $\alpha(X_1)$ are higher than in $\alpha(X_3)$ when comparing **D0** to **D1** indicating
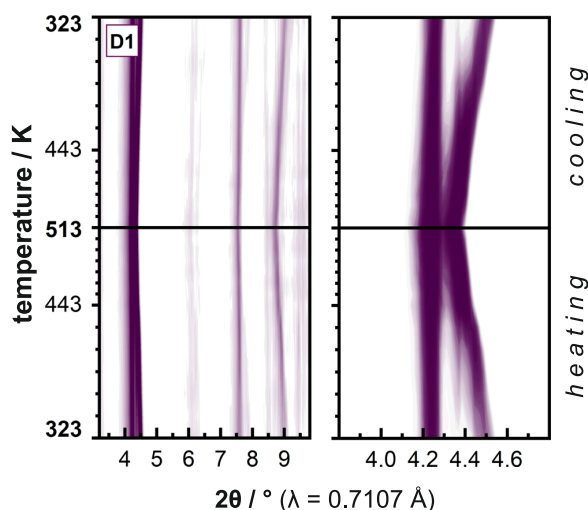
Fig. 3 Contour plot of VTPXRD data of D1. Darker purple corresponds to higher reflection intensity. Pattern in range of $2\theta = 3.2$–$9.8°$ (left) and highlighted main reflections around $2\theta = 4.4°$ (right). Each pattern is normalized to the single highest intensity signal of the complete pattern series. Contour plot and raw patterns for all materials are provided in Supplementary Section S5.
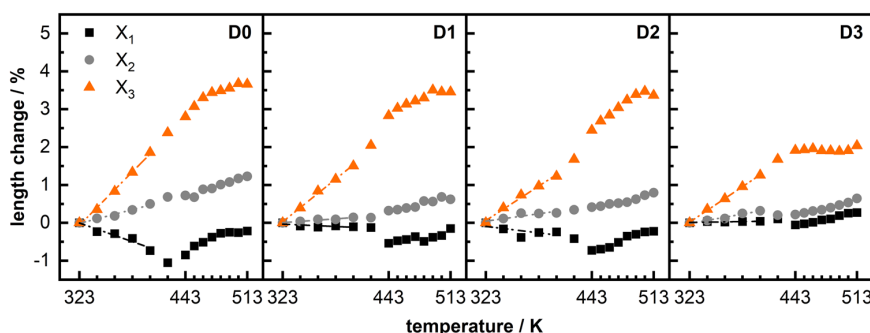
Fig. 4 Thermal expansion along principal axes of D0-3. Principal axes (X_1, X_2, and X_3) length change relative to values at 323 K calculated from lattice parameters using PASCal[40]. Fits as dotted lines for visualization of linear TE up to 403 K. Shown in all graphs is the heating branch; thermal expansion is fully reversible upon cooling (see Supplementary Section S6).

higher sensitivity of the contraction motion to nanoparticle presence than the expansion motion. For $\alpha(X_2)$ no clear correlation between nanoparticle loading and magnitude is obvious aside from a general slight reduction in TE in NP@MOF composites. Overall, when looking at the lower temperature behavior up to 403 K, deposition of Pt nanoparticles on the MOF inhibits the NTE observed along one of the three principal axes, especially in **D3**, while reducing PTE along the primary expansion axis by up to 35%.

In the pursuit to rationalize these observations, it is useful to treat Pt NPs as mesoscopic surface defects which are increasingly explored in flexible MOFs[46,47]. Recently Thompson et al.[48] investigated particle size-dependent flexibility of the pillared-layered MOF DUT-8 (Zn_2ndc_2dabco, ndc^{2-}=2,6-naphthalene dicarboxylate, DUT = Dresden University of Technology). DUT-8 is isostructural with $Zn_2(DP\text{-}bdc)_2dabco$ and large crystals of DUT-8 show an adsorbate-induced first-order phase transition that disappears for its fine-grained powder[45]. It was concluded that not specifically the particle size, but the amount of surface defects and affected nucleation barriers (of the phase transition) govern this difference and that surface modifications by modulators or capping agents offer the opportunity to manipulate this mode of flexibility. These considerations also apply to the composites studied in this work, albeit achievable effects are presumably damped by the fact that a gradual conformation shift and second order phase transition is observed instead of a first order transformation.

An additional perspective on the effect of surface mounted NP on the TE properties is offered when correlating effects of NPs to classical mechanics, effectively treating NPs as a constraint for the network motion of $Zn_2(DP\text{-}bdc)_2dabco$. The topology elaboration above and visualization in Fig. 5 imply that nanoparticles that are surface mounted on the plane spanned by X_1 and X_3 are expected to have a pronounced impact on the wine-rack type motion, effectively blocking any network motion that comes from bond angle, conformation, and geometry changes. While $Zn_2(DP\text{-}bdc)_2dabco$ is no ideal joint-and-bar assembly, our experimental data, especially the absence of temperature-dependent peak broadening in the PXRD pattern, suggest that this effect is large enough to translate to the bulk. Complete rigidification, however, is not expected due to the anisotropic shape of the MOF crystallites which, based on reported behavior of the topologically comparable DUT-8 needle-like crystals[48], grow along the pillar/dabco direction. This presents an excess of side facets, in turn only a few NPs exhibit direct influence on the wine-rack motion, and is the surmised reason why a gradual Pt loading-dependent change in TE behavior is observable in this system, as opposed to complete rigidification with NPs present.

Looking at higher temperatures, deviations from the linear lower-temperature behavior are observable. We attribute this to the gradual second order phase transition linked to the wine-rack motion of the framework becoming more prominent at higher temperatures. The related slope change in principal axis strain progression is most visible in X_1 for **D0**, **D1**, and **D2** and in X_3 for **D3**. In **D0**, after 423 K, the expansion direction of X_1 is inverted and the expansion rate of X_3 decreases; X_2 seems unaffected. **D1** and **D2** mirror this behavior slightly delayed at 443 K. It is less defined in X_1 because the nanoparticles seem to rigidify especially this contractive deformation as was observed at lower temperatures. Notably, PTE in **D3** changes drastically at 423 K. Expansion of the X_3 axis is halted completely until 513 K with a narrow plateau around 443 K close to ZTE. Above 453 K, the temperature-induced strain results again in gradual but reduced TE, however, by minor elongation along X_1 and X_2 as new dominant expansion axes. Overall, when looking at the higher temperature behavior above 443 K, the small step in Pt loading from **D2** to **D3** proves most influential. This suggests that increased nanoparticle loading might in general have higher TE impact at higher temperatures and deposition of otherwise innocent nanoparticles might be of interest to reduce strain exerted onto porous material by their NTE or PTE.

Conclusions

In conclusion, we have developed a one-pot, capping-agent free synthesis route for Pt@ $Zn_2(DP\text{-}bdc)_2dabco$ composites with precise control over homogeneity and nanoparticle surface-loading which enables the study of surface-mounted nanoparticle formation on the TE properties of the MOF support. The surface-mounted platinum nanoparticles in the size regime <3 nm display distinctly different influence on the anisotropic (net positive) thermal expansion of the $Zn_2(DP\text{-}bdc)_2dabco$ support depending on the temperature range observed. First, at temperatures up to 403 K, gradually increasing amounts of Pt NPs proportionally decrease expansion along the main expansion axis by up to 35%, while the introduction of low nanoparticle amounts (1.4 wt.%) significantly inhibits contraction along the secondary expansion axes. Up to 403 K, all investigated composites show reduced but retained net PTE. Second, at temperatures above 403 K, the highest nanoparticle loading (3.1 wt.%) resulted in a large change in TE behavior. Expansion along the main axis is halted from 423 K to 513 K with a narrow plateau close to ZTE around 443 K after which only minor net PTE is observed due to strain along the other axes. We conclude from this that at low nanoparticle loadings and temperatures the TE of NP@MOF composites can be approximated by the MOF support. It is implicated that composite materials with higher NP loading exhibit superior TE properties compared to the pure MOF because their thermal stress is reduced, especially at higher temperatures. It is further intriguing that specifically NTE along a principal direction was inhibited most by the nanoparticles. If, hypothetically, their influence is more pronounced on NTE than PTE, this might open another parameter space for MOF fine-tuning given how prominent NTE is within this material class.

While this study focused on a single model material to highlight temperature and loading dependencies, it is reasonable to assume other NP@MOF composites undergo similar changes to their thermal responsiveness. TE in such composites expectedly correlates to the interplay of nanoparticle loading, metal (oxide), size, and capping agents - all of which are firmly tied to the synthetic challenges of precise NP bulk-incorporation and surface-deposition - as well as MOF support topology, particle size, defect amount, and more. Future studies are envisioned to expand on the phenomenological investigation and, in close

Fig. 5 Thermally induced framework motion. Anisotropic structural transition between lozenge-lattice (left) and square-lattice (right) of a wine-rack motif. Changes along principal axes X_3 (orange) and X_1 (black) are indicated by directed arrows. Structure represents paddlewheel nodes (blue), linker struts (grey) and pillar struts (green).

ARTICLE

collaboration with molecular dynamic simulations, to unravel detailed mechanisms of this complex interplay. Understanding this will play an important role for increasing longevity and perform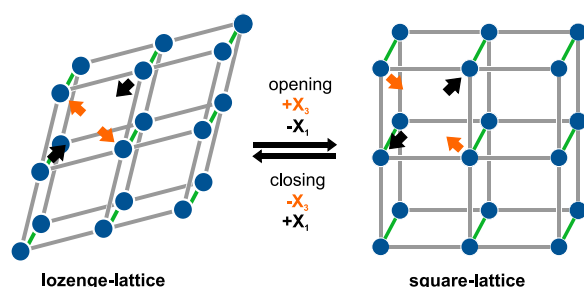ance in applications with repeating heating or cooling cycles which, incidentally, is very likely to be the case in the most prominent uses of these composites as adsorbents, sensors, or catalysts.

Methods

Material synthesis. All chemicals were purchased from commercial suppliers (Sigma-Aldrich, Fluka, Alfa Aesar, and others) and were used without further purification. Ethanol for solvent exchange was purchased as technical grade and redistilled prior to use. The linker was synthesized via Williamson Etherification according to literature known procedures, albeit slightly optimized[38]. All Pt@Zn_2(DP-bdc)$_2$dabco composites were synthesized via a concerted one-pot crystallization of MOF and formation of Pt nanoparticles without any capping agents[34]. This method combines the solvothermal MOF synthesis in dimethyl-formamide (DMF), as known from literature[17], with a solvent mediated Pt^{2+} reduction. Multiple washing and solvent exchange steps were conducted prior to solvent removal *in vacuo*. See Supplementary Methods for details.

Analytical methods. Liquid state NMR spectra were measured on a Bruker Ultrashield DRX400 spectrometer at ambient temperature (see Supplementary Section S1.1). MOF samples were digested and subsequently measured in DMSO-d_6 with DCl, organic linkers were dissolved and measured in DMSO-d_6. CHNS contents were determined via combustion analysis. Adsorption measurements were carried out on a 3Flex Physisorption Instrument by Micromeritics Instrument Corp. Samples were activated at 80 °C for 5 h under dynamic vacuum using a SmartVacPrep by Micromeritics Instrument Corp. to ensure absence of unwanted adsorbates. The adsorbent mass was then recorded, generally in the range of 50–70 mg (for more method details see Supplementary Section S3). All adsorption isotherms are accessible online free of charge as adsorption information files to counter issues with post-publishing adsorption data extraction and facilitate machine learning (see Supplementary Data)[49]. Thermogravimetric analysis coupled with differential scanning calorimetry (TGA-DSC) was conducted on a Netzsch TG-DSC STA 449 F5 in a temperature range from 25 °C to 800 °C with a heating rate of 10 K min^{-1} under argon flow (see Supplementary Fig. 4). Powder X-ray diffraction (PXRD) patterns of the as-synthesized (**as**) and re-solvated samples were measured on a Rigaku Benchtop MiniFlex 600-C (X-ray Cu Kα radiation, $\lambda = 1.5406$ Å). Activated (**dry**) samples and samples after physisorption measurements were measured in Debeye-Scherrer geometry on a PANalytical Empyrean (X-ray Cu Kα radiation, $\lambda = 1.5406$ Å) (for further details see Supplementary Section S2). Variable temperature PXRD (VTPXRD) measurements were done using a STOE INSITU HT2 Furnace on a STOE STADI P Dual (X-ray Mo Kα radiation, $\lambda = 0.7107$ Å). **Dry** samples were filled in borosilicate glass capillaries in a glovebox under argon atmosphere. Sealed capillaries were inserted into an open 1 mm diameter quartz capillary and measured in Debeye-Scherrer geometry from 323 K to 513 K to 323 K (see Supplementary Section S5). Scanning transmission electron microscopy (STEM) with energy dispersive X-ray spectroscopy (EDS) elemental mappings and electron tomography were recorded with a JEM-ARM200F NEOARM microscope from JEOL (Germany) GmbH with a cold FEG electron source operated at 200 kV. Samples were prepared by depositing a drop of the solid dispersed in ethanol onto carbon-coated copper grids (200 mesh) and dried in air (see Supplementary Section S8).

Data availability

The primary data that support the findings of this study are available within the supplementary information files and from either corresponding author upon request.

References

1. Bon, V., Kavoosi, N., Senkovska, I. & Kaskel, S. Tolerance of Flexible MOFs toward Repeated Adsorption Stress. *ACS Appl. Mater. Interfaces.* **7**, 22292–22300 (2015).
2. Xiao, J., Hu, M., Bénard, P. & Chahine, R. Simulation of hydrogen storage tank packed with metal-organic framework. *Int. J. Hydrog. Energy.* **38**, 13000–13010 (2013).
3. Nilsson Pingel, T., Jørgensen, M., Yankovich, A. B., Grönbeck, H. & Olsson, E. Influence of atomic site-specific strain on catalytic activity of supported nanoparticles. *Nat. Commun.* **9**, 2722 (2018).
4. Lai, K.-Y. & Manthiram, A. Self-Regenerating Co–Fe Nanoparticles on Perovskite Oxides as a Hydrocarbon Fuel Oxidation Catalyst in Solid Oxide Fuel Cells. *Chem. Mater.* **30**, 2515–2525 (2018).
5. Zhang, Y. et al. Thermal-expansion offset for high-performance fuel cell cathodes. *Nature* **591**, 246–251 (2021).
6. Yu, C. et al. Plastic and low-cost axial zero thermal expansion alloy by a natural dual-phase composite. *Nat. Commun.* **12**, 4701 (2021).
7. Fedorova, A., Hourlier, D. & Scheffler, M. Polymer derived ceramics with β-eucryptite fillers: A novel processing route to negative and near zero expansion materials. *Ceram. Int.* **43**, 4483–4488 (2017).
8. Stassen, I. et al. An updated roadmap for the integration of metal-organic frameworks with electronic devices and chemical sensors. *Chem. Soc. Rev.* **46**, 3185–3241 (2017).
9. Freund, R. et al. The Current Status of MOF and COF Applications. *Angew. Chem., Int. Ed.* **60**, 23975–24001 (2021).
10. Freund, R. et al. 25 Years of Reticular Chemistry. *Angew. Chem., Int. Ed.* **60**, 23946–23974 (2021).
11. Barrera, G. D., Bruno, J. A. O., Barron, T. H. K. & Allan, N. L. Negative thermal expansion. *J. Phys.: Condens. Matter.* **17**, R217–R252 (2005).
12. Coates, C. S. & Goodwin, A. L. How to quantify isotropic negative thermal expansion: magnitude, range, or both? *Mater. Horiz.* **6**, 211–218 (2019).
13. Chen, J., Hu, L., Deng, J. & Xing, X. Negative thermal expansion in functional materials: controllable thermal expansion by chemical modifications. *Chem. Soc. Rev.* **44**, 3522–3567 (2015).
14. Burtch, N. C. et al. Negative Thermal Expansion Design Strategies in a Diverse Series of Metal–Organic Frameworks. *Adv. Funct. Mater.* **29**, 1904669 (2019).
15. Wieme, J. & van Speybroeck, V. Unravelling thermal stress due to thermal expansion mismatch in metal–organic frameworks for methane storage. *J. Mater. Chem. A.* **9**, 4898–4906 (2021).
16. Cliffe, M. J., Hill, J. A., Murray, C. A., Coudert, F.-X. & Goodwin, A. L. Defect-dependent colossal negative thermal expansion in UiO-66(Hf) metal-organic framework. *Phys. Chem. Chem. Phys.* **17**, 11586–11592 (2015).
17. Henke, S., Schneemann, A. & Fischer, R. A. Massive Anisotropic Thermal Expansion and Thermo-Responsive Breathing in Metal-Organic Frameworks Modulated by Linker Functionalization. *Adv. Funct. Mater.* **23**, 5990–5996 (2013).
18. Schwedler, I. et al. Mixed-linker solid solutions of functionalized pillared-layer MOFs - adjusting structural flexibility, gas sorption, and thermal responsiveness. *Dalton Trans.* **45**, 4230–4241 (2016).
19. Mohamed, S. A., Chong, S. & Kim, J. Thermal Stability of Methyl-Functionalized MOF-5. *J. Phys. Chem. C.* **123**, 29686–29692 (2019).
20. Baxter, S. J. et al. Tuning Thermal Expansion in Metal-Organic Frameworks Using a Mixed Linker Solid Solution Approach. *J. Am. Chem. Soc.* **141**, 12849–12854 (2019).
21. Goodenough, I. et al. Interplay between Intrinsic Thermal Stability and Expansion Properties of Functionalized UiO-67 Metal–Organic Frameworks. *Chem. Mater.* **33**, 910–920 (2021).
22. Petters, L., Burger, S., Kronawitter, S., Drees, M. & Kieslich, G. Linear negative thermal expansion in Pd(acac) 2. *CrystEngComm* **23**, 5425–5429 (2021).
23. Collings, I. E., Tucker, M. G., Keen, D. A. & Goodwin, A. L. Geometric switching of linear to area negative thermal expansion in uniaxial metal–organic frameworks. *CrystEngComm* **16**, 3498–3506 (2014).
24. Cai, W. & Katrusiak, A. Giant negative linear compression positively coupled to massive thermal expansion in a metal-organic framework. *Nat. Commun.* **5**, 4337 (2014).
25. Evans, J. D., Dürholt, J. P., Kaskel, S. & Schmid, R. Assessing negative thermal expansion in mesoporous metal–organic frameworks by molecular simulation. *J. Mater. Chem. A.* **7**, 24019–24026 (2019).
26. Grobler, I., Smith, V. J., Bhatt, P. M., Herbert, S. A. & Barbour, L. J. Tunable anisotropic thermal expansion of a porous zinc(II) metal-organic framework. *J. Am. Chem. Soc.* **135**, 6411–6414 (2013).
27. Garai, B. et al. Reversible switching between positive and negative thermal expansion in a metal–organic framework DUT-49. *J. Mater. Chem. A.* **8**, 20420–20428 (2020).
28. Auckett, J. E. et al. Continuous negative-to-positive tuning of thermal expansion achieved by controlled gas sorption in porous coordination frameworks. *Nat. Commun.* **9**, 4873 (2018).
29. Li, B., Ma, J.-G. & Cheng, P. Integration of Metal Nanoparticles into Metal-Organic Frameworks for Composite Catalysts: Design and Synthetic Strategy. *Small* **15**, e1804849 (2019).
30. Yadav, S. et al. Magnetic metal–organic framework composites: structurally advanced catalytic materials for organic transformations. *Mater. Adv.* **2**, 2153–2187 (2021).
31. Yang, Q., Xu, Q. & Jiang, H.-L. Metal-organic frameworks meet metal nanoparticles: synergistic effect for enhanced catalysis. *Chem. Soc. Rev.* **46**, 4774–4808 (2017).
32. Bavykina, A. et al. Metal-Organic Frameworks in Heterogeneous Catalysis: Recent Progress, New Trends, and Future Perspectives. *Chem. Rev.* **120**, 8468–8535 (2020).

ARTICLE

33. Roldan Cuenya, B. et al. Anomalous lattice dynamics and thermal properties of supported size- and shape-selected Pt nanoparticles. *Phys. Rev. B.* **82**; https://doi.org/10.1103/PhysRevB.82.155450 (2010).

34. Liu, H., Chang, L., Chen, L. & Li, Y. In situ one-step synthesis of metal–organic framework encapsulated naked Pt nanoparticles without additional reductants. *J. Mater. Chem. A.* **3**, 8028–8033 (2015).

35. Pastoriza-Santos, I. & Liz-Marzán, L. M. N, N -Dimethylformamide as a Reaction Medium for Metal Nanoparticle Synthesis. *Adv. Funct. Mater.* **19**, 679–688 (2009).

36. Dai, S. et al. Impact of capping agent removal from Au NPs@MOF core–shell nanoparticle heterogeneous catalysts. *J. Mater. Chem. A.* **10**, 3201–3205 (2022).

37. Henke, S., Schmid, R., Grunwaldt, J.-D. & Fischer, R. A. Flexibility and sorption selectivity in rigid metal-organic frameworks: the impact of ether-functionalised linkers. *Chemistry* **16**, 14296–14306 (2010).

38. Henke, S., Schneemann, A., Wütscher, A. & Fischer, R. A. Directing the breathing behavior of pillared-layered metal-organic frameworks via a systematic library of functionalized linkers bearing flexible substituents. *J. Am. Chem. Soc.* **134**, 9464–9474 (2012).

39. Chen, Y.-Z. et al. Location determination of metal nanoparticles relative to a metal-organic framework. *Nat. Commun.* **10**, 3462 (2019).

40. Cliffe, M. J. & Goodwin, A. L. PASCal: a principal axis strain calculator for thermal expansion and compressibility determination. *J. Appl. Crystallogr.* **45**, 1321–1329 (2012).

41. Vervoorts, P. et al. Configurational Entropy Driven High-Pressure Behaviour of a Flexible Metal-Organic Framework (MOF). *Angew. Chem.* **60**, 787–793 (2021).

42. Seth, S. & Jhulki, S. Porous flexible frameworks: origins of flexibility and applications. *Mater. Horiz.* **8**, 700–727 (2021).

43. Férey, G. & Serre, C. Large breathing effects in three-dimensional porous hybrid matter: facts, analyses, rules and consequences. *Chem. Soc. Rev.* **38**, 1380–1399 (2009).

44. Horcajada, P. et al. How linker's modification controls swelling properties of highly flexible iron(III) dicarboxylates MIL-88. *J. Am. Chem. Soc.* **133**, 17839–17847 (2011).

45. Ehrling, S. et al. Crystal size versus paddle wheel deformability: selective gated adsorption transitions of the switchable metal–organic frameworks DUT-8(Co) and DUT-8(Ni). *J. Mater. Chem. A.* **7**, 21459–21475 (2019).

46. Bennett, T. D., Cheetham, A. K., Fuchs, A. H. & Coudert, F.-X. Interplay between defects, disorder and flexibility in metal-organic frameworks. *Nat. Chem.* **9**, 11–16 (2016).

47. Krause, S. et al. Impact of Defects and Crystal Size on Negative Gas Adsorption in DUT-49 Analyzed by In Situ129Xe NMR Spectroscopy. *Chem. Mater.* **32**, 4641–4650 (2020).

48. Thompson, M. J. et al. Role of particle size and surface functionalisation on the flexibility462 behaviour of switchable metal–organic framework DUT-8(Ni).*J. Mater. Chem.A.* **8**, 22703–22711 (2020).

49. Evans, J. D., Bon, V., Senkovska, I. & Kaskel, S. A Universal Standard Archive File for Adsorption Data. *Langmuir* **37**, 4222–4226 (2021).

Author contributions

J.B. performed material synthesis, analysis, data processing and manuscript writing. A.-S.D. contributed to material prototyping, analysis, and manuscript writing. A.U. and H.B. performed all electron microscopy, its visualization, and contributed to manuscript writing. R.A.F. provided the motivation of this work and contributed to manuscript writing. G.K. provided the motivation of this work and contributed to data processing and manuscript writing.

Funding

Competing interests

The authors declare no competing interests.

Additional information

Supplementary information The online version contains supplementary material available at https://doi.org/10.1038/s42004-022-00793-2.

Correspondence and requests for materials should be addressed to Roland A. Fischer or Gregor Kieslich.

Peer review information *Communications Chemistry* thanks Volodymyr Bon and the other, anonymous, reviewers for their contribution to the peer review of this work. Peer reviewer reports are available.

Reprints and permission information is available at http://www.nature.com/reprints

Publisher's note Springer Nature remains neutral with regard to jurisdictional claims in published maps and institutional affiliations.

4.3 STUDY III. Guest- and Temperature-Switchability of a Flexible Metal-Organic Framework with Surface-Mounted Nanoparticles

This study elaborates the impact surface-mounted platinum and silica nanoparticles have on the CO_2- and temperature-induced switchability of the pillared-layered MOF $Zn_2(BME-bdc)_2dabco$. Focus is the larger scale first order phase transition of the flexible MOF, while in contrast Study II looked at smaller scale structural deformations only triggered by temperature and not constituting a full phase transition. Hybrid composite materials of the type NP@flexibleMOF are yet largely unexplored, but offer great potential to combine expertise on and advantageous properties of both flexible MOFs and nanoparticle loaded MOFs. Herein we synthesized $Pt@Zn_2(BME-bdc)_2dabco$ composites with varying Pt loading following an in situ nanoparticle formation approach from precursors and $SiO_2@Zn_2(BME-bdc)_2dabco$ guided by classical bottle-around-the-ship methods utilizing preformed nanoparticles. Because surface-mounted NPs potentially act as surface-defects, which are known to impact switchability, it would be reasonable to expect pronounced changes especially in composites with higher NP loadings. Experimentally, however, we observe this on very different magnitudes in dependence of the stimulus applied. We show that by CO_2 physisorption triggered flexibility of the MOF is fully retained and reversible for all NP@flexibleMOF composites, irrespective of nanoparticle type, with only minor decreases in accessible porosity. Moreover, NPs stabilize the large pore state of the MOFs, slightly increasing and shifting the switching pressure window. This is also found in temperature-induced switching but Pt@flexMOF composites partially degrade during the reversion to their narrow pore state, while attached SiO_2 NPs allow for a fully reversible transition. We attribute the latter to NP quantity attached to the MOF crystals (with NP size as correlated factor). These findings suggest that the total exerted material strain can undergo significant changes based on NP amount attached, but is drastically different dependent on stimulus applied. Crucially, however, it i shown that guest-induced switchability can be fully realized in NP@flexMOF hybrid materials.

Study III will be accepted in a peer-reviewed journal by time of publication of this dissertation. For updated information please refer to orcid.org/0000-0002-9230-0398.

Guest- and Temperature-Switchability of a Flexible Metal-Organic Framework with Surface-Mounted Nanoparticles

Jan Berger,[†$] Stephanie Terruzzi,[§$] Hana Bunzen,[‡] Marcello Marelli,[ǂ] Luca Braglia,[⁑] Roland A. Fischer,[†] Valentina Colombo,[§ǂ]* and Gregor Kieslich[†]*

[†]Inorganic and Metal-Organic Chemistry, School of Natural Sciences, Technical University of Munich, Lichtenbergstr. 4, 85748 Garching, Germany

[§]Department of Chemistry, University of Milan, Via Golgi 19, 20133 Milan, Italy

[‡]Institute of Physics, University of Augsburg, Universitätsstr. 1, 86159 Augsburg, Germany

[ǂ]CNR SCITEC - Istituto di Scienze e Tecnologie Chimiche "Giulio Natta", Via Fantoli 16/15, 20138 Milan, Italy

[⁑]CNR-Istituto Officina dei Materiali, TASC, 34149 Trieste, Italy

[$]these authors contributed equally

ABSTRACT

Stimulus-responsive materials and control over their responsiveness are of great importance in material science. Within the class of metal-organic frameworks (MOFs) the subset of flexible MOFs (flexMOFs) has been intricately investigated for this reason. Derived hybrid composites like nanoparticle (NP) loaded flexible MOFs, which stand to potentially combine expertise and advantageous properties of both, however, are yet largely unexplored. Here we study the influence of external surface-mounted platinum and silicon dioxide nanoparticles on the stimulus-responsiveness of a flexible MOF in NP@Zn_2(BME-bdc)$_2$dabco (BME-bdc^{2-} = 2,5-bismethoxyethoxy-1,4-benzenedicarboxylate, dabco = 1,4-diazabicyclo[2.2.2]octane) hybrid materials. We show that by CO_2 physisorption triggered flexibility of the MOF is fully retained and reversible for all NP@flexMOF composites. Additionally, NPs stabilize the large pore state of the MOF, slightly increasing and shifting the switching pressure window. This effect is also observed during temperature-induced switching but Pt@flexMOF composites partially lose long-range order during the reversion to their narrow pore state, while attached SiO_2 NPs allow for a fully reversible transition. These findings suggest that the total exerted material strain triggering the switching is heavily dependent on NP size and stimulus applied, but moreover that guest-induced switchability can be fully realized in NP@flexMOF hybrid materials.

INTRODUCTION

The exploration of stimuli-responsive materials, which change their physical properties in reaction to external triggers, and synthetic control over this responsiveness is of great importance across a diverse range of research fields in material science. Metal-organic frameworks (MOFs) are well-known for their versatility in feature design and control.[1] Many examples of stimulus-responsive MOFs exist,[2,3] and especially the increasingly in-depth studied subset of flexible MOFs includes a variety of both modes of response and activating stimuli.[4,5] Their most typical response is a change in accessible porosity by a phase transition from a contracted state (narrow/closed pore, **np/cp**) to an expanded state (large/open pore, **lp/op**). Consequently, flexible MOFs are considered promising candidates for application where this dynamic volume is used as guest capacity, *i.e.* gas storage and separation,[6,7] sensing,[8,9] and drug release,[10,11] or this phase transition is used as energetic sink, *i.e.* as shock absorber and dampener.[12,13]

Focusing on switching between contracted and extended states in flexible MOFs, the most applicable control mechanism is guest adsorption and adsorbate concentration. This was early discovered in now prototypical flexible MOFs like ELM-11,[14] MIL-53,[15] SNU-9,[16] or pillared-layered MOFs DUT-8 and $Zn_2(fu\text{-}bdc)_2dabco$,[17,18] to name a few. Use of adsorbate controlled switchability has by now been demonstrated in, for example, high-throughput separation in pressure vacuum swing adsorption of methane and CO_2,[19] ternary sieving of ethane, ethylene and CO_2,[20] variable-aperture porous organic cage membranes for graded molecular sieving,[21] isotope-responsive breathing,[22] or solvent-induced control over separation selectivity.[23] Of very high interest, because they can be considered fully external conditions, are the stimuli mechanical pressure, temperature, and electric fields. Only few reports investigating electrically inducible phase transitions exist,[24,25] however, it is clear temperature and pressure are key parameters much like adsorbate concentration. On a fundamental level it was found that the temperature- and pressure-influenced configurational entropy of flexible MOFs,[26–28] as well as increased dispersive adsorbate-adsorbent interactions significantly impact transition behavior from different angles.[29] While this creates a highly complex interplay to be considered for switchability design, Chanut *et al.* were able to mechanically control the pore aperture of MIL-53 for size selective separation of CO_2/N_2 and CO_2/CH_4 mixtures in a proof-of-concept study showing how conceptually straight forward such design can yet be.[30]

Apart from switchable phase transitions, almost all conceivable stimuli can be applied to induce changes in linker conformation,[24,31–33] redox states,[34–36] optical properties,[37–39] or conductivity.[40] In front of this, it is surprising that understanding of the impact of nanoparticles (NP) on MOF flexibility – whether they are incorporated into the bulk or mounted on the external surface – is yet in its infancy. It has been found that linker rotation can influence conversion and selectivity for Pt@ZIF-8 materials used in catalysis,[41] however, to the best of our knowledge the inverse question of how flexibility in MOFs is affected by nanoparticles has not been investigated outside of a recent study focusing on thermal expansion properties of Pt@MOF composites.[42]

While the research fields of NP loaded MOF materials and switchable, flexible MOFs are seemingly at this point not interlinked, we see great potential in forming this link and investigating how nanoparticles impact framework switchability. Both scenarios in which switchability regulates catalysis conditions at the nanoparticles, and in which nanoparticles direct framework switching behavior can easily be envisioned. Herein we explore the latter and investigate the influence of surface-mounted Pt and SiO_2 nanoparticles on the phase transition of the functionalized, flexible pillared-layered model system $Zn_2(BME\text{-}bdc)_2dabco$ (see Figure 1), and the effect the type of stimulus used to trigger this transition has. We compare an isoreticular series of $Pt@Zn_2(BME\text{-}bdc)_2dabco$ composites with different Pt loading, a $SiO_2@Zn_2(BME\text{-}bdc)_2dabco$ composite, and a well-studied nanoparticle-free reference. The results suggest that guest-induced switchability can be achieved in NP@MOF composites while the reversal of temperature-induced phase transitions is heavily affected by smaller metal nanoparticles.
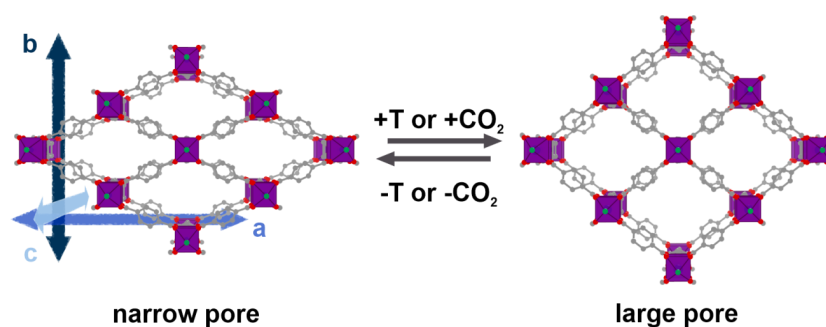
Figure 1. Visualization of $Zn_2(BME\text{-}bdc)_2dabco$ and directions of unit cell parameters a, b, and c. The MOF exhibits a switchable phase transition from its narrow pore (**np**) phase lozenge-lattice to its large pore (**lp**) phase square-lattice. View along the stacked dabco pillars in c direction. C, grey; O, red; N, green; Zn coordination polyhedron, purple; hydrogen atoms and BME functionalizations, omitted for clarity.

METHODS

Material synthesis. Chemicals were purchased from commercial suppliers (Sigma-Aldrich, Alfa Aesar, ABCR and others) and used without further purification. SiO_2 nanoparticles were purchased from Micromod GmbH (Germany). Ethanol for solvent exchange was purchased as technical grade and redistilled prior to use. The linker was synthesized via etherification according to optimized literature known procedures (see S1.2).[43] Pt@Zn$_2$(BME-bdc)$_2$dabco composites were synthesized via a concerted one-pot crystallization of MOF and formation of Pt nanoparticles without any capping agents.[44] This method combines the solvothermal MOF synthesis in dimethylformamide (DMF),[27] with a solvent mediated Pt^{2+} reduction. SiO$_2$@Zn$_2$(BME-bdc)$_2$dabco composites were synthesized by adding a stable colloidal dispersion of pre-formed nanoparticles to the reaction mixture during solvothermal MOF synthesis. See S1.3 for details.

Analytical methods. Liquid state NMR spectra were measured on a Bruker Ultrashield DRX400 at ambient temperature (for details see S1.1). MOF samples were digested and subsequently measured in DMSO-d_6 with DCl, organic linkers were dissolved and measured in DMSO-d_6. CHNS contents were determined via combustion analysis. Powder X-ray diffraction (PXRD) patterns of the as-synthesized (**as**) samples were measured on a Rigaku Benchtop MiniFlex 600-C (X-ray Cu Kα radiation, λ = 1.5406 Å). Samples were measured in activated (**dry**) state and after physisorption measurements in Debeye-Scherrer geometry on a PANalytical Empyrean (X-ray Cu Kα radiation, λ = 1.5406 Å) (for further details see S2). Adsorption measurements were carried out on a 3Flex Physisorption Instrument by Micromeritics Instrument Corp. Samples were activated at 80 °C for 5 h under dynamic vacuum using a SmartVacPrep by Micromeritics Instrument Corp. to ensure absence of unwanted adsorbates. The adsorbent mass was then recorded, generally in the range of 50-70 mg (for more method details see S3). All adsorption isotherms are accessible online free of charge as adsorption information files to counter issues with post-publishing adsorption data extraction and facilitate machine learning (see ESI).[45] Thermogravimetric analysis coupled with differential scanning calorimetry (TGA-DSC) was conducted on a Netzsch TG-DSC STA 449 F5 in a temperature range from 25 to 800 °C under argon flow (for details see S4). Variable temperature PXRD (VTPXRD) measurements were conducted using a custom-made sample heater plugged in a Bruker AXS D8 Advance diffractometer (X-ray Cu Kα radiation, λ = 1.5406 Å) with Bragg-Brentano geometry (see S5). About 10 mg of sample were deposited on an aluminium sample-holder and heated in air from 30

°C up to 290 °C with steps of 20 °C. Scanning transmission electron microscopy (STEM) with energy dispersive X-ray spectroscopy (EDS) elemental mappings of **B1-3** were recorded with a JEM-ARM200F "NEOARM" microscope from JEOL (Germany) GmbH with a cold FEG electron source operated at 200 kV. Energy-filtered TEM (EFTEM) micrographs of sample **B4** were recorded on a ZEISS LIBRA200FE equipped with a Schottky FEG electron source operated at 200 kV. Samples were prepared by depositing a drop of the solid dispersed in ethanol onto carbon-coated copper grids (200 mesh) and dried in air (see S7). X-ray photoemission spectra (XPS) of sample **B3** were recorded using a conventional non-monochromatized X-ray source (Al Kα radiation, λ = 8.3896 Å) with a hemispherical electron energy analyzer in a dedicated chamber of the NFFA UHV MBE-cluster system.[46] The Pt 4f and Zn 2p spectra have been acquired using a pass energy of 50, a dwell time of 500 ms and a channel width of 1.1 mm (see S8).

RESULTS AND DISCUSSION

NP@MOF composite synthesis. The composites investigated in this study include either Pt or SiO$_2$ nanoparticles. The former were chosen due to known experimental accessibility of small Pt NPs (< 5 nm) by reduction of Pt^{2+} precursors; the latter were chosen because our desired second NP size regime of ca. 30 nm is commercially readily available through SiO$_2$ NPs. Pt@Zn$_2$(BME-bdc)$_2$dabco composites were synthesized using a co-crystallization approach which allows one-step one-pot crystallization of MOF and formation of Pt nanoparticles. MOF precursors Zn(NO$_3$)$_2$, dabco, H$_2$BMEbdc and the Pt nanoparticle precursor K$_2$PtCl$_4$ are suspended in dimethylformamide (DMF). During solvothermal MOF synthesis, DMF oxidizes with water originating from trace amounts in the DMF and the hydrated metal salt to its carbamic acid derivative while reducing Pt^{2+} to Pt^0 to facilitate nanoparticle formation.[47] Both MOF and nanoparticle precipitate as composite. This avoids use of capping agents which is expected to improve reproducibility and correlation of nanoparticle impact and MOF behavior.[48] This methodology in general can be applied to create Pt@MOF composites in which Pt NPs are integrated into the bulk volume of a MOF by forming Pt *in situ* inside its pores. Herein, however, we discovered that the extensive functionalization of the MOF Zn$_2$(BME-bdc)$_2$dabco apparently prevents sufficient reagent diffusion into the porous bulk, despite the known porosity towards the reaction medium, and does not result in quantitatively incorporated NPs. Instead, MOF particles crystallize, and Pt precursor reduction takes place predominantly outside the pores. Formed Pt NPs are then attached to the external surface of the MOF particles to yield Pt@ Zn$_2$(BME-bdc)$_2$dabco composites. We were unable to create materials with bulk-incorporated NPs and compare their properties to counterparts with surface-attached NPs. The series of isoreticular functionalized Pt@MOF comprises four materials based on Zn$_2$(BME-bdc)$_2$dabco with external surface-mounted NPs. We further synthesized a SiO$_2$@Zn$_2$(BME-bdc)$_2$dabco composite to compare the most pronounced differences stemming from NP size and type (see Table 1). This composite was made, similar to the bottle-around-a-ship method,[49] by adding a commercially available, stable colloidal aqueous dispersion of SiO$_2$ nanoparticles (30 nm, see Table S2 for specifications) to the educt mixture during solvothermal MOF synthesis and thereby attaching the NPs to the growing MOF crystals' external surface. It should be noted that the amount of colloidal solution added and the surface modifications of the SiO$_2$ nanoparticles has drastic impact on the MOF crystallization.

Table 1. Overview of NP@ Zn_2(BME-bdc)$_2$dabco composites and attached nanoparticles.

composite	NP	[wt.%]	size [nm]	surface funct.
B0	none	-	-	-
B1	Pt	1.1[a]	1-3	none
B2	Pt	2.0[a]	1-3	none
B3	Pt	2.8[a]	1-3	none
B4	SiO_2	1[b]	30	none

[a]per atom absorption spectroscopy and photometry [b]calculated from added colloidal suspension

All composites were extensively washed, solvent exchanged, activated, and subsequently verified in respect to MOF composition and solvent removal by ^{1}H NMR spectroscopy and TGA (see S1). Pt content was determined by atom adsorption spectroscopy and photometry. SiO_2 loading was calculated based on educt concentrations and marks the maximum wt.% value. More
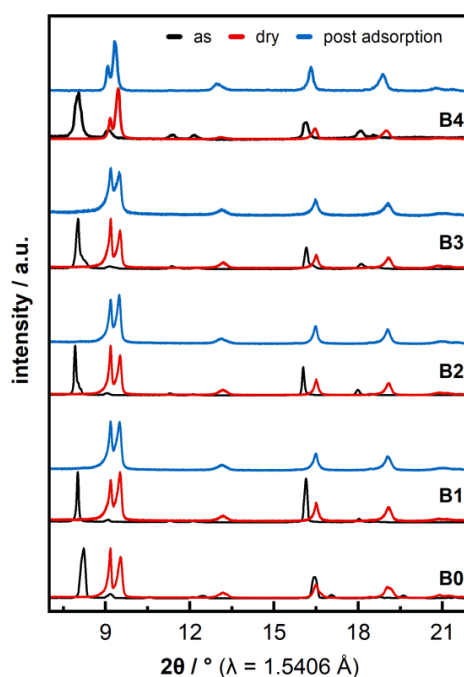
Figure 2. PXRD patterns of **B0-4** in the range of $2\theta = 7\text{-}22°$. Transition from **lp** in **as** to **np** in **dry** is observable by shift of the 110 reflection from $2\theta = 8.0\text{-}8.4°$ to $9.5\text{-}9.7°$ and intensity increase of the 001 reflection at $2\theta = 9.2°$. Blue, measured after all gas adsorption experiments.

direct determination of the very low SiO_2 concentration in the composite was outside the reliable and reproducible analytical capabilities. $Zn_2(BME\text{-}bdc)_2dabco$ is known to exhibit guest induced flexibility triggered by polar solvents/adsorbates like DMF or CO_2.[43] The material is built from a 2D lattices spanned by the linker molecules and metal nodes which are stacked along the third dimension by dabco pillars. This pillared-layered structure can undergo an anisotropic deformation by contracting the 2D square-lattice to a lozenge-lattice and thereby switch between a large pore (**lp**) and narrow pore (**np**) state as visualized in Figure 1. This motion is generally referred to as wine-rack motion or breathing and often found in flexible MOFs with this topology motif.[4] PXRD confirms all materials are isoreticular independent of the Pt or SiO_2 content; both in as-synthesized (**as**), **lp** state directly after synthesis and washing as well as in activated (**dry**), **np** state after solvent removal (see Figure 2). We note that Pt NPs are not observed in diffraction patterns due to the very low NP loading and significant peak broadening coming from diffraction domains in the nano regime (see Figure S1).

Nanoparticle allocation. The size, distribution and location of Pt nanoparticles were investigated by scanning transmission electron microscopy (STEM). The presence of Pt could be detected in samples **B1-3** by annular dark-field (ADF) STEM. Due to the difference in electron density between Pt nanoparticles and MOF, the Pt nanoparticles could be localized by contrast differences (black background vs. grey to white Zn vs. bright white Pt). In all three samples we detected ca. 1-3 nm large Pt nanoparticles with a rather homogenous particle distribution across MOF crystals and limited aggregation. To validate the presence of the Pt nanoparticles and study their distribution, elemental mapping based on energy dispersive X-ray spectroscopy (EDS) was carried out. Both results are shown in Figure 3a and section S7. The recorded elemental distribution revealed high, evenly distributed concentration of Pt on top of the crystals which is pronounced by the heavy degradation of the underlying MOF structure in the electron beam. This indicates NPs are predominantly attached to the surface of the MOF. PXRD and physisorption results confirm this degradation is taking place during STEM, not prior. Electron tomography (ET) which would access more depth-resolution was experimentally unamenable due to the heavy sample degradation. Distribution and location of the SiO_2 nanoparticles of composite **B4** were investigated using energy-filtered scanning transmission electron microscopy (EFSTEM). The preformed nanoparticles are notably bigger than the Pt NPs and therefore well distinguishable (see Figure 3b). The size-ratio of MOF crystals to SiO_2 nanoparticles practically excludes the option of

nanoparticle incorporation and accordingly we only observe surface-attached NPs in **B4**. All STEM micrographs show samples after extensive washing and activation and we therefore conclude, that both types of NPs are properly attached to their MOF supports. Nevertheless, the smaller Pt NPs are more homogeneously distributed across MOF crystals while SiO_2 NPs seemingly aggregate easier and at crystal edges. We further note that changes in NP concentration do not notably affect MOF particle size which otherwise could have an impact on MOF flexibility.[50]
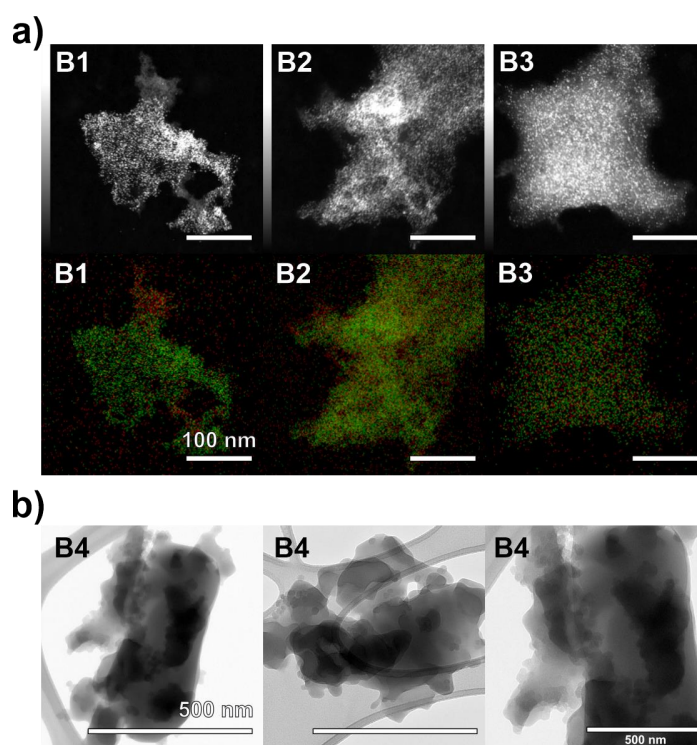
Figure 3. a) **B1-3** with Pt NPs. ADF-STEM images (top row) with heavier elements depicted in brighter white show Pt visible as bright dots distributed across the sample. EDS-STEM image overlays (bottom row; red, Zn; green, Pt; contrast adjusted for visibility) of the same crystals show Pt predominantly on top. All samples show heavy electron beam related degradation. Scale bars are 100 nm. b) **B4** with SiO_2 NPs. EFTEM images show spherical NPs on MOF crystals. The background structure shows the copper grid. Scale bars are 500 nm. See S7 for more details.

Guest-induced switchability. $Zn_2(BME-bdc)_2dabco$ is known to exhibit a reversible, CO_2 adsorption induced phase transition from the **np** to the **lp** phase.[43] Physisorption experiments
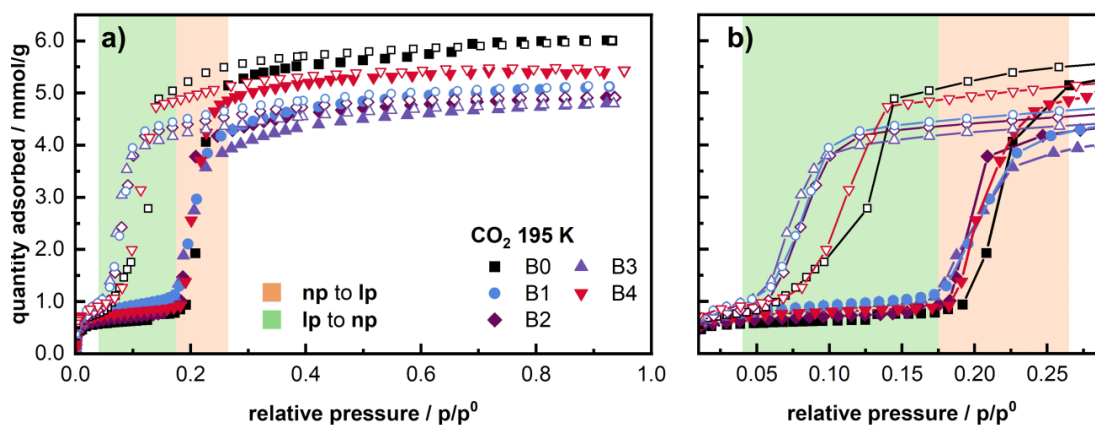
Figure 4. a) CO_2 physisorption isotherms of **B0-4**. Steps in the isotherms correspond to framework opening during adsorption (**np** to **lp**, light orange) and closing during desorption (**lp** to **np**, green). b) Highlighted pressure range of the phase transitions. Adsorption and desorption depicted in full and open symbols, respectively; lines in b) as visual aid only.

reveal that this behavior is fully retained in all NP@MOF (**B1-4**) composites as can be evidenced by their stepped CO_2 physisorption isotherms, see Figure 4a. All materials are non-porous towards nitrogen (see Figure S2).

Composites **B1**, **B2**, and **B3** show a Pt content dependent linear decrease of total absolute uptake of 15 - 25 % when compared to the reference material **B0**. A small part of the uptake reduction can be attributed to the fact that the NPs increase the composite's mass without contributing porosity, therefore decreasing the uptake to mass ratio. In light of the very low mass percentage of the Pt NPs, most of the capacity decrease is likely a result of NP-induced porosity changes to the underlying MOF material. The phase transition pressure for framework opening and closing (see Figure 4b) are shifted to lower pressures in **B1-3** compared to **B0**. This can be rationalized by the fact that Pt NPs are attached to the MOF particles during their initial crystallization in **lp** phase and therefore stabilize this conformation of their support. The slightly bigger shift of the **lp-np** transition during desorption *vs.* the **np-lp** transition during adsorption might be related to a proportional effect of the NPs on the already present hysteresis. The transition pressure ranges for opening and closing do – qualitatively observed – not increase, which supports aforementioned observation on the homogeneity of Pt NP distribution as this suggests consistent effects of the

nanoparticle throughout the composite powder. The bigger, surface-mounted SiO_2 nanoparticles in **B4** also lead to a minor total uptake decrease and shift of both phase transitions during adsorption and desorption to slightly lower pressures. However, the SiO_2 NPs exert a less rigidifying and pore-blocking effect on the MOF support than the Pt NPs, which we correlate to the intuitive factors of NP size and absolute amount: a higher number of smaller NPs exhibits more strain on the support than a lower number of bigger NPs. This is similar to observations made when anchoring flexible MOF thin films on surfaces: it was found that with decreased thickness and therefore higher ratio of anchored external surface area (which would herein translate to higher NP coverage) adsorbate-induced flexibility was reduced.[51] After desorption, framework integrity and completed **np** phase transition of all materials was confirmed by PXRD (see Figure 2).

Overall, porous and guest-switchable NP@MOF composites with low loadings of small Pt NPs and bigger SiO_2 NPs can be realized. The change in bulk material property directed by surface-mounted NPs is conceptually similar to surface-defect altered flexibility in MOFs.[52,53] This can be rationalized especially in light of a recent study by Thompson et al.[50] Therein, they investigate the particle size-dependent flexibility of DUT-8 (Zn_2ndc_2dabco, ndc^{2-} = 2,6-naphthalene dicarboxylate, Dresden University of Technology) but conclude, that in fact not directly particle size but concentration and amount of surface defects and related nucleation barriers (of the phase transition) govern material flexibility. If in herein studied NP@flexMOF composites NPs are seen as such defects, it is reasonable to assume their absolute amount is as or more influential than their size and this is the main reason for differences between sample **B1-3** and **B4**.

Thermal responsiveness. $Zn_2(BME-bdc)_2dabco$ is known to exhibit a reversible, temperature-triggered **np** to **lp** phase transition during heating.[27] We herein assess the impact of Pt or SiO_2 nanoparticle loading and presence on these temperature induced framework changes. All composites were first analyzed by thermogravimetric analysis coupled with differential scanning calorimetry (TGA-DSC). TGA under inert gas flow shows a ca. 50°C earlier decomposition of all Pt containing composites compared to **B0**, whereas **B4** is thermally as stable as the pure MOF. DSC shows that all materials with nanoparticles exhibit phase transitions at 210 °C (**B1-3**) or 215 °C (**B4**) which is 10 °C and 5 °C earlier than observed and known for **B0** (see Figure S3). This qualitatively indicates that neither nanoparticle type does prevent the **np** to **lp** transition, however, Pt might have bigger impact on the high-temperature behavior. In order to investigate detailed
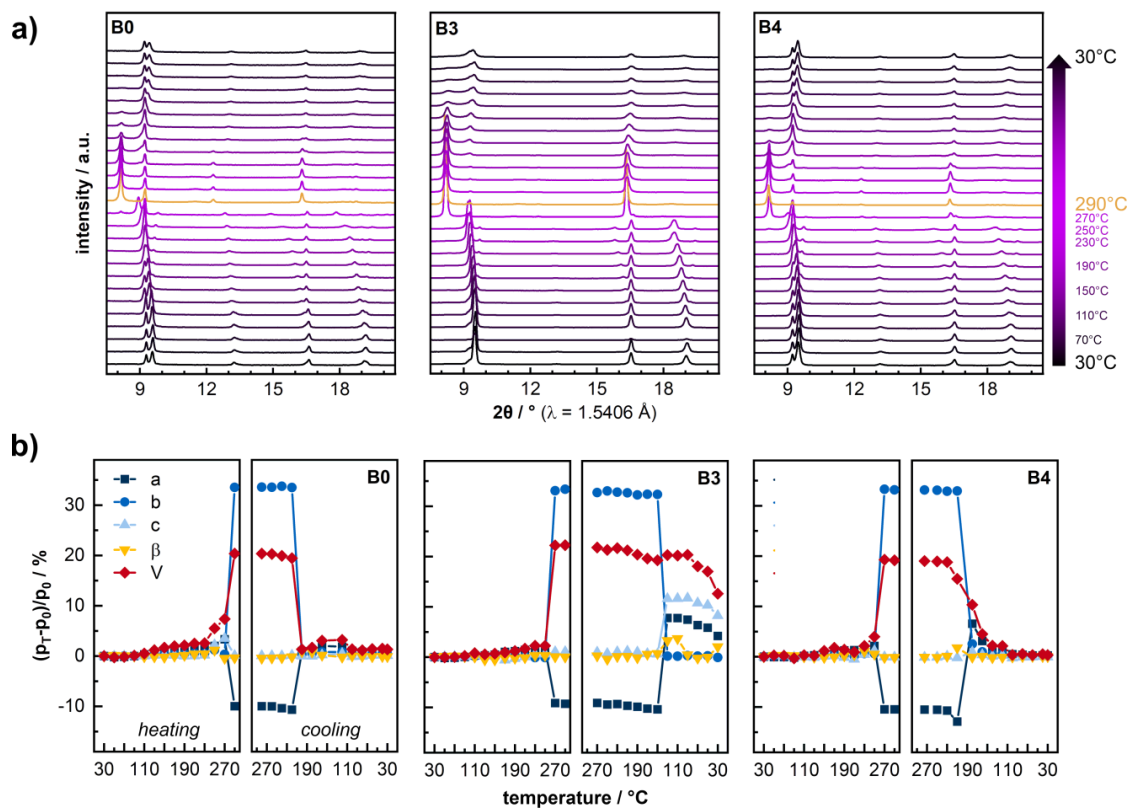
Figure 5. a) VTPXRD pattern series comparing the reference material (**B0**, left), the composite with the highest Pt nanoparticle loading (**B3**, middle), and the SiO$_2$@MOF composite (**B4**, right) in the range of 2θ = 7.5-20.5°. Pattern at highest temperature highlighted in orange. For **B1** and **B2** see Figure S4. b) Corresponding unit cell parameter changes as calculated from Le Bail profile fits and relative to the unit cell at 30 °C before heating. Graphs split into heating (left half) and cooling (right half).

structural changes and reversibility of this transition, variable temperature powder X-ray diffraction (VTPXRD) was conducted for all composites. Samples were subjected to a heating and cooling cycle from 30 to 290 °C and back to 30 °C with diffraction patterns collected every 20 °C. The results are depicted in Figure 5a and Figure S4. Unit cell parameters derived from performed Le Bail profile fits congruently visualize our findings, see Figure 5b and section S6.

Directly observable is the known behavior of **B0**: a phase transition from its **np** phase to its **lp** phase at 290 °C during heating and a slightly delayed closing during cooling at 220 °C. The differences in absolute temperature of this transition when compared to TGA-DSC data and literature reports[27] is attributed to the different experimental conditions (inert atmosphere vs. in

air). **B1-4** show, as seen in DSC, a slightly earlier framework opening during heating observable by the higher intensity of the 110 reflection of the **lp** phase at 8.0-8.4° 2θ in patterns from 270 °C compared to **B0**. This **np-lp** transition occurs in all composites, irrespective of NP type or loading. The correlated anisotropic unit cell parameter changes (increase of b, decrease of a, and no change in c and β) correspond to the wine-rack opening motion which changes the **np** lozenge-lattice to the **lp** square-lattice (see Figure 1). The closing **lp-np** transition during cooling is delayed for all NP@MOF composites. **B4** transitions back to its **np** phase at ca. 210 °C, 10 °C after **B0**, Pt@MOF materials largely revert to their **lp** phase at 190 °C (**B1**), 170 °C (**B2**), and 150 °C (**B3**).

The broadened hysteresis indicates, in similar fashion to the physisorption changes, that the surface-attached NPs stabilize the **lp** form of the MOF once it is in this phase, and that this effect is slightly stronger for Pt than SiO_2. However, a key difference between the composites with SiO_2 and Pt NPs is the fully reversible closing transition in **B4** and the only partially reversible and by decrease of long-range order accompanied closing transition in **B1-3**. Raw patterns of **B3** show a residual 110 reflection of the **lp** phase down to 70 °C and significant overall intensity loss during cooling. We qualitatively interpret this as in parallel occurring **lp-np** and **lp**-amorphous transitions. Unit cell parameters in this temperature range show drastic incoherencies because of this and resulting lower quality Le Bail profile fits which only account for the respective majority phase of the sample. Nevertheless, this highlights sample degradation accordingly. Furthermore, the loss of long-range order is less present with lower Pt content of the composites (see Figure S4). This behavior during framework closing stands in stark contrast to the fully reversible CO_2-induced phase transition of these Pt@MOF composites and specifically suggests a combined influence of the platinum nanoparticles and high temperatures on MOF switchability. To test if Pt NPs could be oxidized under measurement conditions (in air) and then react with the MOF support to facilitate its degradation X-ray photoelectron spectroscopy (XPS) was conducted on a **B3** sample prior and after VTPXRD experiments. Results confirm identical oxidation state of the Pt at both states with only minor spectra differences which can be attributed to the structural framework degradation. In particular, the intensity of Pt 4f core level of **B3** rise after the VTPXRD experiment while the overall spectrum shape remains unchanged (see Figure S8). This behavior can be explained by migration of Pt NPs to the surface during the VTPXRD experiment, confirmed by the fact that the intensity and the profile of the 2p of Zn are unaltered. This points at nanoparticle (surface defect) size and amount, and the resulting difference in exerted strain on the MOF similar

to the discussed findings in guest-induced switching, as responsible factor for the high temperature behavior instead of chemical reactivity of the Pt NPs.

CONCLUSION

In conclusion, we successfully synthesized NP@MOF composites consisting of mesoscopic platinum or silicon dioxide nanoparticles surface-attached to the flexible MOF $Zn_2(BME-bdc)_2dabco$ and showed that they exhibit stimulus-responsive switchability. The materials were made via *in situ* generation of Pt nanoparticles in the size regime < 3 nm from platinum precursors during to the solvothermal MOF crystallization, or addition of pre-formed SiO_2 nanoparticles of around 30 nm in aqueous suspension to the MOF synthesis procedure. We compared CO_2-adsorption induced and thermally induced switchability of an isoreticular series of three Pt@MOF composites (1, 2, and 3 wt.% Pt) and one SiO_2@MOF composite to the pure, flexible MOF. Physisorption experiments show that CO_2-switchability is retained and fully reversible for all composites irrespective of NP type or amount. Loadings of 1-3 wt.% of small Pt NPs keep 85-75 % of the underlying MOF porosity accessible while slightly stabilizing the **lp** phase evidenced by a shift of the transition pressure hysteresis range. The SiO_2@MOF composite retains 90 % of MOF porosity due to the bigger NP size, suggesting yet higher loadings of bigger nanoparticles are feasible in guest-switchable composites without compromising MOF performance. Variable-temperature PXRDs show that thermally induced flexibility is initially retained in all composites. An increased temperature delay between framework opening and closing phase transitions indicate a similar **lp** stabilization in dependence of the NPs as observed for guest-induced switching. However, small, numerous attached Pt NPs drastically influence the thermally induced closing transition. All Pt@MOF composites fully transition to their **lp** phase during heating and revert during cooling, but the latter is accompanied by decreased signal intensity which we attribute to a compromised long-range order. This is increased with higher Pt loadings. In contrast, fewer, bigger NPs in the SiO_2@MOF composite displays reversible switching with fully retained framework crystallinity. We primarily connect this to the absolute NP amount attached to the surface which is higher for smaller NPs at comparable loading and therefore results in higher strain exerted onto the MOF support in addition to the thermal stress at higher temperatures.

Fundamentally, it is highly encouraging to see that low loadings of surface-mounted nanoparticles do not necessarily compromise flexibility (and porosity) of MOFs. Nanoparticle type, size and loading do affect the strain exerted on the MOF, as we indirectly observed in physisorption and VTPXRD experiments, but moreover the type of stimulus (or strain) used to switch the framework state plays an equally important role. The apparent common ground is the

stabilization of the **lp** phase by NPs which could be of more general use for widening the pressure or temperature windows open/large pore phases of flexible MOFs are favored in, as well as changing the point of framework opening to lower pressures or temperatures. Within this focused study we aimed to probe for and highlight this correlation, and we envision future studies expanding on both sets of nanoparticle-related and stimuli-specific contributions to switchability behavior. Understanding this will stepwise allow the transfer and combination of the extensive knowledge on flexible MOFs and NP@MOF composites for potentially both design versatility of each material class and new hybrid materials.

ASSOCIATED CONTENT

Supporting Information. Synthesis procedures; ^{1}H NMR spectra information; elemental analysis; TGA-DSC; PXRD data; N_2 and CO_2 physisorption isotherms; VTPXRD data; Le Bail profile fit data; electron microscopy micrographs; XPS data and further information.

The following files are available free of charge.

Adsorption information files (ZIP)

AUTHOR INFORMATION

Corresponding Authors

E-mail: valentina.colombo@unimi.it, gregor.kieslich@tum.de

Author Contributions

J.B. performed Pt@MOF material synthesis, analysis, data processing, and manuscript writing. S.T. performed SiO$_2$@MOF material synthesis, analysis, data processing, and Le Bail profile fitting. H.B. performed electron microscopy and its visualization. M.M. performed energy-filtered electron microscopy and its visualization. L.B. performed XPS experiments and data processing. V.C. provided the motivation of this work. G.K. provided the motivation of this work and contributed to data processing. R.A.F. provided the motivation of this work. All authors contributed to manuscript writing and have given approval to the final version of the manuscript.

Notes

The authors declare no competing financial interests.

REFERENCES

 (1) Freund, R.; Canossa, S.; Cohen, S. M.; Yan, W.; Deng, H.; Guillerm, V.; Eddaoudi, M.; Madden, D. G.; Fairen-Jimenez, D.;Lyu, H. *et al.* 25 Years of Reticular Chemistry. *Angew. Chem., Int. Ed.* **2021**, *60*, 23946–23974.
 (2) Bigdeli, F.; Lollar, C. T.; Morsali, A.;Zhou, H.-C. Switching in Metal-Organic Frameworks. *Angew. Chem., Int. Ed.* **2020**, *59*, 4652–4669.
 (3) Nagarkar, S. S.; Desai, A. V.;Ghosh, S. K. Stimulus-responsive metal-organic frameworks. *Chem. Asian J.* **2014**, *9*, 2358–2376.
 (4) Seth, S.;Jhulki, S. Porous flexible frameworks: origins of flexibility and applications. *Mater. Horiz.* **2021**, *8*, 700–727.
 (5) Schneemann, A.; Bon, V.; Schwedler, I.; Senkovska, I.; Kaskel, S.;Fischer, R. A. Flexible metal-organic frameworks. *Chem. Soc. Rev.* **2014**, *43*, 6062–6096.
 (6) Li, Y.; Wang, Y.; Fan, W.;Sun, D. Flexible metal-organic frameworks for gas storage and separation. *Dalton Trans.* **2022**.
 (7) Bonneau, M.; Lavenn, C.; Zheng, J.-J.; Legrand, A.; Ogawa, T.; Sugimoto, K.; Coudert, F.-X.; Reau, R.; Sakaki, S.;Otake, K.-I. *et al.* Tunable acetylene sorption by flexible catenated metal-organic frameworks. *Nat. Chem.* **2022**.
 (8) Zhai, Z.; Zhang, X.; Hao, X.; Niu, B.;Li, C. Metal–Organic Frameworks Materials for Capacitive Gas Sensors. *Adv. Mater. Technol.* **2021**, *6*, 2100127.
 (9) Zhang, L.-T.; Zhou, Y.;Han, S.-T. The Role of Metal-Organic Frameworks in Electronic Sensors. *Angew. Chem., Int. Ed.* **2021**, *60*, 15192–15212.
 (10) Osterrieth, J. W. M.;Fairen-Jimenez, D. Metal-Organic Framework Composites for Theragnostics and Drug Delivery Applications. *Biotechnol. J.* **2021**, *16*, e2000005.
 (11) Zhou, Y.; Yang, T.; Liang, K.;Chandrawati, R. Metal-organic frameworks for therapeutic gas delivery. *Adv. Drug. Deliv. Rev.* **2021**, *171*, 199–214.
 (12) Zhou, X.; Miao, Y.-R.; Shaw, W. L.; Suslick, K. S.;Dlott, D. D. Shock Wave Energy Absorption in Metal-Organic Framework. *J. Am. Chem. Soc.* **2019**, *141*, 2220–2223.
 (13) Beurroies, I.; Boulhout, M.; Llewellyn, P. L.; Kuchta, B.; Férey, G.; Serre, C.;Denoyel, R. Using pressure to provoke the structural transition of metal-organic frameworks. *Angew. Chem., Int. Ed.* **2010**, *49*, 7526–7529.
 (14) Kondo, A.; Kojima, N.; Kajiro, H.; Noguchi, H.; Hattori, Y.; Okino, F.; Maeda, K.; Ohba, T.; Kaneko, K.;Kanoh, H. Gas Adsorption Mechanism and Kinetics of an Elastic Layer-Structured Metal–Organic Framework. *J. Phys. Chem. C* **2012**, *116*, 4157–4162.
 (15) Loiseau, T.; Serre, C.; Huguenard, C.; Fink, G.; Taulelle, F.; Henry, M.; Bataille, T.;Férey, G. A rationale for the large breathing of the porous aluminum terephthalate (MIL-53) upon hydration. *Chemistry* **2004**, *10*, 1373–1382.
 (16) Park, H. J.;Suh, M. P. Stepwise and hysteretic sorption of N(2), O(2), CO(2), and H(2) gases in a porous metal-organic framework Zn(2)(BPnDC)(2)(bpy). *Chem. Commun.* **2010**, *46*, 610–612.
 (17) Klein, N.; Hoffmann, H. C.; Cadiau, A.; Getzschmann, J.; Lohe, M. R.; Paasch, S.; Heydenreich, T.; Adil, K.; Senkovska, I.;Brunner, E. *et al.* Structural flexibility and intrinsic dynamics in the M2(2,6-ndc)2(dabco) (M = Ni, Cu, Co, Zn) metal–organic frameworks. *J. Mater. Chem.* **2012**, *22*, 10303.

(18) Henke, S.; Schmid, R.; Grunwaldt, J.-D.;Fischer, R. A. Flexibility and sorption selectivity in rigid metal-organic frameworks: the impact of ether-functionalised linkers. *Chemistry* **2010**, *16*, 14296–14306.

(19) Hiraide, S.; Sakanaka, Y.; Kajiro, H.; Kawaguchi, S.; Miyahara, M. T.;Tanaka, H. High-throughput gas separation by flexible metal-organic frameworks with fast gating and thermal management capabilities. *Nat. Commun.* **2020**, *11*, 3867.

(20) Dong, Q.; Zhang, X.; Liu, S.; Lin, R.-B.; Guo, Y.; Ma, Y.; Yonezu, A.; Krishna, R.; Liu, G.;Duan, J. *et al.* Tuning Gate-Opening of a Flexible Metal-Organic Framework for Ternary Gas Sieving Separation. *Angew. Chem.* **2020**, *59*, 22756–22762.

(21) He, A.; Jiang, Z.; Wu, Y.; Hussain, H.; Rawle, J.; Briggs, M. E.; Little, M. A.; Livingston, A. G.;Cooper, A. I. A smart and responsive crystalline porous organic cage membrane with switchable pore apertures for graded molecular sieving. *Nat. Mater.* **2022**.

(22) Kim, J. Y.; Park, J.; Ha, J.; Jung, M.; Wallacher, D.; Franz, A.; Balderas-Xicohténcatl, R.; Hirscher, M.; Kang, S. G.;Park, J. T. *et al.* Specific Isotope-Responsive Breathing Transition in Flexible Metal-Organic Frameworks. *J. Am. Chem. Soc.* **2020**, *142*, 13278–13282.

(23) Carrington, E. J.; McAnally, C. A.; Fletcher, A. J.; Thompson, S. P.; Warren, M.;Brammer, L. Solvent-switchable continuous-breathing behaviour in a diamondoid metal-organic framework and its influence on CO2 versus CH4 selectivity. *Nat. Chem.* **2017**, *9*, 882–889.

(24) Knebel, A.; Geppert, B.; Volgmann, K.; Kolokolov, D. I.; Stepanov, A. G.; Twiefel, J.; Heitjans, P.; Volkmer, D.;Caro, J. Defibrillation of soft porous metal-organic frameworks with electric fields. *Science (New York, N.Y.)* **2017**, *358*, 347–351.

(25) Ghoufi, A.; Benhamed, K.; Boukli-Hacene, L.;Maurin, G. Electrically Induced Breathing of the MIL-53(Cr) Metal-Organic Framework. *ACS Cent. Sci.* **2017**, *3*, 394–398.

(26) Vervoorts, P.; Keupp, J.; Schneemann, A.; Hobday, C. L.; Daisenberger, D.; Fischer, R. A.; Schmid, R.;Kieslich, G. Configurational Entropy Driven High-Pressure Behaviour of a Flexible Metal-Organic Framework (MOF). *Angew. Chem.* **2021**, *60*, 787–793.

(27) Henke, S.; Schneemann, A.;Fischer, R. A. Massive Anisotropic Thermal Expansion and Thermo-Responsive Breathing in Metal-Organic Frameworks Modulated by Linker Functionalization. *Adv. Funct. Mater.* **2013**, *23*, 5990–5996.

(28) Wieme, J.; Lejaeghere, K.; Kresse, G.;van Speybroeck, V. Tuning the balance between dispersion and entropy to design temperature-responsive flexible metal-organic frameworks. *Nat. Commun.* **2018**, *9*, 4899.

(29) van Heerden, D. P.; Smith, V. J.; Aggarwal, H.;Barbour, L. J. High Pressure In Situ Single-Crystal X-Ray Diffraction Reveals Turnstile Linker Rotation Upon Room-Temperature Stepped Uptake of Alkanes. *Angew. Chem., Int. Ed.* **2021**, *60*, 13430–13435.

(30) Chanut, N.; Ghoufi, A.; Coulet, M.-V.; Bourrelly, S.; Kuchta, B.; Maurin, G.;Llewellyn, P. L. Tailoring the separation properties of flexible metal-organic frameworks using mechanical pressure. *Nat. Commun.* **2020**, *11*, 1216.

(31) Krause, S.; Evans, J. D.; Bon, V.; Crespi, S.; Danowski, W.; Browne, W. R.; Ehrling, S.; Walenszus, F.; Wallacher, D.;Grimm, N. *et al.* Cooperative light-induced breathing of soft porous crystals via azobenzene buckling. *Nat. Commun.* **2022**, *13*, 1951.

(32) Liu, C.; Jiang, Y.; Zhou, C.; Caro, J.;Huang, A. Photo-switchable smart metal–organic framework membranes with tunable and enhanced molecular sieving performance. *J. Mater. Chem. A* **2018**, *6*, 24949–24955.

(33) Qin, P.; Okur, S.; Li, C.; Chandresh, A.; Mutruc, D.; Hecht, S.;Heinke, L. A photoprogrammable electronic nose with switchable selectivity for VOCs using MOF films. *Chem. Sci.* **2021**, *12*, 15700–15709.

(34) Gao, C.; Li, J.; Yin, S.; Sun, J.;Wang, C. Redox-triggered switching in three-dimensional covalent organic frameworks. *Nat. Commun.* **2020**, *11*, 4919.

(35) Carvalho, J. G. M. de; Fischer, R. A.;Pöthig, A. Molecular Oxygen Activation by Redox-Switchable Anthraquinone-Based Metal-Organic Frameworks. *Inorg. Chem.* **2021**, *60*, 4676–4682.

(36) Kulachenkov, N.; Haar, Q.; Shipilovskikh, S.; Yankin, A.; Pierson, J.-F.; Nominé, A.;Milichko, V. A. MOF-Based Sustainable Memory Devices. *Adv. Funct. Mater.* **2021**, 2107949.

(37) Yao, Z.-Q.; Wang, K.; Liu, R.; Yuan, Y.-J.; Pang, J.-J.; Li, Q. W.; Shao, T. Y.; Li, Z. G.; Feng, R.;Zou, B. *et al.* Dynamic Full-Color Tuning of Organic Chromophore in a Multi-Stimuli-Responsive 2D Flexible MOF. *Angew. Chem., Int. Ed.* **2022**, *61*, e202202073.

(38) Serra-Crespo, P.; van der Veen, M. A.; Gobechiya, E.; Houthoofd, K.; Filinchuk, Y.; Kirschhock, C. E. A.; Martens, J. A.; Sels, B. F.; Vos, D. E. de;Kapteijn, F. *et al.* NH2-MIL-53(Al): a high-contrast reversible solid-state nonlinear optical switch. *J. Am. Chem. Soc.* **2012**, *134*, 8314–8317.

(39) Tom, L.;Kurup, M. R. P. A stimuli responsive multifunctional ZMOF based on an unorthodox polytopic ligand: reversible thermochromism and anion triggered metallogelation. *Dalton Trans.* **2019**, *48*, 16604–16614.

(40) Freund, P.; Senkovska, I.;Kaskel, S. Switchable Conductive MOF-Nanocarbon Composite Coatings as Threshold Sensing Architectures. *ACS Appl. Mater. Interfaces* **2017**, *9*, 43782–43789.

(41) Chen, L.; Zhan, W.; Fang, H.; Cao, Z.; Yuan, C.; Xie, Z.; Kuang, Q.;Zheng, L. Selective Catalytic Performances of Noble Metal Nanoparticle@MOF Composites: The Concomitant Effect of Aperture Size and Structural Flexibility of MOF Matrices. *Chemistry* **2017**, *23*, 11397–11403.

(42) Berger, J.; Dönmez, A.-S.; Ullrich, A.; Bunzen, H.; Fischer, R. A.;Kieslich, G. Reduced thermal expansion by surface-mounted nanoparticles in a pillared-layered metal-organic framework. *Commun. Chem.* **2022**, *5*.

(43) Henke, S.; Schneemann, A.; Wütscher, A.;Fischer, R. A. Directing the breathing behavior of pillared-layered metal-organic frameworks via a systematic library of functionalized linkers bearing flexible substituents. *J. Am. Chem. Soc.* **2012**, *134*, 9464–9474.

(44) Liu, H.; Chang, L.; Chen, L.;Li, Y. In situ one-step synthesis of metal–organic framework encapsulated naked Pt nanoparticles without additional reductants. *J. Mater. Chem. A* **2015**, *3*, 8028–8033.

(45) Evans, J. D.; Bon, V.; Senkovska, I.;Kaskel, S. A Universal Standard Archive File for Adsorption Data. *Langmuir* **2021**, *37*, 4222–4226.

(46) Vinai, G.; Motti, F.; Petrov, A. Y.; Polewczyk, V.; Bonanni, V.; Edla, R.; Gobaut, B.; Fujii, J.; Suran, F.;Benedetti, D. *et al.* An integrated ultra-high vacuum apparatus for growth and in situ characterization of complex materials. *Rev. Sci. Instrum.* **2020**, *91*, 85109.

(47) Pastoriza-Santos, I.;Liz-Marzán, L. M. N , N -Dimethylformamide as a Reaction Medium for Metal Nanoparticle Synthesis. *Adv. Funct. Mater.* **2009**, *19*, 679–688.

(48) Dai, S.; Ngoc, K. P.; Grimaud, L.; Zhang, S.; Tissot, A.;Serre, C. Impact of capping agent removal from Au NPs@MOF core–shell nanoparticle heterogeneous catalysts. *J. Mater. Chem. A* **2022**, *10*, 3201–3205.

(49) Li, B.; Ma, J.-G.;Cheng, P. Integration of Metal Nanoparticles into Metal-Organic Frameworks for Composite Catalysts: Design and Synthetic Strategy. *Small* **2019**, *15*, e1804849.

(50) Thompson, M. J.; Hobday, C. L.; Senkovska, I.; Bon, V.; Ehrling, S.; Maliuta, M.; Kaskel, S.;Düren, T. Role of particle size and surface functionalisation on the flexibility behaviour of switchable metal–organic framework DUT-8(Ni). *J. Mater. Chem. A* **2020**, *8*, 22703–22711.

(51) Wannapaiboon, S.; Schneemann, A.; Hante, I.; Tu, M.; Epp, K.; Semrau, A. L.; Sternemann, C.; Paulus, M.; Baxter, S. J.;Kieslich, G. *et al.* Control of structural flexibility of layered-pillared metal-organic frameworks anchored at surfaces. *Nat. Commun.* **2019**, *10*, 346.

(52) Bennett, T. D.; Cheetham, A. K.; Fuchs, A. H.;Coudert, F.-X. Interplay between defects, disorder and flexibility in metal-organic frameworks. *Nat. Chem.* **2016**, *9*, 11–16.

(53) Krause, S.; Reuter, F. S.; Ehrling, S.; Bon, V.; Senkovska, I.; Kaskel, S.;Brunner, E. Impact of Defects and Crystal Size on Negative Gas Adsorption in DUT-49 Analyzed by In Situ129Xe NMR Spectroscopy. *Chem. Mater.* **2020**, *32*, 4641–4650.

4.4 STUDY IV. Solvent-Dependent Switching of a Flexible Pillared-Layered MOF

This study consists of the first experimental and methodological milestones towards elaborating the solvent-switchability of the $Zn_2(fu-bdc)_2dabco$ family. A series of five different derivatives with different linker functionalizations, selected by virtue of their known reversible CO_2-induced switchability, is investigated by PXRD during qualitative resolution experiments.

Presently, solvent-induced switching or sorption selectivity towards solvents (meaning at ambient conditions; instead of gases) is mostly studied if explicit applications are in mind, i.e. xylene isomer separation or trace impurity removal,[102,124,191,192] or if gas physisorption is not sufficient, i.e. for some MOF thin-film characterization if techniques like krypton sorption are unavailable.[201] Fundamental investigation on switchability are less common, however, have been conducted on some individual MOFs.[193,194] Findings on DUT-8(Ni)[195–197] motivated this conceptually closely related study on $Zn_2(fu-bdc)_2dabco$. The experimental methodology was purposefully chosen to be as simple as possible to allow screening of various material-solvent combinations with manageable effort.* Activated MOF was deposited on a silicon wafer sample holder then a drop of the respective solvent was added on top followed by a PXRD measurement scanning the range with the material's main reflection signals indicating activated closed np or in response to the solvent opened lp state within two minutes.
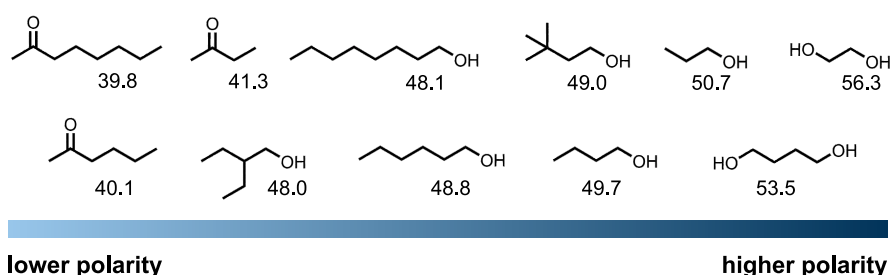
Figure 13. Solvent molecules in ascending polarity from left to right. Numbers correspond to empirical solvent parameters $E_T(30)$ in unit kcal/mol as introduced and determined by Reichardt et al.[202]

The choice of solvents was adapted to account for the fact this is conducted at ambient conditions in air: this series tests alcohols and ketones which are liquid at room temperature and show suitable volatility to not evaporate before a diffraction pattern could be collected. The selection includes variations in polarity, polar moiety count, and sterics (alkyl chain length and branching) as visualized in figure 13. Early testing showed that $5\,\mu l$ of liquid, deposited with a precision pipette, contains sufficient volume to wet the MOF powder and also suppresses excessive measurement

---

* At this point again acknowledgment of Nadine Schmaus who conducted the experiments during her research internship with me.

background which does arise from X-ray scattering if too much solvent is added. Measurement time was found to have some, but limited effect because peak shifts correlated to the phase transition in response to the solvent occur early in the pattern – a speed of 5–10° per minute (and a total range from 5–30° 2Theta) was adequate.
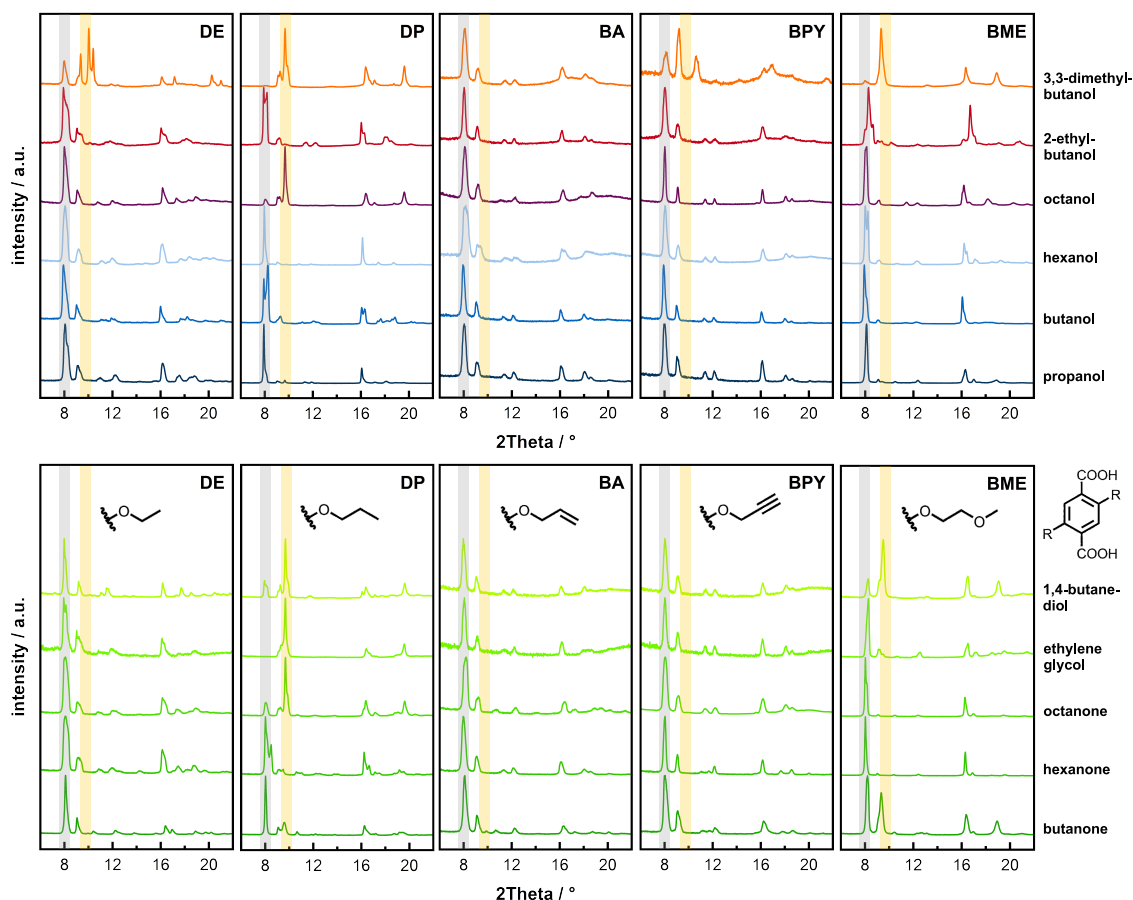
Figure 14. PXRD patterns in range of 5–30° 2Theta of $Zn_2(fu-bdc)_2dabco$ derivatives **DE**, **DP**, **BA**, **BPY**, and **BME** resolvated with respective solvents. Structural formula of bdc-functionalizations shown as insets in bottom row, solvent legend depicted on right axis. Top row shows linear and branched alcohols, bottom row show ketones and diols. Main peaks identifying phases highlighted by orange background for np phase and grey background for lp phase.

Results of the experiments are summarized in figure 14. Immediately discernible is that most combinations of solvent and MOF result in full opening of the frameworks. In few cases main peaks for both np and lp can be observed, indicating that responsive switching is triggered but not completed due to kinetics. Most likely is a limit in liquid diffusion through the deposited powder leading to a mixture of solvent-covered and solvent-free MOF being measured. These two cases, full and partial phase transition, are found to cover all findings of derivatives **DE**, **BA**, **BPY**, and **BME**. 1,4-butanediol (in **BME**) and 3,3-dimethylbutanol (in **BME**, **BPY**, and **DE**) lead to partial transitions. While all patterns of material **BA** show full phase transition and an impact of its functionalizations on this is evident, no trend in responsiveness change correlating to

the side chains can be extracted for any solvent tested. Similarly, changes in polarity or sterics within the selected range show no pronounced effects, with the general exception of the very bulky 3,3-dimethylbutanol and specifically the combination of **BME** and 1,4-butandiol showing the most dominant kinetic effects.

DP, however, features a curiously divers set of responses to the different solvents. First it is (as the only derivative in the series) partially closed for octanol and octanone and does not open when resolvated with 3,3-dimethylbutanol, indicating a stronger steric sensitivity. Investigating a derivative with longer, unpolar functionalization like **DB** (2,5-dibutoxy instead of 2,5-dipropoxy-bdc^{2-} linkers) was envisioned, however, this derivative did not show reproducible switchability during activation. Therefore correlation to side chain length is indicated, but requires further study. More so, because inclusion of a heteroatom apparently changes this hypothesized sterical factor more drastic than raw functionalization length as seen by virtue of **BME** transitioning to its lp phase for i.e. octanol and octanone. Second **DP** remains in its np state when resolvated with ethylene glycol, but (partially) opens with 1,4-butanediol despite the latter having lower polarity and higher steric demand. Structurally this might be linked to the MOF pore dimensions: 1,4-butanediol fits relatively well as adsorbate bridging two metal SBUs along a dabco pillar (not diagonally or along a bdc^{2-} linker). At this point however, this is purely hypothetical and the question remains why this is not observed for other functionalizations.

Overall, these qualitative findings need to be substantiated by further methods. Most pressingly particle sizes should be assessed as influential factors because of their known impact on mass transport and diffusivity in MOFs[203] and vapor physisorption isotherms should be measured (potentially with evaluation of transient data) to properly address the kinetic factor herein only described phenomenologically.

5

CONCLUSION AND OUTLOOK

Stimulus-responsiveness is the key feature utilizing the versatility of MOFs to its fullest and a very attractive property for perspective applications of MOFs as resource or energy efficient material alternatives for industrial processes. The current challenges that need to be overcome to bring this to fruition predominantly lie in two aspects: first, in light of the enormous parameter space for responsiveness design, underlying directing principles have to be identified. This provides guidance and focus to research and development efforts and improves target-driven efficiency. Second, the influence of practically relevant process(ing) and application conditions on responsive MOFs needs to be assessed thoroughly. This allows to close the gap between laboratory performance and application feasibility. This thesis includes four studies investigating different facets of these two aspects.

Two studies focus primarily on the underlying role of extensive linker functionalization: **STUDY I** elucidates principles for creating and directing adsorbate-responsiveness in rigid MOFs by investigating the model system $Zn_2(fu-bdc)_2bipy$. Adsorption site accessibility and pore environment polarizability were found to be key tunable parameters. There is significant potential to design adsorbate responsiveness for multiple separation challenges and apply the studied methodology and design principles to other, homogeneously functionalizable rigid MOF systems. **STUDY IV** looks at changes to (liquid) solvent-responsiveness of the flexible $Zn_2(fu-bdc)_2dabco$. It establishes a matrix correlating qualitative responsiveness, solvents, and functionalizations, as well as an experimental procedure for reproducible analysis for future work to build upon. The current "working horse" $Zn_2(DP-bdc)_2dabco$ shows very intriguing properties, but no clear functionalization- or solvent-correlated trends are discernible yet. Future quantitative studies will need to include vapor physisorption experiments and potentially transient data analysis to identify more intricate correlations.

The other two studies focus on the influence surface-mounted nanoparticles exhibit on stimulus-responsive MOFs. **STUDY II** addresses the question how the in application

relevant thermal expansion behavior changes as function of platinum nanoparticles in $Zn_2(DP-bdc)_2dabco$. It was not only found that it can be approximated by the NP-free material at low NP loadings and temperatures, but that TE properties are superior at higher temperatures and loadings. Specifically the negative fraction of the TE motion was inhibited most by NPs. If, hypothetically, their influence is more pronounced on NTE than PTE, this might open another parameter space for material fine-tuning given how prominent NTE is within MOFs. **STUDY III** investigates the same mechanical motion, but on larger scale in the adsorbate- and temperature-induced switching of $Zn_2(BME-bdc)_2dabco$ with attached Pt or SiO_2 NPs. We show that with both stimuli reversibly switchable NP@flexMOF composites can be realized and low loading of NPs does not compromise flexibility (and porosity) of MOFs. However, different reversibility between SiO_2 and Pt containing derivatives is observed when switching with temperature which we attribute to different nanoparticle sizes.

Each study finds incremental answers to the fundamental "How can we design MOFs with tailored responsiveness?" but in parallel raises new questions to be addressed in future work: Which other rigid MOFs would be suited to transfer the functionalization-directed responsiveness design to? Can solvent-switchability in $Zn_2(DP-bdc)_2dabco$ be kinetically controlled? How big is the impact of NP size vs. amount on MOF switchability and is there a to the type of stimulus correlatable rationale? Is the TE impact of NPs related to material topology and if yes, how so? Questions with such a diverse spread of topics can be stated because very intricate dependencies within materials are by now readily accessible to be studied; much has been achieved in fundamental (MOF) science. Nevertheless, in the nearer future these invaluable insights have to, and undoubtedly will,[204] be developed towards answering the complete overarching question: "How can we design MOFs with tailored responsiveness and bring them into application?"

6

BIBLIOGRAPHY

[1] R. Bogue, "Smart materials: a review of capabilities and applications.", *Assembly Automation* **2014**, *34*, 16–22.

[2] D. S. Sholl, R. P. Lively, "Seven chemical separations to change the world.", *Nature* **2016**, *532*, 435–437.

[3] U. Dessau, Umweltbundesamt. **2022**, https://www.umweltbundesamt.de/daten/energie/energieverbrauch-nach-energietraegern-sektoren#allgemeine-entwicklung-und-einflussfaktoren (visited on 11/22/2022).

[4] N. K. Kulachenkov, Q. Haar, S. Shipilovskikh, A. N. Yankin, J. F. Pierson, A. Nomine, V. A. Milichko, "MOF-Based Sustainable Memory Devices.", *Advanced Functional Materials* **2021**, *32*, 2107949.

[5] W. Xu, O. M. Yaghi, "Metal-Organic Frameworks for Water Harvesting from Air, Anywhere, Anytime.", *ACS Central Science* **2020**, *6*, 1348–1354.

[6] A. Thomas, "Much ado about nothing – a decade of porous materials research.", *Nature Communications* **2020**, *11*, 4985.

[7] L. N. McHugh, T. D. Bennett, "Introducing porosity into Metal-Organic Framework Glasses.", *Journal of Materials Chemistry A* **2022**, 19552–19559.

[8] C. L. Hobday, G. Kieslich, "Structural flexibility in crystalline coordination polymers: a journey along the underlying free energy landscape.", *Dalton transactions* **2021**, *50*, 3759–3768.

[9] S. M. Moosavi, A. Nandy, K. M. Jablonka, D. Ongari, J. P. Janet, P. G. Boyd, Y. Lee, B. Smit, H. J. Kulik, "Understanding the diversity of the metal-organic framework ecosystem.", *Nature Communications* **2020**, *11*, 4068.

[10] A. Li, R. Bueno-Perez, D. G. Madden, D. Fairen-jimenez, "From computational high-throughput screenings to the lab: taking metal-organic frameworks out of the computer.", *Chemical Science* **2022**, *13*, 7990–8002.

[11] W. A., "Beitrag zur Konstitution anorganischer Verbindungen.", *Zeitschrift für anorganische und allgemeine Chemie* **1895**, *8*, 153–188.

[12] F. C. Phillips, PhD thesis, Graduate School of Arts and Sciences, University of Pennsylvania, **1893**.

[13] R. Jira, "Acetaldehyde from Ethylene—A Retrospective on the Discovery of the Wacker Process.", *Angewandte Chemie Int. Ed.* **2009**, *48*, 9034–9037.

[14] K. A. Hofmann, F. Küspert, "Verbindungen von Kohlenwasserstoffen mit Metallsalzen.", *Zeitschrift für anorganische und allgemeine Chemie* **1897**, *15*, 204–207.

[15] H. J. Buser, D. Schwarzenbach, W. Petter, A. Ludi, "The crystal structure of Prussian Blue: Fe4[Fe(CN)6]3.xH2O.", *Inorganic Chemistry* **1977**, *16*, 2704–2710.

[16] J. H. Rayner, H. M. Powell, "Structure of molecular compounds. Part X. Crystal structure of the compound of benzene with an ammonia-nickel cyanide complex.", *Journal of The Chemical Society* **1952**, 319–328.

[17] A. K. Nangia, G. R. Desiraju, "Crystal Engineering: An Outlook for the Future.", *Angewandte Chemie Int. Ed.* **2019**, *58*, 4100–4107.

[18] B. F. Hoskins, R. Robson, "Infinite polymeric frameworks consisting of three dimensionally linked rod-like segments.", *Journal of the American Chemical Society* **1989**, *111*, 5962–5964.

[19] B. F. Hoskins, R. Robson, "Design and construction of a new class of scaffolding-like materials comprising infinite polymeric frameworks of 3D-linked molecular rods. A reappraisal of the zinc cyanide and cadmium cyanide structures and the synthesis and structure of the diamond-related frameworks.", *Journal of the American Chemical Society* **1990**, *112*, 1546–1554.

[20] O. M. Yaghi, H. Li, "Hydrothermal Synthesis of a Metal-Organic Framework Containing Large Rectangular Channels.", *Journal of the American Chemical Society* **1995**, *117*, 10401–10402.

[21] O. M. Yaghi, G. Li, H. Li, "Selective binding and removal of guests in a microporous metal-organic framework.", *Nature* **1995**, *378*, 703–706.

[22] S. S.-Y. Chui, S. M. F. Lo, J. P. H. Charmant, A. G. Orpen, I. D. Williams, "A chemically functionalizable nanoporous material (Cu3(TMA)2(H2O)3)n.", *Science* **1999**, *283*, 1148–1150.

[23] G. Férey, A. K. Cheetham, "Prospects for Giant Pores.", *Science* **1999**, *283*, 1125–1126.

[24] T. C. C. D. Centre, CSD MOF Collection. **2022**, https://www.ccdc.cam.ac.uk/Community/csd-community/csd-mof-collection/ (visited on 10/11/2022).

[25] A. Schneemann, V. Bon, I. Schwedler, I. Senkovska, S. Kaskel, R. A. Fischer, "Flexible metal-organic frameworks.", *Chemical Society Reviews* **2014**, *43*, 6062–96.

[26] F. Bigdeli, C. T. Lollar, A. Morsali, H.-C. Zhou, "Switching in Metal-Organic Frameworks.", *Angewandte Chemie Int. Ed.* **2020**, *59*, 4652–4669.

[27] L. Sun, M. G. Campbell, M. Dinca, "Electrically Conductive Porous Metal-Organic Frameworks.", *Angewandte Chemie Int. Ed.* **2016**, *55*, 3566–79.

[28]   J. Fonseca, T. Gong, L. Jiao, H.-L. Jiang, "Metal-organic frameworks (MOFs) beyond crystallinity: amorphous MOFs, MOF liquids and MOF glasses.", *Journal of Materials Chemistry A* **2021**, *9*, 10562–10611.

[29]   A. V. Bavykina, N. Kolobov, I. S. Khan, J. A. Bau, A. Ramírez, J. Gascón, "Metal-Organic Frameworks in Heterogeneous Catalysis: Recent Progress, New Trends, and Future Perspectives.", *Chemical Reviews* **2020**, 8468–8535.

[30]   P. Mialane, C. Mellot-Draznieks, P. Gairola, M. Duguet, Y. Benseghir, O. Oms, A. Dolbecq, "Heterogenisation of polyoxometalates and other metal-based complexes in metal-organic frameworks: from synthesis to characterisation and applications in catalysis.", *Chemical Society Reviews* **2021**, *50*, 6152–6220.

[31]   B. Li, J. Ma, P. Cheng, "Integration of Metal Nanoparticles into Metal-Organic Frameworks for Composite Catalysts: Design and Synthetic Strategy.", *Small* **2019**, e1804849.

[32]   S. Dai, A. Tissot, C. Serre, "Recent Progresses in Metal-Organic Frameworks Based Core-shell Composites.", *Advanced Energy Materials* **2021**, *12*, 2100061.

[33]   C. Liu, Q. Sun, L. Lin, J. Wang, C. Zhang, C. Xia, T. Bao, J. Wan, R. Huang, J. Zou, C. Yu, "Ternary MOF-on-MOF heterostructures with controllable architectural and compositional complexity via multiple selective assembly.", *Nature Communications* **2020**, *11*, 4971.

[34]   B. H. Monjezi, K. Kutonova, M. Tsotsalas, S. Henke, A. Knebel, "Current Trends in Metal-Organic and Covalent Organic Framework Membrane Materials.", *Angewandte Chemie Int. Ed.* **2020**, *60*, 15153–15164.

[35]   D. Zou, D. Liu, J. Zhang, "From Zeolitic Imidazolate Framework-8 to Metal-Organic Frameworks (MOFs): Representative Substance for the General Study of Pioneering MOF Applications.", *Energy & Environmental Materials* **2018**, *1*, 209–220.

[36]   R. Freund, O. Zaremba, G. Arnauts, R. Ameloot, G. Skorupskii, M. Dinca, A. V. Bavykina, J. Gascón, A. Ejsmont, J. Goscianska, M. J. Kalmutzki, U. Lächelt, E. Ploetz, C. S. Diercks, S. Wuttke, "The Current Status of MOF and COF Applications.", *Angewandte Chemie Int. Ed.* **2021**, *60*, 23975–24001.

[37]   J. Park, J. D. Howe, D. S. Sholl, "How Reproducible Are Isotherm Measurements in Metal-Organic Frameworks?", *Chemistry of Materials* **2017**, *29*, 10487–10495.

[38]   J. D. Evans, V. Bon, I. Senkovska, S. Kaskel, "A Universal Standard Archive File for Adsorption Data.", *Langmuir* **2021**, *37*, 4222–4226.

[39]   D. P. Broom, M. Hirscher, "Irreproducibility in hydrogen storage material research.", *Energy and Environmental Science* **2016**, *9*, 3368–3380.

[40]   A. Li, R. Bueno-Perez, S. Wiggin, D. Fairen-jimenez, "Enabling efficient exploration of metal-organic frameworks in the Cambridge Structural Database.", *CrystEngComm* **2020**, *22*, 7152–7161.

[41]   H. Daglar, H. C. Gulbalkan, G. Avci, G. O. Aksu, O. F. Altundal, C. Altintas, I. Erucar, S. Keskin, "Effect of Metal-Organic Framework (MOF) Database

Selection on the Assessment of Gas Storage and Separation Potentials of MOFs.", *Angewandte Chemie Int. Ed.* **2021**, *60*, 7828–7837.

[42]   A. Bajpai, P. Chandrasekhar, S. Govardhan, R. Banerjee, J. N. Moorthy, "Single crystal-to-single crystal site-selective postsynthetic metal exchange in a Zn-MOF based on semi-rigid tricarboxylic acid and access to bimetallic MOFs.", *Chemistry* **2015**, *21*, 2759–65.

[43]   M. Mendt, P. Vervoorts, A. Schneemann, R. A. Fischer, A. Pöppl, "Probing Local Structural Changes at Cu2+ in a Flexible Mixed-Metal Metal-Organic Framework by in Situ Electron Paramagnetic Resonance during CO2 Ad- and Desorption.", *The Journal of Physical Chemistry C* **2019**, *123*, 2940–2952.

[44]   I. Schwedler, S. Henke, M. T. Wharmby, S. R. Bajpe, A. K. Cheetham, R. A. Fischer, "Mixed-linker solid solutions of functionalized pillared-layer MOFs - adjusting structural flexibility, gas sorption, and thermal responsiveness.", *Dalton transactions* **2016**, *45*, 4230–41.

[45]   H. Deng, C. J. Doonan, H. Furukawa, R. B. Ferreira, J. C. Towne, C. B. Knobler, B. Wang, O. M. Yaghi, "Multiple Functional Groups of Varying Ratios in Metal-Organic Frameworks.", *Science* **2010**, *327*, 846–850.

[46]   W. Fan, X. Zhang, Z. Kang, X. Liu, D. Sun, "Isoreticular chemistry within metal-organic frameworks for gas storage and separation.", *Coordination Chemistry Reviews* **2021**, *443*, 213968.

[47]   R. Freund, S. Canossa, S. M. Cohen, W. Yan, H. Deng, V. Guillerm, M. Eddaoudi, D. G. Madden, D. Fairen-jimenez, H. Lyu, L. K. Macreadie, Z. Ji, Y. Zhang, B. Wang, F. Haase, C. Wöll, O. Zaremba, J. Andreo, S. Wuttke, C. S. Diercks, "25 years of Reticular Chemistry.", *Angewandte Chemie Int. Ed.* **2021**, *60*, 23946–23974.

[48]   C. S. Hawes, "Coordination sphere hydrogen bonding as a structural element in metal-organic Frameworks.", *Dalton transactions* **2021**, *50*, 6034–6049.

[49]   K.-D. Zhang, J. Tian, D. A. Hanifi, Y. Zhang, A. C.-H. Sue, T.-Y. Zhou, L. Zhang, X. Zhao, Y. Liu, Z.-T. Li, "Toward a single-layer two-dimensional honeycomb supramolecular organic framework in water.", *Journal of the American Chemical Society* **2013**, *135*, 17913–17918.

[50]   S. G. Davey, "Exploring new dimensions", *Nature Reviews Chemistry* **2020**, *4*, 563–563.

[51]   R. A. Fischer, "Metal-organic frameworks–the new jack of all trades for (inorganic) chemists.", *Angewandte Chemie Int. Ed.* **2014**, *53*, 5716–5717.

[52]   J. Jiang, H. Furukawa, Y.-B. Zhang, O. M. Yaghi, "High Methane Storage Working Capacity in Metal-Organic Frameworks with Acrylate Links.", *Journal of the American Chemical Society* **2016**, *138*, 10244–10251.

[53]   D. E. Jaramillo, H. Z. H. Jiang, H. A. Evans, R. Chakraborty, H. Furukawa, C. M. Brown, M. Head-Gordon, J. R. Long, "Ambient-Temperature Hydrogen Storage via Vanadium(II)-Dihydrogen Complexation in a Metal-Organic Framework.", *Journal of the American Chemical Society* **2021**, *143*, 6248–6256.

[54] J.-B. Lin, T. T. Nguyen, R. Vaidhyanathan, J. Burner, J. M. Taylor, H. Durekova, F. Akhtar, R. K. Mah, O. Ghaffari-Nik, S. Marx, N. Fylstra, S. S. Iremonger, K. W. Dawson, P. Sarkar, P. Hovington, A. Rajendran, T. K. Woo, G. K. H. Shimizu, "A scalable metal-organic framework as a durable physisorbent for carbon dioxide capture.", *Science* **2021**, *374*, 1464–1469.

[55] O. T. Qazvini, R. Babarao, Z. Shi, Y.-B. Zhang, S. G. Telfer, "A Robust Ethane-Trapping Metal-Organic Framework with a High Capacity for Ethylene Purification.", *Journal of the American Chemical Society* **2019**, *141*, 5014–5020.

[56] G.-D. Wang, Y.-Z. Li, W.-j. Shi, L. Hou, Y.-Y. Wang, Z. Zhu, "One-step C2H4 Purification from Ternary C2H6/C2H4/C2H2 Mixtures by a Robust Metal-Organic Framework with Customized Pore Environment.", *Angewandte Chemie Int. Ed.* **2022**, *61*, e202205427.

[57] Z. Niu, X. Cui, T. Pham, G. Verma, P. C. Lan, C. Shan, H. Xing, K. A. Forrest, S. Suepaul, B. Space, A. Nafady, A. M. Al-Enizi, S. Ma, "A MOF-based Ultra-Strong Acetylene Nano-trap for Highly Efficient C2H2/CO2 Separation.", *Angewandte Chemie Int. Ed.* **2021**, *60*, 5283–5288.

[58] J. Y. Kim, J. Park, J. Ha, M. Jung, D. Wallacher, A. Franz, R. Balderas-Xicohténcatl, M. Hirscher, S. G. Kang, J. T. Park, I. H. Oh, H. R. Moon, H. Oh, "Specific Isotope-Responsive Breathing Transition in Flexible Metal-Organic Frameworks.", *Journal of the American Chemical Society* **2020**, *142*, 13278–13282.

[59] M. I. Gonzalez, M. T. Kapelewski, E. D. Bloch, P. J. Milner, D. A. Reed, M. R. Hudson, J. A. Mason, G. Barin, C. M. Brown, J. R. Long, "Separation of Xylene Isomers through Multiple Metal Site Interactions in Metal-Organic Frameworks.", *Journal of the American Chemical Society* **2018**, *140*, 3412–3422.

[60] Y. Yao, C. Wang, J. Na, M. S. A. Hossain, X. Yan, H. Zhang, M. A. Amin, J. Qi, Y. Yamauchi, J. Li, "Macroscopic MOF Architectures: Effective Strategies for Practical Application in Water Treatment.", *Small* **2021**, e2104387.

[61] Y. Li, Z. Yang, Y. Wang, Z. Bai, T. Zheng, X. Dai, S. Liu, D. Gui, W. Liu, M. Chen, L. Chen, J. Diwu, L. Zhu, R. Zhou, Z. Chai, T. E. Albrecht-Schmitt, S. Wang, "A mesoporous cationic thorium-organic framework that rapidly traps anionic persistent organic pollutants.", *Nature Communications* **2017**, *8*, 1354.

[62] S. Daliran, M. Ghazagh-Miri, A. R. Oveisi, M. Khajeh, S. Navalón, M. Álvaro, M. Ghaffari-Moghaddam, H. S. Delarami, H. García, "A Pyridyltriazol Functionalized Zirconium Metal-Organic Framework for Selective and Highly Efficient Adsorption of Palladium.", *ACS Applied Materials & Interfaces* **2020**, *12*, 25221–25232.

[63] K. Kratzl, T. Kratky, S. Günther, O. Tomanec, R. Zboril, J. Michalika, J. M. Macák, M. Cokoja, R. A. Fischer, "Generation and Stabilization of Small Platinum Clusters inside a Metal-Organic Framework.", *Journal of the American Chemical Society* **2019**, *141*, 13962–13969.

[64] J. Gascón, A. Corma, F. Kapteijn, F. X. L. i Xamena, "Metal Organic Framework Catalysis: Quo vadis?", *ACS Catalysis* **2014**, *4*, 361–378.

[65] J. Schnabel, R. Ettlinger, H. Bunzen, "Zn-MOF-74 as pH-Responsive Drug-Delivery System of Arsenic Trioxide.", *ChemNanoMat* **2020**, *6*, 1229–1236.

[66] S. Zhou, O. Shekhah, A. Ramírez, P. Lyu, E. Abou-hamad, J. Jia, J. Li, P. M. Bhatt, Z. Huang, H. Jiang, T. Jin, G. Maurin, J. Gascon, M. Eddaoudi, "Asymmetric pore windows in MOF membranes for natural gas valorization.", *Nature* **2022**, *606*, 706–712.

[67] A. He, Z. Jiang, Y. Wu, H. Hussain, J. Rawle, M. E. Briggs, M. A. Little, A. G. Livingston, A. I. Cooper, "A smart and responsive crystalline porous organic cage membrane with switchable pore apertures for graded molecular sieving.", *Nature Materials* **2022**, *21*, 463–470.

[68] L. Shu, Y. Peng, R. Yao, H. S. Song, C. Zhu, W. Yang, "Flexible Soft-Solid Metal-Organic Framework Composite Membranes for H2/CO2 Separation.", *Angewandte Chemie Int. Ed.* **2022**, *61*, e202117577.

[69] B. Paschke, A. Wixforth, D. Denysenko, D. Volkmer, "Fast Surface Acoustic Wave-Based Sensors to Investigate the Kinetics of Gas Uptake in Ultra-Microporous Frameworks.", *ACS sensors* **2017**, *2*, 740–747.

[70] I. Stassen, N. C. Burtch, A. A. Talin, P. Falcaro, M. D. Allendorf, R. Ameloot, "An updated roadmap for the integration of metal-organic frameworks with electronic devices and chemical sensors.", *Chemical Society Reviews* **2017**, *46*, 3185–3241.

[71] Z. Zhan, Y. Jia, D. Li, X. Zhang, M. Hu, "A water-stable terbium-MOF sensor for the selective, sensitive, and recyclable detection of Al3+ and CO32- ions.", *Dalton transactions* **2019**, *48*, 15255.

[72] S. Choi, M. Oh, "Well-Arranged and Confined Incorporation of PdCo Nanoparticles within a Hollow and Porous Metal-Organic Framework for Superior Catalytic Activity.", *Angewandte Chemie Int. Ed.* **2019**, *58*, 866–871.

[73] W.-S. Lo, L.-Y. Chou, A. P. Young, C. H. Ren, T. W. Goh, B. P. Williams, Y. Li, S.-Y. Chen, M. N. Ismail, W. Huang, C.-K. Tsung, "Probing the Interface between Encapsulated Nanoparticles and Metal-Organic Frameworks for Catalytic Selectivity Control.", *Chemistry of Materials* **2021**, *33*, 1946–1953.

[74] D. Ukaj, H. Bunzen, J. Berger, G. Kieslich, R. A. Fischer, "Charge-Transfer-Induced Electrical Conductivity in a Tetrathiafulvalene-Based Metal-Organic Framework.", *Chemistry of Materials* **2021**, *33*, 2532–2542.

[75] M. Krishtab, I. Stassen, T. Stassin, A. J. Cruz, O. O. Okudur, S. Armini, C. Wilson, S. D. Gendt, R. Ameloot, "Vapor-deposited zeolitic imidazolate frameworks as gap-filling ultra-low-k dielectrics.", *Nature Communications* **2019**, *10*, 3729.

[76] S. R. Batten, N. R. Champness, X.-M. Chen, J. García-Martínez, S. Kitagawa, L. Öhrström, M. Okeeffe, M. P. Suh, J. Reedijk, "Terminology of metal-organic frameworks and coordination polymers (IUPAC Recommendations 2013).", *Pure and Applied Chemistry* **2013**, *85*, 1715–1724.

[77] S. Seth, A. J. Matzger, "Metal-Organic Frameworks: Examples, Counterexamples, and an Actionable Definition.", *Crystal Growth & Design* **2017**, *17*, 4043–4048.

[78] K. K. Tanabe, S. M. Cohen, "Postsynthetic modification of metal-organic frameworks – a progress report.", *Chemical Society Reviews* **2011**, *40*, 498–519.

[79] Z. Ji, T. Li, O. M. Yaghi, "Sequencing of metals in multivariate metal-organic frameworks.", *Science* **2020**, *369*, 674–680.

[80] W. Fan, S. Yuan, W. Wang, L. Feng, X. Liu, X. Zhang, X. Wang, Z. Kang, F. Dai, D. Yuan, D. Sun, H.-C. Zhou, "Optimizing Multivariate Metal-Organic Frameworks for Efficient C2H2/CO2 Separation.", *Journal of the American Chemical Society* **2020**, *142*, 8728–8737.

[81] S. Nayab, V. Trouillet, H. Gliemann, P. G. Weidler, I. Azeem, S. R. Tariq, A. S. Goldmann, C. Barner-Kowollik, B. Yameen, "Reversible Diels-Alder and Michael Addition Reactions Enable the Facile Postsynthetic Modification of Metal-Organic Frameworks.", *Inorganic Chemistry* **2021**, *60*, 4397–4409.

[82] G. Tuci, A. Rossin, X. Xu, M. Ranocchiari, J. A. Bokhoven, L. Luconi, I. Manet, M. Melucci, G. Giambastiani, "Click on MOFs: A Versatile Tool for the Multimodal Derivatization of N3-Decorated Metal Organic Frameworks.", *Chemistry of Materials* **2013**, *25*, 2297–2308.

[83] A. Gupta, R. K. Deshpande, L. Liu, G. I. N. Waterhouse, S. G. Telfer, "Porosity in metal-organic frameworks following thermolytic postsynthetic deprotection: gas sorption, dye uptake and covalent derivatisation.", *CrystEngComm* **2012**, *14*, 5701–5704.

[84] J. D. Evans, C. J. Sumby, C. J. Doonan, "Post-synthetic metalation of metal-organic frameworks.", *Chemical Society Reviews* **2014**, *43*, 5933–5951.

[85] S. Carrasco, A. Sanz-Marco, B. Martín-Matute, "Fast and Robust Synthesis of Metalated PCN-222 and Their Catalytic Performance in Cycloaddition Reactions with CO2.", *Organometallics* **2019**, *38*, 3429–3435.

[86] M. Eddaoudi, J. Kim, N. Rosi, D. T. Vodak, J. Wachter, M. O'keeffe, O. M. Yaghi, "Systematic Design of Pore Size and Functionality in Isoreticular MOFs and Their Application in Methane Storage.", *Science* **2002**, *295*, 469–472.

[87] W. R. Heinz, I. Aguirrezabal-Telleria, R. Junk, J. Berger, J. Wang, D. I. Sharapa, M. Gil-Calvo, I. Luz, M. Soukri, F. Studt, Y. Wang, C. Wöll, H. Bunzen, M. Drees, R. A. Fischer, "Thermal Defect Engineering of Precious Group Metal-Organic Frameworks: A Case Study on RuRh-HKUST-1 Analogues.", *ACS Applied Materials & Interfaces* **2020**, *12*, 40635–40647.

[88] P. Iacomi, F. Formalik, J. Marreiros, J. Shang, J. Rogacka, A. Mohmeyer, P. Behrens, R. Ameloot, B. Kuchta, P. L. Llewellyn, "Role of Structural Defects in the Adsorption and Separation of C3 Hydrocarbons in Zr-Fumarate-MOF MOF-801.", *Chemistry of Materials* **2019**, 8413–8423.

[89] S. Dissegna, K. Epp, W. R. Heinz, G. Kieslich, R. A. Fischer, "Defective Metal Organic Frameworks.", *Advanced Materials* **2018**, *30*, 1704501.

[90]   S. Kitagawa, M. Kondo, "Functional Micropore Chemistry of Crystalline Metal Complex-Assembled Compounds.", *Bulletin of the Chemical Society of Japan* **1998**, *71*, 1739–1753.

[91]   S. Horike, S. Shimomura, S. Kitagawa, "Soft porous crystals.", *Nature chemistry* **2009**, *1*, 695–704.

[92]   E. V. Alexandrov, A. V. Goltsev, R. A. Eremin, V. A. Blatov, "Anisotropy of Elastic Properties of Metal-Organic Frameworks and the Breathing Phenomenon.", *The Journal of Physical Chemistry C* **2019**, *123*, 24651–24658.

[93]   C. Serre, F. Millange, C. Thouvenot, M. Nogués, G. Marsolier, D. Louër, G. Férey, "Very Large Breathing Effect in the First Nanoporous Chromium(III)-Based Solids: MIL-53 or CrIII(OH)(O2C-C6H4-CO2) (HO2C-C6H4-CO2H) xH2Oy.", *Journal of the American Chemical Society* **2002**, *124*, 13519–13526.

[94]   S. Biswas, T. Ahnfeldt, N. Stock, "New functionalized flexible Al-MIL-53-X (X = -Cl, -Br, -CH3, -NO2, -(OH)2) solids: syntheses, characterization, sorption, and breathing behavior.", *Inorganic Chemistry* **2011**, *50*, 9518–9526.

[95]   N. Klein, C. Herzog, M. Sabo, I. Senkovska, J. Getzschmann, S. Paasch, M. R. Lohe, E. Brunner, S. Kaskel, "Monitoring adsorption-induced switching by (129)Xe NMR spectroscopy in a new metal-organic framework Ni(2)(2,6-ndc)(2)(dabco).", *Physical Chemistry Chemical Physics PCCP* **2010**, *12*, 11778–11784.

[96]   S. Ehrling, M. Mendt, I. Senkovska, J. D. Evans, V. Bon, P. S. Petkov, C. Ehrling, F. Walenszus, A. Pöppl, S. Kaskel, "Tailoring the Adsorption-Induced Flexibility of a Pillared Layer Metal-Organic Framework DUT-8(Ni) by Cobalt Substitution.", *Chemistry of Materials* **2020**, *32*, 5670–5681.

[97]   C. Mellot-Draznieks, C. Serre, S. Surblé, N. Audebrand, G. Férey, "Very large swelling in hybrid frameworks: a combined computational and powder diffraction study.", *Journal of the American Chemical Society* **2005**, *127*, 16273–16278.

[98]   S. Surblé, C. Serre, C. Mellot-Draznieks, F. Millange, G. Férey, "A new isoreticular class of metal-organic frameworks with the MIL-88 topology.", *Chemical Communications* **2006**, *3*, 284–286.

[99]   P. Horcajada, F. Salles, S. Wuttke, T. Devic, D. Heurtaux, G. Maurin, A. Vimont, M. Daturi, O. R. P. David, E. Magnier, N. Stock, Y. Filinchuk, D. Popov, C. Riekel, G. Férey, C. Serre, "How linker's modification controls swelling properties of highly flexible iron(III) dicarboxylates MIL-88.", *Journal of the American Chemical Society* **2011**, *133*, 17839–17847.

[100] D. Li, K. Kaneko, "Hydrogen bond-regulated microporous nature of copper complex-assembled microcrystals.", *Chemical Physics Letters* **2001**, *335*, 50–56.

[101] S. Hiraide, Y. Sakanaka, H. Kajiro, S. Kawaguchi, M. T. Miyahara, H. Tanaka, "High-throughput gas separation by flexible metal-organic frameworks with fast gating and thermal management capabilities.", *Nature Communications* **2020**, *11*, 3867.

[102] S.-Q. Wang, S. Mukherjee, E. Patyk-Kaźmierczak, S. Darwish, A. Bajpai, Q.-Y. Yang, M. J. Zaworotko, "Highly Selective, High-Capacity Separation of o-Xylene from C8 Aromatics by a Switching Adsorbent Layered Material.", *Angewandte Chemie Int Ed.* **2019**, *58*, 6630–6634.

[103] R. Turo-Cortés, C. Bartual-Murgui, J. Castells-Gil, M. C. Muñoz, C. Mart-Gastaldo, J. A. Real, "Reversible guest-induced gate-opening with multiplex spin crossover responses in two-dimensional Hofmann clathrates.", *Chemical Science* **2020**, *11*, 11224–11234.

[104] H. J. Park, M. P. Suh, "Stepwise and hysteretic sorption of N2, O2, CO2, and H2 gases in a porous metal-organic framework [Zn(2)(BPnDC)(2)(bpy)].", *Chemical Communications* **2010**, *46*, 610–612.

[105] R. Kitaura, K. Seki, G. Akiyama, S. Kitagawa, "Porous coordination-polymer crystals with gated channels specific for supercritical gases.", *Angewandte Chemie Int. Ed.* **2003**, *42*, 428–431.

[106] Y. Inubushi, S. Horike, T. Fukushima, G. Akiyama, R. Matsuda, S. Kitagawa, "Modification of flexible part in Cu2+ interdigitated framework for CH4/CO2 separation.", *Chemical Communications* **2010**, *46,* 9229–9231.

[107] B. Chen, C. Liang, J. Yang, D. S. Contreras, Y. L. Clancy, E. B. Lobkovsky, O. M. Yaghi, S. Dai, "A microporous MOF for gas-chromatographic separation of alkanes.", *Angewandte Chemie Int. Ed.* **2006**, *45*, 1390–1393.

[108] M. Bonneau, C. Lavenn, J. J. Zheng, A. Legrand, T. Ogawa, K. Sugimoto, F.-X. Coudert, R. Reau, S. Sakaki, K.-i. Otake, S. Kitagawa, "Tunable acetylene sorption by flexible catenated metal-organic frameworks.", *Nature Chemistry* **2022**, *14*, 816–822.

[109] F. Zarekarizi, M. Joharian, A. Morsali, "Pillar-layered MOFs: Functionality, Interpenetration, Flexibility and Applications.", *Journal of Materials Chemistry* **2018**, *6*, 19288–19329.

[110] M. Shivanna, Q.-Y. Yang, A. Bajpai, S. Sen, N. Hosono, S. Kusaka, T. Pham, K. A. Forrest, B. Space, S. Kitagawa, M. J. Zaworotko, "Readily accessible shape-memory effect in a porous interpenetrated coordination network.", *Science Advances* **2018**, *4*, eaaq1636.

[111] C. O. Ania, E. Garcia-Perez, M. Haro, J. J. Gutiérrez-Sevillano, T. Valdés-Solís, J. B. Parra, S. Calero, "Understanding Gas-Induced Structural Deformation of ZIF-8.", *The Journal of Physical Chemistry Letters* **2012**, *3*, 1159–1164.

[112] D. Fairen-jimenez, S. A. Moggach, M. T. Wharmby, P. A. Wright, S. Parsons, T. Düren, "Opening the gate: framework flexibility in ZIF-8 explored by experiments and simulations.", *Journal of the American Chemical Society* **2011**, *133*, 8900–8902.

[113] X. Meng, B. Gui, D. Yuan, M. Zeller, C. Wang, "Mechanized azobenzene-functionalized zirconium metal-organic framework for on-command cargo release.", *Science Advances* **2016**, *2*, e1600480.

[114] J. P. Dürholt, B. F. Jahromi, R. Schmid, "Tuning the Electric Field Response of MOFs by Rotatable Dipolar Linkers.", *ACS Central Science* **2019**, *5*, 1440–1448.

[115] S. Henke, A. Schneemann, R. A. Fischer, "Massive Anisotropic Thermal Expansion and Thermo-Responsive Breathing in Metal-Organic Frameworks Modulated by Linker Functionalization.", *Advanced Functional Materials* **2013**, *23*, 5990–5996.

[116] N. Chanut, A. Ghoufi, M.-V. Coulet, S. Bourrelly, B. Kuchta, G. Maurin, P. L. Llewellyn, "Tailoring the separation properties of flexible metal-organic frameworks using mechanical pressure.", *Nature Communications* **2020**, *11*, 1216.

[117] C. Gao, J. Li, S. Yin, J. Sun, C. Wang, "Redox-triggered switching in three-dimensional covalent organic frameworks.", *Nature Communications* **2020**, *11*, 4919.

[118] S. Kitagawa, "Future Porous Materials.", *Accounts of chemical research* **2017**, *50 3*, 514–516.

[119] J. D. Evans, V. Bon, I. Senkovska, H.-C. Lee, S. Kaskel, "Four-dimensional metal-organic frameworks.", *Nature Communications* **2020**, *11*, 2690.

[120] A. Kondo, N. Kojima, H. Kajiro, H. Noguchi, Y. Hattori, F. Okino, K. Maeda, T. Ohba, K. Kaneko, H. Kanoh, "Gas Adsorption Mechanism and Kinetics of an Elastic Layer-Structured Metal–Organic Framework.", *Journal of Physical Chemistry C* **2012**, *116*, 4157–4162.

[121] S. Hiraide, H. Tanaka, M. T. Miyahara, "Understanding gate adsorption behaviour of CO2 on elastic layer-structured metal-organic framework-11.", *Dalton transactions* **2016**, *45*, 4193–202.

[122] V. Bon, N. Kavoosi, I. Senkovska, S. Kaskel, "Tolerance of Flexible MOFs toward Repeated Adsorption Stress.", *ACS Applied Materials & Interfaces* **2015**, *7*, 22292–300.

[123] S. Hiraide, H. Arima, H. Tanaka, M. T. Miyahara, "Slacking of Gate Adsorption Behavior on Metal-Organic Frameworks under an External Force.", *ACS Applied Materials & Interfaces* **2021**, *13*, 30213–30223.

[124] M. Agrawal, S. Bhattacharyya, Y. Huang, K. C. Jayachandrababu, C. R. Murdock, J. Bentley, A. Rivas-Cardona, M. M. Mertens, K. S. Walton, D. S. Sholl, S. Nair, "Liquid Phase Multicomponent Adsorption and Separation of Xylene Mixtures by Flexible MIL-53 Adsorbents.", *Journal of Physical Chemistry C* **2018**, *122*, 386–397.

[125] M. Meilikhov, K. V. Yusenko, R. A. Fischer, "Incorporation of metallocenes into the channel structured Metal-Organic Frameworks MIL-53(Al) and MIL-47(V).", *Dalton transactions* **2010**, *39*, 10990–109999.

[126] P. G. Yot, M. Wahiduzzaman, E. Elkaim, P. Fertey, P. Fabry, C. Serre, G. Maurin, "Modulation of the mechanical energy storage performance of the MIL-47(VIV) metal organic framework by ligand functionalization.", *Dalton transactions* **2019**, *48*, 1656–1661.

[127] S. Ehrling, E. M. Reynolds, V. Bon, I. Senkovska, T. E. Gorelik, J. D. Evans, M. Rauche, M. Mendt, M. Weiss, A. Pöppl, E. J. Brunner, U. Kaiser, A. L. Goodwin, S. Kaskel, "Adaptive response of a metal-organic framework through reversible disorder–disorder transitions.", *Nature Chemistry* **2021**, *13*, 568–574.

[128] S. Krause, V. Bon, I. Senkovska, U. Stoeck, D. Wallacher, D. M. Többens, S. Zander, R. S. Pillai, G. Maurin, F.-X. Coudert, S. Kaskel, "A pressure-amplifying framework material with negative gas adsorption transitions.", *Nature* **2016**, *532*, 348–352.

[129] S. Krause, F. S. Reuter, S. Ehrling, V. Bon, I. Senkovska, S. Kaskel, E. Brunner, "Impact of Defects and Crystal Size on Negative Gas Adsorption in DUT-49 Analyzed by In Situ129Xe NMR Spectroscopy.", *Chemistry of Materials* **2020**, *32*, 4641–4650.

[130] R. Goeminne, S. Krause, S. Kaskel, T. Verstraelen, J. D. Evans, "Charting the Complete Thermodynamic Landscape of Gas Adsorption for a Responsive Metal-Organic Framework.", *Journal of the American Chemical Society* **2021**, *143*, 4143–4147.

[131] F. Salles, G. Maurin, C. Serre, P. L. Llewellyn, C. Knöfel, H. J. Choi, Y. Filinchuk, L. Oliviero, A. Vimont, J. R. Long, G. Férey, "Multistep N2 breathing in the metal-organic framework Co(1,4-benzenedipyrazolate).", *Journal of the American Chemical Society* **2010**, *132*, 13782–13788.

[132] J. A. Mason, J. Oktawiec, M. K. Taylor, M. R. Hudson, J. Rodriguez, J. E. Bachman, M. I. Gonzalez, A. Cervellino, A. Guagliardi, C. M. Brown, P. L. Llewellyn, N. Masciocchi, J. R. Long, "Methane storage in flexible metal-organic frameworks with intrinsic thermal management.", *Nature* **2015**, *527*, 357–361.

[133] S. Henke, R. Schmid, J.-D. Grunwaldt, R. A. Fischer, "Flexibility and sorption selectivity in rigid metal-organic frameworks: the impact of ether-functionalised linkers.", *Chemistry* **2010**, *16*, 14296–306.

[134] S. Henke, A. Schneemann, A. Wütscher, R. A. Fischer, "Directing the breathing behavior of pillared-layered metal-organic frameworks via a systematic library of functionalized linkers bearing flexible substituents.", *Journal of the American Chemical Society* **2012**, *134*, 9464–9474.

[135] A. Schneemann, Y. Jing, J. D. Evans, T. Toyao, Y. Hijikata, Y. Kamiya, K.-i. Shimizu, N. C. Burtch, S.-i. Noro, "Alkyl decorated metal-organic frameworks for selective trapping of ethane from ethylene above ambient pressures.", *Dalton transactions* **2021**, *50*, 10423–10435.

[136] S. J. Baxter, A. Schneemann, A. D. Ready, P. Wijeratne, A. P. Wilkinson, N. C. Burtch, "Tuning Thermal Expansion in Metal-Organic Frameworks using a Mixed Linker Solid Solution Approach.", *Journal of the American Chemical Society* **2019**, *141*, 12849–12854.

[137] C. Triguero, F.-X. Coudert, A. Boutin, A. H. Fuchs, A. V. Neimark, "Mechanism of Breathing Transitions in Metal-Organic Frameworks.", *Journal of Physical Chemistry Letters* **2011**, *2*, 2033–2037.

[138] M. Parsaei, K. Akhbari, J. M. White, "Modulating Carbon Dioxide Storage by Facile Synthesis of Nanoporous Pillared-Layered Metal-Organic Framework with Different Synthetic Routes.", *Inorganic chemistry* **2022**, *61*, 3893–3902.

[139] B. Ghalei, K. Sakurai, Y. Kinoshita, K. Wakimoto, A. P. Isfahani, Q. Song, K. Doitomi, S. Furukawa, H. Hirao, H. Kusuda, S. Kitagawa, E. Sivaniah,

"Enhanced selectivity in mixed matrix membranes for CO2 capture through efficient dispersion of amine-functionalized MOF nanoparticles.", *Nature Energy* **2017**, *2*, 17086.

[140] T. M. Mcdonald, J. A. Mason, X. Kong, E. D. Bloch, D. Gygi, A. Dani, V. Crocellà, F. Giordanino, S. O. Odoh, W. S. Drisdell, B. Vlaisavljevich, A. L. Dzubak, R. Poloni, S. K. Schnell, N. Planas, K. Lee, T. A. Pascal, L. F. Wan, D. Prendergast, J. B. Neaton, B. Smit, J. B. Kortright, L. Gagliardi, S. Bordiga, J. A. Reimer, J. R. Long, "Cooperative insertion of CO2 in diamine-appended metal-organic frameworks.", *Nature* **2015**, *519*, 303–308.

[141] B. Dinakar, A. C. Forse, H. Z. H. Jiang, Z. Zhu, J.-H. Lee, E. J. Kim, S. T. Parker, C. J. Pollak, R. L. Siegelman, P. J. Milner, J. A. Reimer, J. R. Long, "Overcoming Metastable CO2 Adsorption in a Bulky Diamine-Appended Metal-Organic Framework.", *Journal of the American Chemical Society* **2021**, *143*, 15258–15270.

[142] S. Couck, J. F. M. Denayer, G. V. Baron, T. Rémy, J. Gascón, F. Kapteijn, "An amine-functionalized MIL-53 metal-organic framework with large separation power for CO2 and CH4.", *Journal of the American Chemical Society* **2009**, *131*, 6326–6327.

[143] Y. Gu, J. J. Zheng, K.-i. Otake, K. Sugimoto, N. Hosono, S. Sakaki, F. Li, S. Kitagawa, "Structural Deformation Energy Modulation Strategy in a Soft Porous Coordination Polymer with Interpenetrated Framework.", *Angewandte Chemie Int. Ed.* **2020**, *59*, 15517–15521.

[144] P. Vervoorts, J. Keupp, A. Schneemann, C. L. Hobday, D. Daisenberger, R. A. Fischer, R. Schmid, G. Kieslich, "Configurational Entropy Driven High-Pressure Behaviour of a Flexible Metal-Organic Framework.", *Angewandte Chemie Int. Ed.* **2020**, *60*, 787–793.

[145] P. Serra-Crespo, M. A. van der Veen, E. R. Gobechiya, K. Houthoofd, Y. Filinchuk, C. E. A. Kirschhock, J. A. Martens, B. F. Sels, D. E. D. Vos, F. Kapteijn, J. Gascón, "NH2-MIL-53(Al): a high-contrast reversible solid-state nonlinear optical switch.", *Journal of the American Chemical Society* **2012**, *134*, 8314–8317.

[146] Y. Kim, R. Haldar, H. Kim, J. Koo, K. Kim, "The guest-dependent thermal response of the flexible MOF Zn2(bdc)2(dabco).", *Dalton transactions* **2016**, *45*, 4187–92.

[147] Z. Wang, S. M. Cohen, "Modulating metal-organic frameworks to breathe: a postsynthetic covalent modification approach.", *Journal of the American Chemical Society* **2009**, *131*, 16675–16677.

[148] J. Wieme, K. Lejaeghere, G. Kresse, V. V. Speybroeck, "Tuning the balance between dispersion and entropy to design temperature-responsive flexible metal-organic frameworks.", *Nature Communications* **2018**, *9*, 4899.

[149] M. Mendt, B. Jee, N. Stock, T. Ahnfeldt, M. Hartmann, D. Himsl, A. Pöppl, "Structural Phase Transitions and Thermal Hysteresis in the Metal-Organic Framework Compound MIL-53 As Studied by Electron Spin Resonance Spectroscopy.", *Journal of Physical Chemistry C* **2010**, *114*, 19443–19451.

[150] Y. Sakata, S. Furukawa, M. Kondo, K. Hirai, N. Horike, Y. Takashima, H. Uehara, N. Louvain, M. Meilikhov, T. Tsuruoka, S. Isoda, W. Kosaka, O. Sakata, S. Kitagawa, "Shape-Memory Nanopores Induced in Coordination Frameworks by Crystal Downsizing.", *Science* **2013**, *339*, 193–196.

[151] C. Commons, Attribution 4.0 International (CC BY 4.0). **2022**, https://creative commons.org/licenses/by/4.0/ (visited on 11/05/2022).

[152] S. Ehrling, I. Senkovska, A. Efimova, V. Bon, L. Abylgazina, P. S. Petkov, J. D. Evans, A. G. Attallah, M. T. Wharmby, M. Roslova, Z. Huang, H. Tanaka, A. Wagner, P. Schmidt, S. Kaskel, "Temperature Driven Transformation of the Flexible Metal-Organic Framework DUT-8(Ni).", *Chemistry* **2022**, *28*, e202201281.

[153] S. Rahman, A. Arami-Niya, X. Yang, G. Xiao, G. Li, E. F. May, "Temperature dependence of adsorption hysteresis in flexible metal organic frameworks.", *Communications Chemistry* **2020**, *3*, 186.

[154] N. Yanai, T. Uemura, M. K. Inoue, R. Matsuda, T. Fukushima, M. Tsujimoto, S. Isoda, S. Kitagawa, "Guest-to-host transmission of structural changes for stimuli-responsive adsorption property.", *Journal of the American Chemical Society* **2012**, *134*, 4501–4504.

[155] J. Park, D. Yuan, K. T. Pham, J.-R. Li, A. A. Yakovenko, H.-C. Zhou, "Reversible alteration of CO2 adsorption upon photochemical or thermal treatment in a metal-organic framework.", *Journal of the American Chemical Society* **2012**, *134*, 99–102.

[156] J. D. Evans, J. P. Dürholt, S. Kaskel, R. Schmid, "Assessing Negative Thermal Expansion in Mesoporous Metal-Organic Frameworks by Molecular Simulation.", *Journal of Materials Chemistry A* **2019**, *7*, 24019–24026.

[157] W. Xiang, Y.-p. Zhang, Y. Chen, C.-j. Liu, X. Tu, "Synthesis, characterization and application of defective metal-organic frameworks: current status and perspectives.", *Journal of Materials Chemistry* **2020**, *8*, 21526–21546.

[158] I. E. Khalil, C. Xue, W. Liu, X. Li, Y. Shen, S. Li, W. Zhang, F. Huo, "The Role of Defects in Metal-Organic Frameworks for Nitrogen Reduction Reaction: When Defects Switch to Features.", *Advanced Functional Materials* **2021**, *31*, 2010052.

[159] V. V. Speybroeck, S. Vandenhaute, A. E. J. Hoffman, S. M. J. Rogge, "Towards modeling spatiotemporal processes in metal-organic frameworks.", *Trends in Chemistry* **2021**, *3*, 605–619.

[160] K. Müller, K. Fink, L. Schöttner, M. Koenig, L. Heinke, C. Wöll, "Defects as Color Centers: The Apparent Color of Metal-Organic Frameworks Containing Cu2+-Based Paddle-Wheel Units.", *ACS Applied Materials & Interfaces* **2017**, *9*, 37463–37467.

[161] C. Commons, Attribution 4.0 International (CC BY NC ND 4.0). **2022**, https://creativecommons.org/licenses/by-nc-nd/4.0/ (visited on 11/17/2022).

[162] T. D. Bennett, A. K. Cheetham, A. H. Fuchs, F.-X. Coudert, "Interplay between defects, disorder and flexibility in metal-organic frameworks.", *Nature chemistry* **2016**, *9*, 11–16.

[163] L. Valenzano, B. Civalleri, S. M. Chavan, S. Bordiga, M. H. Nilsen, S. N. Jakobsen, K. P. Lillerud, C. Lamberti, "Disclosing the Complex Structure of UiO-66 Metal Organic Framework: A Synergic Combination of Experiment and Theory.", *Chemistry of Materials* **2011**, *23*, 1700–1718.

[164] B. Bueken, N. V. Velthoven, A. Krajnc, S. Smolders, F. Taulelle, C. Mellot-Draznieks, G. Mali, T. D. Bennett, D. E. D. Vos, "Tackling the Defect Conundrum in UiO-66: A Mixed-Linker Approach to Engineering Missing Linker Defects.", *Chemistry of Materials* **2017**, *29*, 10478–10486.

[165] A. W. Thornton, R. Babarao, A. Jain, F. Trousselet, F.-X. Coudert, "Defects in metal-organic frameworks: a compromise between adsorption and stability?", *Dalton transactions* **2016**, *45*, 352–359.

[166] S. Krause, V. Bon, I. Senkovska, D. M. Többens, D. Wallacher, R. S. Pillai, G. Maurin, S. Kaskel, "The effect of crystallite size on pressure amplification in switchable porous solids.", *Nature Communications* **2018**, *9*, 1573.

[167] N. Kavoosi, V. Bon, I. Senkovska, S. Krause, C. Atzori, F. Bonino, J. Pallmann, S. Paasch, E. Brunner, S. Kaskel, "Tailoring adsorption induced phase transitions in the pillared-layer type metal-organic framework DUT-8(Ni).", *Dalton transactions* **2017**, *46*, 4685–4695.

[168] H. Miura, V. Bon, I. Senkovska, S. Ehrling, S. Watanabe, M. Ohba, S. Kaskel, "Tuning the gate-opening pressure and particle size distribution of the switchable metal-organic framework DUT-8(Ni) by controlled nucleation in a micromixer.", *Dalton transactions* **2017**, *46*, 14002–14011.

[169] S. Ehrling, I. Senkovska, V. Bon, J. D. Evans, P. S. Petkov, Y. Krupskaya, V. Kataev, T. Wulf, A. S. Krylov, A. N. Vtyurin, S. N. Krylova, S. V. Adichtchev, E. Slyusareva, M. S. Weiss, B. Büchner, T. Heine, S. Kaskel, "Crystal size versus paddle wheel deformability: selective gated adsorption transitions of the switchable metal–organic frameworks DUT-8(Co) and DUT-8(Ni).", *Journal of Materials Chemistry A* **2019**, *7*, 21459–21475.

[170] M. J. Thompson, C. L. Hobday, I. Senkovska, V. Bon, S. Ehrling, M. Maliuta, S. Kaskel, T. Düren, "Role of particle size and surface functionalisation on the flexibility behaviour of switchable metal-organic framework DUT-8(Ni).", *Journal of Materials Chemistry A* **2020**, *8*, 22703–22711.

[171] S. Ma, D. Sun, X.-S. Wang, H.-C. Zhou, "A mesh-adjustable molecular sieve for general use in gas separation.", *Angewandte Chemie Int. Ed.* **2007**, *46*, 2458–2462.

[172] Q. Tan, H. Huang, Y. Peng, Y. Chang, Z. Zhang, D. Liu, C. Zhong, "A temperature-responsive smart molecular gate in a metal-organic framework for task-specific gas separation.", *Journal of Materials Chemistry A* **2019**, *7*, 26574–26579.

[173] C. Gu, N. Hosono, J. J. Zheng, Y. K. Sato, S. Kusaka, S. Sakaki, S. Kitagawa, "Design and control of gas diffusion process in a nanoporous soft crystal.", *Science* **2019**, *363*, 387–391.

[174] P. Qin, S. Okur, C. Li, A. Chandresh, D. Mutruc, S. Hecht, L. Heinke, "A photoprogrammable electronic nose with switchable selectivity for VOCs using MOF films.", *Chemical Science* **2021**, *12*, 15700–15709.

[175] A. Kondo, T. Yashiro, N. Okada, S. Hiraide, T. Ohkubo, H. Tanaka, K. Maeda, "Selective molecular-gating adsorption in a novel copper-based metal-organic framework.", *Journal of Materials Chemistry* **2018**, *6*, 5910–5918.

[176] J. Shang, G. Li, R. Singh, Q. Gu, K. M. Nairn, T. J. Bastow, N. V. Medhekar, C. M. Doherty, A. J. Hill, J. Z. Liu, P. A. Webley, "Discriminative separation of gases by a molecular trapdoor mechanism in chabazite zeolites.", *Journal of the American Chemical Society* **2012**, *134*, 19246–19253.

[177] T. D. Baerdemaeker, D. E. D. Vos, "Gas separation: Trapdoors in zeolites.", *Nature Chemistry* **2013**, *5*, 89–90.

[178] H. Zeng, M. Xie, T. Wang, R.-J. Wei, X.-J. Xie, Y. Zhao, W. Lu, D. Li, "Orthogonal-array dynamic molecular sieving of propylene/propane mixtures.", *Nature* **2021**, *595*, 542–548.

[179] P. Kanoo, R. Matsuda, H. Sato, L. Li, N. Hosono, S. Kitagawa, "Pseudo Gated Adsorption with Negligible Volume Change Evoked by Halogen Bond Interaction in the Nanospace of MOFs.", *Chemistry* **2019**, *26*, 2148–2153.

[180] X. Luo, Z. Yin, M.-H. Zeng, M. Kurmoo, "The construction, structures, and functions of pillared layer metal–organic frameworks.", *Inorganic chemistry frontiers* **2016**, *3*, 1208–1226.

[181] N. C. Burtch, S. J. Baxter, J. Heinen, A. Bird, A. Schneemann, D. Dubbeldam, A. P. Wilkinson, "Negative Thermal Expansion Design Strategies in a Diverse Series of Metal-Organic Frameworks.", *Advanced Functional Materials* **2019**, *29*, 1904669.

[182] K. T. Butler, P. Vervoorts, M. G. Ehrenreich, J. Armstrong, J. M. Skelton, G. Kieslich, "Experimental Evidence for Vibrational Entropy as Driving Parameter of Flexibility in the Metal-Organic Framework ZIF-4(Zn).", *Chemistry of Materials* **2019**, *31*, 8366–8372.

[183] L. Vanduyfhuys, S. M. J. Rogge, J. Wieme, S. Vandenbrande, G. Maurin, M. Waroquier, V. V. Speybroeck, "Thermodynamic insight into stimuli-responsive behaviour of soft porous crystals.", *Nature Communications* **2017**, *9*, 204.

[184] E. Cockayne, "Thermodynamics of the Flexible Metal-Organic Framework Material MIL-53(Cr) From First Principles.", *The Journal of Physical Chemistry. C* **2017**, *121*, 4312–4317.

[185] S. Henke, A. Schneemann, S. Kapoor, R. H. A. Winter, R. A. Fischer, "Zinc-1,4-benzenedicarboxylate-bipyridine frameworks linker functionalization impacts network topology during solvothermal synthesis.", *Journal of Materials Chemistry* **2012**, *22*, 909–918.

[186] Z. Zhang, H. T. H. Nguyen, S. A. Miller, A. M. Ploskonka, J. B. DeCoste, S. M. Cohen, "Polymer-Metal-Organic Frameworks (polyMOFs) as Water Tolerant Materials for Selective Carbon Dioxide Separations.", *Journal of the American Chemical Society* **2016**, *138*, 920–925.

[187] S. Henke, R. A. Fischer, "Gated channels in a honeycomb-like zinc-dicarboxylate-bipyridine framework with flexible alkyl ether side chains.", *Journal of the American Chemical Society* **2011**, *133*, 2064–2067.

[188] N. L. Rosi, J. Kim, M. Eddaoudi, B. Chen, M. O'Keeffe, O. M. Yaghi, "Rod packings and metal-organic frameworks constructed from rod-shaped secondary building units.", *Journal of the American Chemical Society* **2005**, *127*, 1504–18.

[189] U. Böhme, B. S. Barth, C. Paula, A. Kuhnt, W. Schwieger, A. Mundstock, J. Caro, M. Hartmann, "Ethene/ethane and propene/propane separation via the olefin and paraffin selective metal-organic framework adsorbents CPO-27 and ZIF-8.", *Langmuir* **2013**, *29*, 8592–600.

[190] H. Abedini, A. Shariati, M. R. Khosravi-Nikou, "Adsorption of propane and propylene on M-MOF-74 (M = Cu, Co): Equilibrium and kinetic study.", *Chemical Engineering Research & Design* **2020**, *153*, 96–106.

[191] P. Wang, T. Kajiwara, K.-i. Otake, M. Yao, H. Ashitani, Y. Kubota, S. Kitagawa, "Xylene Recognition in Flexible Porous Coordination Polymer by Guest-Dependent Structural Transition.", *ACS Applied Materials & Interfaces* **2021**, *13*, 52144–52151.

[192] T. He, X.-J. Kong, Z.-X. Bian, Y.-Z. Zhang, G.-R. Si, L. Xie, X. Wu, H. Huang, Z. Chang, X.-H. Bu, M. J. Zaworotko, Z.-R. Nie, J.-R. Li, "Trace removal of benzene vapour using double-walled metal–dipyrazolate frameworks.", *Nature Materials* **2022**, *21*, 689–695.

[193] E. J. Carrington, C. A. McAnally, A. J. Fletcher, S. P. Thompson, M. R. Warren, L. Brammer, "Solvent-switchable continuous-breathing behaviour in a diamondoid metal-organic framework and its influence on CO2 versus CH4 selectivity.", *Nature chemistry* **2017**, *9*, 882–889.

[194] T. Kundu, M. Wahiduzzaman, B. B. Shah, G. Maurin, D. Zhao, "Solvent-Induced Control over Breathing Behavior in Flexible Metal-Organic Frameworks for Natural-Gas Delivery.", *Angewandte Chemie Int. Ed.* **2019**, *58*, 8073–8077.

[195] N. Kavoosi, T. M. Savchenko, I. Senkovska, M. Maliuta, V. Bon, A. Eychmüller, S. Kaskel, "Selective pore opening and gating of the pillared layer metal-organic framework DUT-8(Ni) upon liquid phase multi-component adsorption.", *Microporous and Mesoporous Materials* **2018**, *271*, 169–174.

[196] M. Rauche, S. Ehrling, S. Krause, I. Senkovska, S. Kaskel, E. Brunner, "New insights into solvent-induced structural changes of 13C labelled metal-organic frameworks by solid state NMR.", *Chemical Communications* **2019**, *55*, 9140–9143.

[197] P. Freund, I. Senkovska, B. Zheng, V. Bon, B. Krause, G. Maurin, S. Kaskel, "The force of MOFs: the potential of switchable metal-organic frameworks as solvent stimulated actuators.", *Chemical Communications* **2020**, *56*, 7411–7414.

[198] D. S. Sholl, Y. Yang, "A systematic examination of the impacts of MOF flexibility on intracrystalline molecular diffusivities.", *Journal of Materials Chemistry A* **2022**, *10*, 4242–4253.

[199] B. C. Bukowski, F. A. Son, Y. Chen, L. Robison, T. Islamoglu, R. Q. Snurr, O. K. Farha, "Insights into Mass Transfer Barriers in Metal–Organic Frameworks.", *Chemistry of Materials* **2022**, *34*, 4134–4141.

[200] F. A. Son, B. C. Bukowski, T. Islamoglu, R. Q. Snurr, O. K. Farha, "Rapid Quantification of Mass Transfer Barriers in Metal–Organic Framework Crystals.", *Chemistry of Materials* **2021**, *33*, 9093–9100.

[201] M. Tu, S. Wannapaiboon, K. Khaletskaya, R. A. Fischer, "Engineering Zeolitic-Imidazolate Framework (ZIF) Thin Film Devices for Selective Detection of Volatile Organic Compounds.", *Advanced Functional Materials* **2015**, *25*, 4470–4479.

[202] C. Reichardt, "Solvatochromic Dyes as Solvent Polarity Indicators.", *Chemical Reviews* **1994**, *94*, 2319–2358.

[203] C. H. Sharp, B. C. Bukowski, H. Li, E. M. Johnson, S. Ilic, A. J. Morris, D. Gersappe, R. Q. Snurr, J. R. Morris, "Nanoconfinement and mass transport in metal-organic frameworks.", *Chemical Society Reviews* **2021**, *50*, 11530–11558.

[204] A. K. Cheetham, R. Seshadri, F. Wudl, "Chemical synthesis and materials discovery.", *Nature Synthesis* **2022**, *1*, 514–520.

7

SUPPLEMENTARY INFORMATION

7.1 STUDY I

Supporting Information

Designing Adsorptive Gating via Linker Side-Chain Functionalization in a Honeycomb-MOF

Jan Berger,[†] Andreas Schneemann,[○] Inke Hante,[‡] Yuan Jing,[§] Jack D. Evans,[⁑] Yuh Hijikata,[#]

Jenny Pirillo,[#] Takashi Toyao,[§Δ] Ken-ichi Shimizu,[§Δ] Shin-ichiro Noro,[•] Gregor Kieslich[†] and

Roland A. Fischer[†]*

[†]Inorganic and Metal-Organic Chemistry, Technical University of Munich, Lichtenbergstr. 4, 85748 Garching, Germany

[○]Inorganic Chemistry I, Technical University Dresden, Bergstr. 66, 01069 Dresden, Germany

[‡]Inorganic Chemistry II, Ruhr University Bochum, Universitätsstr. 150, 44780 Bochum, Germany

[§]Institute for Catalysis, Hokkaido University, N-21 W-10, Sapporo 001-0021, Japan

[⁑]Centre for Advanced Nanomaterials and Department of Chemistry, The University of Adelaide, North Terrace, Adelaide, South Australia 5000, Australia

[#]Institute for Chemical Reaction Design and Discovery (WPI-ICReDD), Hokkaido University, N-21 W-10, Sapporo 001-0021, Japan

[Δ]Elements Strategy Initiative for Catalysis and Batteries, Kyoto University, Katsura, Kyoto 615-8520, Japan

[•]Faculty of Environmental Earth Science, Hokkaido University, Sapporo 060-0810, Japan

Content

S1 Linker and MOF synthesis

S1.1 General remarks

All chemicals were purchased from commercial suppliers (Sigma-Aldrich, Fluka, Alfa Aesar, ABCR and others) and used without further purification. MOF synthesis was conducted with pure N,N-dimethylformamide (DMF) (99.8%). Fresh DMF was used for solvent exchange. Ethanol for solvent exchange was purchased as technical grade and redistilled prior use. All experiments and procedures were carried out on air unless stated otherwise.

Liquid state NMR spectra were recorded on a Bruker Ultrashield DRX400 spectrometer (^{1}H: 400.13 MHz) at ambient temperature (298 K). Data was processed using MestReNova by Mestrelab Research. The ^{1}H NMR spectroscopic chemical shifts δ are reported in ppm relative to tetramethylsilane. ^{1}H NMR spectra are referenced against the residual proton and natural abundance carbon resonances of the respective deuterated solvent as an internal standard (DMSO-d_6: δ (H) = 2.50 ppm). MOF samples were digested and subsequently measured in 0.5 ml DMSO-d_6 with 0.05 ml DCl (7.6 N), all other substances were dissolved and measured in DMSO-d_6. Elemental analysis was provided and conducted by the TUM CRC Microanalytical Laboratory. CHNS contents were determined *via* combustion analysis.

S1.2 Linker synthesis

Organic linkers were synthesized *via* Williamson Etherification according to literature known procedures,[1] albeit slightly altered/optimized.

Dimethyl-2,5-dihydroxy-1,4-benzenedicarboxylate

2,5-Dihydroxyterephthalic acid (6,0 g, 30.3 mmol) is dispersed in MeOH (180 mL) and H_2SO_4 (98%, 5 mL, 94 mmol) is added dropwise at room temperature while stirring and the reaction mixture is refluxed for 12 h at 75 °C. The precipitate is subsequently filtrated and thoroughly washed with distilled water. After removing residual solvent *in vacuo* at 75 °C, the product is obtained as yellow powder (6.63 g, 28.9 mmol, 95 %).

^{1}H-NMR (400.13 MHz, DMSO-d_6) δ (ppm) = 9.82 (s, 2H, COOH), 7.26 (s, 2H, H$_{Ar}$), 3.86 (s, 6H, CH$_3$).

2,5-Dipropoxy-1,4-benzenedicarboxylic acid (DP-H$_2$bdc)

Dimethyl-2,5-dihydroxy-1,4-benzenedicarboxylate (2.00 g, 8.84 mmol, 1.0 eq.) and dry K_2CO_3 (3.00 g, 21.7 mmol, 2.5 eq.) are suspended in DMF (150 mL). 1-Bromopropane (2.41 mL, 26.5 mmol, 3 eq.) is added dropwise while stirring. The reaction mixture is refluxed overnight at 75 °C, the solvent is subsequently removed at 70 °C under reduced pressure (5 mbar). A solution of KOH (1.74 g, 30.5 mmol, 3.5 eq.) in H_2O (250 mL) is added to the residue. The reaction mixture is again refluxed overnight at 110 °C. After cooling to room temperature HCl (10%) is added dropwise until the carboxylic acid is completely precipitated. The solid is filtered and thoroughly washed with distilled water. After removing residual water *in vacuo* at 70 °C, the product (2.15 g, 4.27 mmol, 86 %) is obtained as white/slightly beige powder.

^{1}H-NMR (400.13 MHz, DMSO-d_6) δ (ppm) = 12.92 (bs, 2H, COOH), 7.26 (s, 2H, H$_{Ar}$), 3.95 (t, *J* = 6.4 Hz, 4H, O-CH$_2$), 1.78 - 1.62 (m, 4H, CH$_2$), 0.97 (t, *J* = 7.4 Hz, 6H, CH$_3$).

2,5-Bis(allyloxy)-1,4-benzenedicarboxylic acid (BA-H$_2$bdc)

Dimethyl-2,5-dihydroxy-1,4-benzenedicarboxylate (2.00 g, 8.84 mmol, 1.0 eq.) and dry K$_2$CO$_3$ (3.00 g, 21.7 mmol, 2.5 eq.) are suspended in DMF (150 mL). Allyl bromide (2.29 mL, 26.5 mmol, 3.0 eq.) is added dropwise while stirring. The reaction mixture is refluxed overnight at 75 °C, the solvent is subsequently removed at 70 °C under reduced pressure (5 mbar). A solution of KOH (1.74 g, 30.5 mmol, 3.5 eq.) in H$_2$O (250 mL) is added to the residue. The reaction mixture is again refluxed overnight at 110 °C. After cooling to room temperature HCl (10%) is added dropwise until the carboxylic acid is completely precipitated. The solid is filtered and thoroughly washed with distilled water. After removing residual solvent *in vacuo* at 70 °C, the product (2.09 g, 7.51 mmol, 85 %) is obtained as beige powder.

^{1}H-NMR (400.13 MHz, DMSO-d_6) δ (ppm) = 13.01 (s, 2H, COOH), 7.31 (s, 2H, H$_{Ar}$), 6.09 – 5.94 (m, 2H, CH), 5.44 (dd, J = 17.2, 1.8 Hz, 2H, CH$_2$), 5.24 (dd, J = 10.6, 1.9 Hz, 2H, CH$_2$), 4.60 (dt, J = 4.8, 1.7 Hz, 4H, O-CH$_2$).

2,5-Bis(prop-2-ynyloxy)-1,4-benzenedicarboxylic acid (BPY-H$_2$bdc)

Dimethyl-2,5-dihydroxy-1,4-benzenedicarboxylate (2.00 g, 8.84 mmol, 1.0 eq.) and dry K$_2$CO$_3$ (3.02 g, 21.9 mmol, 2.5 eq.) are suspended in DMF (100 mL). While stirring and heating the reaction mixture to 70 °C propargyl bromide (1.95 mL, 20.6 mmol, 2.3 eq.) is added dropwise. After the reaction mixture is refluxed for 2 hours at 70 °C a second portion of propargyl bromide (0.2 mL, 2.6 mmol, 0.3 eq.) is added. The reaction mixture is refluxed for 18 h at 75 °C, the solvent is subsequently removed at 70 °C under reduced pressure (5 mbar). A solution of NaOH (2.55 g, 63.8 mmol, 7.2 eq.) in H$_2$O (140 mL) is added to the residue and the reaction mixture is refluxed for 3 h at 75 °C. After cooling to room temperature HCl (10%) is added dropwise until the carboxylic acid is completely precipitated. The solid is filtered and thoroughly washed with water. After removing residual solvent *in vacuo* at 70 °C, the product (2.07 g, 7.53 mmol, 86 %) is obtained as beige/brown powder.

^{1}H-NMR (400.13 MHz, DMSO-d_6) δ (ppm) = 13.12 (s, 2H, COOH), 7.43 (s, 2H, H$_{Ar}$), 4.85 (s, 4H, O-CH$_2$), 3.61 (t, J = 2.4 Hz, 2H, CH).

2,5-Dibutoxy-1,4-benzendicarboxylic acid (DB-H$_2$bdc)

Dimethyl-2,5-dihydroxy-1,4-benzenedicarboxylate (1.36 g, 6.0 mmol, 1.0 eq.) and dry K$_2$CO$_3$ (2.9 g, 21.0 mmol, 3.5 eq.) are suspended in DMF (300 mL). 1-Bromobutane (2.36 mL, 24.0 mmol, 4 eq.) is added dropwise while stirring. The reaction mixture is refluxed overnight at 75 °C, the solvent is subsequently removed at 70 °C under reduced pressure (5 mbar). A solution of KOH (1.18 g, 21.0 mmol, 3.5 eq.) in H$_2$O (300 mL) is added to the residue. The reaction mixture is again refluxed overnight at 110 °C. After cooling to room temperature HCl (10%) is added dropwise until the carboxylic acid is completely precipitated. The solid is filtered and thoroughly washed with distilled water. After removing residual water *in vacuo* at 70 °C, the product (1.52 g, 4.90 mmol, 82 %) is obtained as white powder.

^{1}H-NMR (400.13 MHz, DMSO-d_6) δ (ppm) = 12.90 (bs, 2H, COOH), 7.27 (s, 2H, H$_{Ar}$), 3.99 (t, J = 6.3 Hz, 4H, O-CH$_2$), 1.78 – 1.61 (m, 4H, CH$_2$), 1.55 – 1.38 (m, 4H, CH$_2$'), 0.92 (t, J = 7.4 Hz, 6H, CH$_3$).

2,5-Diethoxy-1,4-benzendicarboxylic acid (DE-H$_2$bdc)

Dimethyl-2,5-dihydroxy-1,4-benzenedicarboxylate (2.00 g, 8.84 mmol, 1.0 eq.) and dry K$_2$CO$_3$ (3.00 g, 21.7 mmol, 2.5 eq.) are suspended in DMF (100 mL). Ethyl bromide (1.39 mL, 18.56 mmol, 2.1 eq.) is added dropwise while stirring. The reaction mixture is refluxed overnight at 75 °C, the solvent is subsequently removed at 70 °C under reduced pressure (5 mbar). A solution of KOH (1.18 g, 21.0 mmol, 3.5 eq.) in H$_2$O (150 mL) is added to the residue. The reaction mixture is again refluxed overnight at 110 °C. After cooling to room temperature HCl (10%) is added dropwise until the carboxylic acid is completely precipitated. The solid is filtered and thoroughly washed with distilled water. After removing residual water *in vacuo* at 70 °C, the product (2.04 g, 8.03 mmol, 91 %) is obtained as white powder.

S1.3 MOF synthesis

General procedure for Zn$_2$(fu-bdc)$_2$bipy

Zn(NO$_3$)$_2$·6 H2O (1 eq.), 4,4-bipyridine (1 eq) and the 2,5-functionalized 1,4-benzenedicarboxylic acid (1 eq, see **Table S1**) are dissolved in dimethyl formamide/ ethanol (2:1 ratio, see **Table S1**) in a screw cap bottle and sonicated for 5 min. The clear solution is heated to 85 °C for 48 h in an oven to yield a crystalline powder (with color ranging from white to brown depending on the linker used).

Washing and activation procedure

Washing and solvent exchange steps are conducted by vigorously shaking solid and solvent in a capped centrifuge tube, then centrifugation and decanting of the supernatant.

The obtained powder is washed with DMF (2x 40 ml) until the supernatant is colorless to remove residual educts and reaction byproducts. To remove DMF, the powder is first washed with ethanol (40 ml), then twice soaked in fresh ethanol (2x 40 ml) overnight, and lastly soaked once in dichloromethane (40 ml) overnight. The wet powder is then pre-dried on air at ambient conditions, before proper activation *in vacuo* at r.t. for 16 h and for 4 h at 80 °C. The resulting **dry** samples are stored under argon for further use.

Table S1: Functionalized linker and solvent amount used.

	[mg]	[mmol]	In DMF/EtOH [ml]
DP-H$_2$bdc	863	3.1	130/65
BA-H$_2$bdc	825	3.0	130/65
BPY-H$_2$bdc	902	3.3	140/70
DB-H$_2$bdc	825	2.7	120/60
DE-H$_2$bdc	803	3.2	140/70

[Zn$_2$(DPbdc)$_2$bipy] ^{1}**H NMR** (400.13 MHz, DMSO-*d6*) δ(ppm) = 9.07 (t, J = 7.3 Hz, 4H, bipy), 8.59 (t, J = 6.4 Hz, 4H, bipy), 7.13 (s, 2H, H$_{Ar}$), 3.83 (q, J = 5.9 Hz, 8H, O-CH$_2$), 1.57 (hept, J = 5.7 Hz, 8H, CH$_2$), 0.84 (q, J = 7.0 Hz, 12H, CH$_3$). **Elemental analysis:** calculated C 53.70, H 4.99, N 3.30, O 22.61, Zn 15.41; found C 53.89, H 4.85, N 3.38;

[Zn$_2$(BAbdc)$_2$bipy] ^{1}**H NMR** (400.13 MHz, DMSO-*d6*) δ (ppm) = 9.04 (d, J = 5.9 Hz, 4H, bipy), 8.57 (d, J = 5.8 Hz, 4H, bipy), 7.11 (s, 2H, H$_{Ar}$), 5.87 (ddq, J = 14.2, 8.6, 4.4 Hz, 4H, CH), 5.20 (dd, J = 56.8, 14.4 Hz, 9H, O-CH$_2$), 4.47 (d, J = 4.6 Hz, 8H, CH2). **Elemental analysis:** calculated C 54.22, H 4.07, N 3.33, O 22.82, Zn 15.55; found C 54.74, H 4.09, N 3.52;

[Zn₂(BPYbdc)₂bipy] ^{1}**H NMR** (400.13 MHz, DMSO-*d6*) δ (ppm) = 9.06 – 8.99 (m, 4H, bipy), 8.57 (d, J = 5.6 Hz, 4H, bipy), 7.12 (s, 9H, H$_{Ar}$), 4.72 (d, J = 2.6 Hz, 8H,O-CH₂), 3.38 (dt, J = 7.0, 3.2 Hz, 4H, CH). **Elemental analysis:** calculated C 54.74, H 3.15, N 3.36, O 23.04, Zn 15.71; found C 53.77, H 3.07, N 3.69;

[Zn₂(DBbdc)₂bipy] ^{1}**H NMR** (400.13 MHz, DMSO-*d6*) δ (ppm) = 9.09 – 9.04 (m, 4H, bipy), 8.62 – 8.56 (m, 4H, bipy), 7.14 (s, 4H, H$_{Ar}$), 3.87 (t, J = 6.3 Hz, 8H, O-CH₂), 1.60 – 1.48 (m, 8H, CH₂), 1.35 – 1.24 (m, 8H, CH₂), 0.78 (t, J = 7.4 Hz, 12H, CH₃). **Elemental analysis:** calculated C 55.68, H 5.57, N 3.09, O 21.21, Zn 14.45; found C 55.15, H 5.50, N 3.26;

[Zn₂(DEbdc)₂bipy] ^{1}**H NMR** (400.13 MHz, DMSO-*d6*) δ (ppm) = 9.03 – 8.96 (m, 4H, bipy), 8.56 – 8.49 (m, 4H, bipy), 7.11 (s, 4H, H$_{Ar}$), 3.89 (q, J = 6.9 Hz, 8H, O-CH₂), 1.13 (t, J = 7.0 Hz, 12H, CH₃). **Elemental analysis:** calculated C 51.60, H 4.08, N 3.54, O 24.26, Zn 16.53; found C 51.04, H 4.08, N 3.58;
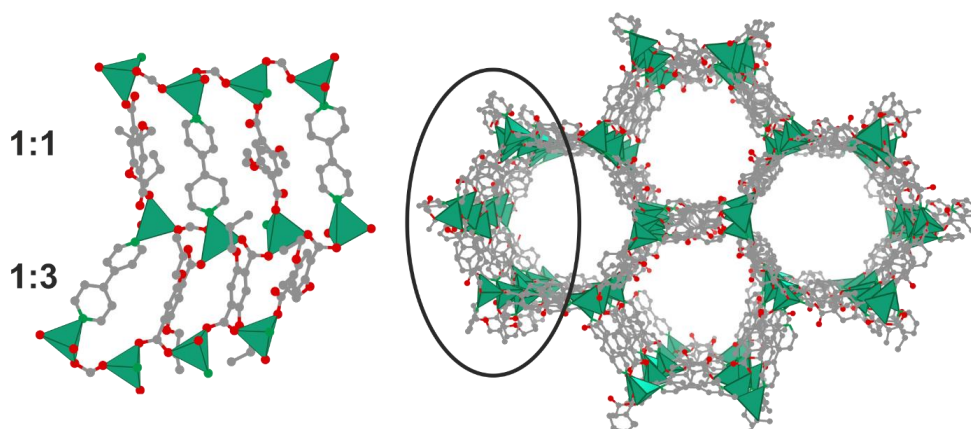
Figure S1. Visualization of linker stacking in both types of pore wall with 1:1 and 1:3 bipy to fu-bdc^{2-} ratio. Shown left is the smallest repeating segment. Grey = carbon, red = oxygen, light green = nitrogen, tetrahedra = coordination sphere of Zn atoms.

S2 Thermogravimetric analysis

TGA was conducted on a Netzsch TG-DSC STA 449 F5 in a temperature range from 25 °C to 800 °C with a heating rate of 10 K min^{-1} under argon flow (flow rate: 20 mL min^{-1}). It should be noted that the sample is briefly (few seconds) exposed to air before the measurement when the aluminium oxide pan is transferred from the Ar filled transport vial to the pan holder stage.
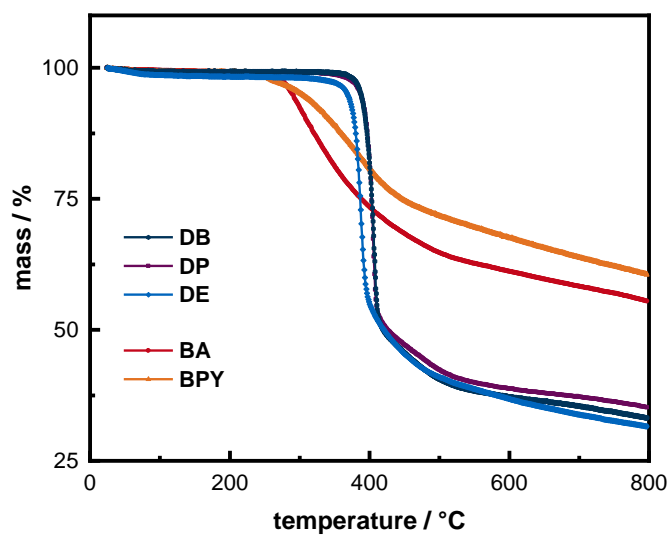
Figure S2: Thermogravimetric analysis of all Honeycomb-MOF materials conducted with **dry** samples. Unsaturated functionalizations (**BA** and **BPY**) lead to material decomposition at lower temperatures (ca. 230 °C) compared to all materials with saturated functionalizations (**DB**, **DP**, and **DE**) that decompose at ca. 350 °C.

S3 Powder X-ray diffraction

Activated **dry** samples were filled in glass capillaries in a glovebox under argon atmosphere and PXRDs were measured in Debeye-Scherrer geometry on a PANalytical Empyrean diffractometer. X-ray Cu Kα radiation (λ = 1.54 Å) with a voltage of 45 kV and current of 40 mA was used.

Figure S3: PXRDs of activated materials **DP**, **BA**, **BPY**, **DB**, and **DE**. All pattern normalized to peaks of highest intensity. Simulated pattern taken from the isostructural parent material .cif file found in literature.[2,3]
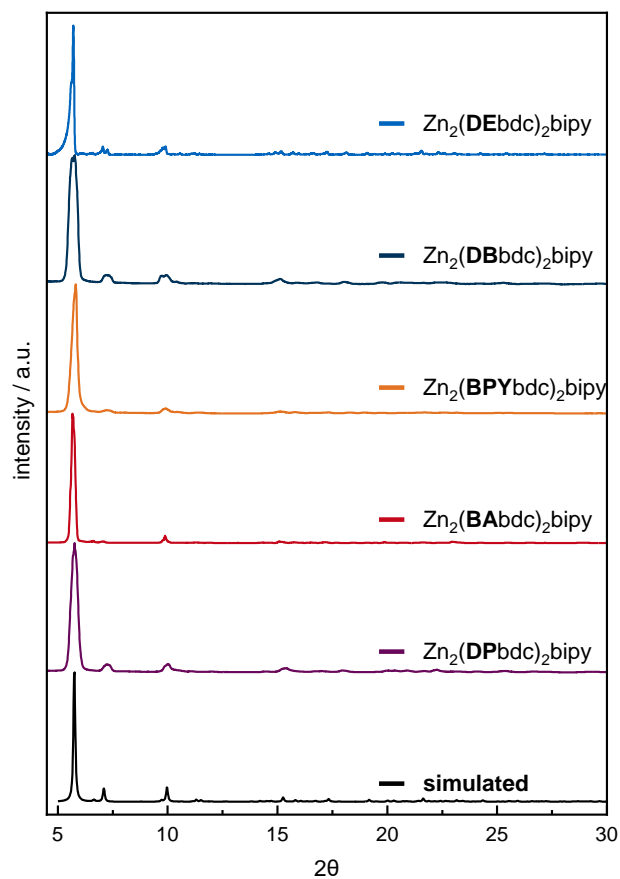
S4 Sorption isotherms

All adsorption isotherms are accessible online free of charge as adsorption information files to counter issues with post-publishing adsorption data extraction and facilitate machine learning (see **ESI**).

Adsorption measurements with N_2 (>99.999 vol%) at 77 K, CO_2 (>99.995 vol%), and C_2H_2 (>99.5 %, solvent free) each at 298 K, 288 K and 278 K were carried out on a 3Flex Physisorption from Micromeritics Instrument Corp., which uses a manometric method to determine the amount adsorbed at an equilibrated gas pressure.

Activated samples were transferred under dry Ar atmosphere into pre-weighed sample tubes and capped with Micromeritics CheckSeals. Samples were subsequently activated again at 80 °C for 5 h under dynamic vacuum of ca. $1x10^{-3}$ mbar using a SmartVacPrep by Micromeritics Instrument Corp. to ensure absence of unwanted adsorbates and identical pre-measurement states of all samples. The mass of the adsorbent was then recorded, generally in the range of 70-100 mg. To facilitate proper degassing in context of the highly diffusion hindering pore environment, prior to each measurement samples were evacuated in situ at 80 °C for 20 h under dynamic vacuum of ca. $1x10^{-5}$ mbar. Free space of the sample tube was determined prior measuring each adsorption isotherm using helium (>99.999 vol%). A liquid nitrogen bath was used for measurements at 77 K and a Peltier device regulated water bath was used for measurements at 298 K, 288 K and 278 K.

S4.1 N_2 sorption isotherms

Nitrogen uptake and equilibration times for **DP**, **BA**, and **BPY** are in accordance with the determined limiting pore diameters. Notably, equilibration times for **DP** and **BA** ranged from 0.5 to 7 h per data point in the low-pressure region and measurements were therefore conducted with more limited resolution.
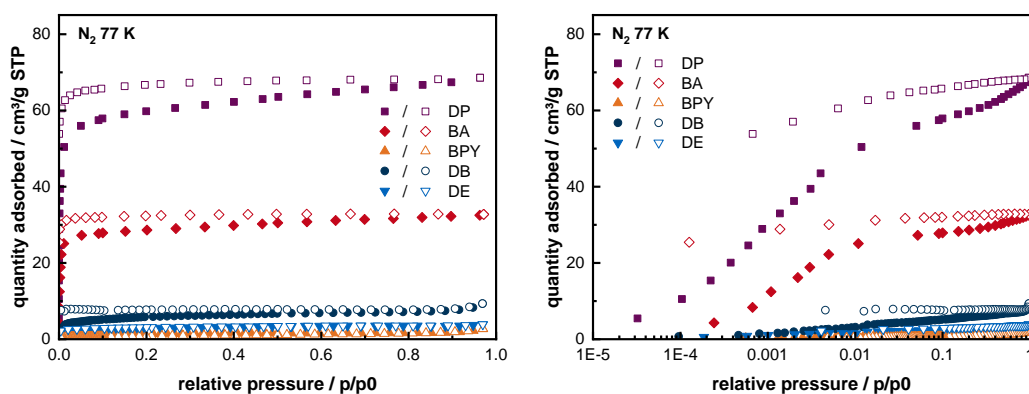
Figure S4: Isotherms of N_2 at 77 K on all functionalized honeycomb MOF derivatives (left: regular; right: semilogarithmic). Adsorption (filled symbols) and desorption (open symbols), respectively.

S4.2 BET surface area determination

The apparent surface areas of all materials were derived using the Brunauer-Emmett-Teller (BET) model, are hence given as apparent BET surface areas, and are based on N_2 isotherms measured at 77 K (see **S4**). To determine the apparent BET areas for microporous materials care was taken to adhere to the Rouquerol criteria.[4,5]

BET surface area: 229,2815 ± 1,2343 m²/g
C: 1.341,943725
Qm: 52,6772 cm³/g STP
Correlation coefficient: 0,9999277

p/p°	cm³/g STP	1/[Q(p°/p - 1)]
0.002	36.21716	5.53388E-5
0.00308	39.42262	7.84525E-5
0.00402	43.4639	9.28263E-5
0.0118	50.37478	2.37072E-4
0.05016	55.91423	9.44406E-4
0.09054	57.42089	0.00173
0.09983	57.87061	0.00192
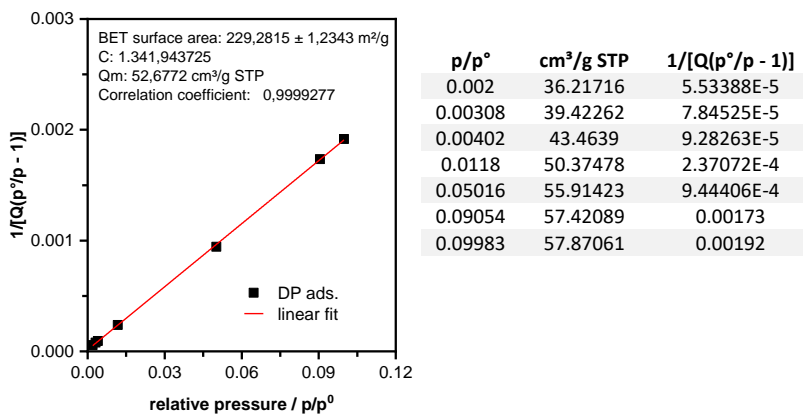
Figure S5: BET plot of fitted region in **DP** N_2 isotherm. Tabular report for reference of monolayer capacity (Qm).

BET surface area: 110,2764 ± 0,9449 m²/g
C: 2.209,643590
Qm: 25,3359 cm³/g STP
Correlation coefficient: 0,9998536

p/p°	cm³/g STP	1/[Q(p°/p - 1)]
0.00301	18.8674	1.60233E-4
0.00497	22.19331	2.25112E-4
0.01087	25.05148	4.38507E-4
0.05189	27.23239	0.00201
0.09062	27.70106	0.0036
0.09994	27.86341	0.00398
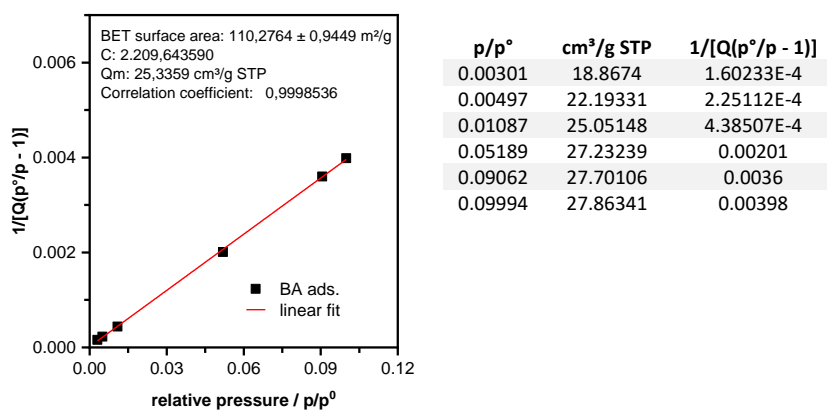
Figure S6: BET plot of fitted region in **BA** N_2 isotherm. Tabular report for reference of monolayer capacity (Qm).

BET surface area: 5,0603 ± 0,0175 m²/g
C: 129,501947
Qm: 1,1626 cm³/g STP
Correlation coefficient: 0,9999038
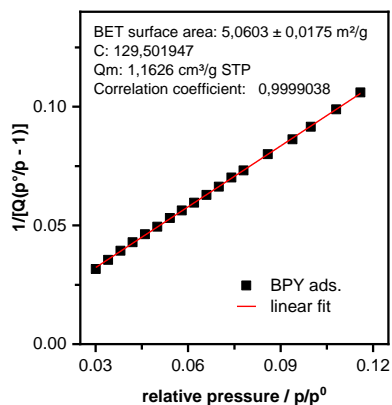
p/p°	cm³/g STP	1/[Q(p°/p - 1)]
0.04198	1.02321	0.04283
0.04601	1.04354	0.04621
0.05	1.06402	0.04946
0.05411	1.07788	0.05307
0.05797	1.0933	0.05629
0.06199	1.10913	0.05959
0.06597	1.12474	0.0628
0.06999	1.13601	0.06624
0.07408	1.14034	0.07016
0.078	1.15688	0.07312
0.08584	1.17463	0.07994
0.0939	1.20169	0.08624
0.09986	1.2118	0.09155
0.10804	1.22509	0.09887
0.11598	1.23771	0.106

Figure S7: BET plot of fitted region in **BPY** N$_2$ isotherm. Tabular report for reference of monolayer capacity (Qm).

BET surface area: 10,3220 ± 0,0654 m²/g
C: 230,649641
Qm: 2,3715 cm³/g STP
Correlation coefficient: 0,9997581
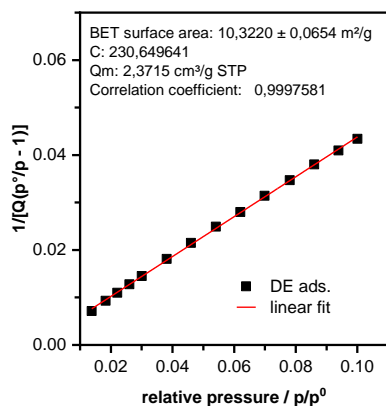
p/p°	cm³/g STP	1/[Q(p°/p - 1)]
0.01382	1.95882	0.00715
0.01835	2.01036	0.0093
0.02207	2.05458	0.01098
0.02607	2.09535	0.01277
0.03006	2.13441	0.01452
0.03816	2.18941	0.01812
0.04603	2.24699	0.02147
0.05413	2.29579	0.02493
0.06202	2.36128	0.028
0.06995	2.39303	0.03143
0.07808	2.44176	0.03469
0.08605	2.47692	0.03801
0.0939	2.52953	0.04097
0.10006	2.56104	0.04342
0.01382	1.95882	0.00715

Figure S8: BET plot of fitted region in **DE** N$_2$ isotherm. Tabular report for reference of monolayer capacity (Qm).

BET surface area: 21,2491 ± 0,0718 m²/g
C: 157,507360
Qm: 4,8819 cm³/g STP
Correlation coefficient: 0,9999252
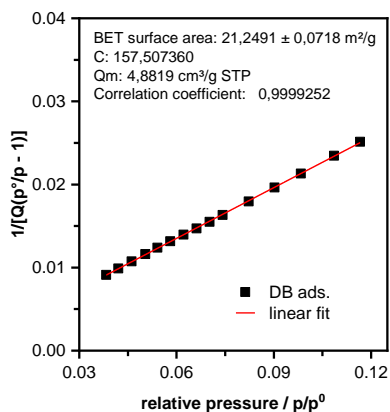
p/p°	cm³/g STP	1/[Q(p°/p - 1)]
0.03835	4.37768	0.00911
0.04208	4.44876	0.00988
0.04617	4.50755	0.01074
0.05035	4.56941	0.0116
0.0541	4.61615	0.01239
0.0581	4.68666	0.01316
0.06213	4.74923	0.01395
0.06616	4.82181	0.01469
0.07018	4.86892	0.0155
0.07422	4.90852	0.01633
0.08224	4.99335	0.01795
0.09026	5.0537	0.01963
0.09834	5.11747	0.02131
0.10857	5.19359	0.02345
0.11662	5.25396	0.02513

Figure S9: BET plot of fitted region in **DB** N$_2$ isotherm. Tabular report for reference of monolayer capacity (Qm).

S4.3 CO₂ and C₂H₂ sorption isotherms
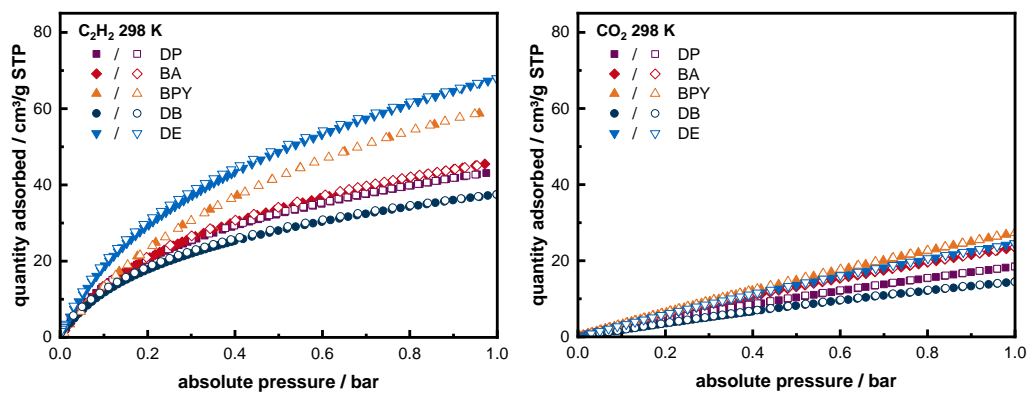
Figure S10: Isotherms of C_2H_2 and CO_2 at 298 K on all functionalized honeycomb-like MOF derivatives. Adsorption (filled symbols) and desorption (open symbols), respectively. For isotherms measured at 288 K and 278 K see **S5**.

S5 Enthalpy of adsorption determination

The binding energy of C_2H_2 and CO_2 to the adsorption sites (isosteric enthalpy of adsorption, ΔH_{ads}) within the materials **DP**, **BA**, **BPY**, **DB**, and **DE** were determined from the temperature dependence of the adsorption isotherms using the Clausius–Clapeyron expression. The isosteric enthalpy of adsorption can be derived at a constant loading by

$$\Delta H_{ads} = -R \frac{d(ln\ p)}{d(1/T)}$$

where R is the ideal gas constant, p is the pressure at a given loading and T is the temperature (278 K, 288 K or 298 K) at which the isotherm was measured.

To obtain a description of p at any given loading, isotherms were fitted using a dual-site Langmuir–Freundlich equation, given by

$$V_{ads} = \frac{q_{sat,1}\ K_1\ p^{v_1}}{1 + K_1\ p^{v_1}} + \frac{q_{sat,2}\ K_2\ p^{v_2}}{1 + K_2\ p^{v_2}}$$

where V_{ads} is the amount adsorbed in cm^3/g, q_{sat} is the amount adsorbed when saturated with the gas in cm^3/g, K is the Langmuir–Freundlich constant in bar^{-1}, p is the gas pressure in bar, v is the dimensionless Freundlich parameter and subscripts *1* and *2* correspond to two different site identities. These parameters and fits are given below (see **Figures S11 – S13**), fits were performed in OriginPro 2020 by OriginLab Corp..
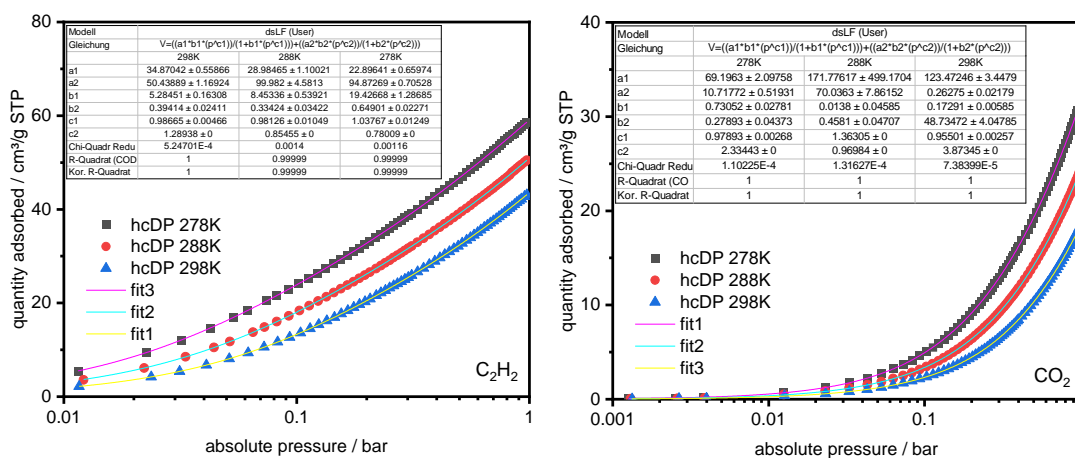
Figure S11: Semilogarithmic plots of isotherms (dots) of C_2H_2 and CO_2 at 298 K, 288 K, and 278 K on **DP** with corresponding fits (solid lines) and fitting parameters.

Figure S12: Semilogarithmic plots of isotherms (dots) of C_2H_2 and CO_2 at 298 K, 288 K, and 278 K on **BA**, **BPY**, and **DB** with corresponding fits (solid lines) and fitting parameters.

C$_2$H$_2$ (left plot):

Modell	dsLF (User)		
Gleichung	V=((a1*b1*(p^c1))/(1+b1*(p^c1)))+((a2*b2*(p^c2))/(1+b2*(p^c2)))		
	278K	288K	298K
a1	13.91013 ± 0.31155	126.82405 ± 5.13158	222.60467 ± 16.29051
a2	222.63649 ± 1.83737	6.60807 ± 3.54433	12.88932 ± 0.8213
b1	38.50053 ± 1.00802	1.55888 ± 0.11225	0.33663 ± 0.03858
b2	0.56639 ± 0.00941	1.4636 ± 1.11751	13.57662 ± 0.51121
c1	1.33263 ± 0	0.74623 ± 0.00855	0.6689 ± 0.00901
c2	0.58942 ± 0	3.90086 ± 1.28794	1.38786 ± 0
Chi-Quadr Redu	0.01234	0.02457	0.00436
R-Quadrat (COD)	0.99999	0.99996	0.99999
Kor. R-Quadrat	0.99999	0.99996	0.99999

Legend: hcDE 278K, hcDE 288K, hcDE 298K, fit1, fit2, fit3 — C$_2$H$_2$

x-axis: absolute pressure / bar; y-axis: quantity adsorbed / cm³/g STP

CO$_2$ (right plot):

Modell	dsLF (User)		
Gleichung	V=((a1*b1*(p^c1))/(1+b1*(p^c1)))+((a2*b2*(p^c2))/(1+b2*(p^c2)))		
Zeichnen	278K	288K	298K
a1	110.92284 ± 1.14036	117.39201 ± 1.59067	126.65926 ± 5.48274
a2	5.59502 ± 0.98912	1.93346 ± 1.29638	0.93122 ± 0.38178
b1	0.5685 ± 0.008	0.3695 ± 0.00546	0.23755 ± 0.01188
b2	0.26146 ± 0.06872	0.45994 ± 0.3654	0.39615 ± 0.3182
c1	0.97541 ± 0.0016	0.97758 ± 0	0.98356 ± 0.0029
c2	4.80886 ± 0	4.81396 ± 1.0404	4.9771 ± 0
Chi-Quadr Redu	2.41097E-4	2.40252E-4	2.13094E-4
R-Quadrat (CO	1	1	1
Kor. R-Quadrat	1	1	1

Legend: hcDE 278K, hcDE 288K, hcDE 298K, fit1, fit2, fit3 — CO$_2$

x-axis: absolute pressure / bar; y-axis: quantity adsorbed / cm³/g STP

Figure S13: Semilogarithmic plots of isotherms (dots) of C$_2$H$_2$ and CO$_2$ at 298 K, 288 K, and 278 K on **DE** with corresponding fits (solid lines) and fitting parameters.

S6 IAST selectivity determination

Isotherm fits were performed on isotherms measured at 298 K with a dual-site Langmuir–Freundlich equation to obtain a description of p at any given loading. For details on fitting see chaperter **S5** and below (**Figures S14 – S16**).

Zn$_2$(DP-bdc)$_2$(bipy)

Equation	Vads=Vmax1*K1*p^n1/(1+K1*p^n1)+Vmax2*K2*p^n2/(1+K2*p^n2)	
Adj. R-Square	1	
C2H2	Value	Standard Error
Quantity Adsorbed Vmax1 (cm³/g STP)	34.81531	3.23394
Quantity Adsorbed K1 (cm³/g STP)	0.05625	0.00345
Quantity Adsorbed n1 (cm³/g STP)	0.98672	0.00633
Quantity Adsorbed Vmax2 (cm³/g STP)	50.70616	14.28195
Quantity Adsorbed K2 (cm³/g STP)	0.00105	7.82071E-4
Quantity Adsorbed n2 (cm³/g STP)	1.28585	0.19511

Equation	Vads=Vmax1*K1*p^n1/(1+K1*p^n1)+Vmax2*K2*p^n2/(1+K2*p^n2)	
Adj. R-Square	0.99997	
CO2	Value	Standard Error
Quantity Adsorbed Vmax1 (cm³/g STP)	0.29449	0.10693
Quantity Adsorbed K1 (cm³/g STP)	4.26788E-6	1.94373E-5
Quantity Adsorbed n1 (cm³/g STP)	4.16984	1.58293
Quantity Adsorbed Vmax2 (cm³/g STP)	163.30294	28.35786
Quantity Adsorbed K2 (cm³/g STP)	0.0015	2.48721E-4
Quantity Adsorbed n2 (cm³/g STP)	0.94227	0.00762

Zn$_2$(BA-bdc)$_2$(bipy)

Equation	Vads=Vmax1*K1*p^n1/(1+K1*p^n1)+Vmax2*K2*p^n2/(1+K2*p^n2)	
Adj. R-Square	0.99999	
C2H2	Value	Standard E
Quantity Adso Vmax1	191.015	36.66225
Quantity Adso K1	9.61958	2.22925E-
Quantity Adso n1	1	0
Quantity Adso Vmax2	35.7888	0.50342
Quantity Adso K2	0.04549	5.58494E-
Quantity Adso n2	1	0

Equation	Vads=Vmax1*K1*p^n1/(1+K1*p^n1)+Vmax2*K2*p^n2/(1+K2*p^n2)	
Adj. R-Square	0.99998	
CO2	Value	Standard Error
Quantity Adsorbed Vmax1 (cm³/g STP)	141.92154	37.88935
Quantity Adsorbed K1 (cm³/g STP)	0.00144	6.40916E-4
Quantity Adsorbed n1 (cm³/g STP)	1.00668	0.03187
Quantity Adsorbed Vmax2 (cm³/g STP)	1.80449	2.12185
Quantity Adsorbed K2 (cm³/g STP)	0.01007	0.009
Quantity Adsorbed n2 (cm³/g STP)	1.44612	0.4936

Figure S14: Semilogarithmic plots of isotherms (dots) of C$_2$H$_2$ and CO$_2$ at 298 K on **DP** and **BA** with corresponding fits (solid lines) and fitting parameters.

Zn$_2$(BPY-bdc)$_2$(bipy)

Equation	Vads=Vmax1*K1*p^n1/(1+K1*p^n1)+Vmax2*K2*p^n2/(1+K2*p^n2)	
Adj. R-Square	0.99999	
C2H2	Value	Standard Error
Quantity Adsorbed (cm³/g STP) Vmax1	43.63745	6.1048
Quantity Adsorbed (cm³/g STP) K1	0.02796	0.00214
Quantity Adsorbed (cm³/g STP) n1	1	0
Quantity Adsorbed (cm³/g STP) Vmax2	82.6819	1.46986
Quantity Adsorbed (cm³/g STP) K2	0.00506	0.001
Quantity Adsorbed (cm³/g STP) n2	1	0

Equation	Vads=Vmax1*K1*p^n1/(1+K1*p^n1)+Vmax2*K2*p^n2/(1+K2*p^n2)	
Adj. R-Square	0.99999	
CO2	Value	Standard Error
Quantity Adsorbed (cm³/g STP) Vmax1	60.97968	13.65989
Quantity Adsorbed (cm³/g STP) K1	3.44889E-4	2.72631E-4
Quantity Adsorbed (cm³/g STP) n1	1.51798	0.15923
Quantity Adsorbed (cm³/g STP) Vmax2	13.80507	9.3109
Quantity Adsorbed (cm³/g STP) K2	0.01891	0.01072
Quantity Adsorbed (cm³/g STP) n2	1	0

Zn$_2$(DB-bdc)$_2$(bipy)

Equation	Vads=Vmax1*K1*p^n1/(1+K1*p^n1)+Vmax2*K2*p^n2/(1+K2*p^n2)	
Adj. R-Square	1	
C2H2	Value	Standard Error
Quantity Adsorbed (cm³/g STP) Vmax1	60.80781	1.28843
Quantity Adsorbed (cm³/g STP) K1	0.00769	2.64726E-4
Quantity Adsorbed (cm³/g STP) n1	0.91793	0.01128
Quantity Adsorbed (cm³/g STP) Vmax2	18.6936	0.20194
Quantity Adsorbed (cm³/g STP) K2	0.07522	6.99461E-4
Quantity Adsorbed (cm³/g STP) n2	1	0

Equation	Vads=Vmax1*K1*p^n1/(1+K1*p^n1)+Vmax2*K2*p^n2/(1+K2*p^n2)	
Adj. R-Square	0.99999	
CO2	Value	Standard Error
Quantity Adsorbed (cm³/g STP) Vmax1	0.0492	0.00671
Quantity Adsorbed (cm³/g STP) K1	1.61998	1.08674
Quantity Adsorbed (cm³/g STP) n1	1	0
Quantity Adsorbed (cm³/g STP) Vmax2	64.80801	0.34244
Quantity Adsorbed (cm³/g STP) K2	0.00286	2.0059E-5
Quantity Adsorbed (cm³/g STP) n2	1	0

Figure S15: Semilogarithmic plots of isotherms (dots) of C$_2$H$_2$ and CO$_2$ at 298 K on **BPY** and **DB** with corresponding fits (solid lines) and fitting parameters.

Zn$_2$(DE-bdc)$_2$(bipy)

Equation	Vads=Vmax1*K1*p^n1/(1+K1*p^n1)+Vmax2*K2 *p^n2/(1+K2*p^n2)	
Adj. R-Square	1	
C2H2	Value	Standard Error
Quantity Adsorbed (cm³/g STP) Vmax1	150.33677	9.68907
Quantity Adsorbed (cm³/g STP) K1	0.00282	1.71994E-4
Quantity Adsorbed (cm³/g STP) n1	1.00047	0.02446
Quantity Adsorbed (cm³/g STP) Vmax2	41.37699	0.64854
Quantity Adsorbed (cm³/g STP) K2	0.05301	4.65689E-4
Quantity Adsorbed (cm³/g STP) n2	1	0

| Equation	Vads=Vmax1*K1*p^n1/(1+K1*p^n1)+Vmax2*K2* p^n2/(1+K2*p^n2)	
Adj. R-Square	0.99997	
CO2	Value	Standard Error
Quantity Adsorbed (cm³/g STP) Vmax1	9.82516E-8	--
Quantity Adsorbed (cm³/g STP) K1	1E-10	--
Quantity Adsorbed (cm³/g STP) n1	1E-10	--
Quantity Adsorbed (cm³/g STP) Vmax2	120.10495	0.88044
Quantity Adsorbed (cm³/g STP) K2	0.00256	2.21011E-5
Quantity Adsorbed (cm³/g STP) n2	1	0

Figure S16: Semilogarithmic plots of isotherms (dots) of C_2H_2 and CO_2 at 298 K on **DE** with corresponding fits (solid lines) and fitting parameters.

The ideal adsorbed solution theory (IAST), invented by Myer and Prausnitz in 1965,[6] is a widely used method to assess the sorption selectivity in a binary mixture based on their single-component isotherms. For its calculation, the fits of the dual-site Langmuir-Freundlich isotherms at 298 K were used (see above). The adsorption selectivity S_{ads} is defined by the following equation:

$$S_{ads} = \frac{q_1/q_2}{p_1/p_2}$$

where q_i is the molar loading of species i in the adsorbed phase and p_i is the bulk gas pressure of species i.

S7 Henry's law constant determination

Henry's law constants were determined using a method suggested by Ruthven[7] and tested in context of other determination methods e.g. by Garcés et al..[8] It uses the virial equation of adsorption expressed as

$$\ln\left(\frac{p}{n}\right) = a_0 + a_1 n + a_2 n^2 + a_3 n^3 + \cdots + a_m n^m$$

where a_m represents the virial coefficients, n the amount adsorbed in cm³/g and p the pressure in bar. The Henry's constant (H_{virial}) is related to a_0 via

$$H_{virial} = \exp\left(-a_0\right)$$

Fits were performed in OriginPro 2020 by OriginLab Corp.. Best fits were found for seven and eight significant coefficients (m = 6; 7), fits and fit parameters are given below (see **Figure S17** and **S18**).
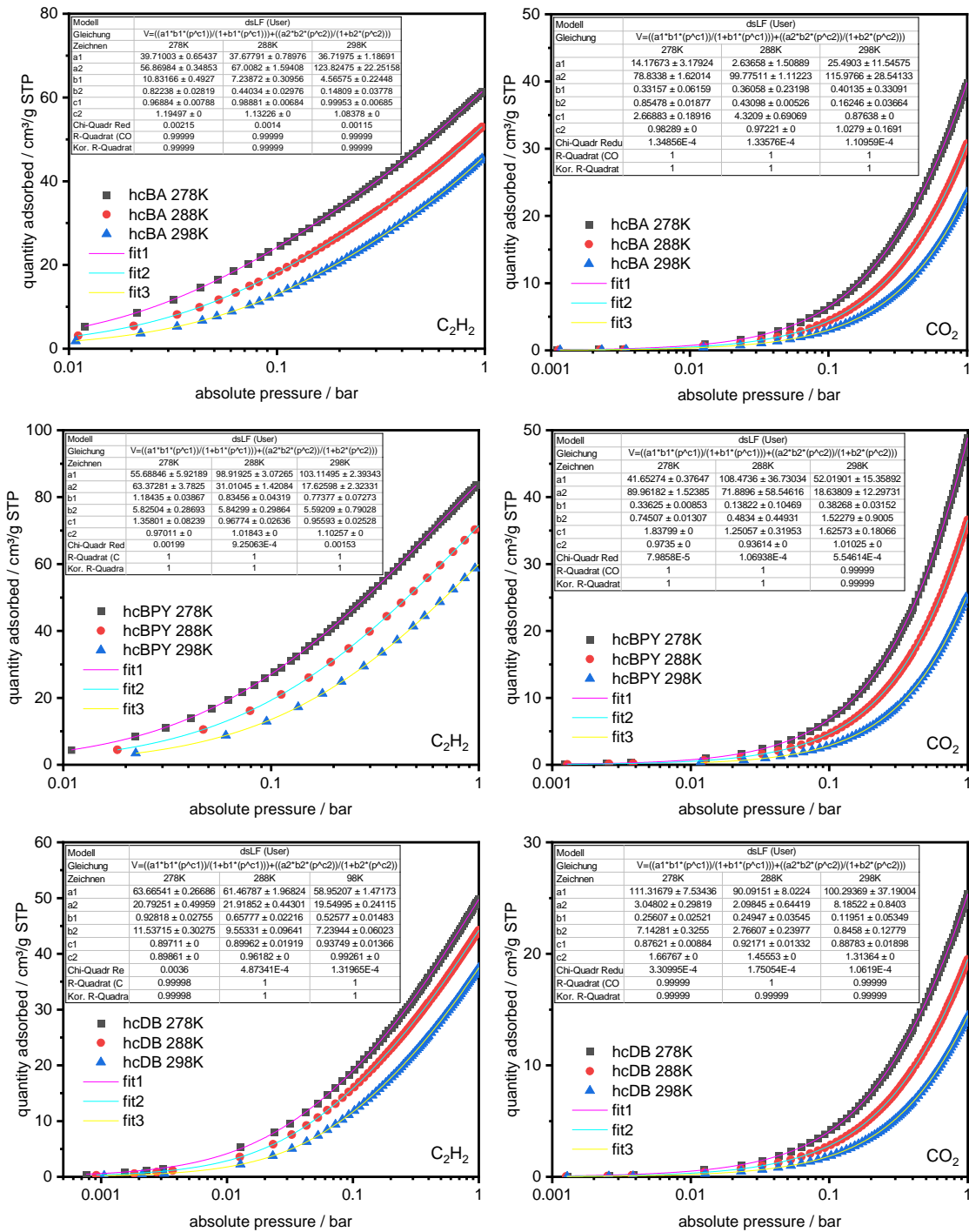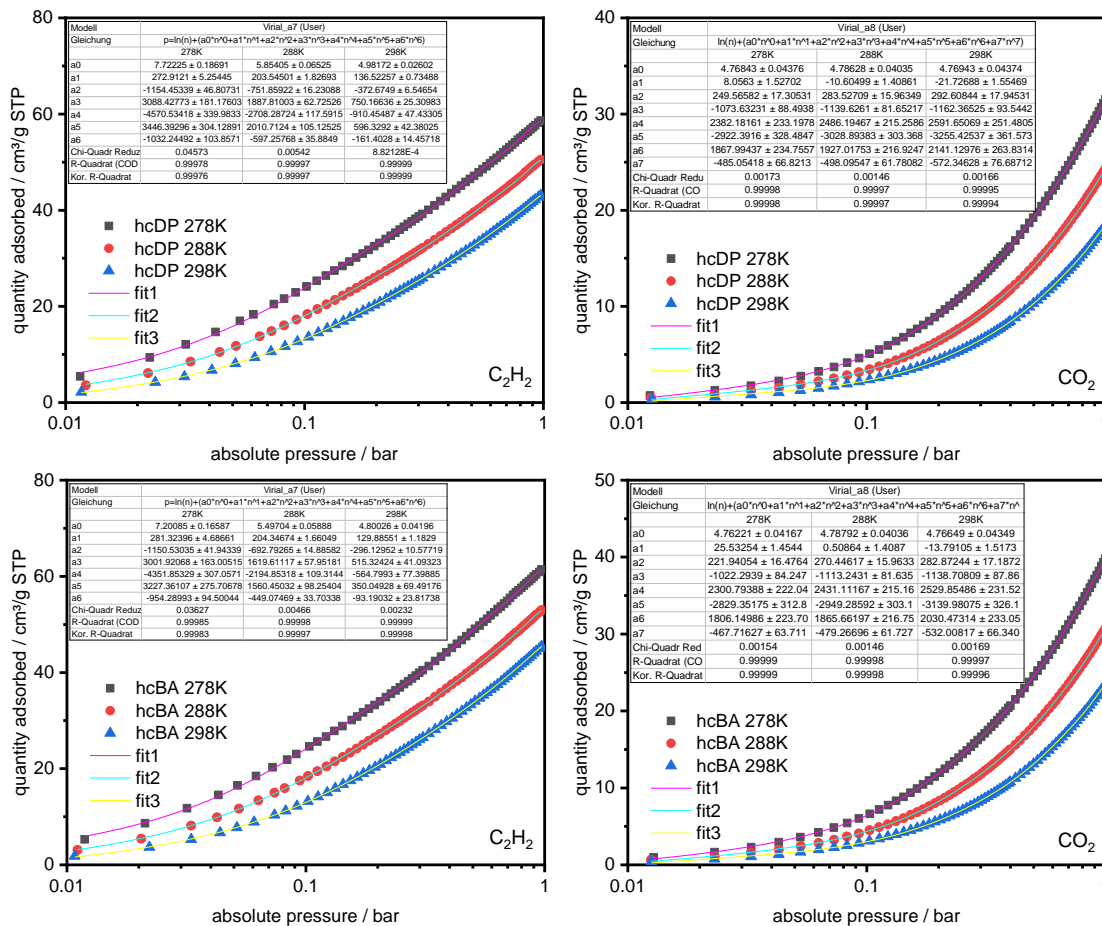

Figure S17: Semilogarithmic plots of isotherms (dots) of C_2H_2 and CO_2 at 298 K, 288 K, and 278 K on **DP** and **BA** with corresponding fits (solid lines) and fitting parameters.
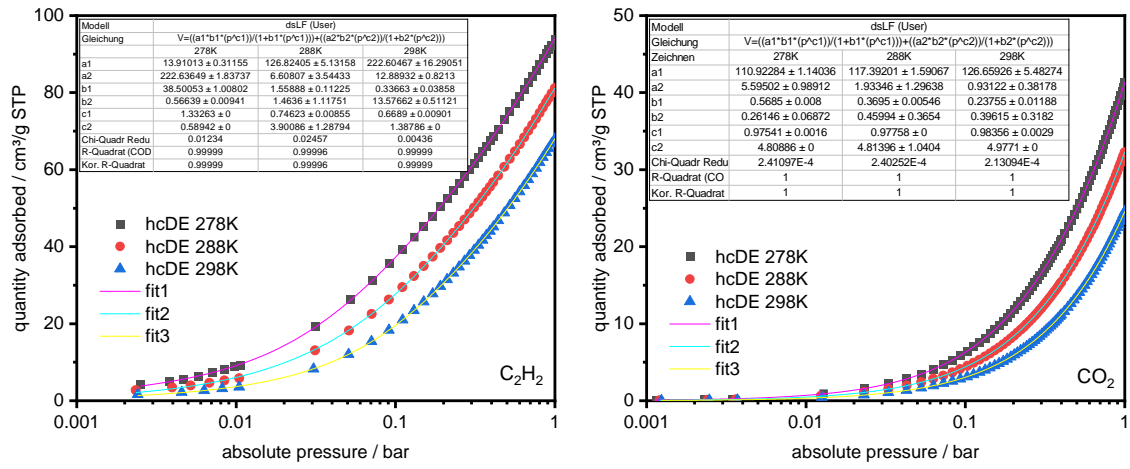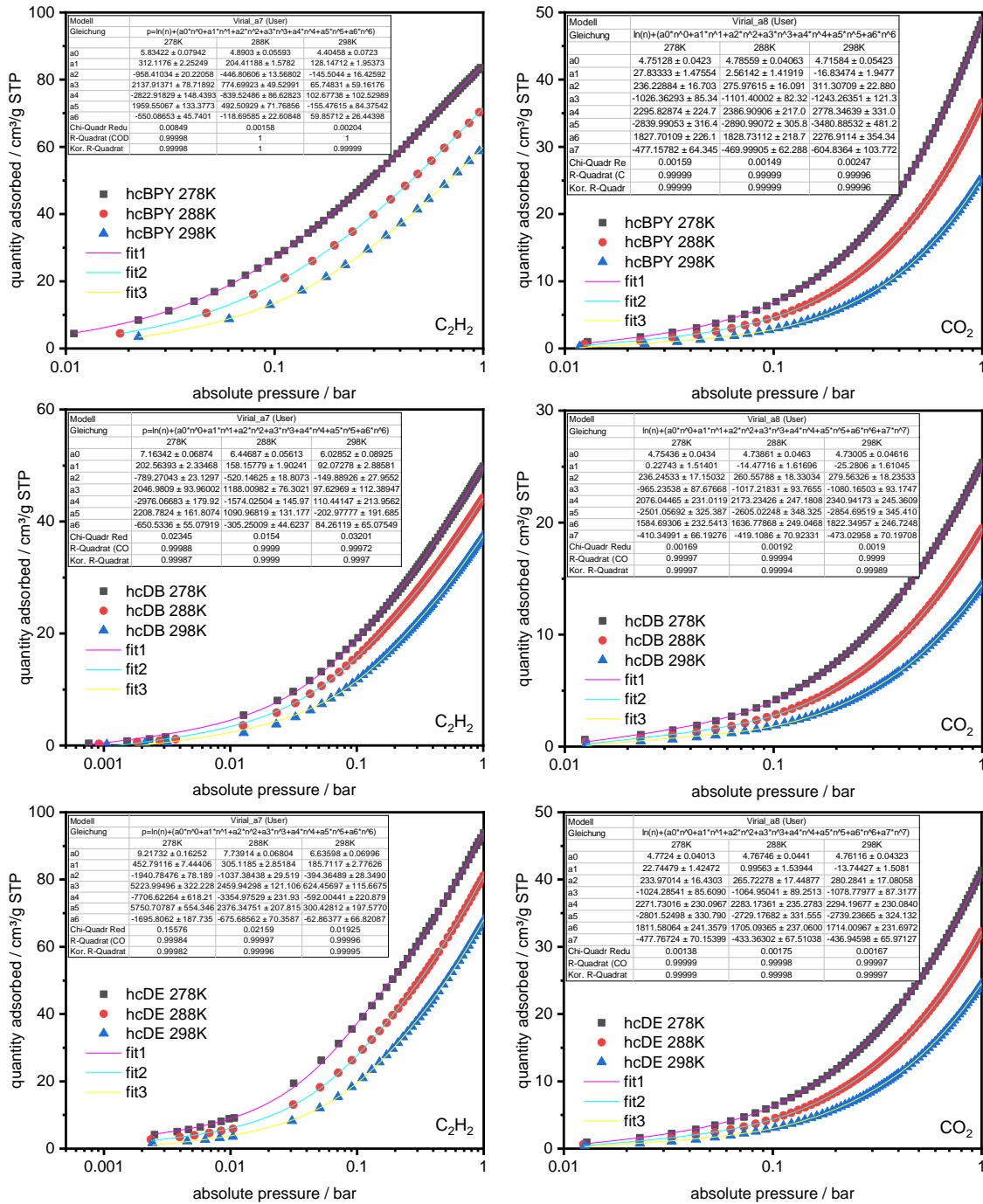
Figure S18: Semilogarithmic plots of isotherms (dots) of C_2H_2 and CO_2 at 298 K, 288 K, and 278 K on **BPY**, **DB**, and **DE** with corresponding fits (solid lines) and fitting parameters.

In their presented form (see **Figure S19**), the Henry's law constants can be compared between all materials within this study and depict a measure of volatility of the adsorbate. Hence, they increase with increased temperature and are conceptually in reciprocal correlation to the adsorption enthalpy. It must be emphasized that here Henry's constants for CO_2 are of limited meaningfulness because uptake at lowest pressures for all temperatures and materials shows only minor differences that could not be translated to different limiting slopes without significantly sacrificing overall goodness of fits. Henry's Law constants for CO_2 are therefore not consulted for data interpretation and conclusion.
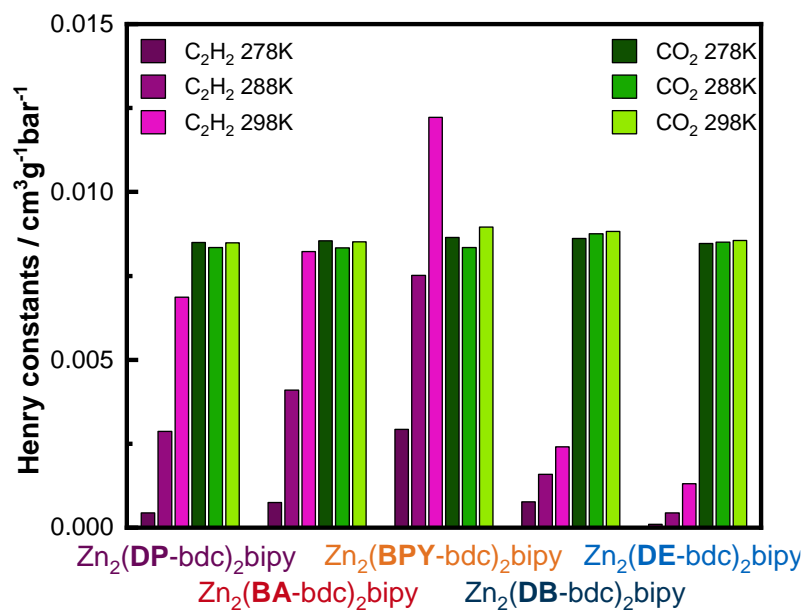
Figure S19: Henry's law constants for all materials for C_2H_2 (purple colors) and CO_2 (green colors), each for 278 K, 288 K, and 298 K.

S8 Breakthrough experiments

Breakthrough experiments for acetylene/carbon dioxide mixtures with 1:1 ratio were carried out at a flow rate of 5 ml/min at 303 K and ambient pressure. No carrier gas was used. MOF materials (1 g each) were placed into a Ø 3 × 350 mm glass cell. Samples were pretreated for 1 h at 120 °C under a He flow of 10 ml/min to remove any other adsorbate. Input gas flow ratio was adjusted and controlled using mass flow controllers and output gas stream composition was monitored via a 990 Micro GC by Agilent Technologies Inc. equipped with a PoraPLOT Q column and thermal conductivity detector (TCD-GC). Flow rate at the outlet is not monitored, only output composition. The GC signals of both gases during the experiment (C) are put in relation to their GC signal after reaching equilibrium (C0). The outlet flow rate is as such expected to be lower before this equilibrium is reached due to gas adsorbing. Equilibrium was reached after 35 min (**DB**), 36 min (**DP**), 39 min (**DE**), 41 min (**BA**), and 50 min (**BPY**).

MFC = mass flow controller
TCD-GC = thermal conductivity detector gas chromatograph
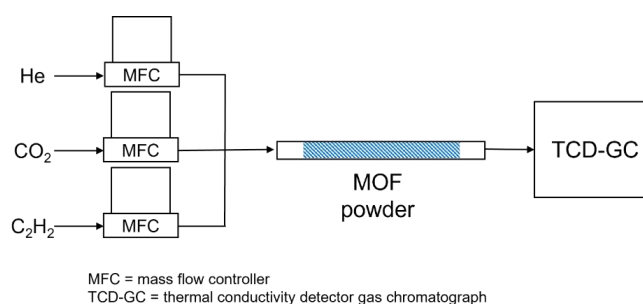
Scheme S1: Schematic illustration of the self-assembly breakthrough experiment setup.
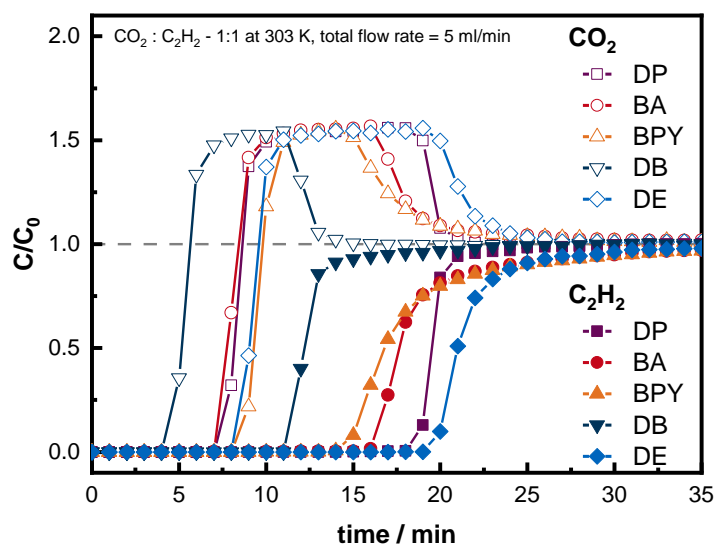
Figure S20: Breakthrough curves for all materials for a 1:1 ratio of C_2H_2/CO_2 at a flow rate of 5 ml/min at 303 K. showing effluent stream gas concentrations relative to the equilibrated output stream (C_2H_2 = full symbols; CO_2 = empty symbols).

S22

Table S2: Selected examples MOF performance in C_2H_2/CO_2 separation. Uptakes all at 1 bar and 298 K from single gas equilibrium isotherms. Selectivities determined by IAST calculations for a 1:1 adsorptive ratio at 1 bar and 298 K. Adsorption enthalpy difference(d(-ΔH_{ads}); $\Delta H(C_2H_2)$- $\Delta H(CO_2)$) at zero-loading.

MOF	C_2H_2 uptake [cm^3/g]	CO_2 uptake [cm^3/g]	d(-ΔH_{ads}) [kJ/mol]	α	ref
Co(btzip)(H₂btzip)	87	73	2	2.5	[9]
JNU-1	63	51	-11	3	[9]
Cu(BDC-Br)	34	24	1	3.9	[9]
FJU-90a	180	103	4	4.3	[9]
ZJNU-8	92	83	6	4.5	[9]
SNNU-45	134	97	13	4.5	[9]
ZJU-195a	214	105	9	4.7	[9]
JXNU-5a	56	35	8	5	[9]
UPC-110	73	24	9	5.1	[9]
TCuI	49	36	7	5.3	[9]
In₁.₅(FBDC)(BDC)	53	34	9	5.3	[9]
NbU-8	183	51	5	5.4	[9]
ZJNU-13	118	88	11	5.6	[9]
CU₂(ade)₂(PA)₂	49	34	3	5.7	[9]
CPM-107	97	35	13	5.7	[9]
PCP-33	122	59	1	6	[9]
NTU-66-Cu	112	49	11	6	[9]
SNNU-65-Cu-Fe	162	65	6	6.7	[9]
UTSA-74a	107	71	6	9	[9]
TCuBr	63	45	10	9.5	[9]
Co₂(HCOO)₂(CPT)₂	145	60	13	11	[9]
SNNU-65-Cu-Sc	179	70	23	13.5	[9]
JCM-1	75	38	4	13.7	[9]
DICRO-4-Ni-i	43	23	4	13.9	[9]
BSF-3-Co	80	47	20	16.3	[9]
TCuCl	67	45	11	16.9	[9]
Ni₃(COOH)₆	94	68	16	22	[9]
FeNi-M'MOF	96	61	2	24	[9]
NKMOF-1-Ni	61	51	19	30	[9]
Ni₂(BTEC)(bipy)₃	77	13	-6	33.5	[9]
ATC-Cu	114	91	43	53.6	[10]
CuI@UiO-66-(COOH)₂	52	18	46	185	[11]
Zn₂(DE-bdc)₂bipy	61	25	15.5#	6.5 / 10.0*	this work
Zn₂(DP-bdc)₂bipy	43	18	8.0#	6.1 / 10.3*	this work
Zn₂(DB-bdc)₂bipy	38	14	1.5#	6.9 / 9.0*	this work
Zn₂(BA-bdc)₂bipy	46	24	7.2#	5.1 / 10.9*	this work
Zn₂(BPY-bdc)₂bipy	61	27	3.2#	3.6 / 4.1*	this work

at 0.5 mmol/g loading; *left value IAST derived (1 bar, 298 K), right value derived from amount adsorbed during breakthrough experiments

S9 Computational details

S9.1 Material structure optimization including functionalizations

Geometry optimizations of the crystal structures of **DP**, **BA**, **BPY**, **DB** and **DE** were initially performed using the self-consistent-charge density-functional tight-binding method[12] with the third-order expansion[13] (DFTB3) method as implemented in the DFTB+ program package version 1.3.1.[14] with periodic boundary conditions. We employed 3ob parameters[15,16] in all calculations with Hubbard parameters -0.1492 for C, -0.1857 for H, -0.1575 for O, -0.1535 for N and -0.0300 for Zn in atomic units, respectively. Grimme's D3 type dispersion was included in all calculations.[17] Since the structures are analogous structures of [Zn_2(2,5-bis(2-methoxyethoxy)-1,4-benzenedicarboxylate)$_2$(bipy)]$_n$,[3] we replaced the 2-methoxyethoxy groups with propoxy groups to construct the initial structure of **DP** for optimization under $P1$ symmetry. The obtained optimized **DP** was used for the initial structures of **BA**, **BPY**, **DE**, and **DB** after replacement of propoxy groups with each substituent group. The experimental unit cell parameters derived from Pawley fits are employed for optimization of each structure. In the case of **DB**, the following step was started directly.

Materials were subsequently optimized with lammps[18] using the UFF4MOF classical potentials[19] as defined by the lammps-interface code.[20] Partial charges of all the atoms were calculated by a message passing neural network trained by Raza et al.[21] Optimization was achieved using a robust loop of box/relax and fire minimization styles with no constraints placed on atom positions or cell shape.

Table S3: Cell parameters derived from structure optimization.

	a [Å]	b [Å]	c [Å]	alpha [°]	beta [°]	gamma [°]	cell volume [Å³]
DE	52.13953	51.97474	35.39438	89.93789	90.17225	120.22376	82875.48612
DP	51.79524	51.90366	35.61893	89.7769	89.93199	119.81605	83077.50657
BA	51.98278	52.1225	35.09725	90.27161	89.30343	120.19707	82181.80337
BPY	51.74711	52.55163	33.55208	92.42776	89.82264	120.51104	78516.3114
DB	52.97766	52.92745	34.02079	90.32821	89.90468	119.81908	82759.30785

S9.2 Pore size distribution determination

Molecular dynamics simulations, using the same code and potentials described above, were performed for each of the materials to capture the porosity changes relating to the dynamics of the side chains. A trajectory in the NPT ensemble of 1 ns was generated after an equilibration period 0.5 ns. Temperature was set to 298 K and pressure set to 1 atm with these external conditions controlled by a Nose-Hoover thermostat and barostat using a 100 fs and 1000 fs dampening parameter, respectively. Snapshots were recorded every 100 fs and the porosity of each snapshot was determined using the zeo++ code.[22] For each snapshot an inert spherical probe (1.3 Å) was used to determine the limiting pore diameter and the largest pore diameter along a free path in the structure. The resulting approach provides realistic distributions of the pore sizes present in the materials.

Table S4: Calculated total pore volumes (min = limiting, max = largest).

	accessible pore volume [cm^3/g]				inaccessible pore volume [cm^3/g]			
	mean	min	max	stdd*	mean	min	max	stdd*
DE	0.0854	0.0805	0.0924	0.0017	1.17E-04	0.00E+00	5.44E-04	7.39E-05
DP	0.0206	0.0125	0.0303	0.0036	0.0105	2.43E-03	0.0184	0.0032
BA	0.0400	0.0275	0.0489	0.0036	0.0029	0.00E+00	0.0129	0.0029
BPY	0.0353	0.0156	0.0419	0.0038	0.0025	0.00E+00	0.0239	0.0034
DB	2.89E-06	0.00E+00	6.43E-04	3.55E-05	0.0053	3.62E-03	0.0080	0.0005

*standard deviation

S9.3 Calculation of enthalpy of adsorption and diffusivity

The adsorption enthalpy and diffusivity for CO_2 and C_2H_2 were also investigated using the same classical approach described in the last two sections. The parameters for CO_2 and C_2H_2 were used with EPM2 model and a rigid two-site model.[23,24] Eight gas molecules were introduced randomly into the pores of the materials and a 1 ns trajectory was simulated using the same parameters and equilibration and described above. Snapshots of this trajectory were recorded every 100 fs to measure the mean-squared displacement and adsorption energy. The mean-squared displacement was computed using the MDanalysis library[25] the one-dimensional diffusivity was subsequently calculated based on the Einstein formula.[26,27] Adsorption energy was simply averaged over the trajectory.
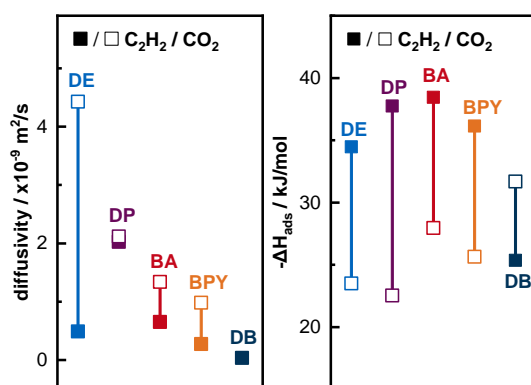
Figure S21: Simulated diffusivities (left) and adsorption enthalpies (right) of CO_2 and C_2H_2 for all materials. Diffusion of CO_2 in **DB** was too slow to be simulated reproducibly and could not be determined.

Table S5: Calculated diffusivities for all materials.

		diffusivity [m^2/s]		correlation coefficient r^2	
	functionalization	C_2H_2	CO_2	C_2H_2	CO_2
DE	diethoxy	4.89124E-10	4.42486E-9	0.96853	0.99931
DP	dipropoxy	2.02457E-9	2.1173E-9	0.99749	0.99504
BA	bisallyloxy	6.52933E-10	1.33776E-9	0.99602	0.98154
BPY	bispropynyloxy	2.72282E-10	9.83135E-10	0.99054	0.99538
DB	dibutoxy	3.45076E-11	-	0.94512	-

Table S6: Calculated enthalpies of adsorption for all materials.

		-ΔH_{ads} [kJ/mol]	
	functionalization	C_2H_2	CO_2
DE	diethoxy	34.46698	23.49701
DP	dipropoxy	37.73610	22.53200
BA	bisallyloxy	38.44397	27.94396
BPY	bispropynyloxy	36.14215	25.63896
DB	dibutoxy	25.35297	31.68973

S10 SEM imaging

Scanning electron microscopy (SEM) images were obtained with a Jeol JSM-7500F field emission scanning electron microscope with the Gentle Beam mode with an accelerating voltage of 1 kV.

All materials in this study show formation of multiple micron-sized needles, crystallite aggregates, and bigger hexagonal structures with preferred growth direction seemingly consisting of needle-like substructures. With the anisotropic pore dimensions in the honeycomb-like MOF, morphology and surface ratio are expected to have an influence especially on breakthrough experiment results where mass transport is more relevant than in equilibrium physisorption. However, we purposefully exclude the aspect of particle size and morphology from the study, because a) we were unable to separate the shown morphology mixture or synthesize crystallites with more uniform morphology and size, b) all powders consist of a similar ratio of above-mentioned particles and aggregates which c) each are in a comparable size regime for each material. As such, size and morphology dependent changes are expected to average out across all studied MOFs.
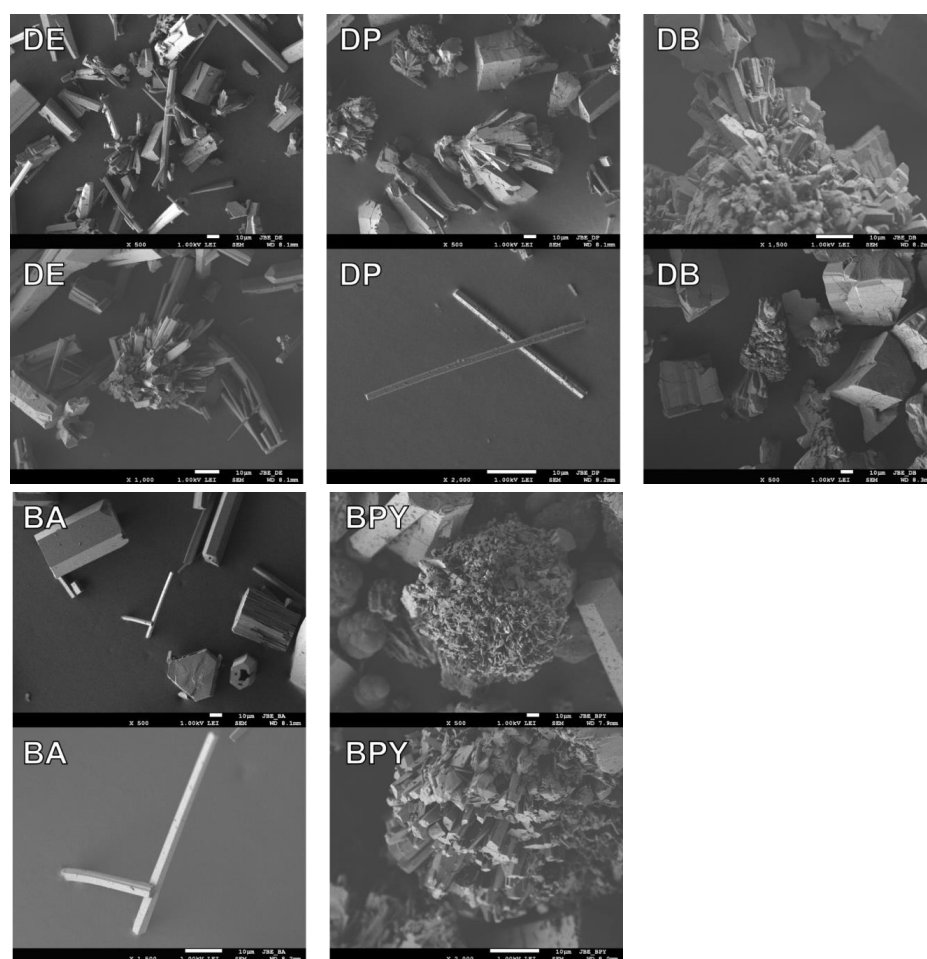

Figure S22: SEM images of all materials. Resolution bar at the bottom is 10 µm.

References

(1) Henke, S.; Schneemann, A.; Wütscher, A.;Fischer, R. A. Directing the breathing behavior of pillared-layered metal-organic frameworks via a systematic library of functionalized linkers bearing flexible substituents. *J. Am. Chem. Soc.* **2012**, *134*, 9464–9474.

(2) Henke, S.;Fischer, R. A. Gated channels in a honeycomb-like zinc-dicarboxylate-bipyridine framework with flexible alkyl ether side chains. *J. Am. Chem. Soc.* **2011**, *133*, 2064–2067.

(3) Henke, S.; Schneemann, A.; Kapoor, S.; Winter, R.;Fischer, R. A. Zinc-1,4-benzenedicarboxylate-bipyridine frameworks – linker functionalization impacts network topology during solvothermal synthesis. *J. Mater. Chem.* **2012**, *22*, 909–918.

(4) Thommes, M.; Kaneko, K.; Neimark, A. V.; Olivier, J. P.; Rodriguez-Reinoso, F.; Rouquerol, J.;Sing, K. S. Physisorption of gases, with special reference to the evaluation of surface area and pore size distribution (IUPAC Technical Report). *Pure Appl. Chem.* **2015**, *87*, 1051–1069.

(5) Rouquerol, J.; Llewellyn, P.;Rouquerol, F. Is the BET equation applicable to microporous adsorbents? *Stud. Surf. Sci. Cat.* **2007**, 49–56.

(6) Myers, A. L.;Prausnitz, J. M. Thermodynamics of mixed-gas adsorption. *AIChE J.* **1965**, *11*, 121–127.

(7) Ruthven, D. M. *Principles of Adsorption and Adsorption Processes*; John Wiley & Sons, 1984.

(8) Garcés, S. I.; Villarroel-Rocha, J.; Sapag, K.; Korili, S. A.;Gil, A. Comparative Study of the Adsorption Equilibrium of CO 2 on Microporous Commercial Materials at Low Pressures. *Ind. Eng. Chem. Res.* **2013**, *52*, 6785–6793.

(9) Fu, X.-P.; Wang, Y.-L.;Liu, Q.-Y. Metal-organic frameworks for C2H2/CO2 separation. *Dalton Trans.* **2020**, *49*, 16598–16607.

(10) Niu, Z.; Cui, X.; Pham, T.; Verma, G.; Lan, P. C.; Shan, C.; Xing, H.; Forrest, K. A.; Suepaul, S.;Space, B. *et al.* A MOF-based Ultra-Strong Acetylene Nano-trap for Highly Efficient C2 H2 /CO2 Separation. *Angew. Chem.* **2021**, *60*, 5283–5288.

(11) Zhang, L.; Jiang, K.; Yang, L.; Li, L.; Hu, E.; Yang, L.; Shao, K.; Xing, H.; Cui, Y.;Yang, Y. *et al.* Benchmark C2 H2 /CO2 Separation in an Ultra-Microporous Metal-Organic Framework via Copper(I)-Alkynyl Chemistry. *Angew. Chem. Int. Ed.* **2021**, *60*, 15995–16002.

(12) Elstner, M.; Porezag, D.; Jungnickel, G.; Elsner, J.; Haugk, M.;Frauenheim, T. Self-consistent-charge density-functional tight-binding method for simulations of complex materials properties. *Phys. Rev. B* **1998**, 7260-7268.

(13) Yang, Y.; Yu, H.; York, D.; Cui, Q.;Elstner, M. Extension of the self-consistent-charge density-functional tight-binding method: third-order expansion of the density functional theory total energy and introduction of a modified effective coulomb interaction. *J. Phys. Chem. A* **2007**, *111*, 10861–10873.

(14) Aradi, B.; Hourahine, B.;Frauenheim, T. DFTB+, a sparse matrix-based implementation of the DFTB method. *J. Phys. Chem. A* **2007**, *111*, 5678–5684.

(15) Gaus, M.; Goez, A.;Elstner, M. Parametrization and Benchmark of DFTB3 for Organic Molecules. *J. Chem. Theory Comput.* **2013**, *9*, 338–354.

(16) Kubillus, M.; Kubař, T.; Gaus, M.; Řezáč, J.;Elstner, M. Parameterization of the DFTB3 method for Br, Ca, Cl, F, I, K, and Na in organic and biological systems. *J. Chem. Theory Comput.* **2015**, *11*, 332–342.

(17) Grimme, S.; Antony, J.; Ehrlich, S.;Krieg, H. A consistent and accurate ab initio parametrization of density functional dispersion correction (DFT-D) for the 94 elements H-Pu. *J. Chem. Phys.* **2010**, *132*, 154104.

(18) Thompson, A. P.; Aktulga, H. M.; Berger, R.; Bolintineanu, D. S.; Brown, W. M.; Crozier, P. S.; Veld, P. J. in 't; Kohlmeyer, A.; Moore, S. G.;Nguyen, T. D. *et al.* LAMMPS - a flexible simulation tool for particle-based materials modeling at the atomic, meso, and continuum scales. *Comput. Phys. Commun.* **2022**, *271*, 108171.

(19) Coupry, D. E.; Addicoat, M. A.;Heine, T. Extension of the Universal Force Field for Metal-Organic Frameworks. *J. Chem. Theory Comput.* **2016**, *12*, 5215–5225.

(20) Boyd, P. G.; Moosavi, S. M.; Witman, M.;Smit, B. Force-Field Prediction of Materials Properties in Metal-Organic Frameworks. *J. Phys. Chem. Lett.* **2017**, *8*, 357–363.

(21) Raza, A.; Sturluson, A.; Simon, C. M.;Fern, X. Message Passing Neural Networks for Partial Charge Assignment to Metal–Organic Frameworks. *J. Phys. Chem. C* **2020**, *124*, 19070–19082.

(22) Willems, T. F.; Rycroft, C. H.; Kazi, M.; Meza, J. C.;Haranczyk, M. Algorithms and tools for high-throughput geometry-based analysis of crystalline porous materials. *Microporous Mesoporous Mat.* **2012**, *149*, 134–141.

(23) Harris, J. G.;Yung, K. H. Carbon Dioxide's Liquid-Vapor Coexistence Curve And Critical Properties as Predicted by a Simple Molecular Model. *J. Phys. Chem.* **1995**, *99*, 12021–12024.

(24) Fischer, M.; Hoffmann, F.;Fröba, M. New microporous materials for acetylene storage and C(2)H(2)/CO(2) separation: insights from molecular simulations. *ChemPhysChem* **2010**, *11*, 2220–2229.

(25) Gowers, Richard J., Linke, Max, Barnoud, Jonathan, Reddy, Tyler John Edward, Melo, Manuel N., Seyler, Sean L., Domanski, Jan, Dotson, David L., Buchoux, Sebastien, Kenney, Ian M., and Beckstein, Oliver. MDAnalysis: A Python Package for the Rapid Analysis of Molecular Dynamics Simulations. *Proceedings of the 15th Python in Science Conference* **2016**, 98–105.

(26) Calandrini, V.; Pellegrini, E.; Calligari, P.; Hinsen, K.;Kneller, G. R. nMoldyn - Interfacing spectroscopic experiments, molecular dynamics simulations and models for time correlation functions. *JDN* **2011**, *12*, 201–232.

(27) Buyl, P. de. tidynamics: A tiny package to compute the dynamics of stochastic and molecular simulations. *JOSS* **2018**, *3*, 877.

7.2 STUDY II

Supplementary Information

Reduced Thermal Expansion by Surface-Mounted Nanoparticles in a Pillared-Layered Metal-Organic Framework

Jan Berger,[1] Alper-Sedat Dönmez,[1] Aladin Ullrich,[2] Hana Bunzen,[2] Roland A. Fischer[1]* and Gregor Kieslich[1]*

[1]Inorganic and Metal-Organic Chemistry, Technical University of Munich, Lichtenbergstr. 4, 85748 Garching, Germany

[2]Institute of Physics, University of Augsburg, Universitätsstr. 1, 86159 Augsburg, Germany

Supplementary Notes

S1 Supplementary Methods

S1.1 General remarks

All chemicals were purchased from commercial suppliers and used without further purification. MOF synthesis was conducted with pure N,N-dimethylformamide (DMF) (99.8%). Fresh DMF was used for solvent exchange. Ethanol for solvent exchange was purchased as technical grade and redistilled prior use. All experiments and procedures were carried out on air unless stated otherwise.

Liquid state NMR spectra were recorded on a Bruker Ultrashield DRX400 spectrometer ([1]H: 400.13 MHz) at ambient temperature (298 K). The ^{1}H NMR spectroscopic chemical shifts δ are reported in ppm relative to tetramethylsilane. ^{1}H NMR spectra are referenced against the residual proton resonances of the respective deuterated solvent as an internal standard (DMSO-d_6: δ (1H) = 2.50 ppm). MOF samples were digested and subsequently measured in 0.5 ml DMSO-d_6 with 0.05 ml DCl (7.6 N), all other substances were dissolved and measured in DMSO-d_6.

S1.2 Linker synthesis

Organic linkers were synthesized via Williamson Etherification according to literature known procedures,[1] albeit slightly altered/optimized.

Dimethyl-2,5-dihydroxy-1,4-benzenedicarboxylate

2,5-Dihydroxyterephthalic acid (6.0 g, 30.3 mmol) is dispersed in MeOH (180 mL) and H_2SO_4 (98%, 5 mL, 94 mmol) is added dropwise at room temperature while stirring and the reaction mixture is refluxed for 12 h at 75 °C. The precipitate is subsequently filtrated and thoroughly washed with distilled water. After removing residual solvent *in vacuo* at 70 °C, the product is obtained as yellow powder (6.63 g, 28.9 mmol, 95 %).

^{1}H-NMR (400.13 MHz, DMSO-d_6) δ (ppm) = 9.82 (s, 2H, COOH), 7.26 (s, 2H, H$_{Ar}$), 3.86 (s, 6H, CH$_3$).

2,5-Dipropoxy-1,4-benzenedicarboxylic acid (H$_2$DPbdc)

Dimethyl-2,5-dihydroxy-1,4-benzenedicarboxylate (2.00 g, 8.84 mmol, 1.0 eq.) and dry K_2CO_3 (3.00 g, 21.7 mmol, 2.5 eq.) are suspended in DMF (150 mL). 1-Bromopropane (2.41 mL, 26.5 mmol, 3 eq.) is added dropwise while stirring. The reaction mixture is refluxed overnight at 75 °C, the solvent is subsequently removed at 70 °C under reduced pressure (5 mbar). A solution of KOH (1.74 g, 30.5 mmol, 3.5 eq.) in H_2O (250 mL) is added to the residue. The reaction mixture is again refluxed overnight at 110 °C. After cooling to room temperature HCl (10%) is added dropwise until the carboxylic acid is completely precipitated. The solid is filtered and thoroughly washed with distilled water. After removing residual water *in vacuo* at 70 °C, the product (2.15 g, 4.27 mmol, 86 %) is obtained as white/slightly beige powder.

^{1}H-NMR (400.13 MHz, DMSO-d_6) δ (ppm) = 12.92 (s, 2H, COOH), 7.26 (s, 2H, H$_{Ar}$), 3.95 (t, *J* = 6.4 Hz, 4H, O-CH$_2$), 1.78 - 1.62 (m, 4H, CH$_2$), 0.97 (t, *J* = 7.4 Hz, 6H, CH$_3$).

S1.3 MOF and Pt@MOF synthesis

General procedure for Zn₂(DP-bdc)₂dabco and Pt@Zn₂(DP-bdc)₂dabco

$Zn(NO_3)_2 \cdot 6\ H_2O$ (89 mg, 0.30 mmol, 1 eq.), 1,4-diazabicyclo[2.2.2]octane (dabco) (34 mg, 0.30 mmol, 1 eq), the 2,5-dipropoxy-1,4-benzenedicarboxylic acid (H_2DPbdc; 85 mg, 0.30 mmol, 1 eq.) and the corresponding amount of potassium tetrachloridoplatinate (see Supplementary Table 1) are suspended in dimethyl formamide (DMF) (10 ml) in a 20 ml screw cap vial. The mixture is sonicated until complete suspension and absence of sedimentation (3-10 min), then heated in an oven for 24 or 48 h (see Supplementary Table 1). After cooling to room temperature, the formed crystalline white to light grey powder is washed and activated.

Washing and activation procedure

Washing and solvent exchange steps are conducted by vigorously shaking solid and solvent in a capped centrifuge tube, then centrifugation and decanting of the supernatant.

The obtained powder is washed immediately with DMF (3x 10 ml) until the supernatant is clear to yield the MOF material in its as-synthesized (**as**) state. While wet, this state is verified by X-ray powder diffraction (see chapter S2).

To remove DMF the **as** material is first washed with ethanol (10 ml), then twice soaked in fresh ethanol (2x 10 ml) overnight, and lastly soaked once in dichloromethane (10 ml) overnight. The wet powder is then pre-dried on air at ambient conditions before proper activation *in vacuo* at r.t. for 16 h and subsequently at 70 °C for 4 h. The resulting **dry** sample is stored under argon for further use to rule out possibility of gradual hydrolysis during prolonged exposure to ambient moisture.

Supplementary Table 1: Platinum precursor amounts and reaction conditions during MOF crystallization procedures.

ID	K₂PtCl₄ [mg]	temperature [°C]	heating time [h]
D0	none	120	48
D1	4.2	100	24
D2	10.4	120	24
D3	10.4	100	24

Linker and pillar incorporation ratio was verified via ^1H NMR (see below for specifications), CHNS contents were determined via combustion analysis. Zn and Pt contents were determined by atom adsorption spectroscopy or photometry for samples with more than 50 mg available with uncertainty of +- 0.1 w%. Elemental analysis was provided and conducted by the TUM CRC Microanalytical laboratory.

[Zn₂(DP-bdc)₂dabco – D0 (reference material)] ^1H **NMR** (400.13 MHz, DMSO-*d6*) δ (ppm) = 7.18 (s, 4H, H$_{Ar}$), 3.87 (t, J = 6.6 Hz, 8H, O-CH₂), 3.54 (s, 12H, dabco), 1.61 (h, J = 7.2 Hz, 8H, CH₂), 0.89 (t, J = 7.3 Hz, 12H, CH₃). **Elemental analysis:** calculated C 50.83, H 5.52, N 3.49, O 23.89, Zn 16.27; found C 50.59, H 5.41, N 3.67, Zn 16.19;

[Pt@Zn₂(DP-bdc)₂dabco – D1] ^1H **NMR** (400.13 MHz, DMSO-*d6*) δ (ppm) = 7.10 (s, 4H, H$_{Ar}$), 3.79 (t, J = 6.3 Hz, 8H, O-CH₂), 3.54 (s, 12H, dabco), 1.52 (h, J = 7.0 Hz, 8H, CH₂), 0.78 (t, J = 7.3 Hz, 12H, CH₃). **Elemental analysis:** found C 49.67, H 5.38, N 3.50, Zn 15.7, Pt 1.4;

[Pt@Zn₂(DP-bdc)₂dabco – D2] **¹H NMR** (400.13 MHz, DMSO-$d6$) δ (ppm) = 7.09 (s, 4H, H$_{Ar}$), 3.78 (t, J = 6.3 Hz, 8H, O-CH$_2$), 3.53 (s, 12H, dabco), 1.52 (q, J = 6.9 Hz, 8H, CH$_2$), 0.78 (t, J = 7.4 Hz, 12H, CH$_3$). **Elemental analysis:** found C 49.67, H 5.38, N 3.50, Zn 15.7, Pt 1.9;

[Pt@Zn₂(DP-bdc)₂dabco – D3] **¹H NMR** (400.13 MHz, DMSO-$d6$) δ (ppm) = 7.10 (s, 4H, H$_{Ar}$), 3.79 (t, J = 6.2 Hz, 8H, O-CH$_2$), 3.54 (s, 12H, dabco), 1.51 (p, J = 7.2 Hz, 8H, CH$_2$), 0.78 (t, J = 7.3 Hz, 12H, CH$_3$). **Elemental analysis:** found C 49.62, H 5.38, N 3.65, Zn 15.1, Pt 3.1;

S1.4 MOF structure and flexibility

Zn₂(DP-bdc)₂dabco is a pillared-layered MOF consisting of two-dimensional square-lattice layers spanned by paddlewheel units and DP-bdc^{2-} linkers which are congruently stacked and connected via the dabco pillars in the third dimension. Many derivatives of the Zn₂(fu-bdc)₂dabco family (fu = 2,5-functionalization) are flexible MOFs which can transition between a contracted **np** phase and an expanded **lp** phase (in a first-order phase transition).[2] The in this work studied MOF only undergoes this transition in response to polar solvents (like DMF, EtOH) and CO₂. Other functionalizations, however, unlock this flexibility in response to temperature or mechanical pressure as well.[3,4] These MOFs are synthesized in their **lp** state (due to the reaction medium DMF) and transitioned to their **np** phase during careful solvent exchange and removal. This state is metastable until exposure to abovementioned polar adsorbates which switch the MOF to its **lp** phase. This is then again reversible by i.e. solvent evaporation, drying, gas removal etc. The interested reader is directed to this review article on flexible MOFs.[5]
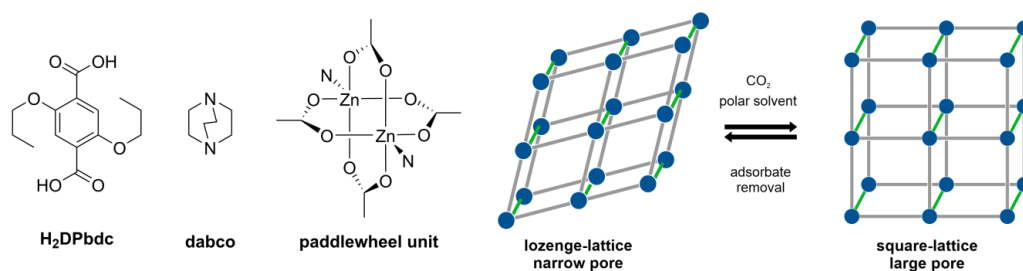
Supplementary Figure 1: From left to right structure of the terephthalic acid derivative linker, dabco pillar, and Zn paddlewheel building block. Only coordinating nitrogen atoms shown in the paddlewheel unit for clarity. Right hand structures visualize the np to lp phase transition as is present and triggered in Zn₂(DP-bdc)₂dabco by polar solvents (like DMF, EtOH) and CO₂. Blue nodes = paddlewheel unit, grey struts = DP-bdc^{2-}, green struts = dabco.

S2 Powder X-ray diffraction

PXRDs of the as-synthesized (**as**) and resolvated samples were measured using Bragg-Bentano geometry with a silicon wafer plate on a Rigaku Benchtop MiniFlex 600-C. X-ray Cu Kα radiation (λ = 1.5406 Å) with a voltage of 40 kV and current of 15 mA was used.

Activated (**dry**) samples and samples after the CO_2 and N_2 physisorption cycles were filled in glass capillaries in a glovebox under argon atmosphere and PXRDs were measured in Debeye-Scherrer geometry on a PANalytical Empyrean diffractometer. X-ray Cu Kα radiation (λ = 1.5406 Å) with a voltage of 45 kV and current of 40 mA was used.
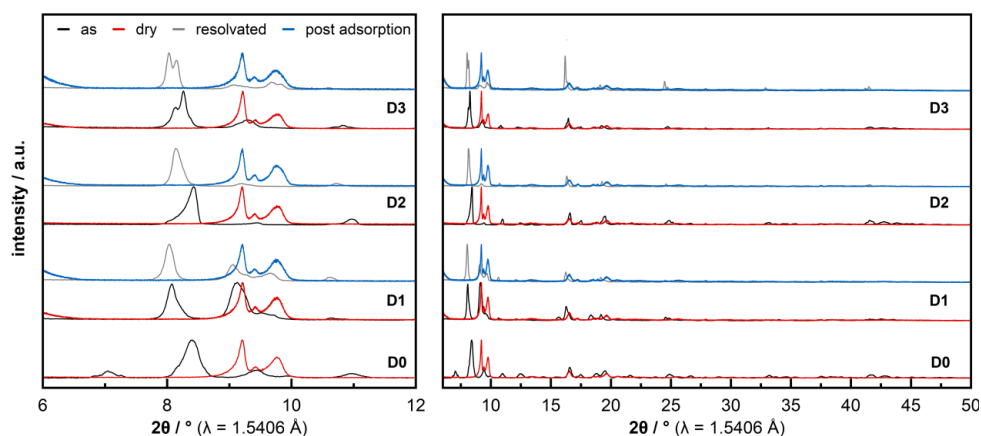
Supplementary Figure 2: PXRD patterns in the range of 2θ = 6-12° and 6-50°. Black: as-synthesized (**as**) with infiltrated DMF; red: activated (**dry**); grey: re-infiltrated with DMF after activation; blue: material state after all conducted gas adsorption measurements presented in this work (N_2 and CO_2). Transition from **lp** state in **as** to **np** state in **dry** is observable by shift of the 110 reflection from 2θ = 8.2-8.4° to 9.7° and intensity increase of the 001 reflection at 2θ = 9.2°.[6] Due to the very low NP loading and significant peak broadening coming from diffraction domains in the nano regime, no peaks corresponding to Pt nanoparticles can be observed at the expected angles around 40° (I(111)) and 47° (I(200)) 2θ.[7]

S3 Sorption isotherms

Adsorption measurements with N_2 (>99.999 vol%) at 77 K and CO_2 (>99.995 vol%) at 195 K were carried out on a 3Flex Physisorption from Micromeritics Instrument Corp., which uses a manometric method to determine the amount adsorbed at an equilibrated gas pressure.

Activated samples were transferred under dry argon atmosphere into preweighed sample tubes and capped with Micromeritics CheckSeals. Samples were subsequently activated again at 80 °C for 5 h under dynamic vacuum of ca. 1×10^{-3} mbar using a SmartVacPrep by Micromeritics Instrument Corp. to ensure absence of unwanted adsorbates and identical pre-measurement states of all samples. The mass of the adsorbent was then recorded, generally in the range of 50-70 mg. To facilitate proper degassing in context of the highly diffusion hindering pore environment, prior to each measurement samples were evacuated in situ at 80 °C for at least 20 h under dynamic vacuum of ca. $1 \times 10^{-5}$ mbar. Free space of the sample tube was determined after measuring each adsorption isotherm using helium (>99.999 vol%). A liquid nitrogen bath was used for measurements at 77 K and a dry ice - acetone bath was used for measurements at 195 K.
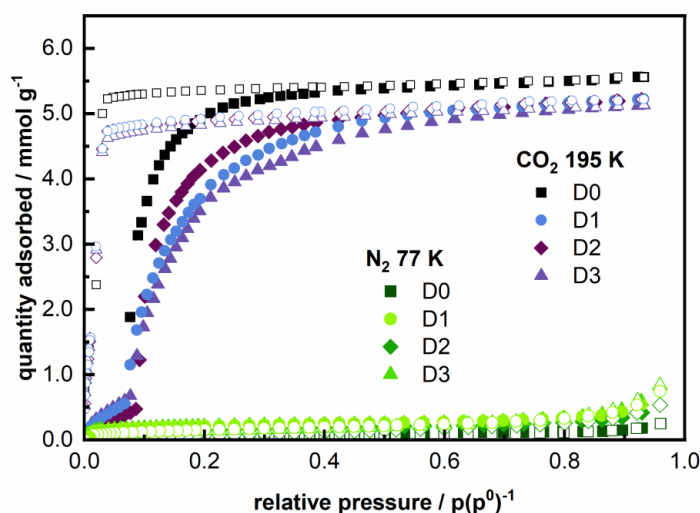
Supplementary Figure 3: Isotherms of N_2 at 77 K (green) and CO_2 at 195 K (blue/purple) on all materials with adsorption (filled symbols) and desorption (empty symbols), respectively. All materials with platinum nanoparticles (**D1-3**) show slightly decreased total absolute uptake compared to the reference material (**D0**), which we attribute to a small loss in accessible porosity due to nanoparticles blocking pores or pore access, and a widened **np** to **lp** transition pressure range. This more gradual opening is attributed to surface stress exhibited by the NPs which slightly rigidify the underlying framework. Layers around the NPs do as a result require a higher CO_2 partial pressure to undergo the opening breathing motion. This could explain both the widening of the opening pressure range, as well as the almost identical onset of the step. The widening is correlated to Pt nanoparticle presence, but not linearly to Pt content. The reverse **lp** to **np** transition during desorption occurs in line with **D0**. After desorption framework integrity and completed **np** phase transition of all materials was confirmed by PXRD (see section S2).

S4 Thermogravimetric analysis and differential scanning calorimetry

Thermogravimetric analysis coupled with differential scanning calorimetry (TGA-DSC) was conducted on a Netzsch TG-DSC STA 449 F5 in a temperature range from 25 °C to 800 °C with a heating rate of 10 K min^{-1} under argon flow (flow rate: 20 mL min^{-1}). It should be noted that the sample is briefly (few seconds) exposed to air before the measurement when the aluminium oxide pan is transferred from the argon filled transport vial to the sample holder stage.
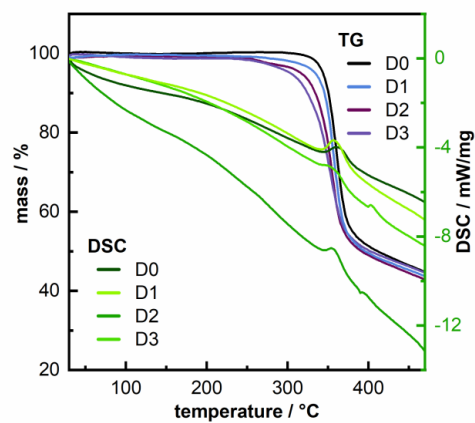
Supplementary Figure 4: TGA-DSC of all materials.

S5 Variable temperature powder X-ray diffraction

Activated **dry** samples were filled in borosilicate glass capillaries in a glovebox under argon atmosphere. Sealed capillaries were inserted into an open 1 mm diameter quartz capillary and measured in Debeye-Scherrer geometry from 323 K to 513 K to 323 K using a STOE INSITU HT2 Furnace on a STOE STADI P Dual. X-ray Mo Kα radiation (λ = 0.7107 Å) with a voltage of 50 kV and current of 40 mA was used.
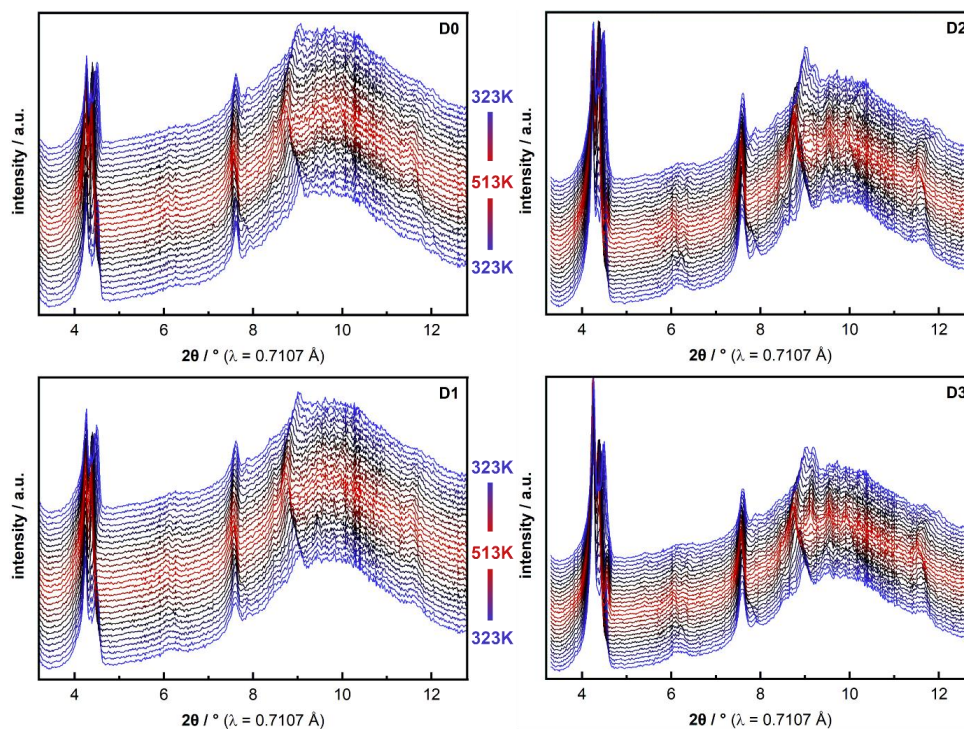
Supplementary Figure 5. Uncorrected VTPXRD patterns of dry **D0** (top left), **D1** (bottom left), **D2** (top right), and **D3** (bottom right) measured from 323K to 513K to 323K (temperature steps = 20K below 443K; 10K above 443K). The notable background is attributed to the secondary quartz glass capillary and polymeric windows of the oven sample stage (as verified by blank measurements). All materials show pronounced anisotropic thermal expansion of the **np** phase.
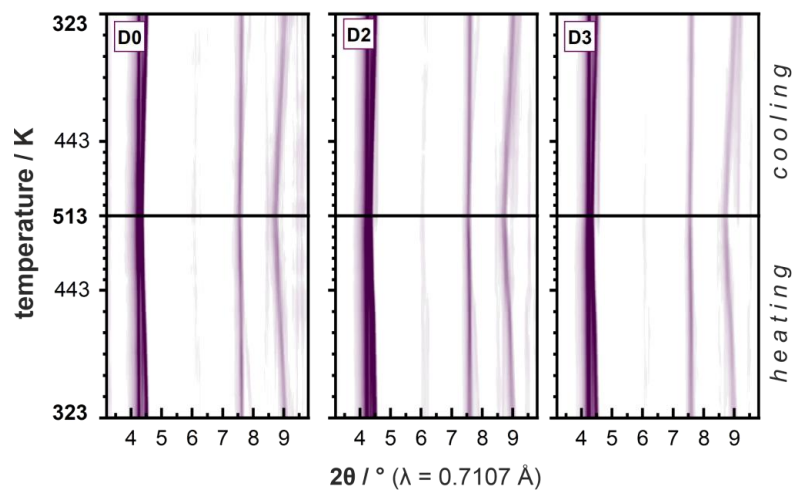
Supplementary Figure 6: Contour plot of VTPXRD data of **D0, D2,** and **D3** in the range of 2θ = 3.2 - 9.8. Darker purple corresponds to higher reflection intensity. Each set of 28 patterns is normalized to its highest intensity signal. Prominent gradual shift of peaks composites to lower angles is attributed to the literature known thermal expansion of $Zn_2(DP\text{-}bdc)_2dabco$.

S6 Pawley fitting and cell parameter

Raw VTXRD pattern (see chapter **S5**) were fitted directly.

Supplementary Table 2. Results of the Pawley fitting of the VTPXRDs recorded for **D0** (*h* = heating branch, *c* = cooling branch). Errors for given values a, b, c, β, and V correspond to last significant position. Space group was fixed for fitting according to literature known parent material property.

T [K]	space group	r_{wp}	a [Å]	b [Å]	c [Å]	α [°]	β [°]	γ [°]	V [Å³]	branch
323	$P2_1/m$	1.67	18.468	10.166	9.444	90	93.53	90	1770	*h*
343	$P2_1/m$	1.51	18.437	10.202	9.451	90	93.67	90	1774	*h*
363	$P2_1/m$	1.66	18.435	10.250	9.453	90	93.74	90	1783	*h*
383	$P2_1/m$	1.65	18.423	10.302	9.464	90	93.87	90	1792	*h*
403	$P2_1/m$	1.62	18.390	10.355	9.468	90	94.11	90	1798	*h*
423	$P2_1/m$	1.50	18.361	10.408	9.473	90	94.37	90	1805	*h*
443	$P2_1/m$	1.50	18.388	10.451	9.481	90	94.29	90	1817	*h*
453	$P2_1/m$	1.52	18.416	10.478	9.483	90	94.14	90	1825	*h*
463	$P2_1/m$	1.51	18.464	10.502	9.490	90	94.26	90	1835	*h*
473	$P2_1/m$	1.51	18.480	10.516	9.495	90	94.20	90	1840	*h*
483	$P2_1/m$	1.67	18.513	10.521	9.498	90	94.23	90	1845	*h*
493	$P2_1/m$	1.50	18.530	10.527	9.498	90	94.27	90	1848	*h*
503	$P2_1/m$	1.47	18.544	10.540	9.500	90	94.33	90	1852	*h*
513	$P2_1/m$	1.47	18.559	10.538	9.502	90	94.34	90	1853	*h*
503	$P2_1/m$	1.50	18.550	10.546	9.499	90	94.34	90	1853	*c*
493	$P2_1/m$	1.37	18.525	10.537	9.496	90	94.35	90	1848	*c*
483	$P2_1/m$	1.46	18.514	10.529	9.495	90	94.35	90	1846	*c*
473	$P2_1/m$	1.44	18.492	10.520	9.495	90	94.41	90	1842	*c*
463	$P2_1/m$	1.46	18.472	10.505	9.491	90	94.39	90	1836	*c*
453	$P2_1/m$	1.46	18.447	10.485	9.490	90	94.38	90	1830	*c*
443	$P2_1/m$	1.57	18.430	10.467	9.486	90	94.44	90	1824	*c*
423	$P2_1/m$	1.51	18.379	10.421	9.479	90	94.52	90	1810	*c*
403	$P2_1/m$	1.52	18.377	10.379	9.474	90	94.41	90	1802	*c*
383	$P2_1/m$	1.64	18.394	10.330	9.460	90	94.29	90	1792	*c*
363	$P2_1/m$	1.70	18.397	10.279	9.453	90	94.13	90	1783	*c*
343	$P2_1/m$	1.75	18.407	10.229	9.443	90	93.90	90	1774	*c*
323	$P2_1/m$	1.68	18.405	10.188	9.436	90	93.94	90	1765	*c*

Supplementary Table 3. Results of the Pawley fitting of the VTPXRDs recorded for **D1** (*h* = heating branch, *c* = cooling branch). Errors for given values a, b, c, β, and V correspond to last significant position. Space group was fixed for fitting according to literature known parent material property.

T [K]	space group	r_{wp}	a [Å]	b [Å]	c [Å]	α [°]	β [°]	γ [°]	V [Å³]	branch
323	$P2_1/m$	1.65	18.626	10.273	9.556	90	93.19	90	1826	*h*
343	$P2_1/m$	1.62	18.612	10.313	9.559	90	93.23	90	1832	*h*
363	$P2_1/m$	1.70	18.610	10.359	9.563	90	93.26	90	1841	*h*
383	$P2_1/m$	1.97	18.611	10.391	9.565	90	93.17	90	1847	*h*
403	$P2_1/m$	2.14	18.611	10.427	9.567	90	93.10	90	1854	*h*
423	$P2_1/m$	2.14	18.603	10.483	9.569	90	93.20	90	1863	*h*
443	$P2_1/m$	1.98	18.565	10.564	9.571	90	93.60	90	1873	*h*
453	$P2_1/m$	1.96	18.587	10.583	9.568	90	93.62	90	1878	*h*
463	$P2_1/m$	1.88	18.596	10.595	9.571	90	93.63	90	1882	*h*
473	$P2_1/m$	1.90	18.613	10.603	9.572	90	93.62	90	1885	*h*
483	$P2_1/m$	1.44	18.615	10.612	9.576	90	93.78	90	1887	*h*
493	$P2_1/m$	1.50	18.634	10.633	9.574	90	93.72	90	1893	*h*
503	$P2_1/m$	1.44	18.657	10.628	9.580	90	93.77	90	1895	*h*
513	$P2_1/m$	1.48	18.679	10.628	9.579	90	93.63	90	1898	*h*
503	$P2_1/m$	1.44	18.660	10.625	9.579	90	93.75	90	1895	*c*
493	$P2_1/m$	1.56	18.640	10.615	9.575	90	93.71	90	1891	*c*
483	$P2_1/m$	1.50	18.615	10.612	9.576	90	93.75	90	1888	*c*
473	$P2_1/m$	1.48	18.625	10.606	9.576	90	94.00	90	1887	*c*
463	$P2_1/m$	1.46	18.604	10.602	9.571	90	93.93	90	1883	*c*
453	$P2_1/m$	1.53	18.585	10.591	9.575	90	94.21	90	1880	*c*
443	$P2_1/m$	1.46	18.568	10.566	9.571	90	94.25	90	1873	*c*
423	$P2_1/m$	1.50	18.532	10.520	9.566	90	94.30	90	1860	*c*
403	$P2_1/m$	1.58	18.515	10.476	9.562	90	94.12	90	1850	*c*
383	$P2_1/m$	1.55	18.539	10.419	9.550	90	93.78	90	1841	*c*
363	$P2_1/m$	1.56	18.546	10.364	9.543	90	93.63	90	1831	*c*
343	$P2_1/m$	1.56	18.556	10.318	9.534	90	93.45	90	1822	*c*
323	$P2_1/m$	1.54	18.580	10.268	9.527	90	93.36	90	1814	*c*

Supplementary Table 4. Results of the Pawley fitting of the VTPXRDs recorded for **D2** (*h* = heating branch, *c* = cooling branch). Errors for given values a, b, c, β, and V correspond to last significant position. Space group was fixed for fitting according to literature known parent material property.

T [K]	space group	r_{wp}	a [Å]	b [Å]	c [Å]	α [°]	β [°]	γ [°]	V [Å³]	branch
323	$P2_1/m$	1.94	18.704	10.329	9.608	90	92.88	90	1854	*h*
343	$P2_1/m$	1.91	18.689	10.370	9.612	90	93.02	90	1860	*h*
363	$P2_1/m$	1.75	18.666	10.405	9.618	90	93.20	90	1865	*h*
383	$P2_1/m$	1.56	18.681	10.429	9.621	90	93.13	90	1872	*h*
403	$P2_1/m$	1.72	18.683	10.456	9.623	90	93.12	90	1877	*h*
423	$P2_1/m$	1.61	18.660	10.502	9.627	90	93.24	90	1884	*h*
443	$P2_1/m$	1.65	18.631	10.581	9.621	90	93.46	90	1893	*h*
453	$P2_1/m$	1.82	18.638	10.606	9.623	90	93.46	90	1899	*h*
463	$P2_1/m$	1.81	18.654	10.622	9.625	90	93.48	90	1904	*h*
473	$P2_1/m$	1.80	18.677	10.643	9.628	90	93.43	90	1910	*h*
483	$P2_1/m$	1.76	18.705	10.663	9.631	90	93.37	90	1918	*h*
493	$P2_1/m$	1.94	18.727	10.679	9.632	90	93.40	90	1923	*h*
503	$P2_1/m$	1.97	18.751	10.687	9.636	90	93.43	90	1928	*h*
513	$P2_1/m$	2.24	18.763	10.676	9.638	90	93.46	90	1927	*h*
503	$P2_1/m$	2.35	18.746	10.683	9.637	90	93.45	90	1926	*c*
493	$P2_1/m$	2.30	18.730	10.674	9.636	90	93.44	90	1923	*c*
483	$P2_1/m$	2.22	18.710	10.665	9.632	90	93.47	90	1919	*c*
473	$P2_1/m$	2.17	18.690	10.651	9.630	90	93.46	90	1914	*c*
463	$P2_1/m$	2.25	18.679	10.642	9.629	90	93.46	90	1911	*c*
453	$P2_1/m$	2.74	18.655	10.618	9.625	90	93.48	90	1903	*c*
443	$P2_1/m$	2.42	18.631	10.601	9.620	90	93.56	90	1896	*c*
423	$P2_1/m$	2.44	18.608	10.549	9.612	90	93.66	90	1883	*c*
403	$P2_1/m$	2.48	18.604	10.497	9.605	90	93.65	90	1872	*c*
383	$P2_1/m$	2.03	18.611	10.450	9.595	90	93.58	90	1862	*c*
363	$P2_1/m$	2.36	18.586	10.408	9.591	90	93.67	90	1851	*c*
343	$P2_1/m$	2.45	18.579	10.371	9.588	90	93.72	90	1844	*c*
323	$P2_1/m$	3.67	18.579	10.371	9.588	90	93.72	90	1844	*c*

Supplementary Table 5. Results of the Pawley fitting of the VTPXRDs recorded for **D3** (*h* = heating branch, *c* = cooling branch). Errors for given values a, b, c, β, and V correspond to last significant position. Space group was fixed for fitting according to literature known parent material property.

| T [K]	space group	r_{wp}	a [Å]	b [Å]	c [Å]	α [°]	β [°]	γ [°]	V [Å³]	branch
323	$P2_1/m$	2.27	18.528	10.305	9.542	90	93.88	90	1818	*h*
343	$P2_1/m$	2.30	18.534	10.342	9.548	90	93.88	90	1826	*h*
363	$P2_1/m$	2.06	18.532	10.371	9.553	90	93.88	90	1832	*h*
383	$P2_1/m$	1.94	18.554	10.404	9.554	90	93.75	90	1840	*h*
403	$P2_1/m$	1.87	18.563	10.435	9.556	90	93.72	90	1847	*h*
423	$P2_1/m$	1.88	18.548	10.478	9.561	90	93.85	90	1854	*h*
443	$P2_1/m$	1.86	18.531	10.502	9.558	90	94.01	90	1856	*h*
453	$P2_1/m$	1.91	18.539	10.504	9.561	90	94.02	90	1857	*h*
463	$P2_1/m$	1.91	18.553	10.507	9.562	90	94.04	90	1859	*h*
473	$P2_1/m$	1.89	18.567	10.501	9.564	90	94.03	90	1860	*h*
483	$P2_1/m$	1.97	18.580	10.501	9.565	90	94.04	90	1862	*h*
493	$P2_1/m$	2.06	18.601	10.500	9.569	90	94.02	90	1864	*h*
503	$P2_1/m$	2.21	18.619	10.501	9.572	90	94.00	90	1867	*h*
513	$P2_1/m$	2.63	18.641	10.515	9.573	90	94.01	90	1872	*h*
503	$P2_1/m$	2.81	18.617	10.511	9.574	90	94.05	90	1869	*c*
493	$P2_1/m$	2.90	18.597	10.504	9.574	90	94.12	90	1865	*c*
483	$P2_1/m$	2.96	18.578	10.502	9.574	90	94.16	90	1863	*c*
473	$P2_1/m$	2.87	18.556	10.500	9.571	90	94.16	90	1860	*c*
463	$P2_1/m$	2.88	18.539	10.500	9.570	90	94.20	90	1858	*c*
453	$P2_1/m$	2.78	18.518	10.502	9.568	90	94.22	90	1856	*c*
443	$P2_1/m$	2.73	18.504	10.503	9.565	90	94.22	90	1854	*c*
423	$P2_1/m$	2.64	18.485	10.497	9.558	90	94.23	90	1850	*c*
403	$P2_1/m$	2.66	18.473	10.484	9.551	90	94.25	90	1845	*c*
383	$P2_1/m$	2.72	18.461	10.447	9.542	90	94.22	90	1835	*c*
363	$P2_1/m$	2.61	18.483	10.388	9.536	90	94.08	90	1826	*c*
343	$P2_1/m$	2.50	18.511	10.326	9.530	90	93.94	90	1817	*c*
323	$P2_1/m$	2.52	18.486	10.293	9.520	90	93.96	90	1807	*c*

S7 Thermal expansion calculation

Cell parameter obtained from Pawley fits (S6) were used as input for PASCal to determine principal axis strain and coefficients of thermal expansion (CTE).[8] Due to the observed second order phase transition CTEs were calculated from separate input data sets for low temperature (up to 403 K). Principal directions are attributed to the approximate axis of projection on [uvw] for best comparison of low and high temperature CTEs.

Supplementary Table 6. Principal axis directions, their approximate projection onto [uvw] and thermal expansion coefficients α for 323-403 K with standard deviation.

|		α [M/K]	Δα [M/K]	u	v	w	appr. axis
D0	X_1	-82.0821	9.0308	0.703	0	0.7112	[101]
	X_2	60.9056	3.1341	-0.2341	0	0.9722	[001]
	X_3	**235.2796**	**8.4081**	**0**	**1**	**0**	**[010]**
	V	216.4853	11.5873				
D1	X_1	-10.3286	4.05	0.8028	0	0.5963	[101]
	X_2	16.7716	0.9286	-0.1681	0	0.9858	[001]
	X_3	**188.1439**	**3.7886**	**0**	**1**	**0**	**[010]**
	V	195.0737	2.3586				
D2	X_1	-28.5696	12.603	0.6458	0	0.7635	[101]
	X_2	32.8041	6.263	-0.2831	0	0.9591	[001]
	X_3	**151.8102**	**7.6035**	**0**	**1**	**0**	**[010]**
	V	156.3307	1.7664				
D3	X_1	4.0495	1.2498	0.9933	0	0.1153	[100]
	X_2	40.9069	1.81	0.004	0	1	[001]
	X_3	**156.0797**	**2.3603**	**0**	**1**	**0**	**[010]**
	V	202.1619	2.4249				

S8 Electron microscopy

Scanning transmission electron microscopy (STEM) micrographs with energy dispersive X-ray spectroscopy (EDS) elemental mappings were recorded with a JEM-ARM200F "NEOARM" microscope from JEOL (Germany) GmbH with a cold FEG electron source operated at 200 kV. Samples were prepared by depositing a drop of the solid dispersed in ethanol onto carbon-coated copper grids (200 mesh) and dried in air. The electron tomography was carried out in a 2 or 3° step using the TEMography™ software for both recording and 3D-image reconstruction.
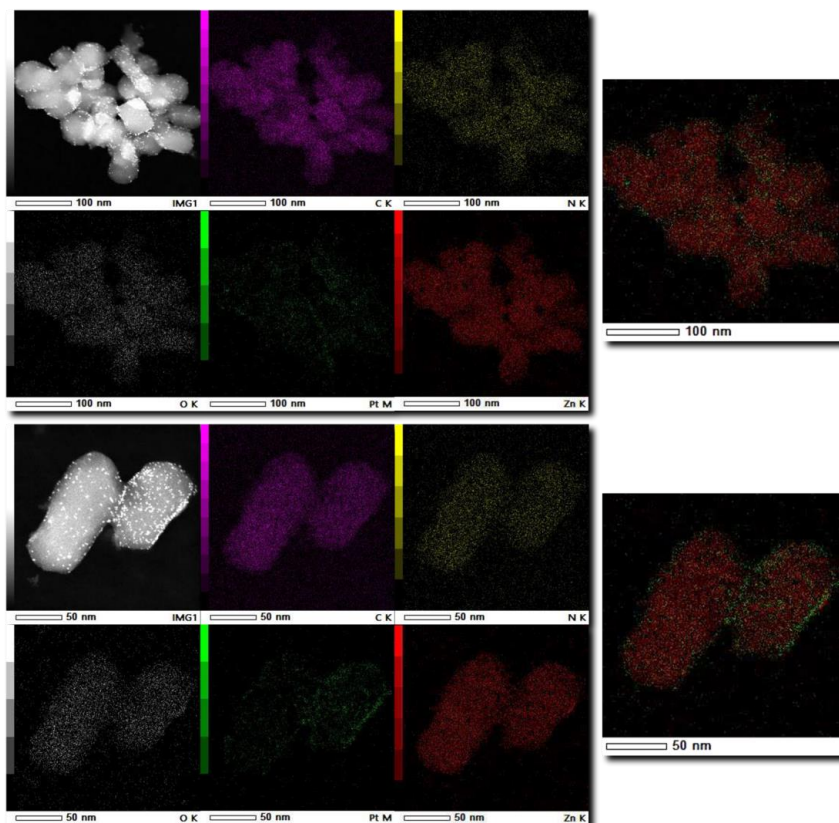
Supplementary Figure 7: STEM-EDS micrographs of two different **D1** crystallite formations. Darkfield TEM micrograph (top left) and EDS elemental mapping (top mid, top right, bottom row) shown with respect to single elements. Larger image (right) with Pt and Zn overlay (contrast adjusted for visibility). Purple: C, yellow: N, white: O, green: Pt, red: Zn.
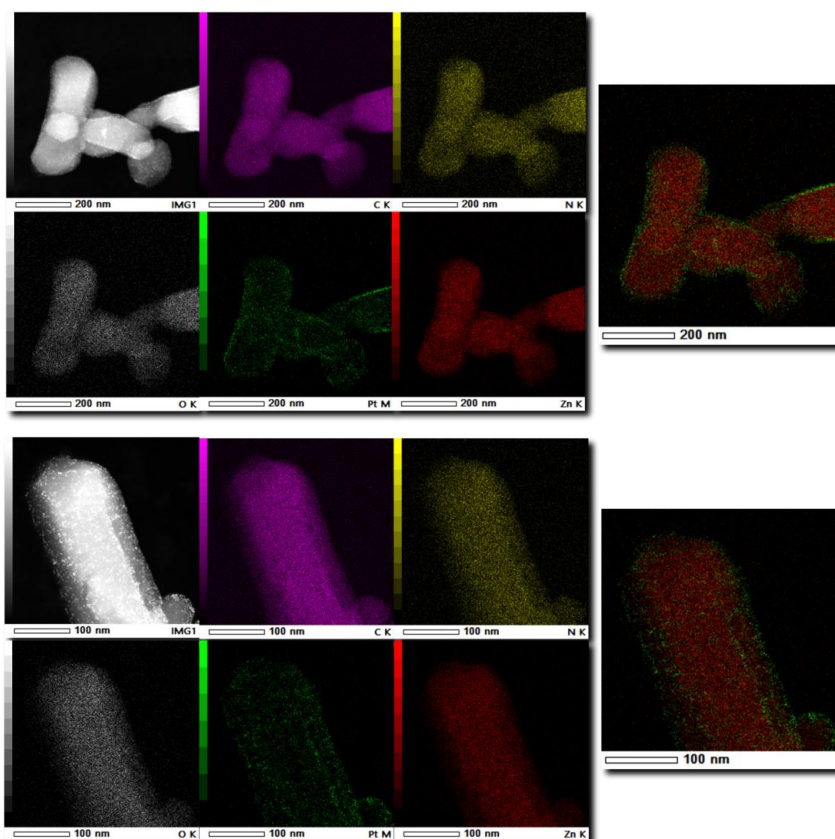
Supplementary Figure 8: STEM-EDS micrographs of two different **D2** crystallite formations. Darkfield TEM micrograph (top left) and EDS elemental mapping (top mid, top right, bottom row) shown with respect to single elements. Larger image (right) with Pt and Zn overlay. Purple: C, yellow: N, white: O, green: Pt, red: Zn.
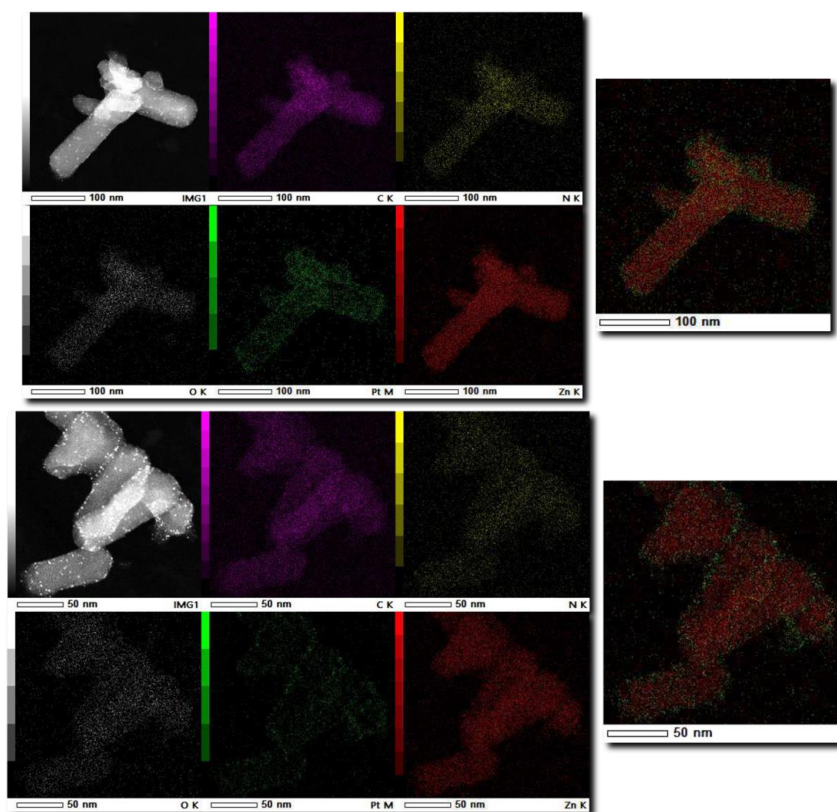
Supplementary Figure 9: STEM-EDS micrographs of two different **D3** crystallite formations. Darkfield TEM micrograph (top left) and EDS elemental mapping (top mid, top right, bottom row) shown with respect to single elements. Larger image (right) with Pt and Zn overlay (contrast adjusted for visibility). Purple: C, yellow: N, white: O, green: Pt, red: Zn.
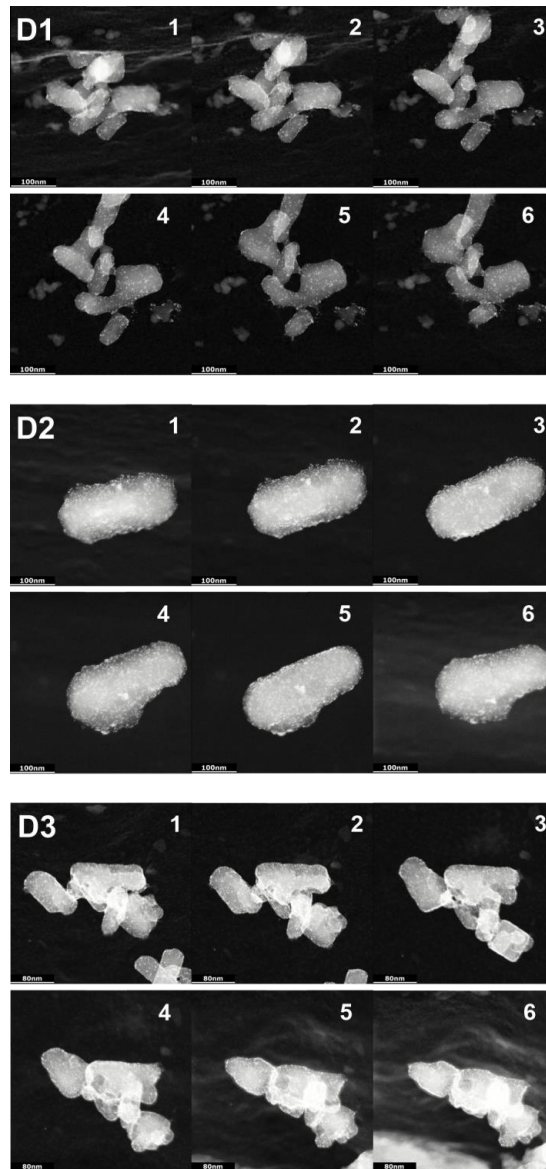
Supplementary Figure 10: Six selected examples of each tilt-series for **D1**, **D2**, and **D3** (out of ca. 40-60 per sample).

S9 Supplementary references

1. Henke, S., Schneemann, A., Wütscher, A. & Fischer, R. A. Directing the breathing behavior of pillared-layered metal-organic frameworks via a systematic library of functionalized linkers bearing flexible substituents. *J. Am. Chem. Soc.* **134,** 9464–9474; 10.1021/ja302991b (2012).

2. Schneemann, A., Henke, S., Schwedler, I. & Fischer, R. A. Targeted manipulation of metal-organic frameworks to direct sorption properties. *ChemPhysChem* **15,** 823–839; 10.1002/cphc.201300976 (2014).

3. Vervoorts, P. *et al.* Configurational Entropy Driven High-Pressure Behaviour of a Flexible Metal-Organic Framework (MOF). *Angew. Chem.* **60,** 787–793; 10.1002/anie.202011004 (2021).

4. Henke, S., Schneemann, A. & Fischer, R. A. Massive Anisotropic Thermal Expansion and Thermo-Responsive Breathing in Metal-Organic Frameworks Modulated by Linker Functionalization. *Adv. Funct. Mater.* **23,** 5990–5996; 10.1002/adfm.201301256 (2013).

5. ZareKarizi, F., Joharian, M. & Morsali, A. Pillar-layered MOFs: functionality, interpenetration, flexibility and applications. *J. Mater. Chem. A* **6,** 19288–19329; 10.1039/C8TA03306D (2018).

6. Henke, S., Schmid, R., Grunwaldt, J.-D. & Fischer, R. A. Flexibility and sorption selectivity in rigid metal-organic frameworks: the impact of ether-functionalised linkers. *Chemistry* **16,** 14296–14306; 10.1002/chem.201002341 (2010).

7. Lee, W.-J. *et al.* Synthesis of highly dispersed Pt nanoparticles into carbon supports by fluidized bed reactor atomic layer deposition to boost PEMFC performance. *NPG Asia Mater* **12**; 10.1038/s41427-020-0223-x (2020).

8. Cliffe, M. J. & Goodwin, A. L. PASCal : a principal axis strain calculator for thermal expansion and compressibility determination. *J. Appl. Crystallogr.* **45,** 1321–1329; 10.1107/S0021889812043026 (2012).

7.3 STUDY III

Supporting Information

Guest- and Temperature-Switchability of a Flexible Metal-Organic Framework with Surface-Mounted Nanoparticles

Jan Berger,[†$] Stephanie Terruzzi,[§$] Hana Bunzen,[‡] Marcello Marelli,[┴] Luca Braglia,[※] Roland A. Fischer,[†] Valentina Colombo,[§┴]* and Gregor Kieslich[†]*

[†]Inorganic and Metal-Organic Chemistry, Technical University of Munich, Lichtenbergstr. 4, 85748 Garching, Germany

[§]Department of Chemistry, University of Milan, Via Golgi 19, 20133 Milan, Italy

[‡]Institute of Physics, University of Augsburg, Universitätsstr. 1, 86159 Augsburg, Germany

[┴]CNR SCITEC - Istituto di Scienze e Tecnologie Chimiche "Giulio Natta", Via Fantoli 16/15, 20138 Milan, Italy

[※]CNR-Istituto Officina dei Materiali, TASC, 34149 Trieste, Italy

[$]these authors contributed equally

Supplementary Sections

S1 Linker, MOF and NP@MOF synthesis

S1.1 General remarks

All chemicals were purchased from commercial suppliers and used without further purification. MOF synthesis was conducted with pure N,N-dimethylformamide (DMF) (99.8%). Fresh DMF was used for solvent exchange. Ethanol for solvent exchange was purchased as technical grade and redistilled prior use. Fluorescent silica nanoparticles were obtained commercially via Micromod Partikeltechnologie GmbH. All experiments and procedures were carried out on air unless stated otherwise.

Liquid state NMR spectra were recorded on a Bruker Ultrashield DRX400 spectrometer (^{1}H: 400.13 MHz) at ambient temperature (298 K). The ^{1}H NMR spectroscopic chemical shifts δ are reported in ppm relative to tetramethyl silane. ^{1}H NMR spectra are referenced against the residual proton resonances of the respective deuterated solvent as an internal standard (DMSO-d_6: δ (1H) = 2.50 ppm). MOF samples were digested and subsequently measured in 0.5 ml DMSO-d_6 with 0.05 ml DCl (7.6 N), all other substances were dissolved and measured in DMSO-d_6.

S1.2 Linker synthesis

Organic linkers were synthesized via Williamson ether synthesis according to literature known procedures,[1] albeit slightly altered/optimized.

Dimethyl-2,5-dihydroxy-1,4-benzenedicarboxylate

2,5-Dihydroxyterephthalic acid (6,0 g, 30.3 mmol) is dispersed in MeOH (180 mL) and H_2SO_4 (98%, 5 mL, 94 mmol) is added dropwise at room temperature while stirring and the reaction mixture is refluxed for 12 h at 75 °C. The precipitate is subsequently filtrated and thoroughly washed with distilled water. After removing residual solvent *in vacuo* at 70 °C, the product is obtained as yellow powder (6.63 g, 28.9 mmol, 95 %).

^{1}H-NMR (400.13 MHz, DMSO-d_6) δ (ppm) = 9.82 (s, 2H, COOH), 7.26 (s, 2H, H$_{Ar}$), 3.86 (s, 6H, CH$_3$).

2,5-Bis(methoxyethoxy)-1,4-benzenedicarboxylic acid (H$_2$BMEbdc)

Dimethyl-2,5-dihydroxy-1,4-benzenedicarboxylate (1.19 g, 5.25 mmol, 1.0 eq.) and dry K_2CO_3 (3.26 g, 23.6 mmol, 4.5 eq.) are suspended in DMF (45 mL). 1-Bromo-2-methoxyethane (1.97 mL, 21.0 mmol, 3.0 eq.) is added dropwise while stirring. The reaction mixture is refluxed overnight at 85 °C, the solvent is subsequently removed at 70 °C under reduced pressure (5 mbar). A solution of NaOH (0.74 g, 18.4 mmol, 3.5 eq.) in H_2O (60 mL) is added to the residue. The reaction mixture is again refluxed overnight at 110 °C. After cooling to room temperature HCl (10%) is added dropwise until the carboxylic acid is completely precipitated. The solid is filtered and thoroughly washed with distilled water. After removing residual solvent *in vacuo* at 70 °C, the product (1.50 g, 4.77 mmol, 90 %) is obtained as slightly yellow powder.

^{1}H NMR (400.13 MHz, DMSO-$d6$) δ (ppm) = 12.93 (bs, 2H, COOH), 7.30 (s, 2H, H$_{Ar}$), 4.15 – 4.07 (m, 4H, O-CH$_2$), 3.67 – 3.60 (m, 4H, O-CH$_2$), 3.30 (s, 6H, O-CH$_3$).

S1.4 $Zn_2(BME-bdc)_2$dabco and $Pt@Zn_2(BME-bdc)_2$dabco synthesis

General procedure for Zn_2(BME-bdc)$_2$dabco and $Pt@Zn_2$(BME-bdc)$_2$dabco

$Zn(NO_3)_2 \cdot 6\ H2O$ (89 mg, 0.30 mmol, 1 eq.), 1,4-diazabicyclo[2.2.2]octane (dabco) (34 mg, 0.30 mmol, 1 eq), the 2,5-functionalized 1,4-benzenedicarboxylic acid (0.30 mmol, 1 eq; $H_2BMEbdc$: 95 mg) and the corresponding amount of potassium tetrachloride platinate (see Table S1) are suspended in dimethyl formamide (DMF) (10 ml) in a 20 ml screw cap vial. The mixture is sonicated until complete suspension and absence of sedimentation (3-10 min), then heated in an oven for 24 or 48 h (see Table S1) to yield crystalline white to light grey powder. After cooling to room temperature, the formed crystalline white to light grey powder is washed and activated.

Washing and activation procedure

Washing and solvent exchange steps are conducted by vigorously shaking solid and solvent in a capped centrifuge tube, then centrifugation and decanting of the supernatant.

The obtained powder is washed immediately with DMF (3x 10 ml) until the supernatant is clear to yield the MOF material in its as-synthesized (**as**) state. While wet, this state is verified by X-ray powder diffraction (see S2).

To remove DMF the **as** material is first washed with ethanol (10 ml), then twice soaked in fresh ethanol (2x 10 ml) overnight, and lastly soaked once in dichloromethane (10 ml) overnight. The wet powder is then pre-dried on air at ambient conditions before proper activation *in vacuo* at r.t. for 16 h and subsequently at 70 °C for 4 h. The resulting **dry** sample is stored under argon for further use to rule out possibility of gradual hydrolysis during prolonged exposure to ambient moisture.

Table S1: Platinum precursor amounts and reaction conditions during MOF crystallization procedures.

ID	K_2PtCl_4 [mg]	temperature [°C]	heating time [h]
B0	none	120	48
B1	4.2	100	24
B2	10.4	120	24
B3	10.4	100	24

Linker and pillar incorporation ratio was verified via ^1H NMR (see above for specifications), CHNS contents were determined via combustion analysis. Zn and Pt contents were determined by atom adsorption spectroscopy or photometry for samples with more than 50 mg available with uncertainty of +- 0.1 w%. Elemental analysis was provided and conducted by the TUM CRC Microanalytical laboratory.

[Zn_2(BME-bdc)$_2$dabco – B0 (reference material)] ^1H NMR (400.13 MHz, DMSO-*d6*) δ (ppm) = 7.16 (s, 4H, H_{Ar}), 4.02 – 3.93 (m, 8H, Ph-O-CH$_2$), 3.54 (s, 12H, dabco), 3.52 – 3.47 (m, 8H, O-CH$_2$), 3.14 (s, 12H, O-CH$_3$). **Elemental analysis:** calculated C 47.08, H 5.11, N 3.23, O 29.51, Zn 15.07; found C 46.92, H 5.03, N 3.37, Zn 15.01;

[$Pt@Zn_2$(BME-bdc)$_2$dabco – B1] ^1H NMR (400.13 MHz, DMSO-*d6*) δ (ppm) = 7.16 (s, 4H, H_{Ar}), 4.03 – 3.87 (m, 8H, Ph-O-CH$_2$), 3.54 (s, 12H, dabco), 3.53 – 3.43 (m, 8H, O-CH$_2$), 3.13 (s, 12H, O-CH$_3$). **Elemental analysis:** found C 45.28, H 4.84, N 3.30, Zn 14.4, Pt 1.1;

[Pt@Zn$_2$(BME-bdc)$_2$dabco – B2] **^{1}H NMR** (400.13 MHz, DMSO-*d*6) δ (ppm) = 7.15 (s, 4H, H$_{Ar}$), 3.96 (s, 8H, Ph-O-CH$_2$), 3.54 (s, 12H, dabco), 3.49 (m, 8H, O-CH$_2$), 3.12 (s, 12H, O-CH$_3$). **Elemental analysis:** found C 44.98, H 4.87, N 3.32, Zn 15.5, Pt 2.0;

[Pt@Zn$_2$(BME-bdc)$_2$dabco – B3] **^{1}H NMR** (400.13 MHz, DMSO-*d*6) δ (ppm) = 7.17 (s, 4H, H$_{Ar}$), 4.04 – 3.93 (m, 8H, Ph-O-CH$_2$), 3.54 (s, 12H, dabco), 3.55 – 3.44 (m, 8H, O-CH$_2$), 3.15 (s, 12H, O-CH$_3$). **Elemental analysis:** found C 44.63, H 4.87, N 3.33, Zn 14.7, Pt 2.8;

S1.5 SiO$_2$@Zn$_2$(BME-bdc)$_2$dabco synthesis

SiO$_2$@Zn$_2$(BME-bdc)$_2$dabco (**B4**) was prepared similar to the *"bottle around the ship"* encapsulation method, where pre-formed fluorescent silica nanoparticles (see Table S2) are added as aqueous colloidal suspension (0.1 mL) to the MOF precursors for solvothermal MOF synthesis. Synthesis conditions are otherwise identical to material **B0** (see above).

Washing and Activation.

Washing was conducted as described above. The as synthesised samples were thermally activated at high temperature under vacuum (150 °C for 2h, plus 80 °C overnight) and stored under argon in a glovebox.

Table S2: Silica nanoparticle suspension properties.

material	type	size [nm]	solvent	quantity [mL]	loading (calc.)
SiO$_2$	fluorescent, suspension (25 mg/mL), red	30	water	0.100	~1%

[SiO$_2$@Zn$_2$(BME-bdc)$_2$dabco – B4] **^{1}H NMR** (400.13 MHz, DMSO-*d*6) δ (ppm) = 7.15 (s, 4H, H$_{Ar}$), 3.98 – 3.88 (m, 8H, Ph-O-CH$_2$), 3.53 (s, 12H, dabco), 3.52 – 3.43 (m, 8H, O-CH$_2$), 3.14 (s, 12H, O-CH$_3$). **Elemental analysis**: found C 44.15, H 4.95, N 3.01;

S2 Powder X-ray diffraction

PXRDs of the as-synthesized (**as**) samples **B0-4** were measured using Bragg-Bentano geometry with a silicon wafer plate on a Rigaku Benchtop MiniFlex 600-C. X-ray Cu Kα radiation (λ = 1.54 Å) with a voltage of 40 kV and current of 15 mA was used

Activated (**dry**) samples and samples after a CO_2 physisorption cycle were filled in glass capillaries in a glovebox under argon atmosphere and PXRDs were measured in Debeye-Scherrer geometry on a PANalytical Empyrean diffractometer. X-ray Cu Kα radiation (λ = 1.54 Å) with a voltage of 45 kV and current of 40 mA was used.
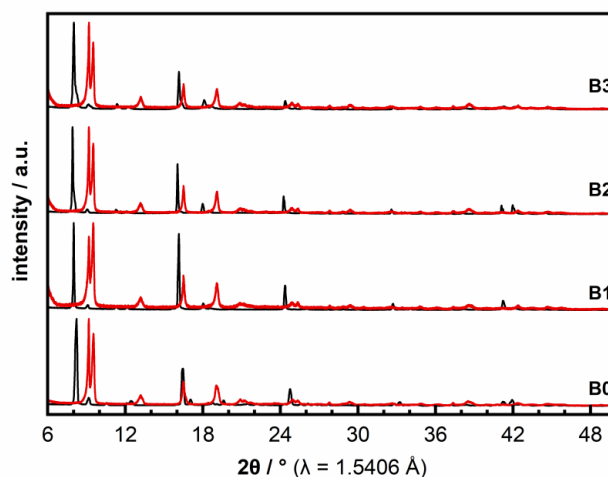
Figure S1. PXRD patterns of all composites with Pt NPs in the range of 2θ = 6-50°. Black: as-synthesized (**as**) with infiltrated DMF; red: activated (**dry**). Transition from **lp** state in **as** to **np** state in **dry** is observable by shift of the 110 reflection from 2θ = 8.2-8.4° to 9.7° and intensity increase of the 001 reflection at 2θ = 9.2°. Due to the very low NP loading and significant peak broadening coming from diffraction domains in the nano regime, no peaks corresponding to Pt nanoparticles can be observed at the expected angles around 40° (I(111)) and 47° (I(200)) 2θ.[2]

S3 Physisorption isotherms

Adsorption measurements with N_2 (>99.999 vol%) at 77 K and CO_2 (>99.995 vol%) at 195 K were carried out on a 3Flex Physisorption from Micromeritics Instrument Corp., which uses a manometric method to determine the amount adsorbed at an equilibrated gas pressure.

Activated samples were transferred under dry argon atmosphere into preweighed sample tubes and capped with Micromeritics CheckSeals. Samples were subsequently activated again at 80 °C for 5 h under dynamic vacuum of ca. $1x10^{-3}$ mbar using a SmartVacPrep by Micromeritics Instrument Corp. to ensure absence of unwanted adsorbates and identical pre-measurement states of all samples. The mass of the adsorbent was then recorded, generally in the range of 50-70 mg. To facilitate proper degassing in context of the highly diffusion hindering pore environment, prior to each measurement samples were evacuated in situ at 80 °C for at least 20 h under dynamic vacuum of ca. $1x10^{-5}$ mbar. Free space of the sample tube was determined after measuring each adsorption isotherm using helium (>99.999 vol%). A liquid nitrogen bath was used for measurements at 77 K and a dry ice - acetone bath was used for measurements at 195 K.
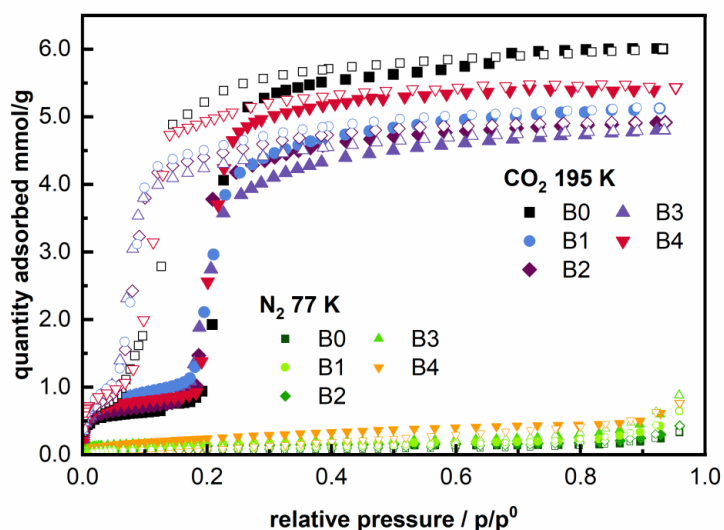

Figure S2: Isotherms of N_2 at 77 K (green) and CO_2 at 195 K (blue/purple) on all materials of the **BME** series with adsorption (filled symbols) and desorption (empty symbols), respectively. N_2 is not adsorbed in significant quantity.

S4 Thermogravimetric analysis and differential scanning calorimetry

Thermogravimetric analysis coupled with differential scanning calorimetry (TGA-DSC) was conducted on a Netzsch TG-DSC STA 449 F5 in a temperature range from 25 °C to 800 °C with a heating rate of 10 K min^{-1} under argon flow (flow rate: 20 mL min^{-1}). It should be noted that the sample is briefly (few seconds) exposed to air before the measurement when the aluminium oxide pan is transferred from the argon filled transport vial to the sample holder stage.
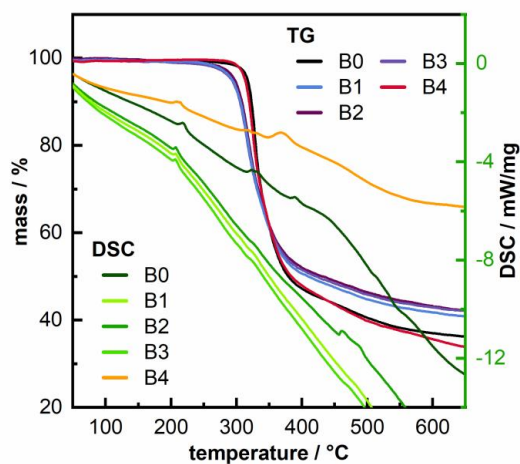
Figure S3: TGA-DSC of **BME** series. Notably, endothermic DSC signals at 210 °C and 220 °C indicate a thermally induced phase transition for each sample of the series.

S5 Variable temperature X-ray powder diffraction

VTPXRD experiments were conducted using a custom-made sample heater (Officina Elettrotecnica di Tenno, Ponte Arche, Italy) plugged in a Bruker AXS D8 Advance diffractometer with Bragg-Brentano geometry (University of Milan). About 10 mg of the compound were deposited on an aluminium sample-holder and heated in air from 30 °C up to 290 °C with steps of 20 °C. Temperature stabilization time between each measurement was two minutes. A PXRD pattern was acquired at each step using X-ray Cu Kα radiation (λ = 1.54 Å). The temperature difference between sensor reading and sample of the D8 heating system is circa -10 °C (*e.g.* measured T of 220 °C corresponds to 210 °C on the sample), less at lower to medium temperatures below 150 °C.
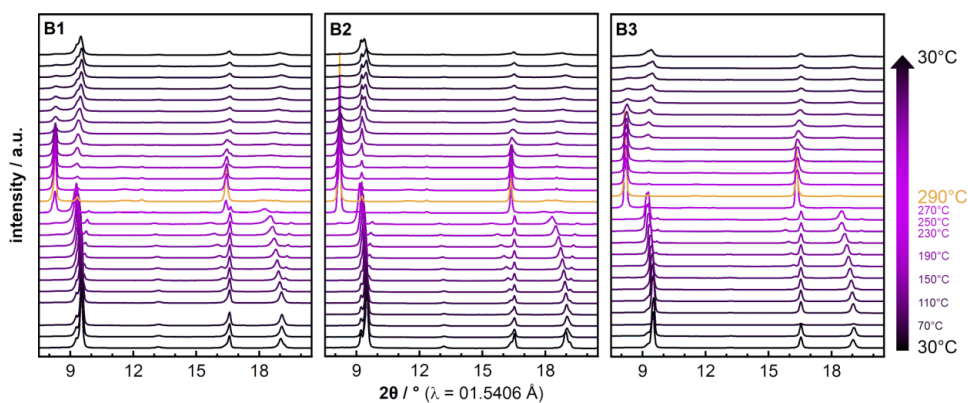

Figure S4. VTPXRD pattern series comparing all Pt@MOF composites in the range of 2θ = 7.5-20.5. Pattern at highest temperature highlighted in orange.

S6 Le Bail profile fitting and unit cell parameters

For experimental details and raw patterns see section S5. Tables S3-6 report the results after whole powder pattern refinements which were carried out adopting the Le Bail method[3] as implemented in TOPAS-Academic version 7 (by Coelho Software).[4] As starting point, the unit cell parameters already reported in the literature were used.

Note that in the temperature range from circa 150 to 270 °C (heating) and from circa 230 to 70 °C (cooling) both the *np* and the *lp* form are present. However, all data presented in Tables S3-5 have been obtained *via* single-phase fits using the monoclinic space group *C*2/*m*, in order to be able to compare unit cell parameters.

Table S3. Results of the Le Bail profile fitting of the VTPXRDs recorded for **B0** (*h* = heating branch, *c* = cooling branch). Errors for given values a, b, c, β, and V correspond to last significant position. Space groups were fixed for fitting according to literature known material property.

T [°C]	space group	a [Å]	b [Å]	c [Å]	α [°]	β [°]	γ [°]	V [Å³]	branch
30	*C*2/*m*	18.693(2)	10.721(4)	9.625(7)	90	90.673(6)	90	1929.0(2)	*h*
50	*C*2/*m*	18.652(2)	10.720(8)	9.622(9)	90	90.820(0)	90	1924.0(6)	*h*
70	*C*2/*m*	18.667(1)	10.722(7)	9.623(4)	90	90.753(2)	90	1926.0(7)	*h*
90	*C*2/*m*	18.694(0)	10.725(9)	9.627(8)	90	90.683(1)	90	1930.3(2)	*h*
110	*C*2/*m*	18.753(6)	10.736(2)	9.628(2)	90	90.568(3)	90	1938.4(8)	*h*
130	*C*2/*m*	18.820(0)	10.758(8)	9.640(2)	90	90.546(4)	90	1951.8(7)	*h*
150	*C*2/*m*	18.883(6)	10.767(8)	9.645(1)	90	90.482(8)	90	1961.1(1)	*h*
170	*C*2/*m*	18.948(7)	10.768(7)	9.639(7)	90	90.674(8)	90	1966.8(6)	*h*
190	*C*2/*m*	19.009(2)	10.765(4)	9.626(4)	90	90.805(6)	90	1969.7(6)	*h*
210	*C*2/*m*	19.051(6)	10.781(2)	9.627(5)	90	91.057(4)	90	1977.1(4)	*h*
230	*C*2/*m*	19.050(7)	10.771(4)	9.643(2)	90	91.078(3)	90	1978.4(5)	*h*
250	*C*2/*m*	19.070(2)	10.851(3)	9.839(0)	90	91.754(7)	90	2035.0(9)	*h*
270	*C*2/*m*	19.319(8)	10.759(5)	9.964(5)	90	90.273(9)	90	2071.3(2)	*h*
290	*C*2/*m*	16.832(5)	14.314(5)	9.636(2)	90	90.361(6)	90	2321.7(7)	*h*
280	*C*2/*m*	16.830(6)	14.321(7)	9.631(7)	90	90.302(0)	90	2321.6(3)	*c*
260	*C*2/*m*	16.826(8)	14.319(0)	9.630(6)	90	90.349(5)	90	2320.3(9)	*c*
240	*C*2/*m*	16.756(1)	14.338(0)	9.629(3)	90	90.382(8)	90	2313.3(7)	*c*
220	*C*2/*m*	16.704(2)	14.312(2)	9.639(1)	90	90.541(2)	90	2304.3(6)	*c*
200	*C*2/*m*	18.880(3)	10.759(3)	9.625(0)	90	91.473(7)	90	1954.5(6)	*c*
180	*C*2/*m*	18.918(1)	10.774(1)	9.624(5)	90	91.409(3)	90	1961.1(2)	*c*
160	*C*2/*m*	19.074(9)	10.806(0)	9.647(1)	90	90.832(7)	90	1988.2(7)	*c*
120	*C*2/*m*	19.038(3)	10.812(2)	9.673(9)	90	90.511(3)	90	1991.2(5)	*c*
100	*C*2/*m*	18.887(1)	10.766(0)	9.617(2)	90	90.697(2)	90	1955.4(0)	*c*
80	*C*2/*m*	18.849(3)	10.761(5)	9.622(0)	90	90.626(2)	90	1951.6(7)	*c*
60	*C*2/*m*	18.846(2)	10.769(1)	9.639(1)	90	90.584(8)	90	1956.2(0)	*c*
40	*C*2/*m*	18.850(3)	10.769(4)	9.642(7)	90	90.621(1)	90	1957.4(2)	*c*
30	*C*2/*m*	18.846(3)	10.762(7)	9.636(8)	90	90.600(6)	90	1954.5(9)	*c*

Table S4. Results of the Le Bail profile fitting of the VTPXRDs recorded for **B1** (*h* = heating branch, *c* = cooling branch). Errors for given values a, b, c, β, and V correspond to last significant position. Space groups were fixed for fitting according to literature known parent material property.

T [°C]	space group	a [Å]	b [Å]	c [Å]	α [°]	β [°]	γ [°]	V [Å³]	branch
30	C2/m	18.712(9)	10.705(4)	9.550(1)	90	91.021(5)	90	1912.8(7)	*h*
50	C2/m	18.680(3)	10.712(0)	9.563(1)	90	91.044(6)	90	1913.2(9)	*h*
70	C2/m	18.744(0)	10.727(9)	9.583(7)	90	91.020(3)	90	1926.8(3)	*h*
90	C2/m	18.735(3)	10.722(2)	9.571(6)	90	90.982(1)	90	1922.5(2)	*h*
110	C2/m	18.722(9)	10.685(5)	9.514(7)	90	91.117(1)	90	1903.2(0)	*h*
130	C2/m	18.757(7)	10.655(3)	9.481(0)	90	90.618(0)	90	1894.8(6)	*h*
150	C2/m	18.816(6)	10.628(6)	9.551(2)	90	90.743(5)	90	1910.0(4)	*h*
170	C2/m	18.759(2)	10.585(9)	9.555(9)	90	90.698(2)	90	1897.5(1)	*h*
190	C2/m	18.662(6)	10.517(9)	9.448(5)	90	91.257(9)	90	1854.2(3)	*h*
210	C2/m	18.609(2)	10.454(0)	9.427(6)	90	91.187(3)	90	1833.6(7)	*h*
230	C2/m	18.797(2)	10.360(9)	9.619(1)	90	90.640(3)	90	1873.2(7)	*h*
250	C2/m	17.802(0)	13.903(2)	9.659(5)	90	90.647(8)	90	2385.2(4)	*h*
270	C2/m	17.830(1)	13.901(4)	9.695(7)	90	90.646(0)	90	2403.0(7)	*h*
290	C2/m	17.925(1)	14.189(4)	9.820(5)	90	91.104(0)	90	2497.3(7)	*h*
270	C2/m	17.791(5)	13.859(9)	9.946(9)	90	91.528(2)	90	2451.9(3)	*c*
250	C2/m	17.750(2)	13.617(0)	9.986(3)	90	92.322(1)	90	2411.7(7)	*c*
230	C2/m	18.365(0)	13.486(4)	9.638(8)	90	91.159(7)	90	2386.8(6)	*c*
210	C2/m	18.342(2)	13.128(3)	9.550(1)	90	90.517(1)	90	2355.5(3)	*c*
190	C2/m	18.490(3)	13.172(3)	9.512(3)	90	90.762(9)	90	2316.6(3)	*c*
170	C2/m	19.447(7)	10.829(3)	10.74(2)	90	92.311(0)	90	2260.6(6)	*c*
150	C2/m	19.320(2)	10.842(1)	10.76(7)	90	91.982(1)	90	2254.1(0)	*c*
130	C2/m	19.212(8)	10.755(5)	10.71(4)	90	91.605(7)	90	2213.1(6)	*c*
110	C2/m	19.284(2)	10.771(6)	10.74(3)	90	91.543(9)	90	2230.8(9)	*c*
90	C2/m	19.354(5)	10.789(2)	10.28(7)	90	93.963(4)	90	2143.1(7)	*c*
70	C2/m	19.366(3)	10.793(1)	10.26(9)	90	94.135(0)	90	2141.0(4)	*c*
50	C2/m	19.287(8)	10.766(3)	10.22(7)	90	93.997(4)	90	2118.7(0)	*c*
30	C2/m	19.220(4)	10.752(0)	10.05(6)	90	92.918(1)	90	2075.6(5)	*c*

Table S5. Results of the Le Bail profile fitting of the VTPXRDs recorded for **B2** (*h* = heating branch, *c* = cooling branch). Errors for given values a, b, c, β, and V correspond to last significant position. Space groups were fixed for fitting according to literature known parent material property.

T [°C]	space group	a [Å]	b [Å]	c [Å]	α [°]	β [°]	γ [°]	V [Å³]	branch
30	C2/m	18.755(3)	10.715(5)	9.5626(3)	90	90.698(1)	90	1921.7(6)	*h*
50	C2/m	18.773(7)	10.745(5)	9.603(8)	90	90.751(3)	90	1937.2(5)	*h*
70	C2/m	18.773(1)	10.746(4)	9.606(5)	90	90.788(0)	90	1937.8(8)	*h*
90	C2/m	18.794(1)	10.740(0)	9.594(8)	90	91.026(8)	90	1936.3(9)	*h*
110	C2/m	18.950(0)	10.764(6)	9.617(5)	90	91.118(6)	90	1961.5(2)	*h*
130	C2/m	18.950(2)	10.736(2)	9.577(1)	90	91.101(0)	90	1948.1(4)	*h*
150	C2/m	18.970(5)	10.691(4)	9.523(5)	90	91.195(0)	90	1931.1(7)	*h*
170	C2/m	18.903(9)	10.758(1)	9.625(0)	90	90.545(6)	90	1957.3(8)	*h*
190	C2/m	18.905(9)	10.734(8)	9.581(2)	90	90.662(3)	90	1944.4(0)	*h*
210	C2/m	18.942(6)	10.716(9)	9.561(1)	90	90.852(2)	90	1940.7(4)	*h*
230	C2/m	19.019(8)	10.694(8)	9.617(1)	90	91.153(5)	90	1955.8(6)	*h*
250	C2/m	16.291(1)	14.264(0)	9.683(3)	90	91.893(8)	90	2248.9(4)	*h*
270	C2/m	17.000(8)	14.179(2)	9.641(7)	90	90.717(9)	90	2324.0(4)	*h*
290	C2/m	17.007(9)	14.187(4)	9.634(7)	90	90.579(6)	90	2324.7(4)	*h*
270	C2/m	17.015(5)	14.160(2)	9.630(4)	90	90.540(7)	90	2320.3(0)	*c*
250	C2/m	17.018(9)	14.166(0)	9.636(7)	90	90.496(6)	90	2323.2(5)	*c*
230	C2/m	16.956(5)	14.182(7)	9.647(6)	90	90.654(8)	90	2319.9(9)	*c*
210	C2/m	16.914(4)	14.153(6)	9.652(1)	90	90.763(1)	90	2310.5(2)	*c*
190	C2/m	16.906(5)	14.117(1)	9.620(0)	90	90.734(7)	90	2295.8(5)	*c*
170	C2/m	16.726(5)	14.210(7)	9.612(9)	90	91.749(9)	90	2283.8(9)	*c*
150	C2/m	16.756(1)	14.207(6)	9.617(9)	90	91.704(4)	90	2288.6(8)	*c*
130	C2/m	18.572(7)	10.540(8)	9.708(7)	90	91.509(7)	90	2015.5(0)	*c*
110	C2/m	18.993(0)	10.705(3)	9.585(3)	90	91.102(3)	90	1948.6(0)	*c*
90	C2/m	19.078(2)	10.752(0)	9.593(9)	90	90.777(3)	90	1967.8(1)	*c*
70	C2/m	18.971(3)	10.746(5)	9.585(6)	90	90.541(1)	90	1954.1(9)	*c*
50	C2/m	18.980(3)	10.753(5)	9.596(0)	90	90.542(1)	90	1958.5(3)	*c*
30	C2/m	18.993(3)	10.750(0)	9.589(7)	90	90.649(9)	90	1957.9(0)	*c*

Table S6. Results of the Le Bail profile fitting of the VTPXRDs recorded for **B3** (*h* = heating branch, *c* = cooling branch). Errors for given values a, b, c, β, and V correspond to last significant position. Space groups were fixed for fitting according to literature known parent material property.

T [°C]	space group	a [Å]	b [Å]	c [Å]	α [°]	β [°]	γ [°]	V [Å³]	branch
30	C2/m	18.688(6)	10.710(9)	9.565(4)	90	90.884(4)	90	1914.5(1)	h
50	C2/m	18.659(1)	10.716(3)	9.572(3)	90	91.035(8)	90	1913.7(5)	h
70	C2/m	18.666(8)	10.713(0)	9.578(0)	90	91.088(6)	90	1915.0(5)	h
90	C2/m	18.693(6)	10.720(9)	9.576(3)	90	90.984(7)	90	1918.9(3)	h
110	C2/m	18.748(9)	10.727(0)	9.595(5)	90	90.913(8)	90	1929.6(1)	h
130	C2/m	18.755(3)	10.709(2)	9.583(3)	90	90.389(1)	90	1924.8(2)	h
150	C2/m	18.781(0)	10.705(5)	9.588(7)	90	90.399(3)	90	1927.8(9)	h
170	C2/m	18.880(2)	10.753(7)	9.519(7)	90	90.762(1)	90	1932.6(6)	h
190	C2/m	18.908(3)	10.746(0)	9.537(1)	90	90.687(0)	90	1937.7(0)	h
210	C2/m	18.955(6)	10.730(2)	9.570(3)	90	90.799(0)	90	1946.4(0)	h
230	C2/m	19.017(8)	10.699(7)	9.622(9)	90	91.174(4)	90	1957.7(3)	h
250	C2/m	19.018(1)	10.699(7)	9.624(0)	90	91.185(8)	90	1957.9(5)	h
270	C2/m	16.983(4)	14.253(9)	9.665(6)	90	90.946(7)	90	2339.5(4)	h
290	C2/m	16.954(7)	14.284(5)	9.666(1)	90	90.909(1)	90	2340.7(4)	h
270	C2/m	16.987(1)	14.213(5)	9.658(7)	90	91.106(5)	90	2331.6(2)	c
250	C2/m	16.926(7)	14.247(1)	9.632(6)	90	90.505(8)	90	2322.8(9)	c
230	C2/m	16.945(5)	14.222(0)	9.665(8)	90	90.990(6)	90	2329.1(3)	c
210	C2/m	16.883(7)	14.208(7)	9.675(4)	90	91.030(4)	90	2320.7(3)	c
190	C2/m	16.846(1)	14.164(1)	9.660(6)	90	90.768(3)	90	2304.9(1)	c
170	C2/m	16.775(5)	14.177(9)	9.629(6)	90	91.395(4)	90	2289.6(5)	c
150	C2/m	16.746(8)	14.175(0)	9.621(6)	90	91.542(7)	90	2283.2(4)	c
130	C2/m	20.146(2)	10.731(8)	10.677(2)	90	93.877(1)	90	2303.1(8)	c
110	C2/m	20.137(9)	10.730(7)	10.678(4)	90	94.243(6)	90	2301.2(3)	c
90	C2/m	20.078(1)	10.741(2)	10.686(5)	90	91.304(4)	90	2304.1(0)	c
70	C2/m	19.878(0)	10.732(3)	10.595(7)	90	90.711(0)	90	2260.2(9)	c
50	C2/m	19.779(4)	10.737(2)	10.551(4)	90	90.876(6)	90	2240.6(3)	c
30	C2/m	19.475(6)	10.703(0)	10.355(4)	90	92.775(1)	90	2156.0(4)	c

Table S7. Results of the Le Bail profile fitting of the VTPXRDs recorded for **B4** (*h* = heating branch, *c* = cooling branch). Errors for given values a, b, c, β, and V correspond to last significant position. Space groups were fixed for fitting according to literature known parent material property.

T [°C]	space group	a [Å]	b [Å]	c [Å]	α [°]	β [°]	γ [°]	V [Å³]	branch
30	*C*2/*m*	18.757(7)	10.740(2)	9.633(9)	90	90.656(6)	90	1940.7(3)	*h*
50	*C*2/*m*	18.745(8)	10.750(2)	9.655(8)	90	90.900(1)	90	1945.6(0)	*h*
70	*C*2/*m*	18.745(1)	10.749(3)	9.652(6)	90	90.915(3)	90	1944.7(1)	*h*
90	*C*2/*m*	18.726(1)	10.734(5)	9.624(3)	90	90.870(2)	90	1934.4(1)	*h*
110	*C*2/*m*	18.789(0)	10.752(3)	9.635(3)	90	90.641(7)	90	1946.4(5)	*h*
130	*C*2/*m*	18.809(9)	10.749(7)	9.620(8)	90	90.581(9)	90	1945.2(1)	*h*
150	*C*2/*m*	18.899(6)	10.772(9)	9.643(8)	90	90.534(9)	90	1963.4(2)	*h*
170	*C*2/*m*	18.981(0)	10.785(0)	9.650(1)	90	90.614(9)	90	1975.3(6)	*h*
190	*C*2/*m*	18.995(2)	10.769(6)	9.620(3)	90	90.836(0)	90	1967.8(2)	*h*
210	*C*2/*m*	19.004(8)	10.750(8)	9.586(2)	90	91.022(2)	90	1958.3(1)	*h*
230	*C*2/*m*	18.962(4)	10.807(2)	9.675(9)	90	91.613(6)	90	1982.1(0)	*h*
250	*C*2/*m*	19.161(5)	10.806(3)	9.747(1)	90	91.129(0)	90	2017.9(0)	*h*
270	*C*2/*m*	16.795(7)	14.314(1)	9.628(6)	90	90.524(0)	90	2314.7(6)	*h*
290	*C*2/*m*	16.798(7)	14.301(1)	9.627(2)	90	90.558(7)	90	2312.7(3)	*h*
275	*C*2/*m*	16.788(4)	14.298(5)	9.622(7)	90	90.562(5)	90	2309.8(0)	*c*
250	*C*2/*m*	16.781(1)	14.294(4)	9.623(6)	90	90.537(4)	90	2308.3(6)	*c*
230	*C*2/*m*	16.751(9)	14.271(8)	9.643(4)	90	90.750(8)	90	2305.3(4)	*c*
210	*C*2/*m*	16.340(4)	14.277(0)	9.613(6)	90	92.266(6)	90	2241.0(0)	*c*
180	*C*2/*m*	19.990(1)	11.011(8)	9.727(4)	90	90.596(1)	90	2141.1(5)	*c*
160	*C*2/*m*	19.342(3)	10.844(0)	9.670(9)	90	90.718(5)	90	2028.2(7)	*c*
140	*C*2/*m*	19.051(6)	10.795(9)	9.643(3)	90	90.516(0)	90	1983.3(4)	*c*
120	*C*2/*m*	19.001(1)	10.800(4)	9.659(4)	90	90.574(0)	90	1982.2(1)	*c*
100	*C*2/*m*	18.849(1)	10.755(0)	9.609(5)	90	90.625(8)	90	1947.9(3)	*c*
80	*C*2/*m*	18.832(8)	10.762(8)	9.626(7)	90	90.702(6)	90	1951.1(2)	*c*
60	*C*2/*m*	18.804(2)	10.755(5)	9.628(2)	90	90.721(3)	90	1947.1(4)	*c*
40	*C*2/*m*	18.807(2)	10.759(8)	9.639(3)	90	90.716(2)	90	1950.4(6)	*c*
30	*C*2/*m*	18.804(5)	10.752(6)	9.630(6)	90	90.683(3)	90	1947.1(4)	*c*

S7 Electron microscopy

Scanning transmission electron microscopy (STEM) micrographs with energy dispersive X-ray spectroscopy (EDS) elemental mappings were recorded with a JEM-ARM200F "NEOARM" microscope from JEOL (Germany) GmbH with a cold FEG electron source operated at 200 kV. Samples **B1-3** were prepared by depositing a drop of the solid dispersed in ethanol onto carbon-coated copper grids (200 mesh) and dried in air.

Energy-filtered transmission electron microscopy (EFTEM) micrographs of sample **B4** were recorded on a ZEISS LIBRA200FE (LabCAT Istem, CNR-SCITEC) equipped with a Schottky FEG electron source operated at 200 kV, Kohler type (4 lenses) illumination, a HR objective lens (f = 1.7 mm, C_s = 1.2 mm, C_c = 1.2 mm) and a 2k × 2k SS-CCD detector, with the objective of observing the morphological and structural details of MOFs' crystallites and the nanoparticles with sub-nanometre resolution (point resolution = 0.24 nm).
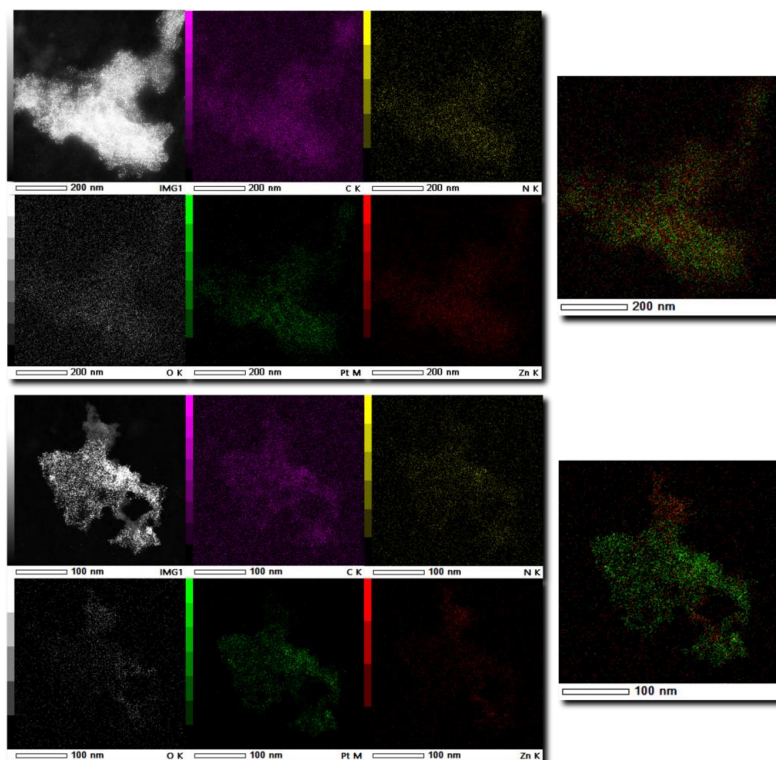
Figure S5. STEM-EDS micrographs of two different **B1** crystal formations. Darkfield TEM micrograph (top left) and EDS elemental mapping (top mid, top right, bottom row) shown with respect to single elements. Larger image (right) with Pt and Zn overlay (contrast adjusted for visibility). Purple: C, yellow: N, white: O, green: Pt, red: Zn.
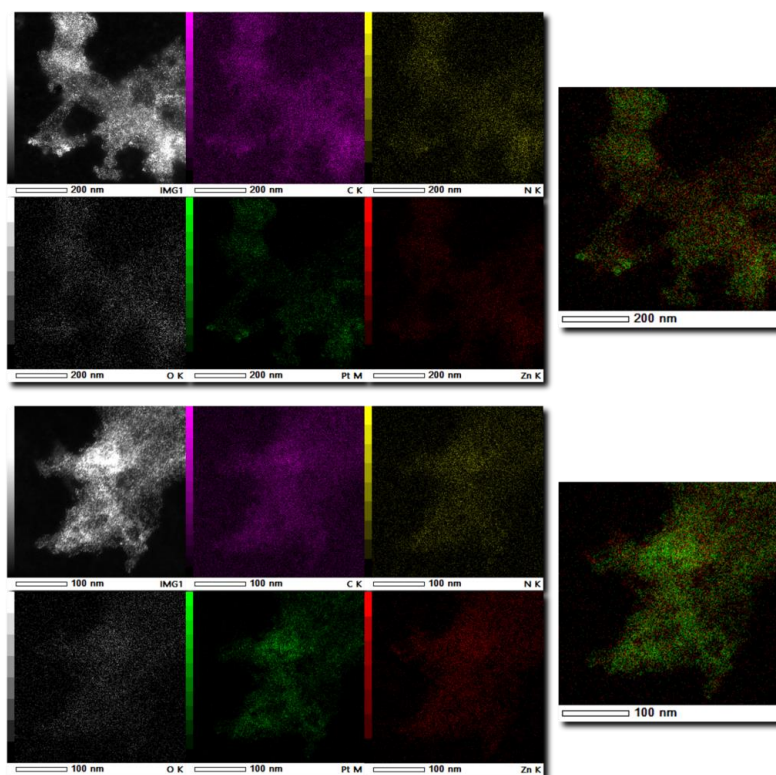
Figure S6. STEM-EDS micrographs of two different **B2** crystal formations. Darkfield TEM micrograph (top left) and EDS elemental mapping (top mid, top right, bottom row) shown with respect to single elements. Larger image (right) with Pt and Zn overlay (contrast adjusted for visibility). Purple: C, yellow: N, white: O, green: Pt, red: Zn.
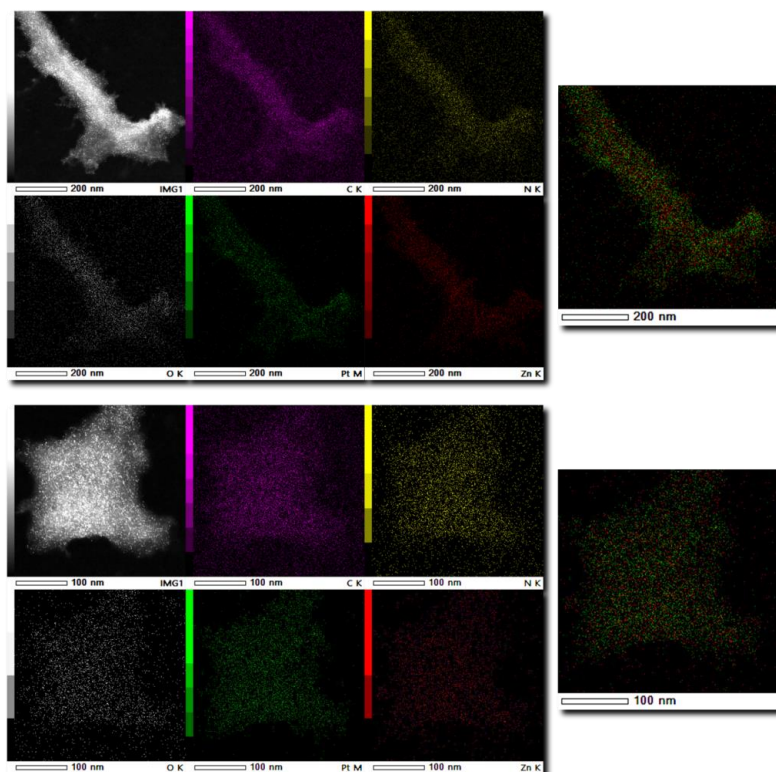
Figure S7. STEM-EDS micrographs of two different **B3** crystal formations. Darkfield TEM micrograph (top left) and EDS elemental mapping (top mid, top right, bottom row) shown with respect to single elements. Larger image (right) with Pt and Zn overlay (contrast adjusted for visibility). Purple: C, yellow: N, white: O, green: Pt, red: Zn.

S8 X-ray photoelectron spectroscopy

X-ray photoemission spectra (XPS) of sample **B3** were recorded using a conventional non-monochromatized X-ray source (Al Kα radiation, λ = 8.3896 Å.) with a hemispherical electron energy analyzer in a dedicated chamber of the NFFA UHV MBE-cluster system. We subtract contribution of Kα$_{3,4}$ from the Pt 4f and Zn 2p core level spectra. The powders have been glued on the sample holder using a conductive silver paste. The samples have been positioned at 45° with respect to the incident beam, probing an area of ~1 mm2 and a depth of ~1 nm. The Pt 4f and Zn 2p spectra have been acquired using a pass energy of 50, a dwell time of 500 ms and a channel width of 1.1 mm; they have been aligned using the Au valence band spectra of a reference Au foil positioned just above the sample.
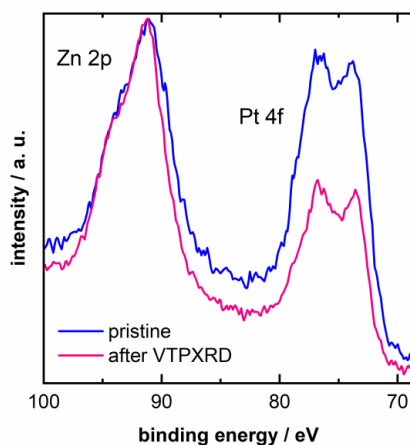
Figure S8. XPS spectra of sample B3 before (pristine, blue, top line) and after (magenta, bottom line) VTPXRD experiments.

S9 Supporting references

[1] S. Henke, A. Schneemann, A. Wütscher, R. A. Fischer, *J. Am. Chem. Soc.* **2012**, *134*, 9464–9474.

[2] W.-J. Lee, S. Bera, C. M. Kim, E.-K. Koh, W.-P. Hong, S.-J. Oh, E. Cho, S.-H. Kwon, *NPG Asia Mater* **2020**, *12*.

[3] A. Le Bail, H. Duroy, J. L. Fourquet., *Mat. Res. Bull.* **1988**, *23*, 447–452.

[4] A. A. Coelho, *J. Appl. Crystallogr.* **2018**, *51*, 210–218.

7.4 STUDY IV

MATERIAL SYNTHESIS

Linker molecules were synthesized and characterized following the procedures described in **STUDY I** and **III** (see chapter 7). MOFs were synthesized according to the procedure for $Zn_2(DP-bdc)_2dabco$ (nanoparticle-free reference) described in **STUDY II** (see chapter 7), although at 100 °C oven temperature.

X-RAY DIFFRACTION

PXRD patterns of as synthesized samples and resolution experiments were measured using Bragg-Bentano geometry with a silicon wafer plate on a Rigaku Benchtop MiniFlex 600-C with a D/teX Ultra 1D silicon strip detector. X-ray Cu Kα radiation (λ = 1.54Å) with a voltage of 40kV and current of 15mA was used. For confirmation of complete and successful activation, activated samples were filled in glass capillaries in a glovebox under argon atmosphere. Then PXRD patterns were measured in Debeye-Scherrer geometry on a PANalytical Empyrean diffractometer equipped with a PANalytical PIXcel 1D detector (PASS). X-ray Cu Kα radiation (λ = 1.54Å) with a voltage of 40kV and current of 40mA was used.

PHYSISORPTION

Adsorption measurements with N_2 (99.999vol%) at 77K and CO_2 (99.995vl%) at 195K were carried following the procedure described in **STUDY II** (see chapter 7). kstop
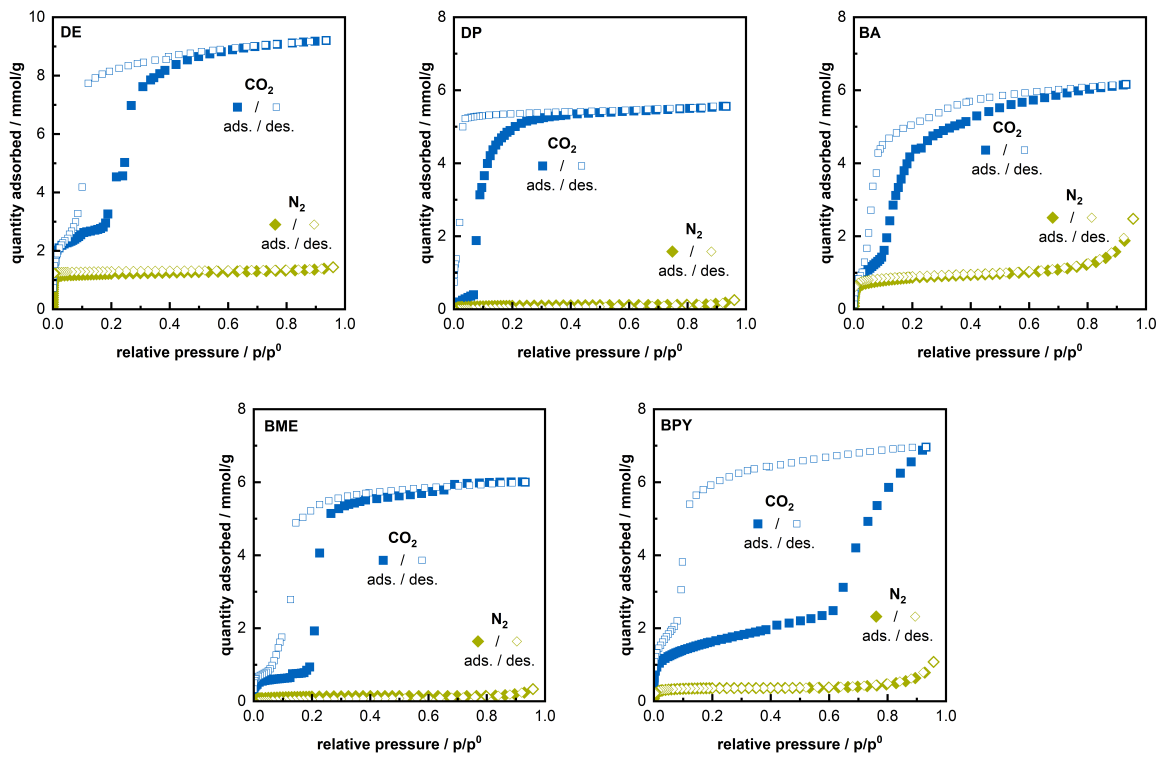
Figure 15. Isotherms of N_2 at 77K (green) and CO_2 at 195K (blue) on all functionalized pillared-layered MOFs studied in the resolvation tests. Adsorption (filled symbols) and desorption (open symbols), respectively.

8

APPENDIX

8.1 DEUTSCHE ÜBERSETZUNGEN

Im folgenden finden sich deutsche Übersetzungen der Kapitel 1, 2.1, 3 und 5. Diese sind sinngemäß identisch zu den englischen Kapiteln, für Zitationen, weiterführende Informationen und Abbildungen wird an dieser Stelle jedoch ausdrücklich auf die Englischen Originaltexte in dieser Dissertation verwiesen.

8.1.1 KAPITEL 1

DAS TRANSFORMATIVE POTENZIAL INTELLIGENTER, PORÖSER MATERIALIEN UND DIE FRAGE IHRES DESIGNS

Die Materialchemie ist ein breit aufgestelltes Forschungsgebiet, das eine Fülle von Materialklassen, Fachgebieten und Anwendungen umfasst. Sie ist in unserem Leben fast allgegenwärtig, sei es bei der Herstellung von Polymeren/Produkten aus fossilen Brennstoffen oder erneuerbaren (z. B. ligninbasierten) Analoga, bei der Erleichterung der Lebensmittelverarbeitung und -konservierung, bei der Gasaufbereitung (z. B. Biogasreinigung), bei der Erzeugung und Speicherung von Wind- und Sonnenenergie oder in der Mikroelektronik. Aufgrund dieser Reichweite spielt sie eine wesentliche Rolle im überfälligen Wandel hin zu einer nachhaltigen Gesellschaft, Wirtschaft und Industrie - ein Wandel, der monumentale, universelle Anstrengungen erfordert.* Im Mittelpunkt dieses Wandels stehen die Nachhaltigkeit und Effizienz von Ressourcen

---

* Viele Fachzeitschriften (z. B. Nature) und Universitäten bieten interessierten Lesenden regelmäßig frei zugängliche Leitartikel und Perspektiven zu diesem breiten Thema; Suchbegriff "nachhaltige Materialwissenschaft".

und Energie: weniger Ressourcen für den gleichen Effekt verwenden und sicherstellen, dass das, was verwendet wird, wiederverwendet oder recycelt werden kann.

Der Schwerpunkt dieser Arbeit liegt auf der Klasse der intelligenten, porösen Materialien und ihrem Design, insbesondere den metallorganischen Gerüsten (MOFs; was die sind, ist Thema von Kapitel 2). Wenn wir innerhalb dieses MOF-Zweigs der Materialchemie die laufende Nachhaltigkeitstransformation betrachten, stellen sich zwei Schlüsselfragen:

1. Wie können smarte, poröse MOFs zur Nachhaltigkeitstransformation beitragen?

Der Begriff "smart" ist mehr oder weniger ein Synonym für "responsiv" und beschreibt die Fähigkeit eines Materials, auf äußere Reize wie thermische, mechanische, optische, magnetische oder chemische Stimuli in einer Weise zu reagieren und sich anzupassen, die gezielt genutzt werden kann.[*] Die Kombination von "Intelligenz" oder Responsivität und Porosität ermöglicht eine Reaktion auf Gastmoleküle, die an der inneren Porenoberfläche solcher Materialien adsorbieren können.

Die zusätzliche Porosität bietet zwei Möglichkeiten zur Nachhaltigkeitstransformation beizutragen und führt zu den Antworten auf die erste Frage: Energieeffizienz und Ressourcennachhaltigkeit. Ein beeindruckendes Potenzial zur Steigerung der Energieeffizienz ist bei chemischen Trennungen zu finden. Die Reinigung von Gemischen in industriellem Maßstab erfolgt immer noch überwiegend durch Destillation, Trocknung oder Verdampfung, d. h. durch Prozesse, bei denen gewaltige Mengen an Energie zum Erhitzen oder Kühlen von Flüssigkeiten und Gasen verbraucht werden. Wenn stattdessen die Trennung durch maßgeschneiderte, smarte Materialien erleichtert werden könnte, die selektiv sieben (z.B. als Membranen) oder einige Komponenten eines Gemischs adsorbieren (und dies dann zyklisch tun, z.B. in Druckwechsel-Adsorption), könnte der Verbrauch von Wärmeenergie erheblich reduziert werden. 80% der Trennverfahren verbrauchen Wärme, was 10–15% des globalen Energieverbrauchs ausmacht, und 90% davon könnte eingespart werden, wenn Membranen anstelle von Destillation eingesetzt werden könnten. In Relation: In den USA entspräche dies etwa 33% des Energieverbrauchs der Industrie oder 3000TW/h (der Gesamtenergieverbrauch Deutschlands beträgt 2500TW/h).[†]

Weiter im Bezug zu Ressourcennachhaltigkeit: Die größten Auswirkungen metallhaltiger Feststoffe sind mit der Gewinnung und Verarbeitung von Erzen und Rohmetall

---

[*] Um einige Beispiele aus dem Alltag zu nennen: selbsttönende Gläser (Reaktion auf UV/sichtbares Licht), Formgedächtnislegierungen im Kamera-Autofokus (Reaktion auf Erwärmung) oder Datenspeicherzellen (Reaktion auf Magnetfelder).

[†] Wenn in Deutschland 33% des industriellen Energieverbrauchs eingespart werden könnte, entspräche dies etwa dem Anteil des industriellen Energieverbrauchs in Form von Erdgas (37% im Jahr 2020).

verbunden. Die Verringerung des Metallgehalts in Verbrauchsmaterialien für die Anwendung ist immer zielführend. Poröse MOFs sind leere Gerüste, die aus Metallen und organischen Molekülen aufgebaut sind und einen wesentlich geringeren Metallanteil aufweisen als beispielsweise ein nicht poröses Metalloxid. Eine höhere Porosität korreliert proportional mit einem geringeren Metallgehalt. Wenn ein MOF in seiner Anwendung ein Metalloxid ersetzen kann, trägt die Gesamtreduzierung des verwendeten Metalls erheblich zur Ressourcennachhaltigkeit bei (einschließlich des Faktors, dass der MOF organische Moleküle enthält, die noch aus Erdöl hergestellt werden). Eine solche potenzielle Anwendung sind Datenspeichermedien. Diese nutzen die stimulusabhängigen Übergänge poröser, schaltbarer MOFs zwischen zwei metastabilen Zuständen (d.h. 0 und 1), um Daten zu speichern. Aktuelle MOF-basierte Speicher erreichen im Labormaßstab Oberflächenspeicherdichten vergleichbar zu etablierten state-of-the-art Produkten mit vielversprechender Zyklisierbarkeit. Von unfassbarem Wert ist dabei, dass einige Speichertechnologien 20–30Einheit% der derzeitigen Jahresproduktion an Roherzen verbrauchen, um ihren Metallbedarf zu decken, während MOF-Alternativen stattdessen je nach Element nur zwischen einzelnen Prozenten und einigen Teilen pro Million (ppm!) verbrauchen würden.

Darüber hinaus wartet eine Reihe von Anwendungen, die derzeit durch einen Mangel an geeigneten Adsorbentien behindert werden, quasi darauf, entwickelt zu werden. Die Entsalzung von Meerwasser oder die Extraktion von Metallen aus Meerwasser sind möglich, aber kommerziell noch nicht in größerem Maßstab durchführbar. Ähnlich verhält es sich bei der Wassergewinnung aus der Luft, wobei inzwischen einige Prototypen mit MOFs vielversprechende Resultate liefern.

Zusammenfassend lässt sich sagen, dass die erste Frage leicht zu beantworten ist und es eine Vielzahl an Verbesserungen gibt, die neue responsive MOFs bringen könnten. Aber um den Elefanten im Raum anzusprechen: Es gibt noch keine industriell relevante Anwendung für MOFs. Es gilt, die zweite Frage zu beantworten und responsive MOFs weiterzuentwickeln, zu verstehen und zu designen, die die Anforderungen der oben genannten Anwendungen erfüllen können.

2. Wie können wir MOFs mit maßgeschneiderter Responsivität designen und in Anwendungen einbringen?

Der Ansatz, dies zu enträtseln, ist - wie die Frage selbst - zweigeteilt. Auf der einen Seite stehen Untersuchungen der Anwendbarkeit von MOFs. Vielversprechende (oft zufällig entdeckte) Materialien müssen erneut überprüft werden, um anwendungsrelevante Eigenschaften zu bestimmen, die für den Einsatz im Labormaßstab erst nicht von Bedeutung waren, z.B. thermische Ausdehnungseigenschaften, Stabilität bei längerer Einwirkung von Feuchtigkeit oder Upscaling der Herstellung. Darüber hinaus müssen die Methoden zur Verarbeitung von Pulvern, z.B. die Formung zu Pellets, so angepasst werden, dass die gewünschten Leistungsfaktoren nicht kompromitiert werden; neue Verfahren zur Herstellung von MOF-Membranen oder die in den letzten

Jahren entdeckten (porösen) MOF-Gläser müssen verstanden und etabliert werden, bevor sie ihr Potenzial entfalten können.[7] Durch diese Procedere werden sowohl Materialeigenschaften herausgearbeitet, die für die Anwendung essentiell sind, als auch solche, die für die Anwendung nachteilig sind.

Dies ist dann der Nährboden der anderen Seite: die Bewältigung der grundlegenden Herausforderung, die praktisch unbegrenzte Menge an synthetisierbaren MOFs zu kategorisieren und zu abstrahieren. Wir müssen in der Lage sein, die zugrundeliegenden Designprinzipien der Responsivität zu identifizieren und anschließend das für die jeweils gewünschte Aufgabe am besten geeignete Material zu finden und herzustellen. Nur so können wir die Designvielfalt von MOFs voll ausschöpfen. Der Zusammenhang, welche Merkmale eine bestimmte Eigenschaft bestimmen, wie z.B. strukturelle Flexibilität oder dynamische Responsivität als Reaktion auf einen äußeren Reiz, und wie diese dem Chemiker im Labor experimentell zugänglich gemacht werden können, liegt jedoch noch weitgehend im Dunkeln. Glücklicherweise ist das modulare Baukastenprinzip der MOFs ein großer Beschleuniger bei der Entschlüsselung dieses Problems. Es ermöglicht den Vergleich mit anderen Klassen kristalliner Koordinationspolymeren, die aus unterschiedlichen Bausteinen bestehen, aber bestimmte Aspekte der Responsivität teilen, wie z. B. cyanidbasierte Koordinationsnetzwerke und hybride organisch-anorganische Perowskite. Weiterhin erlaubt es die Vermeidung der extrem ineffizienten Versuch-und-Irrtum-Schleife zugunsten des strategischeren Ansatzes der Suche nach Trends in Struktur-Eigenschafts-Beziehungen innerhalb von Serien von inkrementell veränderten Materialien. Mit gut korrelierbaren Trends, explizit wenn sie über verschiedene MOF-Familien hinweg bestehen, und einem tiefgreifenden Verständnis der responsiven Eigenschaften können Vorhersagemodelle erstellt werden, die durch den enormen Parameterraum führen, den diese Materialplattform bietet. Die Kombination aus dieser konzeptionellen Anleitung, dem Bewusstsein für interdisziplinäre Möglichkeiten und einer breiten Perspektive für die Nutzung von Responsivität kann letztendlich intelligente MOFs zur Anwendung bringen.

Insgesamt kann die zweite Frage also nicht mit einem einfachen Rezept beantwortet werden, aber der Weg zu ihrer Beantwortung ist klar. Ein Schritt auf diesem Weg wird in dieser Dissertation vorgestellt.

8.1.2 Kapitel 2.1

Eine kurze Geschichte der metallorganischen Gerüststrukturen (MOFs)

Im wahrscheinlich am einfachsten zu visualisierenden Fall besteht ein MOF aus einer Sorte von Metallzentrum, das als Knoten fungiert, typischerweise aus Metallionen oder Metall-Oxo-Clustern aufgebaut, und einer Sorte von organischem

Molekül als Strebe/Linker. Eine Strebe verbindet zwei verschiedene Knoten linear durch Koordinationsbindungen, und wenn ein Knoten mit z. B. vier Streben entlang einer Ebene verbunden werden kann, ergibt sich eine gitterartige Schicht, wie sie in figure 1 skizziert ist. Eine Struktur, die aus mehreren solcher übereinander gestapelten Schichten besteht (wie Graphenschichten oder ein Stapel von Untersetzern), wäre ein MOF. Wenn in diesem Beispiel ein Knoten stattdessen mit sechs Streben (oktaedrisch) verbunden ist, ergibt sich ein Würfel, der sich in drei Dimensionen erstreckt und ebenfalls ein MOF darstellen würde. Der zentrale Aspekt jeder Struktur ist immer die Verbindung zwischen Metall und organischem Liganden durch eine Koordinationsbindung und deren zwei- oder dreidimensionale Ausbreitung. Daher ist die Entwicklung von MOFs eng mit der Geschichte der Koordinationschemie verbunden; einige Verbindungen, die wir heute als MOFs kategorisieren, wurden lange bevor diese Materialklasse überhaupt definiert oder ihr Potenzial erkannt wurde entdeckt.

Die moderne Koordinationschemie begann mit dem grundlegenden Verständnis der räumlichen Anordnung von Metallen und Liganden in Komplexen. Als ALFRED WERNER 1893 eine Struktur für $[Co(NH_3)_6]Cl_3$ vorschlug, die sich als korrekt herausstellte und zur Benennung der Werner-Komplexe führte, erfuhr dieses Wissenschaftsgebiet eine umfassende Veränderung. Dieses Verständnis ermöglichte sowohl eine klare, eindeutigere Definition von Komplexen, die den wissenschaftlichen Diskurs förderte, als auch eine Verlagerung der Forschung von Diskusisonen über die Struktur zu Fragen über Struktur-Eigenschafts-Korrelationen. Ab diesem Moment ist das Merkmal, das sich durch die Geschichte der Koordinationschemie in Richtung MOFs zieht, die Dimensionalität. WERNERs $[Co(NH_3)_6]Cl_3$ ist ein 0D-Komplex, ein einzelnes Metallatom mit sechs monodendaten Ammoniak-Liganden, die es umgeben und ein Oktaeder ohne gemeinsame Koordinationsbindungen zum nächsten $[Co(NH_3)_6]Cl_3$-Oktaeder bilden. Um dies in eine erste, zweite oder dritte Dimension auszudehnen (was dann eine Linie, eine Schicht bzw. ein Quader wäre), müssen überbrückende Liganden vorhanden sein. Interessanterweise sind 1D, 2D und 3D Koordinationspolymere (KP) bereits vor oder um die Zeit der Entdeckung von WERNER entwickelt und verwendet worden: Das Metallcyanid Berliner Blau $(Fe_4[Fe(CN)_6]_3)$ wurde seit dem 18. Jahrhundert als Farbstoff verwendet und ist ein 3D-KP, Palladium(II)-chlorid $(PdCl_2)$ ist ein 1D-KP, dessen erste Verwendung für die Ethylenoxidation von FRANCIS C. PHILLIPS im Jahr 1894 entwickelt wurde, und KARL A. HOFMANN berichtete 1897 über $[Ni(CN)_2NH_3]C_6H_6$ (später Hofmann-Clathrate genannt), das aus 2D geschichtetem $Ni(CN)_2NH_3$ mit dazwischenliegenden Benzolmolekülen besteht. Aufgrund limitierter Analysetechniken und -geräte verzögerte sich die Strukturaufklärung der Hofmann-Clathrate jedoch bis in die 1950er Jahre und die des seit langem bekannten Berliner Blau sogar bis 1977. Erst mit weiterentwickelten analytischen Möglichkeiten konnte das Interesse an spezifisch 3D-Koordinationsnetzwerken, Kristall-Engineering, und das Konzept der supramolekularen Synthons in den späten 1980er und frühen 1990er Jahren Früchte tragen. ROBSON und HOSKINS schlugen 1989 vor, *"dass eine neue und potenziell um-*

fangreiche Klasse fester Materialien mit noch nie dagewesenen und möglicherweise nützlichen Eigenschaften herstellbar ist, indem Zentren mit einer tetragonalen oder oktaedrischen Anordnung von Valenzen durch stäbchenförmige Verbindungseinheiten miteinander verbunden werden. [...] Diese Gerüste würden eine regelmäßige Anordnung von Hohlräumen erzeugen, die durch Fenster miteinander verbunden sind." Ein Jahr später folgten eine Neubewertung einiger Metall-Cyanid-Strukturen sowie die Synthese und Strukturanalyse kristalliner Polymere auf der Basis von Metall-Nitril-Komplexen mit Hohlräumen, die von Gegenionen und Lösungsmittelmolekülen besetzt sind. In ihrer Studie wird ein entscheidender Vorteil solcher Materialien hervorgehoben: Ihre Porosität und geordnete/kristalline Struktur bietet die Möglichkeit, eine diskrete (im Gegensatz zu einer zufälligen) chemische Funktionalisierung vorzunehmen. Sie waren in der Lage, ein mehrdimensionales Netzwerk mit einer geordneten Struktur und Porosität zu kombinieren und schufen damit wohl den Prototyp eines MOFs, auch wenn die Bezeichnung so noch nicht existierte. Dennoch war der damals entscheidende letzte Schritt, das Lösungsmittel aus der Poren zu entfernen ohne das Material zu zerstören, um ein leeres, nutzbares Innenvolumen zu schaffen, eine ungelöste Herausforderung.

1995 überwanden OMAR M. YAGHI und Mitarbeiter dieses Hindernis mit ihren bahnbrechenden Arbeiten über $Cu(bpy)_{1.5} \cdot NO_3(H_2O)_{1.25}$ und $CoC_6H_3(COOH_{1/3})_3(py)_2 \cdot \frac{2}{3}py$, in denen sie einen Einblick in das unglaubliche Potenzial dieser Art von Material geben und den Begriff "metallorganische Gerüststruktur" (engl. MOF) prägen. Und während diese beiden MOFs vielleicht nicht intuitiv aufregend und strukturell leicht erkennbar visualisiert sind, wurden spätestens 1999 zwei der ikonischsten MOFs prominent veröffentlicht: MOF-5 von HAILIAN LI (assoziiert mit YAGHI) und Mitarbeitern und HKUST-1 von STEPHEN S.-Y. CHUI (assoziiert mit IAN D. WILLIAMS) und Mitarbeitern, beide Strukturen sind in figure 2 dargestellt. Mit diesen Beispielen und der unmittelbaren Zugkraft, die sie aufgrund ihrer hohen zugänglichen Porenoberfläche, ihrer geringen Dichte und ihrer guten thermischen Stabilität erzeugten, verbreitete sich in der internationalen Chemiegemeinschaft ein sehr großes Interesse und ein regelrechter Forschungstrend um MOFs. Lenztendlich kristallisierte sich ein neues, bis heute hochkarätiges Gebiet der Materialwissenschaft heraus.

Dessen ersten 10–15 Jahre konzentrierten sich vor allem auf die Entwicklung neuer MOFs. Sei es, um zu versuchen die Möglichkeiten für das Design von MOFs auszuschöpfen (und unausweichlich noch mehr Designoptionen zu finden), oder um als Erster ein Material zu synthetisieren, ihm einen Namen zu geben und zu hoffen, dass es gute Eigenschaften hat. Parallel dazu wurden wichtige analytische und theoretische Methoden entwickelt und angepasst, um die Anforderungen an die Charakterisierung dieser neuen Materialien zu erfüllen. Mit den Fortschritten in der Methodik rückten Mitte bis Ende der 2010er Jahre Untersuchungen zu den Feinheiten von MOFs, zu Struktur-Eigenschafts-Beziehungen, zu exotischem Verhalten, das normalerweise in solchen Festkörpern nicht vorkommt, und die Frage, wie man universellere Prinzipien für MOF-Design und Modulation finden und entschlüsseln kann in den Vordergrund.

Heute, im Jahr 2022, sind mehr als 100.000 MOF-ähnliche Strukturen in der Cambridge Structure Database registriert und es werden ständig Fortschritte bei der zielgerichteten Modifikation von MOFs erzielt. Das Forschungsfeld selbst hat weites Netz aus verschiedenen, miteinander verflochtenen Zweigen entwickelt: flexible MOFs, schaltbare MOFs, leitfähige MOFs, amorphe MOFs, MOF Katalysatoren, MOF Gläser, flüssige MOFs, Nanopartikel-MOF-Komposite - um nur einige zu nennen und die entsprechende Unterteilung in Anwendungsbereiche gar nicht erst zu erwähnen.

Darüber hinaus werden große Anstrengungen unternommen, um die enorme Menge an gesammeltem und laufend hinzukommendem Wissen und Daten zu verwalten: Kuratieren hochwertiger Datenbanken (wie die CSD MOF-Sammlung mit derzeit knapp über 10. 000 Einträgen), die Standardisierung analytischer Verfahren für eine bessere Vergleichbarkeit der Materialcharakterisierung, die Sicherstellung der Wiederholbarkeit von Synthesen, Simulationen und Anwendungs-Leistungen, und das Erreichen von Eindeutigkeit bei Material- und Merkmalsdeskriptoren. Dies hilft dem experimentellen Chemiker bei der Bewertung geeigneter Synthesebedingungen und des Leitens der Intuition im Labor, aber ebenso wichtig ist die Bereitstellung kuratierter Datenbanken, damit sie als Input, Referenzen oder Trainingssätze für Simulationen und maschinelle Lernalgorithmen verwendet werden können, die ein grundlegender Pfeiler für das Verständnis und die Entwicklung von MOFs waren, sind und sein werden.

8.1.3 KAPITEL 3

ZENTRALE FRAGESTELLUNG

MOFs sind eine extrem modifizierbare Materialplattform, die für die Entwicklung dynamischer, responsiver, und intelligenter Materialien prädestiniert ist. Das Spektrum an Eigenschaften, das sie abdecken können - als Membranen für Trennungen von Substanzmischungen, Speicher für Gase, Sensoren oder Informationsspeichern in Mikroelektronik - ist für Anwendungen der nächsten Generation, die auf mehr Nachhaltigkeit und Effizienz bei Ressourcen und Energie abzielen, konkret gefragt. Sie ermöglichen einerseits die inkrementelle Veränderung einzelner Parameter, was in Verbindung mit ihrer Kristallinität und relativ einfachen strukturellen Charakterisierung methodische Untersuchungen gezielter Designs ermöglicht. Andererseits ist es unmöglich die unüberschaubare Anzahl von möglichen Kombinationen von Bestandteilen durch manuelles Screening und Trial-and-Error zu ergründen. Daher ist es erstens notwendig zu verstehen, wie und welche mikroskopischen chemischen Veränderungen genutzt werden können, um makroskopische Materialeigenschaften zu manipulieren, und zweitens die zugrundeliegenden Prinzipien des Designs zu ex-

und abstrahieren, um so viel Wissen wie möglich zwischen den verschiedenen MOF-Familien zu übertragen. Insbesondere im Hinblick auf das Design der dynamischen Responsivität von MOFs stehen beide Aspekte im Mittelpunkt des Interesses der Forschungsgemeinschaft, da die gezielte Synthese von Stimulus-responsiven MOFs nachwievor weitgehend unzugänglich bleibt.

Dennoch wird steter Fortschritte gemacht, um diese Herausforderung zu überwinden. Die Forschungseinheit "FOR2433 – Switchable MOFs", in deren Kontext diese Dissertation eingebettet ist, trägt zu diesem Bestreben mit Studien bei, die sich auf das Zusammenspiel von Materialsynthese, in situ Charakterisierungstechniken und Simulationen konzentrieren. Ihr Hauptziel ist die Verbesserung des grundlegenden Verständnisses dynamischer Responsivität und der Korrelation zu den grundlegenden Konstruktionsprinzipien. Die Arbeit der Forschungseinheit konzentriert sich auf die Untersuchung von schaltbaren Säulenschichten aus MOFs (hauptsächlich $M_2(fu-bdc)_2dabco$ und DUT-8), um neue auf Stimuli reagierende MOFs vorherzusagen, zu simulieren und sie Richtung Anwendung zu entwickeln. Dieses übergreifende Ziel wird in vier Bereiche und Aufgaben gegliedert: 1) Entwicklung eines vorhersagendenden theoretischen Models, 2) Entwicklung maßgeschneiderter in situ Charakterisierungstechniken, 3) Auswirkung von kooperativen Phänomenen, Heterostrukturen (Kompositen), Unordnung und Defekten auf die Schaltbarkeit von MOFs und 4) Unterscheidung zwischen spezifischer und unspezifischer Responsivität in Bezug auf Adorbat-Adsorbent-Wechselwirkungen, funktionelle Gruppen und entropische Faktoren.

In den hier vorgestellten Studien wird untersucht, wie sich eine umfassende Funktionalisierung von Linkern auf die durch Gastmoleküle ausgelöste dynamische Responsivität in starren und flexiblen MOFs auswirkt und wie sich die Schaltbarkeit in flexiblen MOF-Kompositen mit mesoskopischen, auf der Oberfläche verankerten Nanopartikeln im Vergleich zu den unfunktionalisierten Materialien verändert.

STUDIE I befasst sich mit der Entschlüsselung der durch die Funktionalisierung hervorgerufenen, adsorbat-induzierten Responsivität in dem starren $Zn_2(fu-bdc)_2bipy$. Dieses System weist 1D-Porenkanäle auf, die homogen mit Linkerfunktionalisierungen ausgekleidet sind. Der MOF ist daher gut geeignet, um deren Einfluss auf die Adsorbat-Responsivität zu untersuchen. Die Studie fragt und elaboriert:

> *"Welche Faktoren der eingeführten Linkerfunktionalisierungen sind für die beobachtete dynamische Responsivität in starren MOFs verantwortlich?"*

Da nur die Funktionalisierungen schrittweise verändert werden und kein anderer Aspekt des Materials dynamisch ist, können relativ klare Korrelationen zwischen diesen Gruppen und insgesamt beobachteten Materialeigenschaft gezogen werden. Da zudem die besagten Linkergruppen die dominierenden Faktoren sind lassen sich die Resultate konzeptionell so einfach wie möglich auf andere MOFs mit ähnlicher Topologie übertragen.

STUDIE II und **III** untersuchen die Auswirkung von an der Oberfläche verankerten Nanopartikeln - effektiv mesoskope Oberflächendefekte - auf die Responsivität der resultierenden NP@Zn_2(fu$-$bdc)$_2$dabco-Komposite. Dieses flexible MOF-System basiert auf dem starren DMOF-, wird aber durch die zusätzlichen Linker-Seitenketten flexibel/schaltbar. Die Schaltbarkeit ist funktionalisierungsabhängig und durch Physisorption und für eine bestimmtes Derivat zusätzlich durch Temperatur kontrollierbar. Wir haben diese 2-in-1-Responsivität zum Anlass genommen, den bisher unbekannten Komposittyp NP@flexibleMOF zu untersuchen und zu fragen:

"Wie beeinflussen mesoskope Nanopartikel/Defekte die Responsivität von flexiblen MOFs?"

STUDIE III befasst sich direkt mit beiden Stimuli; Nanopartikel auf dem durch Adsorption und Temperatur schaltbare Derivat verankert. Die Änderung der Eigenschaften der NP@MOF-Komposite im Vergleich zum nanopartikelfreien Ausgangsmaterial werden erörtert, und der Einfluss von Nanopartikeln mit unterschiedlichen Größen untersucht. **STUDIE II** hingegen testet NP@Zn_2(fu$-$bdc)$_2$dabco-Komposite, die auf einem MOF basieren, der keine thermisch induzierte Schaltbarkeit zeigt. Stattdessen wird seine Thermische Expansion beobachtet, die jedoch der gleichen mechanischen Bewegung entsprechen.

STUDIE IV unterscheidet sich von den oben genannten insofern, als es sich nicht um eine abgeschlossene/veröffentlichte Studie handelt, sondern um einen ersten experimentellen und methodischen Meilenstein zur Erforschung der Lösungsmittel/ Solvent-Responsivität einer Zn_2(fu$-$bdc)$_2$dabco-Serie mit verschiedenen Linker-Funktionalisierungen. Die zu bearbeitende(n) Fragestellung(en) ist/sind:

"Wie groß ist das Ausmaß der dynamischen Solvent-Responsivität in der Zn_2(fu$-$bdc)$_2$dabco MOF-Reihe und welche strukturellen Faktoren steuern sie?"

Gegenwärtig wird Solvent-Responsivität oder Sorptionsselektivität gegenüber Lösungsmitteln (d. h. bei Standardbedingungen; anstelle von Gasen) meist dann untersucht, wenn explizite Anwendungen im Vordergrund stehen, z. B. Xylol-Isomerentrennung oder Entfernung von Spurenverunreinigungen, oder wenn die Physisorption von Gasen nicht aussagekräftig genug ist. Grundlegende Untersuchungen zur Schaltbarkeit sind seltener, wurden jedoch an manchen einzelnen MOFs durchgeführt. Befunde zu DUT-8(Ni) motivierten diese konzeptionell eng verwandte Studie zu Zn_2(fu$-$bdc)$_2$dabco. Sowohl eine erste Matrix, die das qualitative Verhalten der Materialien, das Lösungsmittel und die Linkerfunktionalisierungen in Korrelation setzt, als auch eine experimentelles Methodik für eine reproduzierbare Analyse werden für zukünftige Arbeiten festgehalten.

8.1.4 Kapitel 5

Schlussfolgerung und Ausblick

Stimulus-Responsivität ist die Schlüsseleigenschaft von MOFs, die deren Vielseitigkeit in vollem Umfang nutzt, und sehr attraktiv für perspektivische Anwendungen von MOFs als ressourcen- oder energieeffiziente Materialalternativen in industriellen Prozessen. Die aktuellen Herausforderungen, die es zu bewältigen gilt, um dies zu verwirklichen, liegen vor allem in zwei Aspekten: Erstens müssen angesichts des enormen Parameterraums für die Gestaltung von Responsivität die zugrunde liegenden Designprinzipien gefunden werden. Dies dient zur Orientierung und Fokussierung der Forschungsanstrengungen und Verbesserung die zielgerichtete Effizienz. Zweitens muss der Einfluss praktisch relevanter Prozess- und Anwendungsbedingungen auf Responsivität gründlich untersucht werden. Dadurch kann die Lücke zwischen Leistung unter Laborbedingungen und realer Anwendungsmöglichkeit geschlossen werden. Die vorliegende Arbeit umfasst vier Studien, die verschiedene Facetten dieser beiden Aspekte untersuchen.

Zwei Studien konzentrieren sich in erster Linie auf die zugrundeliegende Rolle umfassender Linkerfunktionalisierung: **Studie I** abstrahiert Prinzipien für die Schaffung und Steuerung der Adsorbat-Empfindlichkeit in starren MOFs durch Untersuchung des Modellsystems $Zn_2(fu-bdc)_2bipy$. Die Zugänglichkeit der Adsorptionsstellen und die Polarisierbarkeit der Porenumgebung erwiesen sich als einstellbare Schlüsselparameter. Es existiert ein erhebliches Potenzial für die Gestaltung der Adsorbatempfindlichkeit für verschiedene Trennaufgaben und die Anwendung der untersuchten Methodik und Gestaltungsprinzipien auf andere, homogen funktionalisierbare MOF-Systeme. **Studie IV** befasst sich mit den Veränderungen der (als Flüssigkeit vorliegenden) Lösungsmittel-Responsivität des flexiblen $Zn_2(fu-bdc)_2dabco$. Sie zeichnet eine Matrix, die das qualitative Ansprechverhalten, die Lösungsmittel und verschiedene Funktionalisierungen der MOFs miteinander in Beziehung setzt. Weiterhin wird ein experimentelles Verfahren für eine reproduzierbare Analyse etabliert, auf dem zukünftige Arbeiten aufbauen können. Das derzeitige "Arbeitspferd" $Zn_2(DP-bdc)_2dabco$ zeigt interessante Eigenschaften, aber es sind noch keine klaren funktionalisierungs- oder lösungsmittelkorrelierten Trends erkennbar. Künftige quantitative Studien müssen Dampf-Physisorptionsexperimente und möglicherweise die Analyse von Adsorptionskinetiken umfassen, um kompliziertere Korrelationen zu ermitteln.

Die beiden anderen Studien befassen sich mit dem Einfluss von oberflächen-verankerten Nanopartikeln auf die Stimulus-Responsivität. **Studie II** geht der Frage nach, wie sich das sehr anwendungsrelevante, thermische Ausdehnungsverhalten (TE) in Abhängigkeit von Platinnanopartikeln in $Zn_2(DP-bdc)_2dabco$ verändert. Es wurde nicht nur festgestellt, dass TE bei niedrigen NP-Beladungen und Temperaturen durch das NP-freie Material geschätzt werden kann, sondern dass die TE-

Eigenschaften bei Kompositen mit höheren Beladungen bei höheren Tempaeraturen überlegen sind. Insbesondere der negative Anteil der anisotropen TE-Bewegung wurde durch NPs am stärksten gehemmt. Wenn, hypothetisch gesehen, ihr Einfluss auf NTE ausgeprägter ist als auf PTE, könnte dies einen weiteren Parameter für die Feinabstimmung des Materials erschließen, wenn man bedenkt wie verbreitet NTE innerhalb von MOFs ist. **STUDIE III** untersucht dieselbe mechanische Bewegung, jedoch in größerem Maßstab bei der adsorptions- und temperaturinduzierten Schaltung von $Zn_2(BME-bdc)_2dabco$ mit verankerten Pt oder SiO_2 NPs. Es wird gezeigt, dass mit beiden Stimuli reversibel schaltbare NP@flexMOF-Komposite realisiert werden können und, dass eine geringe Beladung von NPs die Flexibilität (und Porosität) von MOFs nicht beeinträchtigt. Allerdings wird beim Schalten mit der Temperatur ein unterschiedlicher Grad an Reversibilität zwischen SiO_2 und Pt-haltigen Derivaten beobachtet, was auf die unterschiedlichen Größen der Nanopartikel zurückgeführt wird.

Jede der Studien findet schrittweise Antworten auf die grundlegende Frage "Wie können wir MOFs mit maßgeschneiderter Responsivität entwerfen?", wirft aber gleichzeitig neue Fragen auf, die in künftigen Arbeiten behandelt werden müssen: Welche anderen starren MOFs würden sich eignen, um das durch die Funktionalisierung bestimmte Responsivitätsdesign zu übertragen? Kann die Lösungsmittel-Responsivität in $Zn_2(DP-bdc)_2dabco$ kinetisch kontrolliert werden? Wie groß ist der Einfluss der NP-Größe im Vergleich zur Menge auf die MOF-Schaltbarkeit und gibt es eine mit der Art des Stimulus korrelierende Begründung? Ist der Einfluss von TE auf NPs mit der Materialtopologie verbunden und wenn ja, wie? Fragen derartiger Bandbreite können gestellt werden, weil die Analyse komplizierter Abhängigkeiten innerhalb von Materialien inzwischen relativ leicht zugänglich ist und verstanden werden können; in der Grundlagenwissenschaft wurde bereits viel erreicht. Nichtsdestotrotz müssen und werden diese unschätzbaren Erkenntnisse in naher Zukunft weiterentwickelt werden, um die übergreifende Frage zu beantworten: "Wie können wir MOFs mit maßgeschneiderter Responsivität entwerfen und sie in die Anwendung bringen?"

8.2 COMPLETE LIST OF PUBLICATIONS

A continuously updated list of publications is permanently available at orcid.org/0000-0002-9230-0398.

PUBLICATIONS AS FIRST AUTHOR ON WHICH THIS THESIS IS BASED

Berger, J.; Schneemann, A.; Hante, I.; Jing, Y.; Evans, J. D.; Hijikata, Y.; Pirillo, J.; Toyao, T.; Shimizu, K.-I.; Noro, S.-I.; Kieslich, G.; Fischer, R. A. Designing Adsorptive Gating via Linker Side-Chain Functionalization in a Honeycomb-MOF. J. Phys. Chem. C **2022**, *126* (30), 12755–12764. DOI: 10.1021/acs.jpcc.2c01979.

Berger, J.; Dönmez, A.-S.; Ullrich, A.; Bunzen, H.; Fischer, R. A.; Kieslich, G. Reduced Thermal Expansion by Surface-Mounted Nanoparticles in a Pillared-Layered Metal-Organic Framework. Commun. Chem. **2022**, *5*, 177. DOI: 10.1038/s42004-022-00793-2. Creative Commons Attribution 4.0 International License (CC BY 4.0).

Study III will be accepted in a peer-reviewed journal by time of publication of this dissertation. For updated information please refer to the orcid.org link above.

PUBLICATIONS AS CO-AUTHOR

Li, N.; Guo, R.; Oechsle, A. L.; Reus, M. A.; Liang, S.; Song, L.; Wang, K.; Yang, D.; Allegretti, F.; Kumar, A.; Nuber, M.; Berger, J.; Bernstorff, S.; Iglev, H.; Hauer, J.; Fischer, R. A.; Barth, J. V.; Müller-Buschbaum, P. Operando Study of Structure Degradation in Solid-State Dye-Sensitized Solar Cells with a TiO_2 Photoanode Having Ordered Mesopore Arrays. Solar RRL **2022**, 2200373. DOI: 10.1002/solr.202200373.

Consultation on porosity determination and impact, measurement of physisorption isotherms and related data processing, analysis and interpretation.

Ukaj, D.; Bunzen, H.; Berger, J.; Kieslich, G.; Fischer, R. A. Charge-Transfer-Induced Electrical Conductivity in a Tetrathiafulvalene-Based Metal-Organic Framework. Chem. Mater. **2021**, *33* (7), 2532-2542. DOI: 10.1021/acs.chemmater.0c04897.

Physisorption isotherm measurements and related sample preparation optimization, data processing, analysis, and interpretation.

Heinz, W. R.; Agirrezabal-Telleria, I.; Junk, R.; Berger, J.; Wang, J.; Sharapa, D. I.; Gil-Calvo, M.; Luz, I.; Soukri, M.; Studt, F.; Wang, Y.; Wöll, C.; Bunzen, H.; Drees, M.; Fischer, R. A. Thermal Defect Engineering of Precious Group Metal-Organic Frameworks: A Case Study on Ru/Rh-HKUST-1 Analogues. ACS Appl. Mater. Interfaces **2020**, *12* (36), 40635-40647. DOI: 10.1021/acsami.0c10721.

Integration, planning, and conducting of extensive physisorption study and adsorption enthalpy determination. Sorption data processing, analysis, and interpretation.

8.3 REPRINT PERMISSIONS

8.3.1 STUDY I

8.3.2 STUDY II

8.3.3 FIGURE 7

SPRINGER NATURE LICENSE
TERMS AND CONDITIONS

Nov 14, 2022

This Agreement between Technical University of Munich -- Jan Berger ("You") and Springer Nature ("Springer Nature") consists of your license details and the terms and conditions provided by Springer Nature and Copyright Clearance Center.

License Number	5427571345701
License date	Nov 14, 2022
Licensed Content Publisher	Springer Nature
Licensed Content Publication	Nature Chemistry
Licensed Content Title	Tunable acetylene sorption by flexible catenated metal–organic frameworks
Licensed Content Author	Mickaele Bonneau et al
Licensed Content Date	Apr 21, 2022
Type of Use	Thesis/Dissertation
Requestor type	academic/university or research institute
Format	print and electronic
Portion	figures/tables/illustrations
Number of figures/tables/illustrations	1
High-res required	no

Will you be translating?	no
Circulation/distribution	50000 or greater
Author of this Springer Nature content	no
Title	Elucidating Dynamic Responsiveness in Model Rigid and Flexible Metal-Organic Frameworks
Institution name	Technical University of Munich
Expected presentation date	Jan 2023
Portions	Figure 1
Requestor Location	Technical University of Munich Lichtenbergstr. 4 Garching, 85748 Germany Attn: Technical University of Munich
Total	0.00 EUR

Terms and Conditions

Springer Nature Customer Service Centre GmbH
Terms and Conditions

This agreement sets out the terms and conditions of the licence (the **Licence**) between you and **Springer Nature Customer Service Centre GmbH** (the **Licensor**). By clicking 'accept' and completing the transaction for the material (**Licensed Material**), you also confirm your acceptance of these terms and conditions.

1. Grant of License

1. 1. The Licensor grants you a personal, non-exclusive, non-transferable, world-wide licence to reproduce the Licensed Material for the purpose specified in your order only. Licences are granted for the specific use requested in the order and for no other use, subject to the conditions below.

1. 2. The Licensor warrants that it has, to the best of its knowledge, the rights to license reuse of the Licensed Material. However, you should ensure that the material you are requesting is original to the Licensor and does not carry the copyright of

another entity (as credited in the published version).

1. 3. If the credit line on any part of the material you have requested indicates that it was reprinted or adapted with permission from another source, then you should also seek permission from that source to reuse the material.

2. Scope of Licence

2. 1. You may only use the Licensed Content in the manner and to the extent permitted by these Ts&Cs and any applicable laws.

2. 2. A separate licence may be required for any additional use of the Licensed Material, e.g. where a licence has been purchased for print only use, separate permission must be obtained for electronic re-use. Similarly, a licence is only valid in the language selected and does not apply for editions in other languages unless additional translation rights have been granted separately in the licence. Any content owned by third parties are expressly excluded from the licence.

2. 3. Similarly, rights for additional components such as custom editions and derivatives require additional permission and may be subject to an additional fee. Please apply to Journalpermissions@springernature.com/bookpermissions@springernature.com for these rights.

2. 4. Where permission has been granted **free of charge** for material in print, permission may also be granted for any electronic version of that work, provided that the material is incidental to your work as a whole and that the electronic version is essentially equivalent to, or substitutes for, the print version.

2. 5. An alternative scope of licence may apply to signatories of the STM Permissions Guidelines, as amended from time to time.

3. Duration of Licence

3. 1. A licence for is valid from the date of purchase ('Licence Date') at the end of the relevant period in the below table:

Scope of Licence	Duration of Licence
Post on a website	12 months
Presentations	12 months
Books and journals	Lifetime of the edition in the language purchased

4. Acknowledgement

4. 1. The Licensor's permission must be acknowledged next to the Licenced Material in print. In electronic form, this acknowledgement must be visible at the same time as the figures/tables/illustrations or abstract, and must be hyperlinked to the journal/book's homepage. Our required acknowledgement format is in the Appendix below.

5. Restrictions on use

5. 1. Use of the Licensed Material may be permitted for incidental promotional use and minor editing privileges e.g. minor adaptations of single figures, changes of format, colour and/or style where the adaptation is credited as set out in Appendix 1 below. Any other changes including but not limited to, cropping, adapting, omitting material that affect the meaning, intention or moral rights of the author are strictly prohibited.

5. 2. You must not use any Licensed Material as part of any design or trademark.

5. 3. Licensed Material may be used in Open Access Publications (OAP) before publication by Springer Nature, but any Licensed Material must be removed from OAP sites prior to final publication.

6. Ownership of Rights

6. 1. Licensed Material remains the property of either Licensor or the relevant third party and any rights not explicitly granted herein are expressly reserved.

7. Warranty

IN NO EVENT SHALL LICENSOR BE LIABLE TO YOU OR ANY OTHER PARTY OR ANY OTHER PERSON OR FOR ANY SPECIAL, CONSEQUENTIAL, INCIDENTAL OR INDIRECT DAMAGES, HOWEVER CAUSED, ARISING OUT OF OR IN CONNECTION WITH THE DOWNLOADING, VIEWING OR USE OF THE MATERIALS REGARDLESS OF THE FORM OF ACTION, WHETHER FOR BREACH OF CONTRACT, BREACH OF WARRANTY, TORT, NEGLIGENCE, INFRINGEMENT OR OTHERWISE (INCLUDING, WITHOUT LIMITATION, DAMAGES BASED ON LOSS OF PROFITS, DATA, FILES, USE, BUSINESS OPPORTUNITY OR CLAIMS OF THIRD PARTIES), AND
WHETHER OR NOT THE PARTY HAS BEEN ADVISED OF THE POSSIBILITY OF SUCH DAMAGES. THIS LIMITATION SHALL APPLY NOTWITHSTANDING ANY FAILURE OF ESSENTIAL PURPOSE OF ANY LIMITED REMEDY PROVIDED HEREIN.

8. Limitations

8. 1. _BOOKS ONLY:_Where **'reuse in a dissertation/thesis'** has been selected the following terms apply: Print rights of the final author's accepted manuscript (for clarity, NOT the published version) for up to 100 copies, electronic rights for use only on a personal website or institutional repository as defined by the Sherpa guideline (www.sherpa.ac.uk/romeo/).

8. 2. For content reuse requests that qualify for permission under the STM Permissions Guidelines, which may be updated from time to time, the STM Permissions Guidelines supersede the terms and conditions contained in this licence.

9. Termination and Cancellation

9. 1. Licences will expire after the period shown in Clause 3 (above).

9. 2. Licensee reserves the right to terminate the Licence in the event that payment is not received in full or if there has been a breach of this agreement by you.

Appendix 1 — Acknowledgements:

For Journal Content:
Reprinted by permission from [**the Licensor**]: [**Journal Publisher** (e.g. Nature/Springer/Palgrave)] [**JOURNAL NAME**] [**REFERENCE CITATION** (Article name, Author(s) Name), [**COPYRIGHT**] (year of publication)

For **Advance Online Publication papers:**
Reprinted by permission from [**the Licensor**]: [**Journal Publisher** (e.g. Nature/Springer/Palgrave)] [**JOURNAL NAME**] [**REFERENCE CITATION** (Article name, Author(s) Name), [**COPYRIGHT**] (year of publication), advance online publication, day month year (doi: 10.1038/sj.[JOURNAL ACRONYM].)

For Adaptations/Translations:
Adapted/Translated by permission from [**the Licensor**]: [**Journal Publisher** (e.g. Nature/Springer/Palgrave)] [**JOURNAL NAME**] [**REFERENCE CITATION** (Article name, Author(s) Name), [**COPYRIGHT**] (year of publication)

Note: For any republication from the British Journal of Cancer, the following credit line style applies:

Reprinted/adapted/translated by permission from [**the Licensor**]: on behalf of Cancer Research UK: : [**Journal Publisher** (e.g. Nature/Springer/Palgrave)] [**JOURNAL NAME**] [**REFERENCE CITATION** (Article name, Author(s) Name), [**COPYRIGHT**] (year of publication)

For **Advance Online Publication** papers:
Reprinted by permission from The [**the Licensor**]: on behalf of Cancer Research UK: [**Journal Publisher** (e.g. Nature/Springer/Palgrave)] [**JOURNAL NAME**] [**REFERENCE CITATION** (Article name, Author(s) Name), [**COPYRIGHT**] (year of publication), advance online publication, day month year (doi: 10.1038/sj.[JOURNAL ACRONYM])

For Book content:
Reprinted/adapted by permission from [**the Licensor**]: [**Book Publisher** (e.g. Palgrave Macmillan, Springer etc) [**Book Title**] by [**Book author**(s)] [**COPYRIGHT**] (year of publication)

Other Conditions:

Version 1.3

Questions? **customercare@copyright.com** **or +1-855-239-3415 (toll free in the US) or +1-978-646-2777.**

"Remember kids, the only difference between screwing around and science is writing it down."

ADAM SAVAGE & ALEX JASON